Metallicity Map of M33

by

Alice H. Koning

A thesis submitted in partial fulfillment of the requirements for the degree of

Master of Science

Department of Physics

University of Alberta

Abstract

I use Keck I spectroscopic observations of 701 Hα sources in the nearby spiral galaxy M33 to determine oxygen, nitrogen, sulfur, and neon abundances in H II regions across the face of the galactic disk. Abundance measurements are obtained with two separate methods (PyNeb and NEAT) through the use of the only known direct metallicity determination method, which relies on detections of weak, temperature-sensitive auroral lines. This data set is approximately double the size of any previous H II region metallicity study in M33. Reliable oxygen abundances are determined for 88 H II regions with PyNeb, and 108 H II regions with NEAT (with significant overlap between the two samples).

I investigate the temperature and density distributions, as well as the relation between strong-line metallicity indicators and the metallicity derived from weak auroral lines. I plot radial abundance gradients for [O/H], [N/H], [N II/O II], [S/H], [S/O], [Ne/H], and [Ne/O]. The [O/H] gradient has more scatter than the [N/H] gradient, although both show clear signs of decreasing abundances with increasing galactic radius. The [N II/O II] gradient supports previous evidence that the nitrogen abundance falls off more rapidly than oxygen at larger radii. Conversely, the [Ne/O] gradient indicates that neon falls off more slowly than oxygen at larger radii. The sulfur radial gradient is consistent with a flat slope.

I present 2D metallicity maps for [O/H], [N/H], and [N II/O II]. The [O/H] map indicates significant azimuthal fluctuations across the disk of M33, although it is uncertain whether the dominant factor is true azimuthal structure or the relatively large uncertainties on the oxygen abundance measurements. The [N/H] and [N II/O II] abundance maps are much smoother than the [O/H] map.

Preface

This thesis makes use of observations taken on the Keck I telescope by Erik W. Rosolowsky and Josh D. Simon in 2004, 2007, and 2008. Preliminary results from the observations taken in 2004 were published as Rosolowsky, E. and J. D. Simon. "The M33 Metallicity Project: Resolving the Abundance Gradient Discrepancies in M33." The Astrophysical Journal 675 (March 2008): 1213? 1222.

This thesis is an original work by Alice H. Koning—no part of this thesis has been previously published as it is presented herein. I (AHK) was responsible for reducing all the observations (including those from 2004 that had already been reduced by EWR and JDS) with a modified version of XIDL. Most modifications that were made to XIDL were investigated and implemented by me, however a substantial amount of work to improve the sky subtraction was completed by EWR.

Dedicated to Alex,
My favourite thinking and drinking buddy.

Acknowledgements

First and foremost, I must thank my supervisor, Erik Rosolowsky, who has driven me to learn more than I ever thought I needed to know about interstellar chemistry, the real life hardships colour-blind people face every day, and the importance of drinking while grading. . . And thanks for letting me escape to Greece for a month! But seriously, thank you so much for everything you've done for me, Erik.

I thank Josh Simon for many insightful comments into the data reduction process, and the Observatories of the Carnegie Institution of Washington for hosting my week-long visit in January so I could witness people wearing down winter coats in *literally* 15° C weather. My committee members and all other members of the Astronomy group at the University of Alberta also deserve my thanks for supporting me over the past two years. Even if sometimes this support was heavily masked by sarcasm, I know it was there.

Regarding the actual data, this research made use of APLpy, an open-source plotting package for Python hosted at http://aplpy.github.com, and I would also like to acknowledge Jason X. Prochaska for his assistance with and the use of XIDL. I am grateful to the Keck telescope and the indigenous Hawaiian community for the opportunity to conduct observations from the summit of Mauna Kea. I acknowledge the funding support I received from NSERC of Canada.

Contents

List of Tables

List of Figures

CHAPTER 1

Introduction

The aim of my thesis is to calculate the oxygen abundance in numerous H II regions across the face of the spiral galaxy M33 as part of an ongoing work called the M33 Metallicity Project. In §1.1, I give an overview of the source of various elements in the Universe, including oxygen, and a discussion of how the abundances of these elements evolves over cosmic time. I describe the importance of my observations in a larger context in §1.2, while an explanation of how my observations yield oxygen abundance measurements in H II regions is given in §§1.3–1.5. Lastly, I provide a complete description of the M33 Metallicity Project in §1.6.

1.1   Cosmic chemical abundances

Hydrogen and helium compose roughly 98% of the visible baryonic matter in the Universe. All the hydrogen and nearly all of the helium in the Universe today was created within the first $\sim$ 3 min after the Big Bang, in a process known as Big Bang Nucleosynthesis (BBNS). At a much later time, the vast majority of all metals[1] and a small percentage of helium were produced through stellar nucleosynthesis and supernovae. Thus, the chemical abundances in stars and the interstellar medium (ISM) of hydrogen, helium, and metals have a profound effect on our understanding of the standard cosmological model, stellar processes, and galactic chemical evolution.

---

[1]In astronomy, all elements other than hydrogen or helium are referred to as "metals", and the "metallicity" is the abundance of these heavy elements. That said, throughout this work, "metallicity" will usually refer to, specifically, the oxygen abundance, since oxygen is the third most abundant element after hydrogen and helium, making it the most readily observed metal.

1.1.1   Big Bang nucleosynthesis

Big Bang nucleosynthesis refers to the creation of light elements—namely hydrogen, helium, and lithium—during the Big Bang. The major reactions that created these elements are as follows

$$p + n \rightarrow D + \gamma$$
$$D + n \rightarrow {}^3H + \gamma$$
$$D + p \rightarrow {}^3He + \gamma$$
$${}^3H + p \rightarrow {}^4He + \gamma$$
$${}^3He + n \rightarrow {}^4He + \gamma$$
$$D + D \rightarrow {}^3H + p$$
$$D + D \rightarrow {}^3He + n$$
$${}^3He + D \rightarrow {}^4He + p$$
$${}^3H + D \rightarrow {}^4He + n$$
$${}^3H + {}^4He \rightarrow {}^7Li + \gamma.$$
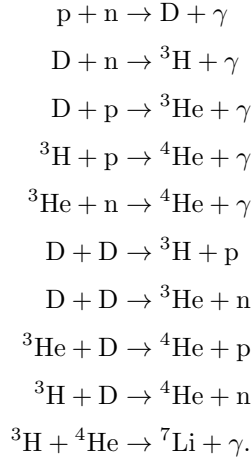
According to BBNS, the primordial abundances of the light elements D, ^{3}He, ^{4}He, and ^{7}Li relative to hydrogen are functions of the baryon to photon ratio. This is because it is the average photon energy that determines what nuclear reactions will occur at any given Universal epoch. Accurately determining the primordial helium abundance[2], Y_p, is therefore critical to testing the consistency of the BBNS theory.

One method of establishing Y_p that has seen some success is to plot the helium abundance, Y, of hot H ii regions with low metallicities and weak underlying stellar continua, against the metallicities, Z, of the H ii regions. By assuming $Z_p = 0$ during the epoch of BBNS, it is clear that the intercept of this plot will correspond to the primordial helium abundance: $Y = Y_p + Z(dY/dZ)$. Using this technique Pagel et al. (1992) determined $Y_p = 0.228 \pm 0.005$.

1.1.2   Stellar fusion nucleosynthesis

Stellar nucleosynthesis and supernovae must have produced all the metals present in the Universe today, since the processes required for their formation did not exist in the era of BBNS. Although metals only compose ∼2% of the Universe by mass, planets such as the

---

[2]According to convention, X refers to the mass fraction of hydrogen, Y to the mass fraction of helium, and Z to the current metallicity or mass fraction of metals. The addition of the subscript $_p$ denotes primordial abundances.

Earth and all of its countless life forms could not exist without them, and the presence of metals significantly alters the heating and cooling rates of the ISM. Stars derive energy from nucleosynthesis by fusing protons and neutrons into more stable nuclei, which releases energy. Some of the key processes by which they do this are called the p-p chain, the CNO cycle, the s-process, and the r-process. Each of these will be briefly explained.

The p-p chain and CNO cycle are both processes that convert hydrogen to helium. The p-p chain begins by converting two protons to a ^{3}He nucleus:

$$p + p \rightarrow {}^2H + e^+ + \nu$$
$$^2H + p \rightarrow {}^3He + \gamma.$$
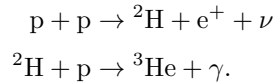
The ^{3}He may then collide with another ^{3}He to form ^{4}He and two protons, or it may interact with an already formed ^{4}He and proceed to make two ^{4}He nuclei,

$$^3He + {}^4He \rightarrow {}^7Be + \gamma$$
$$^7Be + e^- \rightarrow {}^7Li + \nu$$
$$^7Li + p \rightarrow 2 \; {}^4He.$$
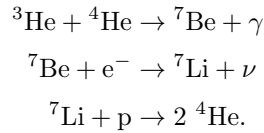
Alternatively, hydrogen may fuse to form helium through the CNO cycle. This cycle uses carbon, nitrogen, and oxygen as catalysts, and has multiple branches due to its inherent complexity compared to the p-p chain. The most important branch is:

$$^{12}C + p \rightarrow {}^{13}N + \gamma$$
$$^{13}N \rightarrow {}^{13}C + e^+ + \nu$$
$$^{13}C + p \rightarrow {}^{14}N + \gamma$$
$$^{14}N + p \rightarrow {}^{15}O + \gamma$$
$$^{15}O \rightarrow {}^{15}N + e^+ + \nu$$
$$^{15}N + p \rightarrow {}^{12}C + {}^4He.$$
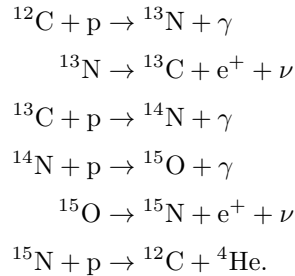
At low temperatures (i.e., in low mass stars) the p-p chain is the dominant helium formation reaction because it takes less energy to fuse two protons than to fuse a proton and a carbon nuclide. The CNO cycle takes over at high temperatures (i.e., in high mass stars) because it is faster than the p-p chain process (Hansen et al., 2004). The transition between which process dominates occurs at stellar masses of $M \sim 1.3 \; M_\odot$ (Salaris and Cassisi, 2005), where M is the initial mass of the star and $M_\odot$ is the mass of the Sun.

All stars with initial masses $M \gtrsim 0.8 \; M_\odot$ evolve along the Red Giant Branch (RGB) once the hydrogen fuel in their cores is depleted and therefore nuclear fusion reactions must come

to a halt. While on the RGB, hydrogen fusion occurs in a shell surrounding an inert helium core and the core contracts due to the absence of any exothermic nuclear reactions occurring in the core. Regardless of the star's initial mass, hydrogen shell burning always proceeds via the CNO cycle (Hansen et al., 2004), which is the dominant source of nitrogen in the Universe (discussed further in §1.1.4).

As the star contracts, the core temperature rises until the helium in the core is hot enough to begin fusing. Whether or not this helium ignition is a peaceful process depends on the initial mass. Stars of $M \gtrsim 1.5\ M_\odot$ ignite helium peacefully because the core temperature attains sufficiently high temperatures when the core is still at low enough densities that it is not degenerate (i.e., the core density is less than 10^6 g/cm^3). Meanwhile, stars with M between 0.8–1.5 $M_\odot$ ignite helium in a short-lived "flash" because the high temperatures required for this are not attained until the core is partially degenerate (i.e., the core density is approximately 10^6 g/cm^3). Regardless of how helium burning begins, stars that have reached the red giant phase burn helium via the triple-α-process in their cores for about 10% as long as the main-sequence hydrogen core burning phase lasted (Hansen et al., 2004).

The triple-α-process converts three ^{4}He nuclei into one ^{12}C nuclide:

$$^4\mathrm{He} + {}^4\mathrm{He} \rightarrow {}^8\mathrm{Be} + \gamma$$
$$^8\mathrm{Be} + {}^4\mathrm{He} \rightarrow {}^{12}\mathrm{C}^* + \gamma$$
$$^{12}\mathrm{C}^* \rightarrow {}^{12}\mathrm{C} + \gamma.$$
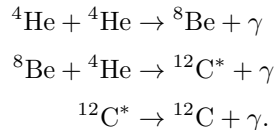
If a fourth α particle is available, helium burning will also produce oxygen

$$^{12}\mathrm{C} + {}^4\mathrm{He} \rightarrow {}^{16}\mathrm{O} + \gamma.$$
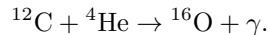
Further α particles can be used to form ^{20}Ne and ^{24}Mg, however carbon and oxygen are the dominant products of helium burning due to the low reaction rates of the neon and magnesium reactions (Meyer et al., 2006; LeBlanc, 2010). It should also be noted that lower mass stars produce more carbon than oxygen from helium burning, whereas higher mass stars favour oxygen (Hansen et al., 2004).

At the end of the red giant phase, helium core burning ceases because the fuel has once again been exhausted, leaving behind a C-O core. As before, the star contracts, and eventually a shell of helium surrounding the core is hot enough to ignite. A second shell of hydrogen CNO burning continues to survive, and the star now evolves along the Asymptotic Giant Branch (AGB). Stars along the AGB have very strong winds that result in the loss of up to 50% of the initial mass through the removal of envelope material (Hansen et al., 2004). At the end of the AGB phase, lower mass stars ($M \sim 0.8$–8 $M_\odot$) end their lives by ejecting their remaining outer layers in what is known as a planetary nebula, leaving behind the

core of the original star in the form of a C-O white dwarf. Higher mass stars ($M \gtrsim 8\ M_\odot$) continue the cycle of fuel exhaustion, followed by core contraction, which heats the core and ignites the next stage of nuclear burning for heavier and heavier elements.

Table 1.1 outlines the order in which the major nuclear burning phases occur for a 25 $M_\odot$ star. As each new phase commences, a shell of the previous phase surrounds the core, followed by the shells of all other previous phases (as shown in Figure 1.1). Table 1.1 also shows that the duration of each phase decreases as the star evolves because the prevailing reactions produce less energy per nuclear reaction yet the luminosity increases with each phase due to an increase in the reaction rate as the core temperature increases. Stellar fusion nucleosynthesis ceases when the nuclei in the core are at their most stable and therefore unable to produce energy through fusion. These "most stable" nuclei are ^{56}Fe and all of its atomic neighbours (Sc, Ti, V, Cr, Mn, Co, Ni, and Cu), called the iron-peak nuclides (Binney and Merrifield, 1998).

Thus, at the end of a $M \gtrsim 8\ M_\odot$ star's lifetime, the core is iron rich. At this stage, the weight of the outer layers is supported by electron degeneracy pressure rather than thermal pressure. In other words, the core resembles a white dwarf star. Chandrasekhar (1931) derived the maximum mass of an ideal white dwarf star based on how much weight the degeneracy pressure could support. Analogously, when the degenerate iron-rich core attains its Chandrasekhar mass, the degeneracy pressure is no longer able to support the weight of the outer layers of the star so the core collapses (Baron and Cooperstein, 1990).

During core collapse, temperatures in the core are so high that the iron nuclei are photo-disintegrated, such as by the reaction

$$^{56}\text{Fe} + \gamma \rightarrow 13\ ^4\text{He} + 4\ \text{n}.$$
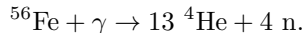
This reaction removes γ-rays from the radiation field, which decreases the core pressure further, thereby speeding up the contraction. Eventually even helium is destroyed through photodisintegration, leaving a core composed mainly of protons and electrons. These in turn fuse to form a core of neutrons ($\text{p} + \text{e}^- \rightarrow \text{n} + \nu_\text{e}$). The removal of electrons reduces the degeneracy pressure, which once again feeds the core contraction, forming a neutron star (or black hole in stars more massive than $\sim$ 25 $M_\odot$, Hansen et al. 2004). During this process, the outer layers detach from the rapidly collapsing core and later get expelled as a supernova (Types Ib, Ic, and II).

In addition to the aforementioned nuclear burning phases, stars can also go through "dredge-up" phases where elements created in the core by nuclear fusion are brought to the surface of the star through convective mixing. Specifically, during the transition from hydrogen burning to helium burning in the core and helium burning to heavier element burning (i.e.,
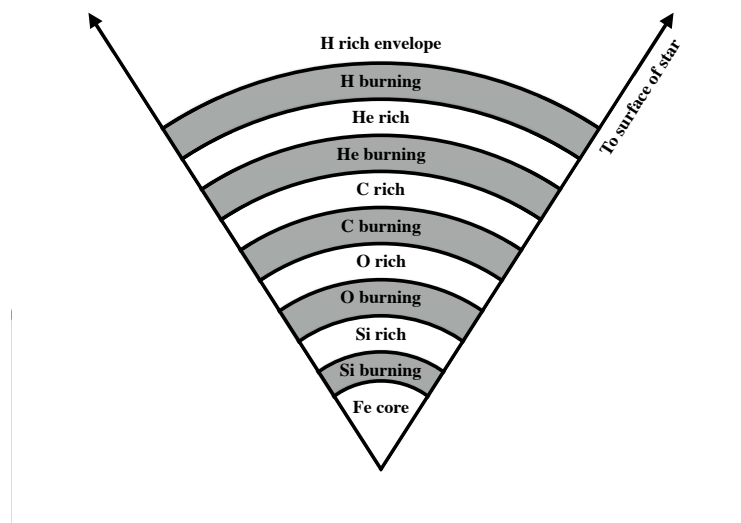
Figure 1.1 Schematic of the onion-like shell structure of a massive star after silicon burning has commenced (not to scale).

Table 1.1.   Phases of nuclear burning in a 25 $M_\odot$ star

Burning phase	Primary products	Core temperature K	Core density g cm^{-3}	Timescale
H	He	6.0×10^7	5	6×10^7 years
He	C,O	2.0×10^8	700	5×10^5 years
C	O,Ne,Mg	9.0×10^8	2×10^5	600 years
Ne	O,Mg,Si	1.7×10^9	4×10^6	6 months
O	Si,S	2.3×10^9	10^7	6 days
Si	Fe, Fe-peak nuclides	4.0×10^9	3×10^7	1 day

Note. — Adapted from Arnould and Samyn (2000) Figure 20.

RGB and AGB stars), the convective zone at the surface of the star deepens to include radii closer to the centre of star that have been enriched through hydrogen burning. These enriched products travel through the convective zone to the surface of the star in the first dredge-up phase. A second dredge-up phase occurs when the convective zone deepens again during the transition from helium to carbon burning. These dredge-up phases are more important in higher mass stars ($M \gtrsim 2.5M_\odot$) since in lower mass stars the convective zones do not grow as deep, and the shell burning between dredge-up phases can act to erase the effects of the dredge-up (Boothroyd and Sackmann, 1999).

That said, low-mass stars can be dramatically affected by "cool bottom processing" (CBP), an alternative mixing mechanism to dredge-up. Below the convective envelope in lower mass stars, there lies a radiative energy transport zone. In CBP, material is slowly brought from the convective zone at the surface, through the radiative zone to the hydrogen burning shell, then returned to the surface. As this material encounters the hydrogen burning shell, it is enriched through the permissible nuclear processes. Importantly, CBP has been shown to correctly predict the $\frac{^{12}C}{^{13}C}$ ratio observed at the surfaces of low-mass red giants (e.g., Wasserburg et al., 1995; Boothroyd and Sackmann, 1999).

1.1.3   Heavy element nucleosynthesis

BBNS and stellar nucleosynthesis cannot fully explain the abundances of all the elements observed in the Universe today. Two important paths by which nuclei heavier than ^{56}Fe are formed are known as the s- and r-processes, where "s" and "r" refer to the slow and rapid speeds at which they proceed. Some heavy elements are formed when there is a weak neutron flux, through the s-process. Others require a strong neutron flux and form through the r-process. The strength of the neutron flux varies with the age of the star, so it is possible for both types of heavy elements to be produced in the same star.

A weak neutron flux is generated from previous reactions which took place in the star, such as during carbon and oxygen burning (LeBlanc, 2010)

$$^{12}C + {}^{12}C \rightarrow {}^{23}Mg + n$$
$$^{16}O + {}^{16}O \rightarrow {}^{31}S + n.$$
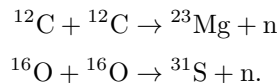
In the s-process, an already present iron-peak nuclide or stable heavy element from a previous stellar generation captures a free neutron to form an unstable isotope. The unstable isotope β^--decays ($n \rightarrow p + e^- + \bar{\nu}_e$) before capturing another free neutron. This process of neutron capture followed by β^--decay repeats until the reactions producing free neutrons cease or a stable isotope is formed. An example of how the s-process can transform a ^{114}Cd nuclide

into ^{116}Sn is

$$^{114}\text{Cd} + \text{n} \rightarrow {}^{115}\text{Cd} + \gamma$$
$$^{115}\text{Cd} \rightarrow {}^{115}\text{In} + \text{e}^- + \bar{\nu}_\text{e}$$
$$^{115}\text{In} + \text{n} \rightarrow {}^{116}\text{In} + \gamma$$
$$^{116}\text{In} \rightarrow {}^{116}\text{Sn} + \text{e}^- + \bar{\nu}_\text{e}$$
$$^{116}\text{In} + \text{n} \rightarrow {}^{116}\text{Sn} + \gamma.$$
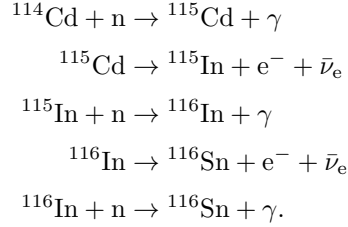
In the above reactions, ^{115}Cd has a half-life of 54 hours and ^{116}In has a half-life of 14 seconds. All other isotopes are stable.

Alternatively, a strong neutron flux can be created either when the core temperature reaches values higher than approximately 10^9K (such that high energy photons can eject a neutron from nuclei), or during the late evolutionary stage of high mass stars when protons and electrons in the core fuse to form neutrons ($\text{p} + \text{e}^- \rightarrow \text{n} + \nu_\text{e}$) (LeBlanc, 2010). When this occurs, the r-process works to form heavy elements. In the r-process, an initial neutron capture results in the production of an unstable isotope, however there is not enough time for the unstable isotope to β^--decay before a second neutron capture occurs. Free neutrons continue to be captured until the nucleus is so unstable that the time for β^--decay becomes comparable to the time between successive neutron captures. At this point, the nucleus will β^--decay until it reaches a stable state. An example of this process is in the production of ^{122}Sn from ^{115}In

$$^{115}\text{In} + \text{n} \rightarrow {}^{116}\text{In} + \gamma$$
$$^{116}\text{In} + \text{n} \rightarrow {}^{117}\text{In} + \gamma$$
$$^{117}\text{In} + \text{n} \rightarrow {}^{118}\text{In} + \gamma$$
$$^{118}\text{In} + \text{n} \rightarrow {}^{119}\text{In} + \gamma$$
$$^{119}\text{In} + \text{n} \rightarrow {}^{121}\text{In} + \gamma$$
$$^{121}\text{In} + \text{n} \rightarrow {}^{122}\text{In} + \gamma$$
$$^{122}\text{In} \rightarrow {}^{122}\text{Sn} + \text{e}^- + \bar{\nu}_\text{e}.$$
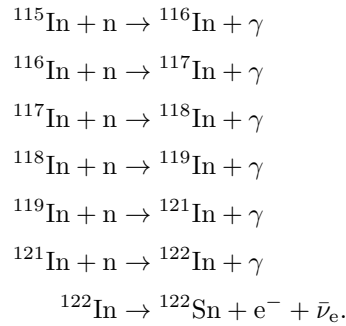
1.1.4   Primary and secondary enrichment elements

Primary enrichment elements can be made in a star that was purely hydrogen at birth, and therefore the yield of primary enrichment elements from a star is independent of the star's initial metallicity. Conversely, secondary enrichment elements require the presence of a primary enrichment element from a previous stellar generation, and therefore the yield is

dependent on the star's initial metallicity.

For example, oxygen is a primary element because it is produced during helium burning (Meyer et al., 2006), so the final abundance has no dependence on the initial metallicity of the star. Meanwhile, nitrogen can behave as either a primary or secondary element. This is because the synthesis of nitrogen mainly happens through the CNO cycle, and the reaction $^{14}\text{N} + \text{p} \rightarrow\ ^{15}\text{O} + \gamma$ is the bottleneck of the entire cycle. Therefore, the cycle achieves equilibrium only when high levels of ^{14}N accumulate (Henry et al., 2000; Hansen et al., 2004). In other words, after CNO-burning is complete, ^{4}He and ^{14}N are enriched, while ^{12}C and ^{16}O are depleted (Meyer et al., 2006). For metal-poor stars, the carbon and oxygen that form nitrogen are they themselves primarily created within the star, making the yield of nitrogen independent of the initial metallicity (like a primary element). For metal-rich stars, the yield of nitrogen primarily depends on the initial amounts of carbon and oxygen and therefore behaves as a secondary element (Esteban et al., 2001).

Thus, the abundance ratio [N/O], or its frequently used proxy [N II/O II] (Peimbert, 1967), traces primary versus secondary enrichment products. Due to the the dual nature of nitrogen, at low metallicity, [N II/O II] is constant as a function of oxygen abundance (underabundant), but at high metallicity [N II/O II] increases as a function of oxygen abundance (overabundant) (e.g., Peimbert, 1975; Andrews and Martini, 2013). The transition between the two regimes marks the transition between primary and secondary nitrogen. Mapping the [N II/O II] ratio in various stellar environments (e.g., different types of galaxies, or at different radii within a single galaxy) is important for constructing accurate enrichment models, and it can also aid in deriving the primordial helium abundance (Pagel and Kazlauskas, 1992).

1.1.5 Injection of metals into the ISM

The initial mass of a star affects everything from the duration of the star's lifetime to the type of stellar remnant that will eventually form. Of particular importance to the current work is how the initial mass affects the star's ability to enrich the ISM, as well as through what mechanisms this enrichment takes place.

Low mass stars ($M \lesssim 0.8\ M_{\odot}$) have lifetimes longer than the age of the Universe (10^{11}–10^{12} years for a 0.1 $M_{\odot}$ star, Hansen et al. 2004). This is partly due to their low luminosity and accordingly low rate of fuel consumption, and partly due to the abundance of fuel available to the hydrogen burning in the core thanks to the fact that these low mass stars are expected to be completely convective (meaning the expended hydrogen in the core is continually replenished by unprocessed hydrogen from the outer layers). Additionally, there is not enough gravitational energy to ever achieve helium burning (Hansen et al., 2004).

Table 1.2. Stellar origins of ISM metals

Initial Stellar Mass $M_\odot$	Relevant Burning Phases	End State	ISM Metal Contribution
$\lesssim 0.8$	H (p-p chain)	—	—
0.8–1.5	H (p-p chain), He	Planetary nebula, White dwarf, (thermal instability supernova)	^{3}He, ^{14}N, (heavy elements)
1.5–8.0	H (CNO cycle), He	Planetary nebula, White dwarf, (thermal instability supernova)	^{14}N
8–25	H (CNO cycle), He, C, Ne, O, Si	Core-collapse supernova, neutron star	^{14}N, O, Fe, Fe-peak nuclides, heavy elements
$\gtrsim 25$	H (CNO cycle), He, C, Ne, O, Si	Core-collapse supernova, black hole	^{14}N, O, Fe, Fe-peak nuclides, heavy elements

Consequently, the material that composes these stars is not metal rich, and is locked in the star for very long time scales. Therefore, these stars do not contribute to the enrichment of the ISM (LeBlanc, 2010), and will not be considered further here.

As already discussed in §1.1.2, and reiterated in Table 1.2, stars of intermediate initial masses ($M \sim 0.8$–8.0 $M_\odot$) become planetary nebulae and white dwarfs, while high mass stars ($M \gtrsim 8$ $M_\odot$) end up as neutron stars and black holes after a core-collapse supernova. I will now look at which metals are injected into the ISM by these two mass categories in more detail. First, a closer look at the intermediate mass stars. From the description given in §1.1.2, it is clear that material is injected into the ISM primarily through the AGB winds and the ensuing planetary nebula ejection. Both of these events expel envelope material, whereas the core material remains locked in the white dwarf. The envelope material contains significant amounts of ^{14}N from CNO shell burning, as well as some ^{13}C, ^{17}O, and ^{23}Na (Arnett, 1996). Iben and Truran (1978) note that intermediate mass stars are the main contributors of ^{3}He in the ISM.

Another important mechanism by which intermediate mass stars inject enriched material into the ISM is through a specific class of supernova called Type Ia. In the simplest scenario, these supernovae occur when a white dwarf accretes mass from a binary companion star. At some point, enough matter will have accreted onto the white dwarf such that it is no longer able to support its own weight through degeneracy pressure, so it collapses. This collapse and resultant high temperatures lead to runaway thermonuclear reactions that produce so much energy the star explodes as a supernova. At higher densities—close to the centre of the white dwarf—isotopes such as the radioactive ^{56}Ni are produced (^{56}Ni then decays to ^{56}Co and ^{56}Fe). At lower densities—in the outer layers of the white dwarf—intermediate

mass elements are observed, most notably silicon (Mazzali et al., 2007). After a Type Ia supernova, the white dwarf is completely destroyed (no central remnant remains) and the heavy elements produced during the supernova event are injected into the ISM.

For high mass stars, material is injected into the ISM primarily through core-collapse supernovae. During a core-collapse supernova, several solar masses worth of envelope material is expelled (Detre, 2013). Although the iron in the photodisintegration region is destroyed when the core collapses, iron and other heavy elements that rose to the surface through the dredge-up processes survive and are injected into the ISM during the supernova event. The material ejected by the different types of supernovae do not have identical enrichment signatures. Matteucci and Greggio (1986) argue Type Ia supernovae contribute ∼70% of the observed iron in the ISM, while core collapse supernovae contribute the remaining iron and all, or nearly all, of the observed oxygen. Overall, even though high mass stars compose a tiny fraction of the total number of stars, they are by far the greatest contributors to the metal enrichment of the ISM.

1.2   Galactic metallicity gradients and enrichment models

Traditionally, the metallicity gradient in disk galaxies has been considered the key quantity that simplifies the study of very complex processes of metal enrichment and chemical evolution in a galaxy. Metal enrichment occurs in localized regions—notably due to star formation and supernovae explosions, but many other factors play a role (see §1.1)—and the metallicity gradient is affected by these enrichment processes. The metallicity gradient is therefore a vital constraint in models of star formation histories, stellar populations, the interstellar medium (ISM), and galaxy chemical evolution (e.g., Kudritzki et al., 2015; Werk et al., 2011).

Aller (1942) studied the spectra of "emission nebulosities" (what we now call H ɪɪ regions) in M33 and remarked "the O ɪɪɪ lines seem frequently prominent in those objects which are farther from the nucleus than 20′, while in those nebulosities nearer than 20′ these lines are often weak or missing." Although not fully understood by Aller at the time, this was in fact one of the first observations of a metallicity gradient in another spiral galaxy. Quantifying such gradients improved with the advent of enrichment models, which aided in the difficult task of converting emission line fluxes to metallicity values. For example, Searle (1971) made use of simple models in his study of several nearby galaxies to deduce the presence of three abundance gradients: O/H, N/H, and N/O. Searle observed a moderate rise in O/H towards the centres of galaxies was accompanied by a much larger increase in N/H.

The physical origin of these negative radial metallicity gradients in spiral galaxies remains unclear. Vila-Costas and Edmunds (1992) used data for some 30 spiral galaxies that was available in the literature and found evidence that the effective yield (or amount of newly created metals returned to the ISM compared to the amount of gas locked up in stars) "decreases with radius and/or increases with abundance". One plausible explanation of this relation is that galactic disks promote the inward drift of enriched gas, and gas at large galactic radii is replenished by the accretion of metal-poor intergalactic gas (Binney and Merrifield, 1998).

Other factors that must be taken into account are the effects of stellar "feedback". Stellar feedback acts on both small and large scales, and can act to either enhance or suppress star formation (Draine, 2011). At small scales, individual supernovae, radiation pressure, stellar winds and jets, outflows, and turbulence dominate the stellar feedback cycle (e.g., Franco and Cox, 1983; McKee, 1989). The cumulative effect of supernovae, spiral arms, the presence or absence of a central bar, and the inward drift of gas play a role at large scales (e.g., Firmani and Tutukov, 1994; Dobbs et al., 2011). Unfortunately, accounting for all these complex phenomena is difficult, so we must attempt to relate more straightforward proxies, such as metallicity gradients, to simplified enrichment models, such as the closed-box and leaky-box models.

The closed-box enrichment model, considers a galactocentric annulus, and assumes there is a constant total mass M made up of stars (M_*) and gas (M_g) contained within a volume that is not necessarily constant (R. J. Talbot and Arnett, 1971). It is assumed that the metallicity Z is zero at time zero, $Z(t = 0) = 0$, and a new generation of massive stars' heavy elements are instantaneously injected into the gas. The yield p of the remaining less-massive stars is the percentage of the stars' mass that is converted into heavy elements. Equating the change in gas mass to the mass of the newborn stars shows that the metallicity as a function of time is given by (R. J. Talbot and Arnett, 1971; Binney and Merrifield, 1998)

$$Z(t) = -p \ln \left[\frac{M_g(t)}{M_g(0)} \right]. \tag{1.1}$$

A variation on the closed-box model is the leaky-box model, where gas is driven from the galactocentric annulus by stellar winds and supernovae at a rate that is proportional to star formation (by a factor c). Then the yield is reduced by a factor $1/(1 + c)$, as compared to the closed-box model. Hartwick (1976) modified the closed-box model in this way so as to explain the observed [Fe/H] distribution in the Milky Way halo. However, neither the closed-box nor leaky-box models accurately predicts the under-abundance of low metallicity stars in the solar neighbourhood (the "G dwarf problem"), so there is certainly still room for improvement.

Advancements in enrichment models have allowed parameters such as radiative heating and cooling, radiation pressure, the growth and evaporation of cold clouds, galactic and stellar winds, and the supernova rate to be taken into account (e.g., Springel and Hernquist, 2003; Scannapieco et al., 2006; Hopkins et al., 2012). Constraints used in these simulations include the stellar mass to gas-phase metallicity relation, galaxy stellar mass function, and chemical enrichment of the ISM and intergalactic medium.

1.3 Metallicity determination methods: H II region observations

The type of object that is observed spectroscopically can have a significant effect on the measured metallicity value and uncertainties. Three options are usually considered: i) supergiant stars, ii) planetary nebulae, and iii) H II regions.

Compared to stellar populations as a whole, supergiants are a good target because they are relatively short-lived. This is important because metallicity changes as a function of both time and galactic position. A short-lived target cannot have wandered far from its birth site, so the resulting measurement will be well-constrained in both time and space, as is required to construct an accurate enrichment history. That said, using the spectra from supergiants is generally ill-advised because to translate the observed spectral line fluxes to metallicity values, a firm understanding of supergiant atmospheres is required. The current state of supergiant atmospheric models shows there is still much work required to match the observed properties to observations (e.g., Martins et al., 2005; Ekström et al., 2012) and so this introduces myriad uncertainties and assumptions into any metallicity measurement, thereby making the result less reliable than desired.

For the second target option, recall that the spectral fluxes measured in planetary nebulae include a bias in helium, nitrogen, and carbon because these elements are produced by the star during its lifetime. The metallicity at formation must therefore be reverse-engineered, which is unfortunately a rather difficult task, especially in metal-rich ISM conditions (Binney and Merrifield, 1998). Additionally, planetary nebulae are older than supergiant stars or H II regions, so it is possible their galacto-centric orbits have changed non-negligibly since birth. This leaves H II regions as the best choice to observe spectra that will be used to determine the current metallicity in the ISM at that location.

The term H II region refers to the sphere of photoionized gas surrounding a hot star. In such a region, photons emitted by the central star have energies above the ionization threshold of the gas, which is predominantly hydrogen. The ejected electrons have nonzero kinetic energy, thereby contributing to the heating of the gas. Meanwhile, cooling takes place primarily

Table 1.3. Principal collisionally excited cooling lines in optical spectra of H II regions

Ion	Lines	$h\nu$ (eV)
N II	6549 Å, 6583 Å	14.53
O II	3727 Å, 3729 Å	13.62
O III	4959 Å, 5007 Å	35.12
S II	6716 Å, 6730 Å	10.36
S III	9069 Å, 9531 Å	23.33

Note. — Adapted from Draine (2011) Tables 15.2 and 27.2.

through radiative recombination—which removes electrons from the plasma, along with their kinetic energy—and collisional excitation of metals, followed by radiative de-excitation—which transforms the kinetic energy of the exciting electron to a photon that escapes the gas and is observed as a Collisionally Excited cooling Line (CEL). The temperature of the gas ($\sim$6000K–15000K) and the geometrical extent of the H II region ($\sim$few pc) are governed by the balance between these heating and cooling processes (Binney and Merrifield, 1998; Draine, 2011).

Given that H II regions are composed largely of hydrogen and the most effective cooling process is the emission of CELs, the optical spectrum of an H II region is dominated by hydrogen Balmer lines and emission from CELs. Table 1.3 provides a brief overview of the principal CELs in H II regions. The ionizing radiation is strongest closest to the central star, so this is where the CELs associated with more highly ionized ions originate. Thus, the H II region can be considered to be composed of several spherical zones, according to what ions are present. For instance, the first ionization energy of oxygen (13.62 eV) is remarkably close to that of hydrogen (13.60 eV), so O II will be found wherever H II is present. The first ionization energy of helium however is much larger (24.59 eV), so the He II zone extends to a smaller radius than the H II zone. For the ions listed in Table 1.3, O III and S III are the only two that can only be found in the He II zone, while all the others can be found (roughly) anywhere H II is present.

1.4 Metallicity determination methods: Theory

H II regions are commonly assumed to be in thermal equilibrium, meaning that the heating and cooling rates balance one another. The dominant heating mechanism in an H II

region is photoionization, while the dominant cooling mechanism is through CEL radiation (Osterbrock, 1989), both of which are dependent on the local temperature and density. Understanding the heating and cooling mechanisms at work is essential to deriving the populations of excited atoms and ions in the medium. Therefore, to convert spectral data into information on ionic abundances, the temperature and density of the emitting medium must be known.

It is well-established that the main emission processes at work in low-density H II regions are two-body collisions. Specifically, collisional excitation followed by emission of a line photon, or photoionization followed by recombination with a free electron and radiative decay to lower levels. Osterbrock (1988) states that the emission coefficient must therefore be proportional to: (1) the density of the ion responsible for the emission line, (2) the free electron density, and (3) the rate of the process, which is itself a function of the temperature and the probability of the emission of a photon. The intensity of a line is an integral of the emission coefficient over the observed path through the H II region. However, if the ratio of two intensities is instead measured, then the free electron density and any spatial effects will cancel, assuming the two ions in question have the same distribution over the observed path length. Therefore, to calculate the abundance, n, of O III from the intensity, I, of [O III] $\lambda 5007$ Å relative to Hβ, the following equation can be used (Draine, 2011).

$$\frac{n(\text{O III})}{n(\text{H}^+)} = C \; \frac{I(\text{[O III]} \; \lambda 5007 \; \text{Å})}{I(\text{H}\beta)} \; T_4^{-0.37} \; e^{\frac{2.917}{T_4}},$$

where C is a known constant, T_4 is the temperature in units of 10^4 K, and $n(\text{H}^+)$ is the approximate local density in the H II region. Ionic abundances are then converted to element abundances by summing over all the ions present in the medium. For oxygen in H II regions, O II and O III are the only ions that can exist since O II has a nearly identical ionization energy to H II, and O IV has a greater ionization energy than all but the very hottest O stars can produce (and even then it will only be in very small quantities). Thus, the total oxygen abundance is simply

$$n(\text{O}) = n(\text{O II}) + n(\text{O III}). \tag{1.2}$$

But all of this is useless if we cannot determine the local temperature and density. In the most straightforward method, the ratios of two pairs of emission lines are all that is required to calculate the temperature and density. One pair of emission lines is widely spaced in energy but is approximately density independent, so it reveals the temperature of the ionizing medium. The second pair of lines is closely spaced in excitation energy—and therefore independent of temperature—but each line has a different collisional de-excitation rate, so it reveals the density of the ionizing medium (Osterbrock, 1989). This is also the

only known *direct* method to determine temperature and density and therefore metallicity.

The choice of which pairs of emission lines to use depends on the wavelength regime available from observations. For this study, optical spectra are observed, so the temperature is determined from the ratio [O III] λ4363 Å/[O III] $\lambda\lambda$4959,5007 Å and the density from the ratio [S II] λ6716 Å/[S II] λ6730 Å. Figure 1.2 shows the energy levels from which these optical transitions in O III and S II originate. It should be noted that [O III] λ4363 Å is an auroral line that is very difficult to observe due to how weak it is, so this method is called the weak-line or auroral-line method for metallically determination.

Figure 1.3 shows the behaviour of the O III temperature diagnostic ratio and S II density diagnostic ratio. In Figure 1.3a it is clear that for densities between 10^2–10^4 cm^{-3}, the ratio [O III] λ4363 Å/[O III] $\lambda\lambda$4959,5007 Å is completely density independent, while at slightly larger densities ($\sim 10^5$ cm^{-3}) there begins to be a slight density dependence. Regardless, the O III ratio increases monotonically over the entire temperature range plotted (4000–18000 K). In Figure 1.3b, the S II ratio decreases dramatically from density $\sim 10^2$ cm^{-3} to $\sim 10^4$ cm^{-3}, but is nearly unchanging at densities lower and higher than these. However, typical H II regions have temperatures and densities around 10^4 K and 10^0–10^4 cm^{-3} (Draine, 2011), so both ratios are well within their "useful regimes".

Unfortunately, as the metallicity increases, so does the cooling via metal lines. The electron temperature therefore decreases, meaning all the emission lines get fainter. The critical auroral line [O III] λ4363 Å, which even at high electron temperature is a weak emission line, becomes too faint to observe at low electron temperatures, so an alternative abundance indicator must be constructed. These alternative abundance indicators are called "empirical" because they are calibrated by plotting the new indicator against metallicities derived from auroral line measurements using the direct method. Empirical methods are employed whenever the auroral lines become too weak to observe, and so it comes as no surprise that each empirical indicator is based on strong-lines, as §1.5 explains.

1.5 Metallicity determination methods: Practical approach

The most widely used empirical strong-line method that is based on optical emission lines was first suggested by Pagel et al. (1979) and later revised by Pilyugin (2000). Pagel et al. (1979) argued the sum of O II and O III relative to Hβ should be used as the primary oxygen abundance diagnostic (in cases where the weak-line method could not be employed) because it "varies smoothly as a function of stellar effective temperature and oxygen abundance", but is nearly invariant with respect to other unknown parameters. By plotting this oxygen
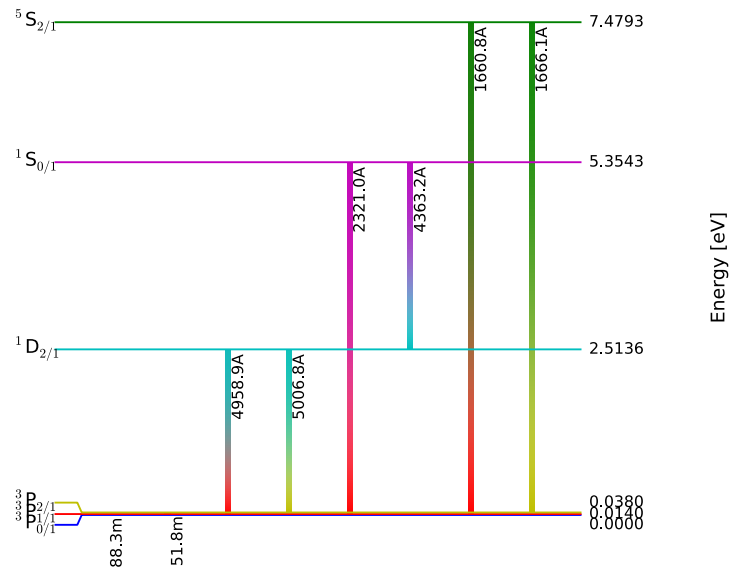
(a) O III
The weak auroral line [O III] $\lambda 4363$ Å originates from the $^1S_{0/1}$ energy level, while the lines [O III] $\lambda\lambda 4959,5007$ Å originate from the level $^1D_{2/1}$, which is much lower in energy. The large energy difference is what allows a temperature to be estimated from their ratio.
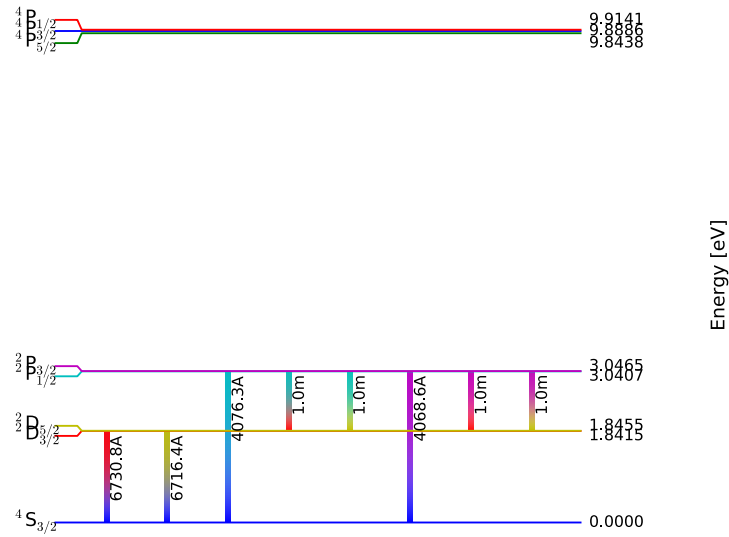
(b) S II
[S II] $\lambda 6716$ Å and [S II] $\lambda 6730$ Å originate from the splitting of the ^2D energy level. They require nearly the same energy to be excited, but the probability of exciting each level (given by the Einstein B coefficients) is dependent on the medium's density and is not the same for the two levels (Weedman, 1968).

Figure 1.2 Grotrian plots for the ions O III and S II. Produced using the PyNeb package.
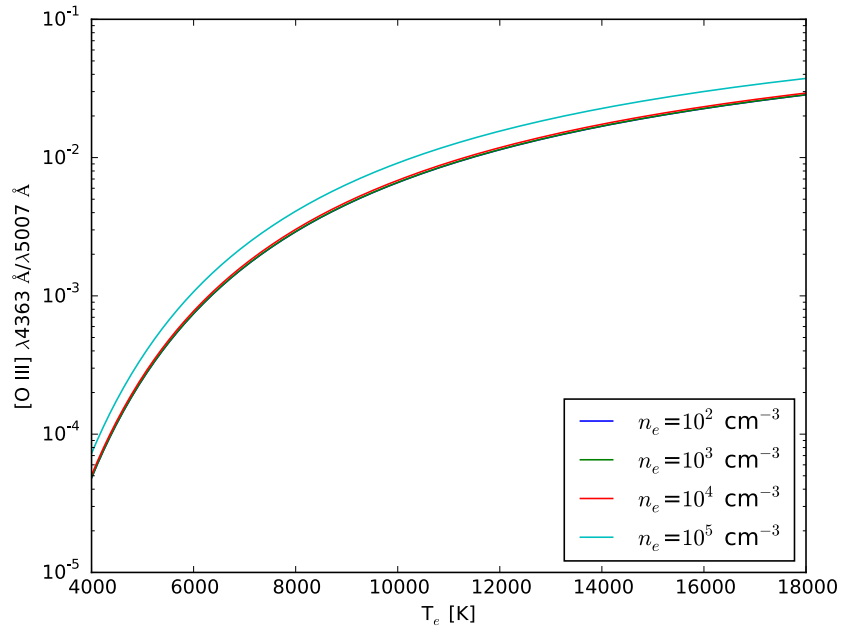
(a) Temperature diagnostic
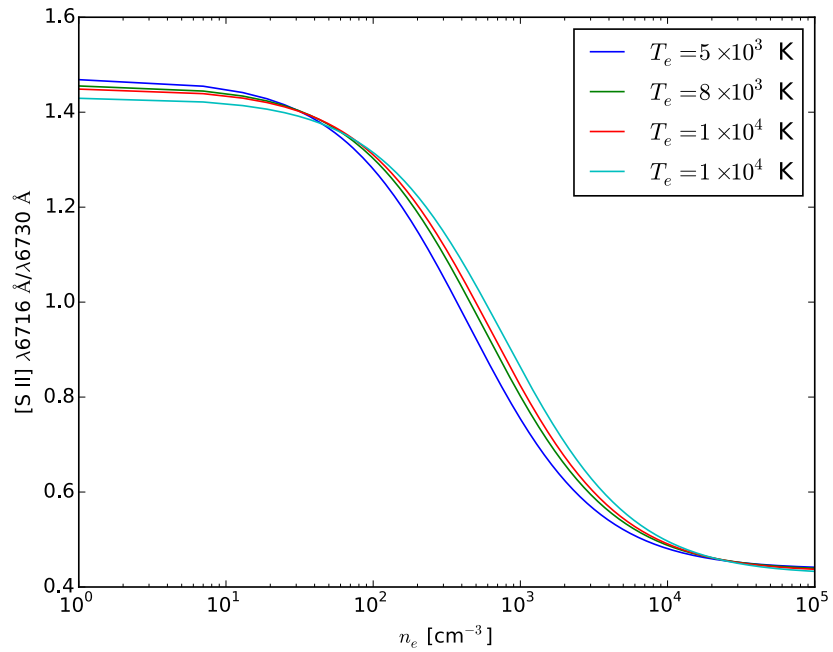
(b) Density diagnostic

Figure 1.3 Intensity ratios for temperature- and density-sensitive lines [O III] $\lambda 4363$ Å/[O III] $\lambda\lambda 4959,5007$ Å and [S II] $\lambda 6716$ Å/[S II] $\lambda 6730$ Å.

abundance diagnostic, called R_{23}, as a function of $12 + \log(O/H)$ and electron temperature from a handful of models and weak-line derived values, it was possible to derive a primitive calibration.

Pilyugin (2000) improved on this calibration thanks to advances in observational data quality and quantity. The $12 + \log(O/H)$ values used for the improved calibration came from a much larger data set of weak-line determined oxygen abundances than was available a couple decades earlier. Pilyugin (2000) defined the R_{23} diagnostic as

$$R_{23} = \log \frac{[\text{O \textsc{ii}}] \ \lambda\lambda 3726{,}3729 \text{ \AA} + [\text{O \textsc{iii}}] \ \lambda\lambda 4959{,}5007 \text{ \AA}}{\text{H}\beta} \tag{1.3}$$

and calibrated to produce the metallicity as

$$12 + \log(O/H) = 6.53 + 1.40 \ R_{23} \quad \text{for oxygen-poor H \textsc{ii} regions,}$$
$$12 + \log(O/H) = 9.50 - 1.40 \ R_{23} \quad \text{for oxygen-rich H \textsc{ii} regions.}$$

R_{23} is a robust metallicity indicator because all the quantities included in the fraction are proportional to electron density and most O atoms are either singly- or doubly-ionized in the H \textsc{ii} region, so R_{23} scales with oxygen abundance.

A few other strong-line abundance indicators are also worth mentioning. The definition of these indicators, as well as how each of them relates to the metallicity are as follows,

$$N_2 \quad = \log \frac{[\text{N \textsc{ii}}] \ \lambda 6583 \text{ \AA}}{\text{H}\alpha} \qquad 12 + \log(O/H) = 8.90 + 0.57 \ N_2$$

$$O_3N_2 \ = \log \frac{[\text{O \textsc{iii}}] \ \lambda 5007 \text{ \AA}/\text{H}\beta}{[\text{N \textsc{ii}}] \ \lambda 6583 \text{ \AA}/\text{H}\alpha} \quad 12 + \log(O/H) = 8.73 - 0.32 \ O_3N_2$$

$$Ar_3O_3 = \log \frac{[\text{Ar \textsc{iii}}] \ \lambda 7135 \text{ \AA}}{[\text{O \textsc{iii}}] \ \lambda 5007 \text{ \AA}} \qquad 12 + \log(O/H) = 8.91 + 0.34 \ Ar_3O_3 + 0.27 \ (Ar_3O_3)^2 + 0.20(Ar_3O_3)^3$$

$$S_3O_3 \ = \log \frac{[\text{S \textsc{iii}}] \ \lambda 9069 \text{ \AA}}{[\text{O \textsc{iii}}] \ \lambda 5007 \text{ \AA}} \qquad 12 + \log(O/H) = 8.70 + 0.28 \ S_3O_3 + 0.03 \ (S_3O_3)^2 + 0.1 \ (S_3O_3)^3$$

The metallicity relations for the first two indicators, N_2 and O_3N_2, were fit by Pettini and Pagel (2004), while the relations for the last two, Ar_3O_3 and S_3O_3, are from the work of Stasińska (2006). Each of these indicators has its own advantages and shortcomings. For example, Pettini and Pagel (2004) argue N_2 and O_3N_2 are better choices than R_{23} for high-redshift galaxies, where new difficulties arise due to both the faintness of the lines and the shift of optical lines to the near-infrared regime that is plagued by sky background signal and atmospheric absorption. In particular, O_3N_2 is an improvement over N_2 at solar and super-solar metallicities because N \textsc{ii} saturates but the intensity of O \textsc{iii} continues to decrease as metallicity increases.

On the other hand, Stasińska (2006) warns N_2 and O_3N_2 must be used with caution when the astrophysical nature (e.g., hardness of the ionizing radiation) of the objects being studied differs from that of the objects used to calibrate the relations. Furthermore, both indicators rely on the low-excitation line [N II] $\lambda 6583$ Å, which may originate from the diffuse ionized medium as well as the H II region in question. To circumvent these issues, Stasińska recommends the indicators Ar_3O_3 and S_3O_3, especially for integrating galaxy spectra in the low metallicity regime. The caveat at higher metallicities is that the calibration for Ar_3O_3 and S_3O_3 relied on $12 + \log(O/H)$ estimates from R_{23} measurements due to a lack of [O III] $\lambda 4363$ Å observations. Stasińska also notes that, unlike for N_2, a reliable reddening correction is needed for Ar_3O_3 and S_3O_3.

As already mentioned, the present work aims to measure weak-line metallicities for all observed H II regions, however strong-line metallicity measurements will also be available. This means another extremely important outcome of this study will be a further improved strong-line method calibration, thanks to the extraordinary number of data points that will be available with an oxygen abundance derived from both strong- and weak-line methods.

1.6 The M33 Metallicity Project

The M33 Metallicity Project aims to create the first high-resolution metallicity map of a spiral galaxy. M33, also referred to as the Triangulum Galaxy or NGC 598, is the optimal choice for such a study because it is the nearest relatively face-on spiral galaxy to the Milky Way (see Table 1.4). Its proximity means individual H II regions can be resolved even in the crowded central region—which therefore produces a higher resolution metallicity map than a more distant galaxy—and being face-on is crucial for avoiding projection effects when plotting the 2D metallicity map. Although the Andromeda spiral galaxy, M31, is closer to the Milky Way than M33, the plane of the Andromeda galaxy is at a more inclined angle. Additionally, M33 is smaller than M31 and this, combined with its sub-solar metallicity, means that the enrichment effects of one stellar generation are less likely to be washed away from the formation site in M33 compared to M31.

A number of key physical properties of M33 can be found in Table 1.4. It should also be noted that M33 is well-studied at many wavelengths, which means it will be possible to compare the completed 2D metallicity map produced here to previous studies' observations to look for any trends or anomalies.

As mentioned in §1.2, previous metallicity studies have only focused on measuring the radial gradient in a galaxy. Unfortunately, this approach may not reveal the whole story. For M33 in particular, many studies that have derived a metallicity gradient of the entire

Table 1.4. Physical properties of M33

Property	Unit	Value	Reference
Right Ascension (J2000)	h:m:s	01 33 50.9	Jarrett et al. (2003)
Declination (J2000)	°:′:″	+30 39 35.8	Jarrett et al. (2003)
Hubble Type		SA(s)cd	Jarrett et al. (2003)
Heliocentric Radial Velocity	km/s	−179	de Vaucouleurs et al. (1991)
Distance	kpc	840	Freedman et al. (2001)
Inclination	°	53	Magrini et al. (2009)
Major Axis	kpc	9.14	Jarrett et al. (2003)
Minor Axis	kpc	7.32	Jarrett et al. (2003)
Total Stellar Mass	$M_\odot$	3–6 $\times 10^9$	Corbelli (2003)

Table 1.5. Previously derived oxygen gradients of M33

Gradient $12 + \log(O/H)$ dex kpc^{-1}	Type of observations	Number of observations	Number of good data points	Galactic radial range kpc	Reference
-0.012 ± 0.011	HII	13	6[a]	1–7	Crockett et al. (2006)
-0.027 ± 0.012	HII	61	61	0–7	Rosolowsky and Simon (2008)
-0.031 ± 0.013	PNe	102	93	0–8	Magrini et al. (2009)
-0.07 ± 0.01	Supergiants	22	22	0–7	U et al. (2009)
-0.042 ± 0.010	HII	25	8[b]	0–8	Bresolin (2011)

[a]Combined with 5 data points from the literature for a total of 11.

[b]Combined with 42 data points from the literature for a total of 50.

galaxy are not consistent with one another, as seen in Table 1.5. Compared to the present work, each of the studies in Table 1.5 either only used a limited number of data points, or used observations of a type of object that is known to introduce further uncertainties (see §1.3). Using a limited number of data points is ill-advised since it is possible that a large scatter in the metallicity at any given radius could significantly affect the results and therefore contribute to the discrepancies seen between the studies outlined here. Note that Rosolowsky and Simon (2008) presented the preliminary results of this work, the M33 Metallicity Project.

Another interesting study (Beasley et al., 2015) observed stellar clusters in M33 and found evidence that the disc's radial metallicity gradient is getting less negative with time (d[M/H]dt/ dR = 0.03 dex/kpc/Gyr). This is an important finding since the temporal evolution of the disk's metallicity gradient is directly related to disk formation and growth. Other outcomes from the work on M33 of Beasley et al. that are pertinent to the present work are: i) young clusters are more metal-rich than older clusters (age-metallicity relation), ii) clusters have
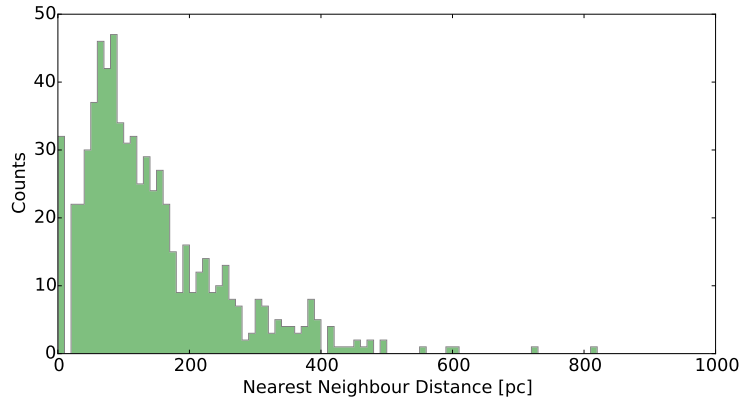
Figure 1.4 This histogram shows the distance to the nearest neighbouring H II region for each H II region that was observed. The peak near zero is an effect of the bin choice (10 pc) and the clustering of values at distances less than 5 pc (since this is the *nearest* neighbour). The shortest distance between two H II regions is 0.047 pc.

formed in the disk throughout the disk lifetime (no radial age gradient), and iii) the globular clusters of M33 are significantly more metal-rich than the globular clusters of the Milky Way halo, and may therefore be better associated with M33's disk rather than its halo.

For the M33 Metallicity Project, deep spectroscopy of 701 H II regions has been obtained from the Keck I 10-m telescope. These data cover the entire disk of M33 out to $\sim$7 kpc, with a mean sampling rate of $\gtrsim$ 2 measurements per square kpc, and sampling down to separations of $\lesssim$ 50 pc in some regions. Figure 1.4 shows a histogram of the distance to each observed H II region's nearest neighbour, and it can be seen that most nearest neighbours are closer than 200 pc.

By mapping the metallicity of the entire galactic disk in detail, we will not only acquire a less biased value of the gradient, but we will also be able to quantify the scatter at any given radius. Additionally, a whole new realm of possible studies will be opened up. For the first time, it will be possible to calculate a correlation function, and to relate the metallicity to a number of other quantities for which we already have 2D maps such as molecular gas, temperature, star formation rate, or star formation efficiency. We may also be able to place new constraints on the chemical evolution and mixing of metals produced in supernovae and AGB stars through the interstellar medium, and the role of turbulence.

The observations and data reduction process are described in §2. In §3 I explain how metallicity measurements were derived from the observations. Major astrophysical results are discussed in §4, followed by a summary of the entire work in §5.

CHAPTER 2

Observational Methods and Reduction

2.1 Instrument description

We obtained spectroscopic observations using the Keck I 10-m telescope on Mauna Kea. The Low-Resolution Imaging Spectrometer (LRIS) for the Cassegrain focus of this telescope has both imaging and spectroscopic capabilities. This instrument was used with custom-made slit masks for the M33 Metallicity Project. The field-of-view of LRIS is 6×7.8 arcmin. LRIS divides the incoming light into red and blue components using a dichroic mirror. The dichroic mirror reflects light $\lesssim \lambda 5500$ Å (blue component) and transmits light $\gtrsim \lambda 5500$ Å (red component). The blue component proceeds to a grism (combined diffraction grating and prism), while the red component proceeds to a diffraction grating. Each component is then imaged separately by two different CCD detectors, as depicted in Figure 2.1. The blue detector is composed of two Marconi CCD's, each of which has 2048×4096 back-side illuminated 15 μm pixels (Keck Observatory, 2015). The red detector is a cooled back-illuminated Tektronics Inc. 2048×2048 CCD which gives a sampling rate of 4.685 pixels per arcsec (Oke et al., 1995).

2.2 Observation details

Over the course of two nights in 2004, three nights in 2007, and three night in 2008, we observed 35 slit masks with one to four 15 minute exposures per slit mask (see Table 2.1 for details). The slit masks were placed across the face of M33's spiral disk, at galactic radii ranging from 0 to 7 kpc, as depicted in Figure 2.2. The 35 masks had an average of ~ 19
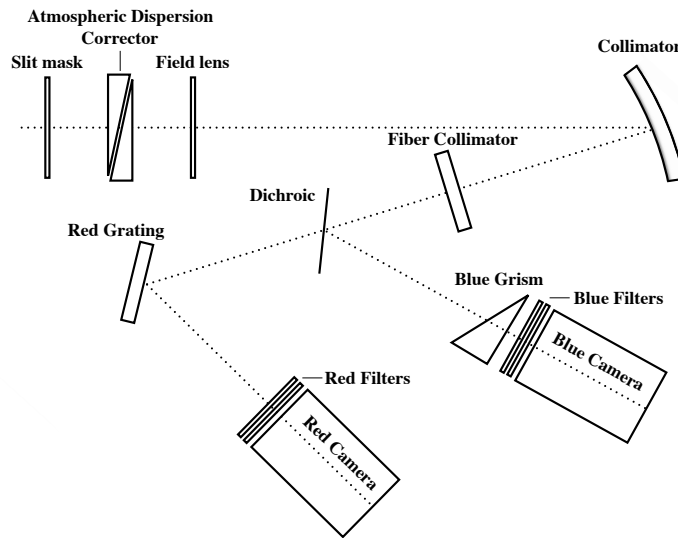
Figure 2.1 Schematic of LRIS's optical layout. Adapted from Figure 1 in Oke et al. (1995).

slits per mask, and each slit was $1''$ wide and at least $10''$ long. This produced spectra for 701 Hα sources in M33.

For each Hα source observed, I combine three separate spectra to produce the full spectral coverage required for the metallicity analysis: i) the Blue 600/4000 grism covers the wavelength range from [O II] $\lambda\lambda$3726,3729 Å to [O III] $\lambda\lambda$4959,5007 Å ii) the Red 900/5500 grating provides spectra from the D560 dichroic cutoff to well past the [S II] $\lambda\lambda$6716,6730 Å lines, iii) the Red 400/8500 grating produces spectra with lower resolution but a larger wavelength range (including the near-IR [S III] $\lambda\lambda$9069,9531 Å lines) compared to the Red 900/5500 spectra. Exact wavelength coverage depends on the slit's physical position relative to the CCD, so the ranges given here are approximate.

2.3 Spectrum extraction

I reduced the spectroscopic data using XIDL[1], an IDL code that is capable of reducing longslit and multislit data from a number of telescopes, including Keck/LRIS observations. This code was initially intended for use with faint point sources (quasars), not extended sources such as H II regions, which do not always lie at the centre of the slit with sky at the edges of the slit. To account for the differences between reducing faint point sources and extended H II regions, we had to extensively edit the sky subtraction and object identification

---

[1] http://www.ucolick.org/~xavier/IDL/
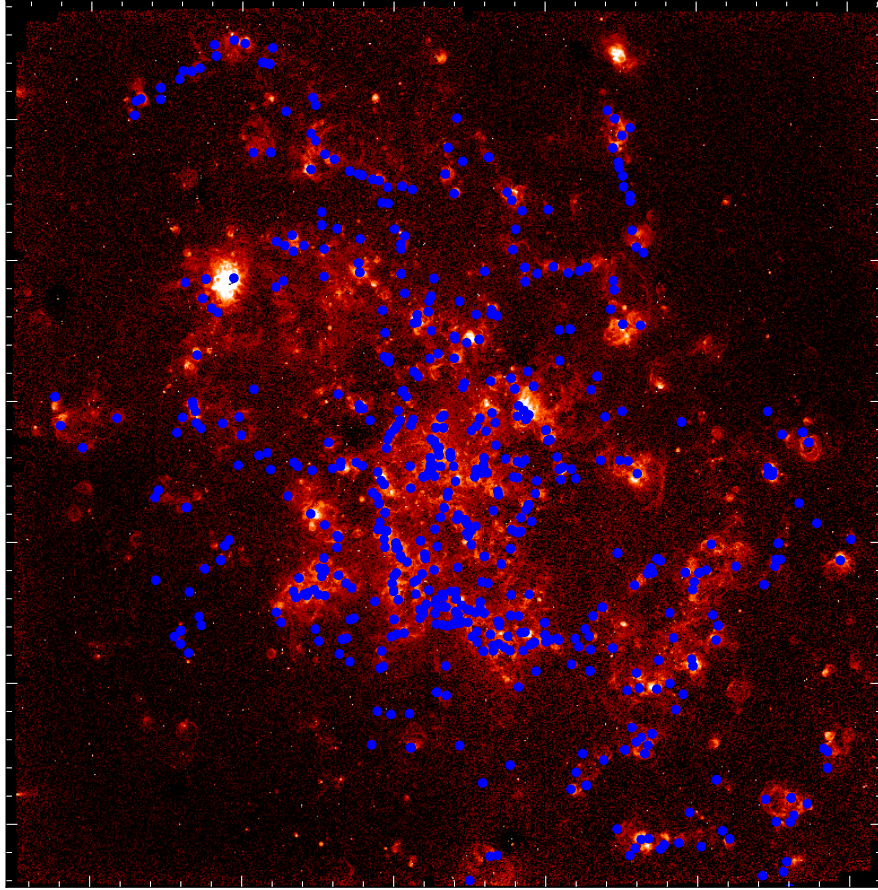
Figure 2.2 The relative positions of all observed slits across the galactic plane are shown as blue dots. These are superimposed on a continuum-subtracted Hα image of M33 produced from the survey data of Massey et al. (2006) displayed with a red colour scale.

Table 2.1. Observation details and number of exposures in each grating/grism

Date	Mask Designation	Number of Exposures			Comments
		Blue 600/4000	Red 900/5500	Red 400/8500	
2004 September 22	M33-1c	4	4	1	
2004 September 22	M33-2c	3	3	0	
2004 September 22	M33-3c	3	2	1	
2004 October 22	M33oct-2d	1	1	0	
2004 October 22	M33oct-3d	3	3	1	some clouds
2004 October 22	M33oct-4d	4	3	1	some clouds
2004 October 22	M33oct-5d	2	2	0	cloudy
2007 November 08	M33r3-3c	4	3	1	
2007 November 08	M33r3-6B	4	3	1	
2007 November 08	M33r3-10	4	3	1	
2007 November 09	M33r3-1c	3	3	1	
2007 November 09	M33r3-2c	3	3	1	
2007 November 09	M33r3-4c	2	3	1	
2007 November 09	M33r3-9c	4	3	1	
2007 November 09	M33r3-18c	4	3	1	
2007 November 09	M33r3-26c	3	2	0	
2007 November 10	M33r3-5c	3	1	0	
2007 November 10	M33r3-8	2	3	0	
2007 November 10	M33r3-11	4	2	1	
2007 November 10	M33r3-12b	4	3	2	
2007 November 10	M33r3-17	4	2	1	
2008 November 04	M33r3-15	2	2	0	cloudy
2008 November 04	M33r3-16	4	3	1	cloudy
2008 November 04	M33r3-22	4	3	1	cloudy
2008 November 04	M33r3-28	4	3	1	cloudy
2008 November 04	M33r3-30	4	3	1	very cloudy
2008 November 05	M33r3-20	6	5	1	
2008 November 05	M33r3-27	5	4	1	
2008 November 05	M33r4-1	4	3	1	some clouds
2008 November 06	M33r3-7	3	2	1	
2008 November 06	M33r3-13	4	3	1	some clouds
2008 November 06	M33r3-14	4	3	1	
2008 November 06	M33r3-21	4	3	1	
2008 November 06	M33r4-2	5	3	1	
2008 November 06	M33r4-3	4	3	1	
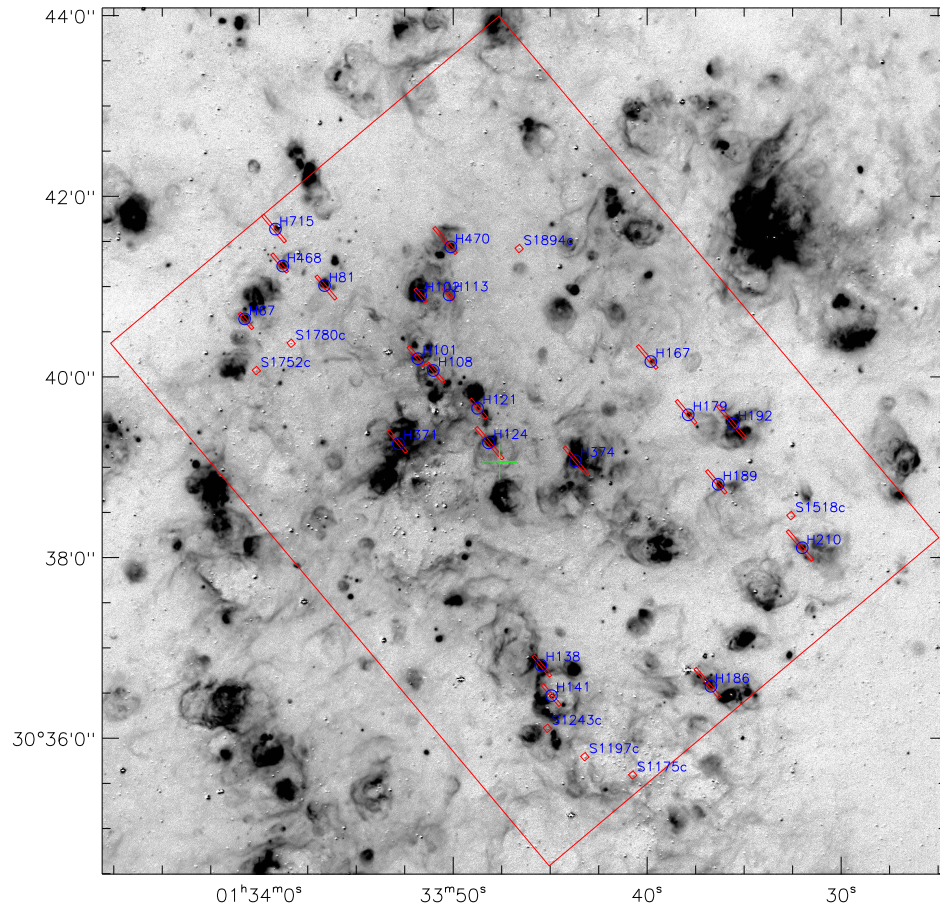
Figure 2.3 Example of how the slits were placed within the slit mask in order to observe as many H II regions as possible. The background grayscale image is an Hα map of the galaxy, the slit and alignment box positions are marked by open red rectangles and squares, the ID names are written in blue, and the mask dimensions are given by the large red rectangle that encompasses all the others. Notice that because the wavelength coverage shifts as the physical position of the slit shifts from side to side within the mask dimensions, all slits are as close to the centre of the mask as possible.

(a) H274 (b) H280
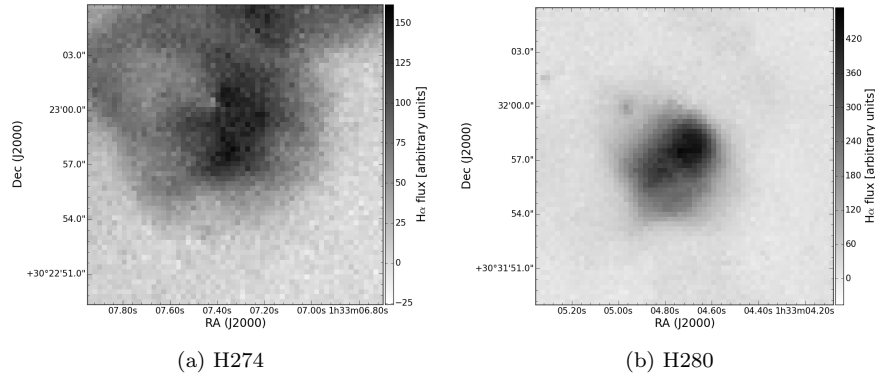
Figure 2.4 Example figures of target H II regions in Hα, highlighting the two main morphological types. H274 is a low surface brightness, extended H II region. H280 is a high surface brightness, compact H II region. In general, highly extended H II regions such as H274 do not yield reliable metallicity measurements.

routines, as described later in this section.

All spectroscopic science observations (see Figure 2.5) must be accompanied by four types of calibration observations:

- Bias—A zero second exposure that characterize the variations in pixel-to-pixel offset levels across the CCD. Multiple bias frames are averaged to create a "superbias", the superbias is then subtracted from all other observations.

- Flat Field—An exposure of a uniformly illuminated surface or part of the sky that is 2–120 seconds long. Flat fields are taken through the same slit mask as the scientific observations. Multiple flat fields are averaged to create a "superflat" that is then used to correct for variations in pixel-to-pixel sensitivity by dividing the science and calibration frames (except bias frames) by the superflat. See Figure 2.6 for an example of a flat field observation.

- Arc—A spectroscopic observation through the same slit mask as the scientific observations of a spectrum with well-known emission line wavelengths, such as of a neon lamp. The observed emission lines only lie at the known wavelengths of neon transitions. It is therefore possible to associate a wavelength value with each pixel in the science image. Lamps with emission lines from several chemicals allow for a better wavelength solution. See Figure 2.7 for an example of an arc observation.

- Standard—A spectroscopic observations of one or more "standard" stars. These are stars whose absolute fluxes are well-known across a wide range of wavelengths, and

that usually have very few spectral features. White dwarfs are a common choice because they satisfy these requirements.

XIDL begins the reduction process by making a superbias, then uses the flat fields and arc observations to generate a slitmask file. The slitmask is an integer-valued 2D array that is used to mask pixels that do not correspond to a slit. The two dimensions of this file correspond to the spatial position on the physical slit mask (x-coordinate in Figures 2.5–2.7) and the wavelength of the dispersed light (y-coordinate). XIDL determines which pixels to mask and which to keep by analyzing the rows of a flat field image and noting where the observed flux sharply drops then increases again. These areas of decreased flux are marked as 0s on the slitmask because they correspond to the regions *between* slits. XIDL also takes into account that "good" slits will have a known minimum width. Any areas initially marked as a part of a slit that is sandwiched by two non-slit areas closer to each other than this minimum value will also become 0s. For the slit masks used in the M33 Metallicity project, I set the minimum slit length to 5.4″ because the alignment box slits are 4.0″ and all science slits are at least 10″ long.

The slitmask file is used in conjunction with all the observed flat fields to create a superflat, as previously mentioned. The slitmask file is also used to help create a full wavelength solution from the arc observations. To calculate a wavelength solution, XIDL searches for emission lines (i.e., peaks) in the arc spectra, then fits a polynomial to the positions of these peaks and their known wavelengths. An example of the output from this peak-finding algorithm is shown in Figure 2.8. Parameters used by the wavelength solution algorithm therefore fall into two categories: peak finding and polynomial fitting parameters. The default wavelength solutions calculated by XIDL were not as accurate as would be expected for the quality of the data, so I adjusted the following parameters until more reasonable results were acquired.

I changed the peak finding parameters so that thinner peaks were deemed acceptable, but these were limited to peaks with higher significance than XIDL initially required (5σ instead of 4σ for Blue 600/4000 and 10σ instead of 4σ for Red 400/8500; Red 900/5500 significance parameter was not changed from its default value of 4σ). The overall effect of these changes improved the quality and quantity of peaks that were used to find the polynomial fit. The major changes I made to the polynomial fitting parameters were to shorten the list of known peak wavelengths to not include emission lines that were extremely faint or part of a doublet.

Additionally, I changed the training set of spectra and known wavelengths to be a set of spectra with good wavelength solutions from the M33 Metallicity Project data set, rather than the set included in XIDL. This allowed for a more robust wavelength identification since XIDL was comparing spectra to a set of archived spectra of a similar quality and wavelength range. Then I increased the number of iterations in the XIDL peak-finding function from
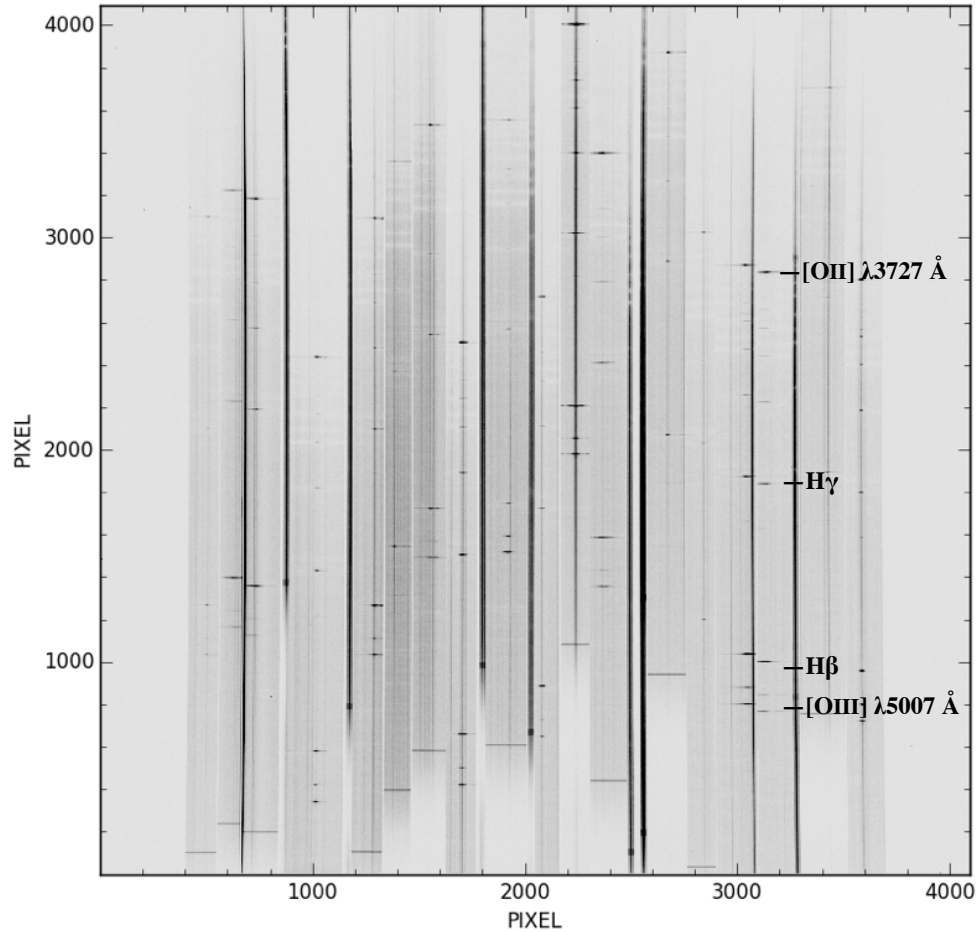
Figure 2.5 Example of a reduced science observation. Each slit's spectrum is shown in a vertical strip. That is, the *x*-coordinate shows different slits, and the *y*-coordinate is actually wavelength. For example, in the slit spanning *x*-coordinate pixels ∼3100–3300, it is easy to pick out the emission lines (from top to bottom): [O II] $\lambda\lambda$3726,3729 Å, Hγ, Hβ, [O III] λ5007 Å. The short slits that do not show emission lines and are instead completely saturated (thick vertical black lines) correspond to alignment boxes. The fainter, and much thinner vertical black lines that often appear in the middle of slits that do show emission lines are the result of the stellar continuum surrounding the H II region being studied in the slit.
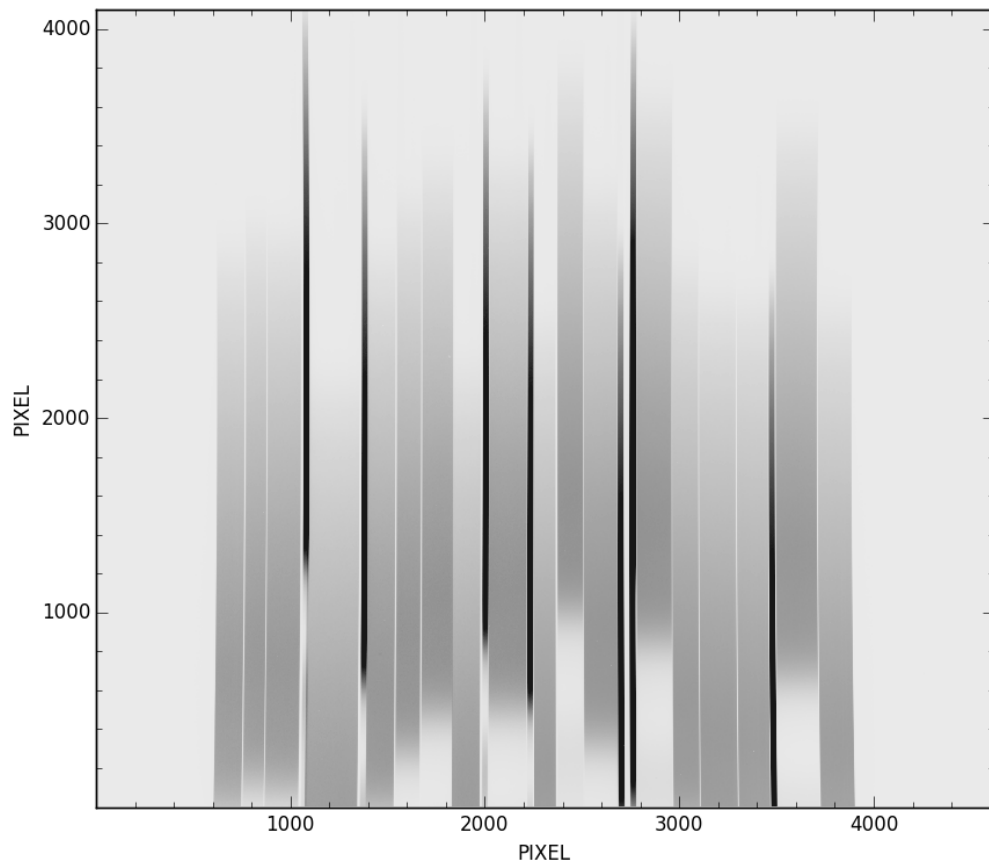
Figure 2.6 Example of a raw flat field observation. This flat field corresponds to the same mask as was used to take the science observation shown in Figure 2.5. The slit positions and wavelength direction are also the same as Figure 2.5.
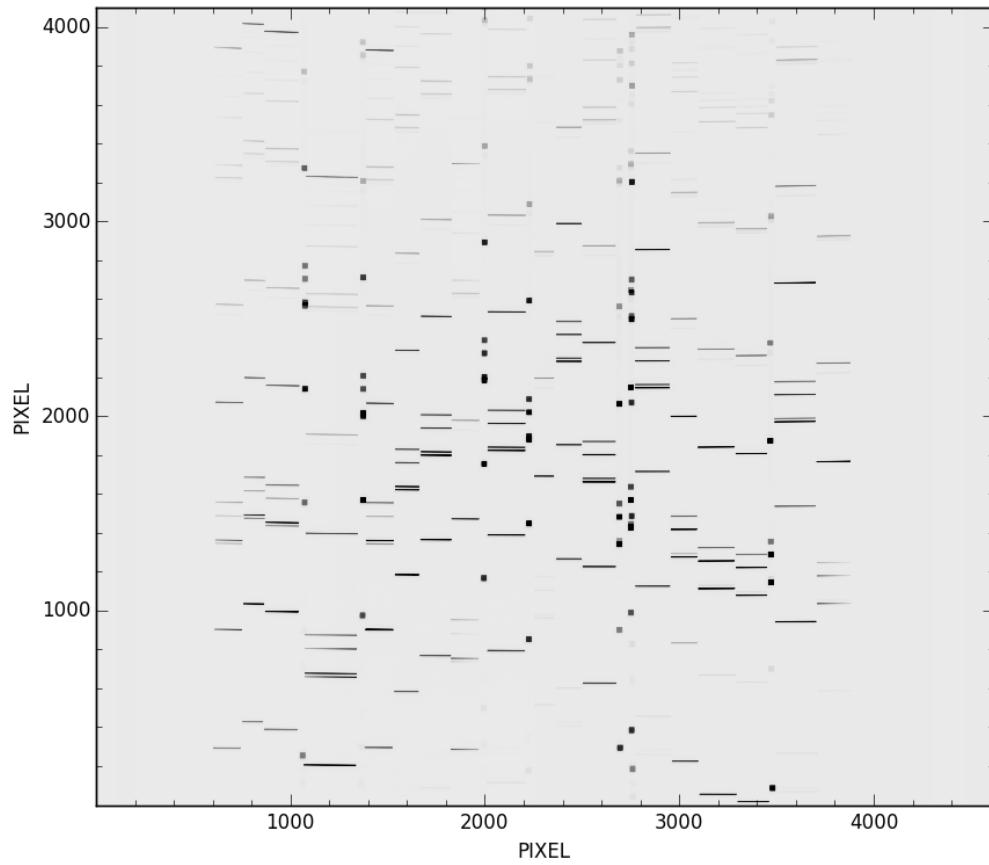
Figure 2.7 Example of a raw arc spectroscopic observation. This arc corresponds to the same mask as was used to take the science observation shown in Figure 2.5. The slit positions and wavelength direction are also the same as Figure 2.5.
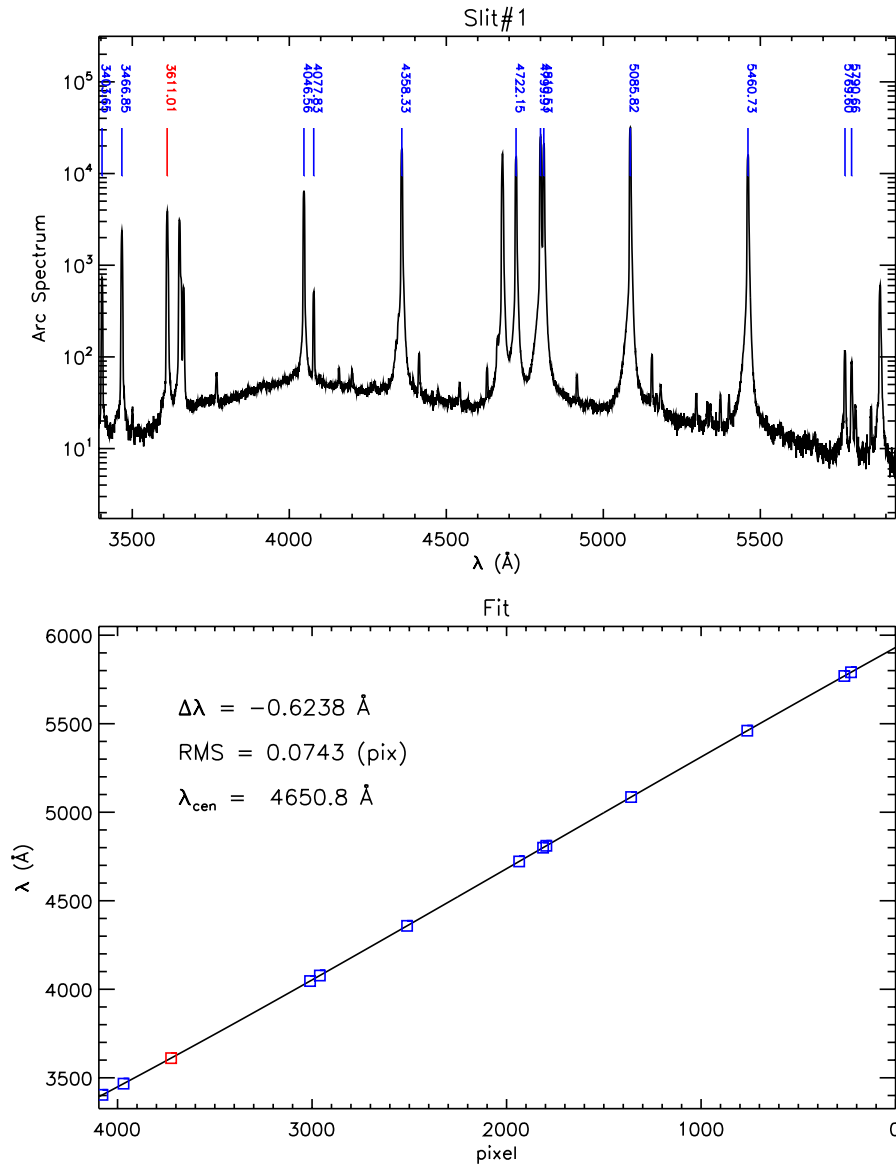
Figure 2.8 Example of the output from XIDL's peak-finding algorithm. The top panel show the input arc spectrum and the wavelengths of peaks that were identified by XIDL. Wavelengths written in red are peaks that were later rejected. The bottom panel shows the polynomial wavelength solution to the identified peaks.

five to six. The first iteration uses the training set of spectra previously mentioned as an initial guess, and each subsequent iteration uses the previous iteration's fit as its initial guess.

Now that a superbias, superflat, and wavelength solution have been calculated, the science observations can be reduced. To begin with, cosmic rays are removed using IDL's `qzap` procedure, with a few input parameters modified after inspecting several images (skyfiltsize = 40, nsigma = 11, fluxratio = 0.15). Next, sky subtraction takes place—the first routine with major deviations from the original XIDL code. The sky subtraction problem is significantly more difficult than the case for a single compact source. Since nebular emission extends across the slit with an arbitrary emission profile, the reduction code must identify those regions in the slit that can be regarded as background. The sky includes both atmospheric emission/absorption features as well as features in the stellar continuum of M33 that span the slit. This stellar background is the light from the old stellar disk and is found across the entire slit. To identify these sky regions, the algorithm creates an emission profile by identifying all pixels that have an associated wavelength within a window $w =$ 3.5 Å of any of the nebular lines identified (i.e., the hydrogen emission lines, as well as lines from oxygen, nitrogen, argon, sulphur and chlorine). Using only these pixels, I use the XIDL utilities to extract a spatial profile of the emission across the slit. This generates a (flux-weighted) function of emission vs. spatial offset in the slit, which contains light from both the nebular emission and the underlying stellar continuum. I also generate a second emission profile using all pixels between w and $2w$ of a nebular emission line that are not included in the emission line profile. This profile is then a prediction for the continuum levels in the first emission profile. I then generate a spatial profile of only the nebular emission by subtracting the continuum vector from the first vector leaving only an estimate of the nebular emission.

Next, I identify regions to use as sky background using a model that the sky data should be normally distributed around a mean value μ with a dispersion σ. The spatial profile also contains nebular emission in discrete spatial sections, which leads to an asymmetric distribution for data in the profile. The sky emission is identified as regions with values $< \mu$ but the mean cannot be directly estimated from the data since nebular emission occupies a large fraction of the slit. Instead μ is estimated from the smallest values in the emission profile. By considering the profile data at the 2.28th (p_2) and 15.8th (p_1) percentiles, I estimate the -2σ and -1σ quantiles of the normal distribution while avoiding data at higher percentiles which are likely to contain nebular emission. The quantity $2p_1 - p_2$ then provides an estimate of μ. Regions of the nebular emission that are larger than 2 pixels and have values below μ are flagged as sky regions. These sky regions are further trimmed to ignore bright, compact continuum emission features where the continuum level is larger than 25% above a smoothed continuum profile with smoothing width of 7 pixels.

Given these spatial regions of the slit that are likely to be sky, I then use XIDL routines to estimate a smooth functional representation of the sky as a function of wavelength. The XIDL approach uses fourth-order b-splines to create this smooth estimate, iteratively estimating the function by fitting a spline to the flat-fielded data, using only those points identified as sky in the previous step. The spline breakpoints are set every n pixels, where n is the number of pixels in the spatial direction for a given slit. The spline fitting iteratively rejects data larger than 3σ, where this σ corresponds to an estimate of the standard deviation for the data contributing to the fit. This minimizes the impact of remaining nebular emission and isolates bad data. Finally, I create a model for the sky by evaluating the b-spline for the fit at every wavelength value in the original image.

Once sky subtraction is complete, the code continues on to object identification—the second routine that differs significantly from the original XIDL code. Object identification refers to the location where the H II region intersects a given slit, since this does not necessarily coincide with the centre of that slit. It is even possible that more than one H II region intersects a single slit. Thus, it is necessary to determine the location of the H II region(s) along the slit length, defined as x_{cen}, as well as the spatial extent of the H II region(s) to either side of this central location, defined as x_{box}.

To calculate x_{cen} and x_{box}, I first needed to define the spatial profile. This was achieved by extracting the spatial profile of brightness across the slit in one exposure from each grism and grating. In some cases, the first or last slit may be missing in one or both of the red grating observations, meaning the spatial profile for a given slit may be defined in one, two, or three exposures. When only one spatial profile is defined, it is simply smoothed with a $2.0''$ boxcar kernel then renormalized. When two or three profiles are defined, the geometric mean is calculated before smoothing and normalization take place. For example, if the profiles from each grism or grating are given by P_1, P_2, and P_3, then the geometric mean will be

$$P_{mean} = \sqrt{P_1 P_2} \qquad \text{if two profiles are defined,}$$
$$P_{mean} = \sqrt[3]{P_1 \times P_2 \times P_3} \quad \text{if three profiles are defined.}$$

A set of three profiles for a single slit and their resultant smoothed and normalized profile are shown in Figures 2.9a and 2.9b. In some cases, the three profiles from the blue grism and red gratings are not very well correlated. In particular, the Red 400/8500 grating's profile is often poorly known because sky subtraction for that grating is extremely challenging. To circumvent this issue, when all three profiles are defined, I included a correlation factor for each pair of profiles (i.e., three correlation factors for three defined profiles). η, defined below, is close to zero if profile P_1 is significantly different from profile P_2, and close to one

if the two profiles are in good agreement.

$$\eta = \frac{\sum\limits_{i=1}^{n} \left(P_{1,i} \times P_{2,i}\right)}{\sqrt{\sum\limits_{i=1}^{n}(P_{1,i}^2) \times \sum\limits_{i=1}^{n}(P_{2,i}^2)}}$$

By repeating this calculation for each pair of profiles, it is straightforward to determine which profile, if any, differs significantly from the others and should therefore be excluded from the subsequent geometric mean calculation. Figure 2.10a shows an example of a slit for which the Red 400/8500 profile differs significantly from the Blue 600/4000 and Red 900/5500 profiles. The use of η ensures the final combined profile is determined from only considering the two profiles that are in good agreement, as shown in Figure 2.10b.

Next, I normalized the area under the spatial profile and analyzed the profile for peaks with a maximum height greater than a minimum criterion of 0.01. I chose the value 0.01 after examining several normalized profiles and I adjusted it up or down by up to 0.004 in cases where a choice of 0.01 resulted in discontinuities because a local extremum coincided very closely with this value.

I label the part of the profile that is greater than the minimum criterion as the peak region, then set x_{cen} equal to the median position of the peak region and x_{box} is half the total length of the peak region (see Figure 2.11). Fluxes are extracted from the sky subtracted science image from within $1.5 \times x_{\mathrm{box}}$ to either side of x_{cen} (shaded blue region in Figure 2.11), with the statistical weights given by the normalized profile height. The flux extraction is done by an XIDL routine that I did not need to adjust in any way to use with our data. This routine masks any bad pixels, applies the appropriate weights, then sums all the fluxes within the given region.

The last two steps in the reduction process are to calibrate the fluxes to absolute units using the standard star observations, then co-add the exposures whenever multiple exposures of the same slit mask and same grating were taken. Both of these are handled in XIDL and I only had to make minimal modifications for the current data set. That said, some care was needed when choosing which standard star observations to use for the flux calibration.

As previously mentioned, flux calibration is done by comparing the observed spectrum of a standard star to its known absolute flux. The relation between these two quantities is known as the sensitivity function, and an example of how this function behaves is shown in Figure 2.13. The shape of the sensitivity function is affected by the response of the CCD and telescope optics, and the amplitude is affected mainly by the amount of cloud cover. Clouds are assumed to only affect the amplitude and not the shape of the sensitivity function
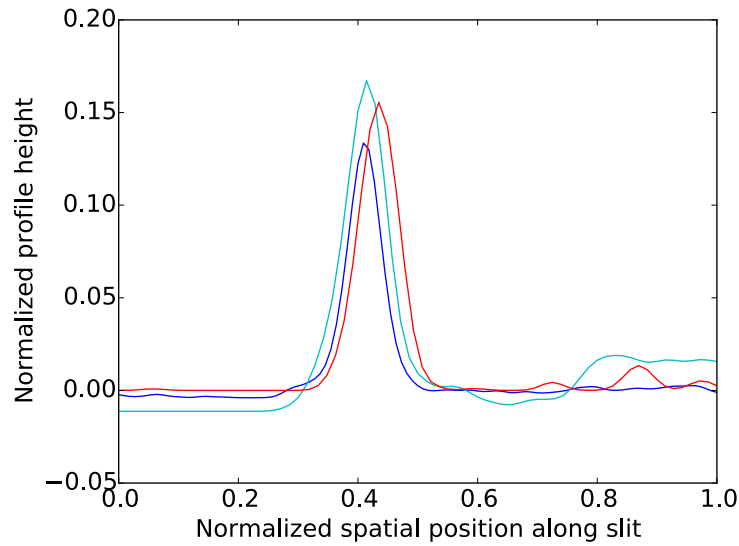
(a) Profiles for a single slit from the Blue 600/4000 grism (blue solid line), the Red 900/5500 grating (red solid line), and the Red 400/8500 grating (black solid line).
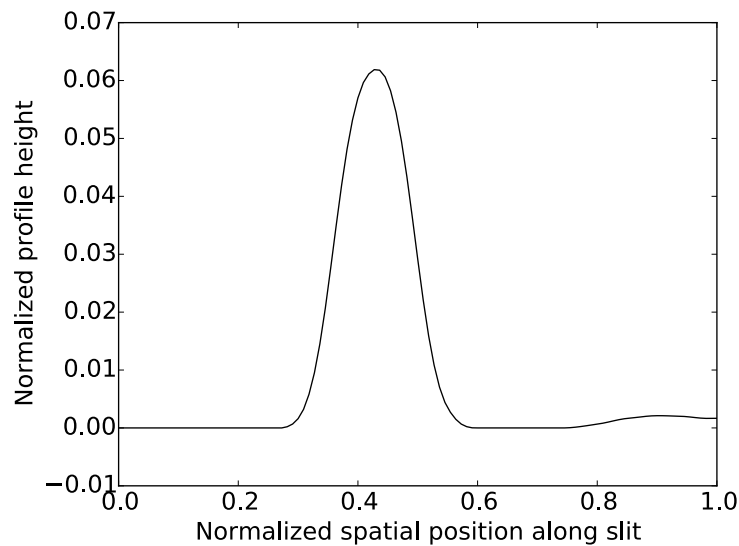
(b) Smoothed and normalized profile derived from the geometric mean of the three profiles shown in Figure 2.9a.

Figure 2.9 Panel (a) shows an example of a slit where the individual profiles from Blue 600/4000, Red 900/5500, and Red 400/8500 show good agreement. Panel (b) shows the smoothed and normalized profile created by taking the geometric mean of the three profiles in panel (a).
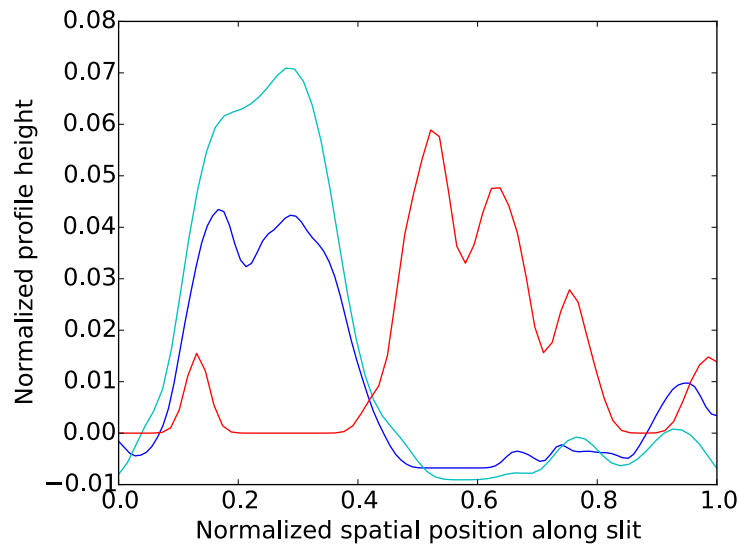
(a) Same as Figure 2.9a but for a slit where one of the three profiles does not correlate well with the other two.
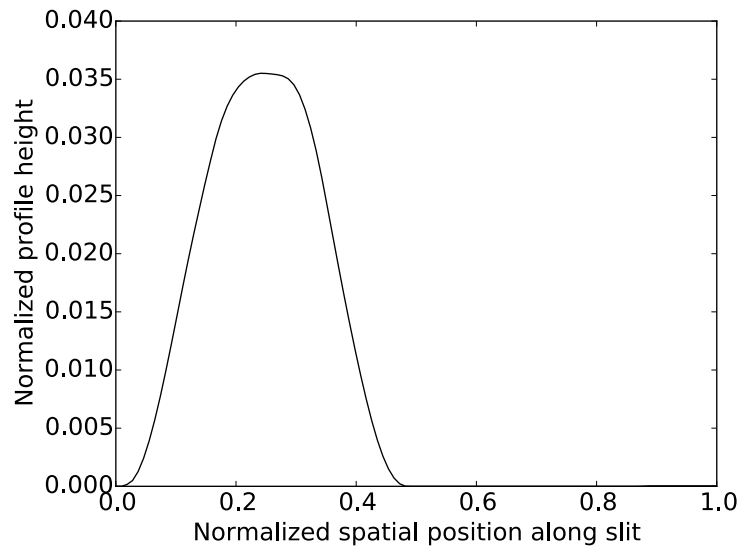
(b) Smoothed and normalized profile derived from the geometric mean of the Blue 600/4000 and Red 900/5500 profiles shown in Figure 2.10a. The Red 400/8500 grating's profile is excluded because it differs significantly from the other two, which indicates there were likely difficulties encountered in the sky subtraction routine.

Figure 2.10 Panel (a) shows an example of a slit where the individual profiles from Blue 600/4000, Red 900/5500, and Red 400/8500 do not show good agreement. Panel (b) shows the smoothed and normalized profile created by taking the geometric mean of only the Blue 600/4000 (blue line) and Red 900/5500 (red line) profiles in panel (a).
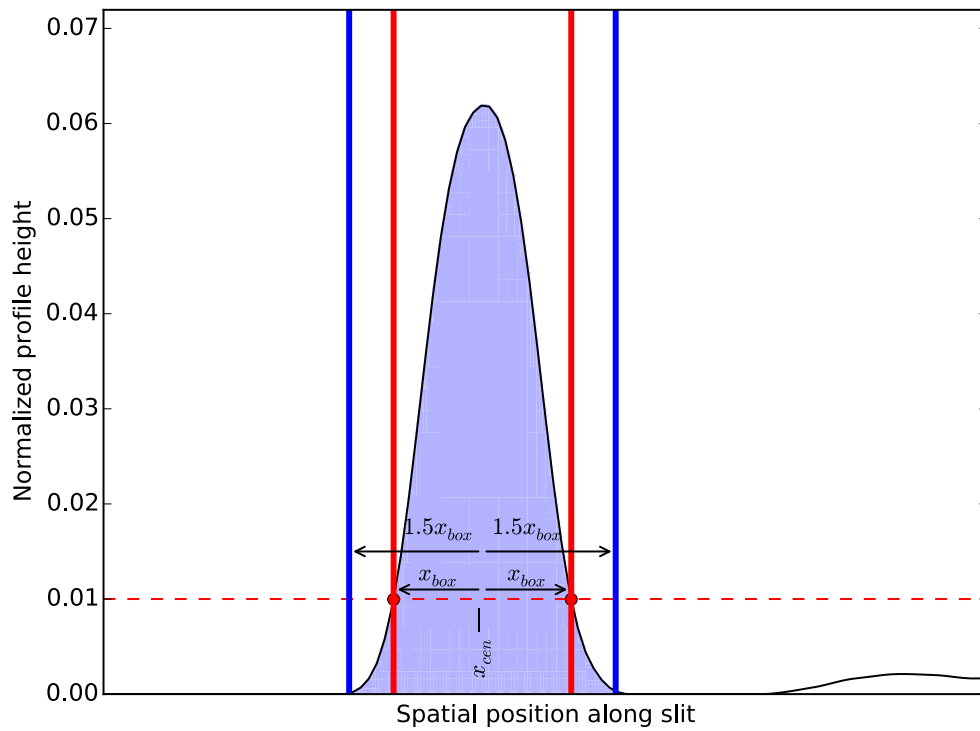
Figure 2.11 Normalized, smoothed profile of a single slit across the spatial direction. x_{cen} and x_{box}, as described in the text, are marked. The shaded blue region shows the extent to which this H II region is considered to be located.

because they are "gray absorbers" [2].

Multiple standard star observations were taken during each observing night, and the sensitivity is not expected to change from night to night (although it may drift over longer periods of time), so I set out to find the best "set" of standard stars from each observing run. One "set" of standard stars includes a Blue 600/4000 and Red 900/5500 observation taken simultaneously, and a Blue 600/4000 and Red 400/8500 observation taken simultaneously. To avoid any systematic offset between Red 900/5500 and Red 400/8500 flux calibrations, I choose the best set of observations to be that for which the two Blue 600/4000 observations have the same overall flux. An example of the best set of standard star observations before and after flux calibration is shown in Figure 2.12.

As a finished product, XIDL produces a reduced science image along with numerous calibration files, but the outputs that are of utmost importance to this work are the multi-extension FITS files for each H II region that contain arrays of wavelength [Å], flux [F_λ], and 1-σ error in flux [F_λ], where the units of F_λ are 10^{-17} erg s^{-1} cm^{-2} Å^{-1}. Together, these data are the spectra from which I determine the total flux in each spectral line, and eventually the metallicity of each H II region. Figure 2.14 shows an example of one of these spectra by plotting the flux as a function of the wavelength.

2.4 Spectral line total flux

With spectra in hand, I wrote a Python script to calculate the total flux within each emission line. In this script, first the brightest emission lines in each spectra are fit with a multi-Gaussian component model to determine the Doppler shift that will recover the rest wavelengths. This fit is performed in wavelength chunks of $\sim$500 Å, unless the scarcity of bright lines forced me to use a larger chunk, such as between $\sim$5900–6500 Å and $\sim$7400–9000 Å. By doing the multi-Gaussian model fit in chunks, a more accurate rest wavelength solution for each individual line is obtained, which helps correct for any lingering inconsistencies from the linear wavelength solution performed in XIDL. Once the spectra have been returned to their rest wavelengths, the exact location of every emission line is known, even if a given line is not observed in this particular spectrum. This is especially useful for determining upper limits on faint lines such as [O III] λ4363 Å.

Now that the central (rest) wavelengths of each line are known, the next step is to decide how many data points to either side of the central wavelength should be used in the sum to calculate the total line flux. I plotted the cumulative sums of the Hβ line from several H II regions' spectra as a function of wavelength, and all showed the full line width to be close to

---

[2] A gray absorber is an object whose absorption properties are independent of wavelength.
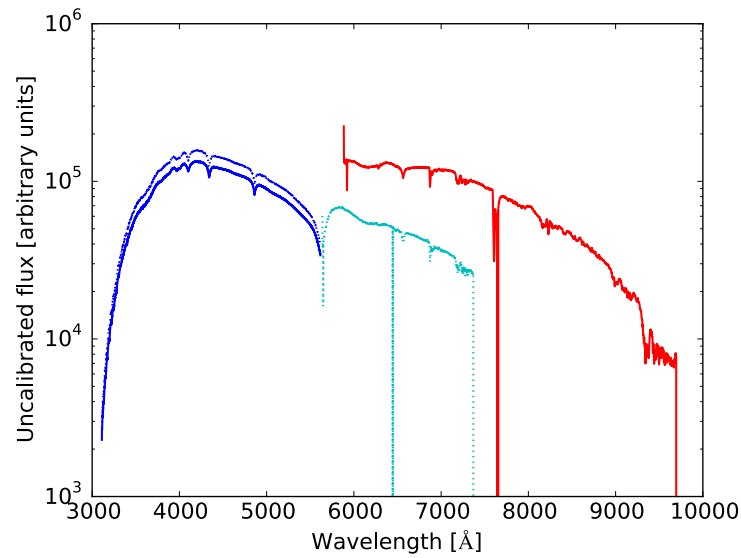
(a)
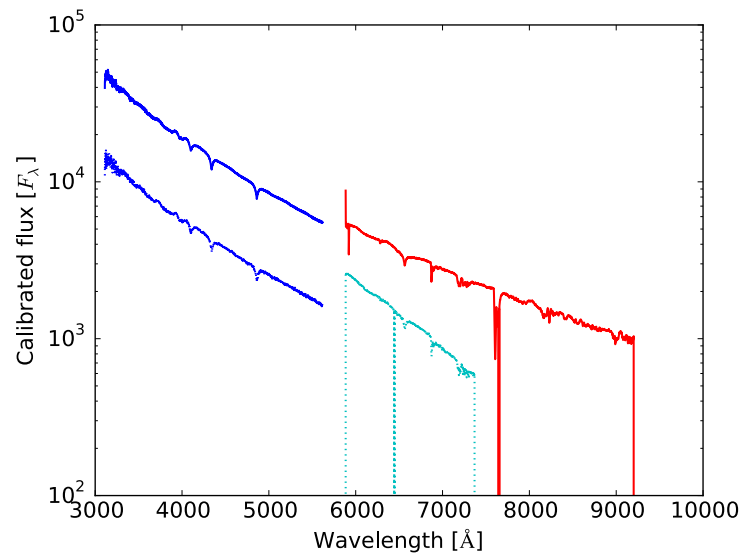
(b)

Figure 2.12 The best set of standard star spectra from the 2004 run. Spectra are from the Blue 600/4000 grism (blue dotted line and blue solid line), and Red 900/5500 (cyan dotted line) and Red 400/8500 (cyan solid line) gratings. The dotted Blue 600/4000 spectrum was observed concurrently with the dotted Red 900/5500 spectrum, and similarly for the solid Blue 600/4000 and solid Red 400/8500 spectra. I chose these four spectra to be the "best set" because the two Blue 600/4000 spectra have very little offset in the uncalibrated flux.
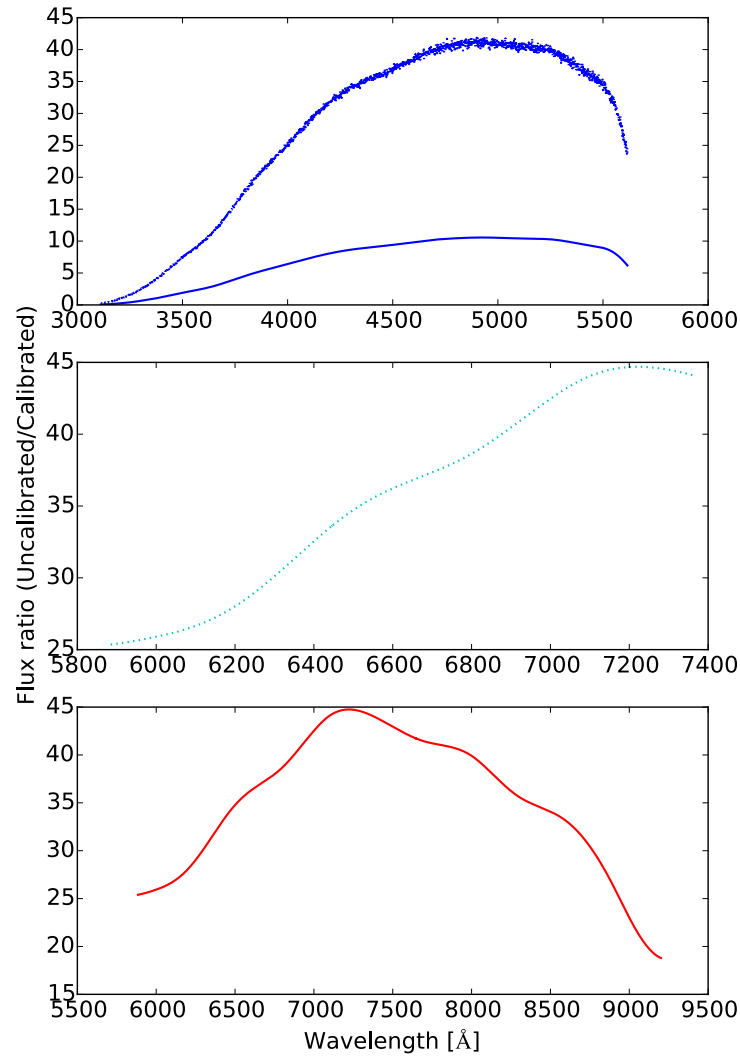
Figure 2.13 Sensitivity functions from the standard stars observed on 2004 October 22. Each plot shows the ratio of the uncalibrated to calibrated flux of the standard star as a function of wavelength. In regions where the unfluxed spectrum is small compared to the fluxed spectrum, the CCD sensitivity is lower. Line colours and styles are the same as in Figure 2.12.

Figure 2.14 Spectrum output from XIDL of the H II region H140. Important spectral lines are labelled.
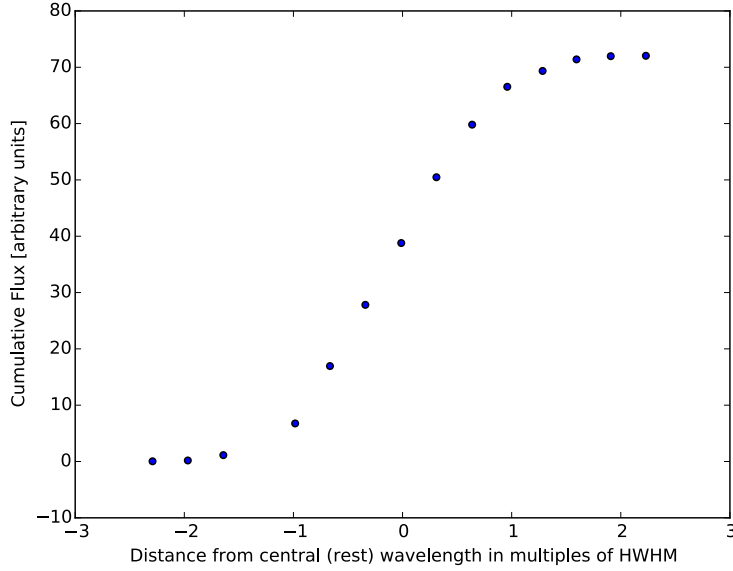
Figure 2.15 Cumulative sum of the Hβ line flux in the spectrum of H140. There is very little change in the sum as the x-position nears the limits of $\pm 2.5 \times$ HWHM.

$5.0 \times$ the half width at half maximum (HWHM). Figure 2.15 shows one of these plots. The full line width does not noticeably change between different spectra or even between different spectral lines because our instrumental resolution is approximately 1 Å, which is much larger than any of the expected effects from the various broadening mechanisms that would change the full line widths of different lines—such as natural broadening at $\sim 10^{-4}$ Å (LeBlanc, 2010), Doppler broadening at $\sim 10^{-1}$ Å (Cayless et al., 2015), and pressure broadening at $\sim 10^{-2}$ Å (NIST, 2007). It should also be noted that although some spectral lines showed a slightly different profile (especially in the Blue 600/4000 spectrum), the factor of $5.0 \times$ HWHM still correctly identified all the data points that should or should not be included in the sum of the total flux calculation.

Thus, all flux measurements within $2.5 \times$ HWHM of either side of the rest wavelength were considered to be part of the given emission line. The only exception to this was the [O II] $\lambda\lambda 3726,3729$ Å doublet, which required a factor of $4.0 \times$ HWHM because the doublet lines were partially blended and therefore had a larger HWHM than a single line. The adjusted factor of 4.0 was found by plotting the cumulative flux in the wavelength range close to 3727 Å.

To accurately calculate the total flux within a given emission line, it was first necessary to calculate the continuum level across that emission line. All flux measurements not within 2.5

$\times$ HWHM of *any* emission line are considered continuum flux measurements (in Figure 2.16 continuum flux measurements are marked with a blue cross). It is fairly straightforward to fit a polynomial to the continuum flux measurements to either side of an emission line then interpolate to determine the continuum flux within an emission line. I investigated the optimal polynomial order to use by calculating the flux of [O III] $\lambda 4363$ Å in three different slits, with a range of possible polynomial orders: 1, 3, 5, 7, 9. The results of this test are plotted in Figure 2.17. Based mainly on the behaviour of the weakest [O III] $\lambda 4363$ Å, the optimal polynomial was chosen to be of order seven. The order of the polynomial did not have a noticeable effect on any bright lines.

I denote true flux measurements with an l subscript and flux measurements from the polynomial of order seven fit that form the continuum with the subscript c, and let a $'$ symbol differentiate values outside of the $5.0 \times$ HWHM region of any spectral line from those within it. The interpolated continuum values ($F_{i,c}$) at wavelengths within the $2.5 \times$ HWHM boundaries were subtracted from their respective emission line flux measurements ($F_{i,l}$). Next, the continuum-subtracted flux measurements were multiplied by the wavelength difference between adjacent data points ($\delta\lambda$). Lastly, these were summed together to obtain the total line flux (F_{tot}),

$$F_{\text{tot}} = \sum_{i=1}^{n} (F_{i,l} - F_{i,c})\ \delta\lambda.$$

Figure 2.16 shows the continuum flux measurements, continuum polynomial fit, and emission line flux measurements for a single emission line in a spectrum.

To determine the error on the total line flux (δF_{tot}), I accounted for the errors from the emission line flux measurements as output by XIDL ($\delta F_{i,l}$), as well as the error from the polynomial fit to the continuum ($\delta F_{i,c}$). The error in the polynomial fit was calculated as follows

$$\delta F_{i,c} = \sqrt{\sum_{i=1}^{n'} \frac{(f_{i,c'} - f_{i,l'})^2}{n' - 1}},$$

where n' is the number of data points used to fit the polynomial continuum flux ($f_{i,c'}$) to the observed flux ($f_{i,l'}$). The error in the continuum was constant for all points, so $\delta F_{i,c} = \delta F_c$ for all i. The errors were then summed in quadrature and multiplied by $\delta\lambda$ to obtain δF_{tot},

$$\delta F_{\text{tot}} = \sqrt{\sum_{i=1}^{n} (\delta F_{i,l}^2 + \delta F_c^2)}\ \delta\lambda.$$

With the total flux of each emission calculated as outlined above, only two corrections remain before these total fluxes can be used to derive the metallicity: (1) Balmer absorption correction, and (2) Interstellar reddening correction. The Balmer absorption correction
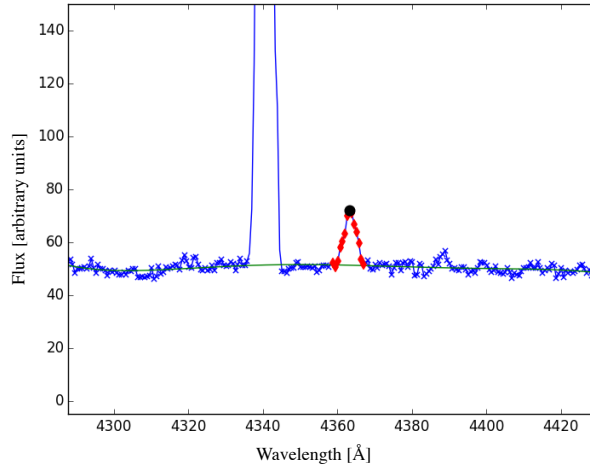
Figure 2.16 Close up of [O III] λ4363 Å in a single slit's spectrum, showing the continuum fit (solid green line), the flux measurements used to calculate the continuum fit (blue crosses), the flux measurements within $2.5 \times$ HWHM of the rest wavelength that were used to calculate the total flux (red diamonds), and the data point closest to the rest wavelength that was also used in the total flux calculation (black circle).
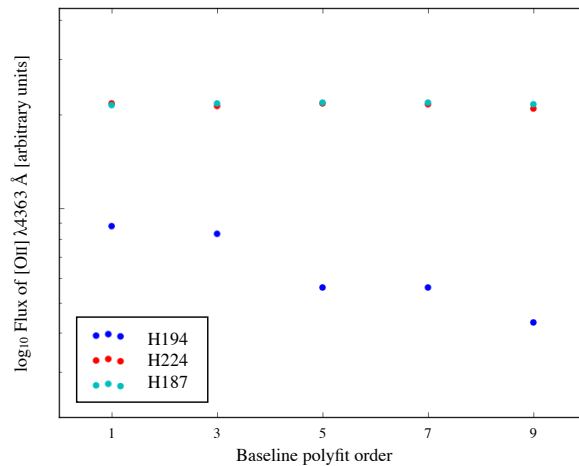
Figure 2.17 This figure shows how the total flux calculated in [O III] λ4363 Å varies as a the order of the polynomial fit to the continuum flux is changed. The fluxes from a few slits are plotted, but we see the greatest effect when the flux of [O III] λ4363 Å is the weakest (i.e., in H194).

corrects the observed fluxes of the Balmer series spectral lines for the absorption that takes place in the photospheres of the stars that are emitting the observed light. The interstellar reddening correction adds light to the blue side of the observed spectrum to correct for the preferential scattering and absorption of blue light by dust in the ISM. Both corrections must be solved for simultaneously to accurately infer the individual strength of each.

2.5   Balmer absorption correction

To produce Balmer absorption lines, there must be hydrogen atoms present and they must be in the $n = 2$ excited state. For cooler stars, the hydrogen atoms are in the ground state and so cannot produce Balmer absorption lines, while in warmer stars, the hydrogen atoms may be completely ionized and therefore unable to produce any absorption lines. Thus, it is in the goldilocks zone of ~ 10000 K surface temperatures where stellar atmospheres produce the strongest Balmer absorption lines, and this happens to coincide with spectral type A stars (LeBlanc, 2010).

The total line fluxes of Balmer emission lines are corrected for underlying stellar absorption effects according to the prescription derived by Olive and Skillman (2001), and illustrated in Figure 2.18. This approach relies on the well-known, intrinsic ratio of Balmer lines, and considers the correction required to get the observed Balmer ratios equal to their theoretical values. For example, the intrinsic ratio of $\frac{\text{H}\alpha}{\text{H}\beta}$ is 2.86, assuming Case-B recombination and a temperature of 10000 K and an electron density of 100 cm^{-3} (Osterbrock, 1989).

In the simplest case, when only the Hγ and Hβ lines are used to calculate the correction, the function

$$\frac{(X_R - 0.468)^2}{\sigma_{X_R}^2} \ ,$$

where X_R is given below and σ_{X_R} is its uncertainty, is minimized with respect to two variables: (1) Equivalent width, EW, and (2) Extinction constant at 4861 Å, $c(\text{H}\beta)$. Recall the equivalent width is the width of the rectangle with area equal to the total spectral line flux and height equal to the continuum level, and the extinction constant at Hβ is the logarithmic extinction caused by interstellar reddening, discussed further in §2.6. The value 0.468 appears in the function to be minimized because this is the intrinsic line ratio of Hγ to Hβ for an assumed temperature of 10000 K, as calculated by Hummer and Storey (1987) .

$$X_R = \frac{\text{H}\gamma_{\text{flux}}}{\text{H}\beta_{\text{flux}}} \left[\frac{1 + \text{EW}(\text{H}\gamma_{\text{continuum}}/\text{H}\gamma_{\text{flux}})}{1 + \text{EW}(\text{H}\beta_{\text{continuum}}/\text{H}\beta_{\text{flux}})} \right] \times 10^{0.13c(\text{H}\beta)}$$

It has been known for some time that the stellar Balmer absorption lines have approximately constant equivalent width within a given spectrum (Gonzàlez Delgado et al., 1999), and it
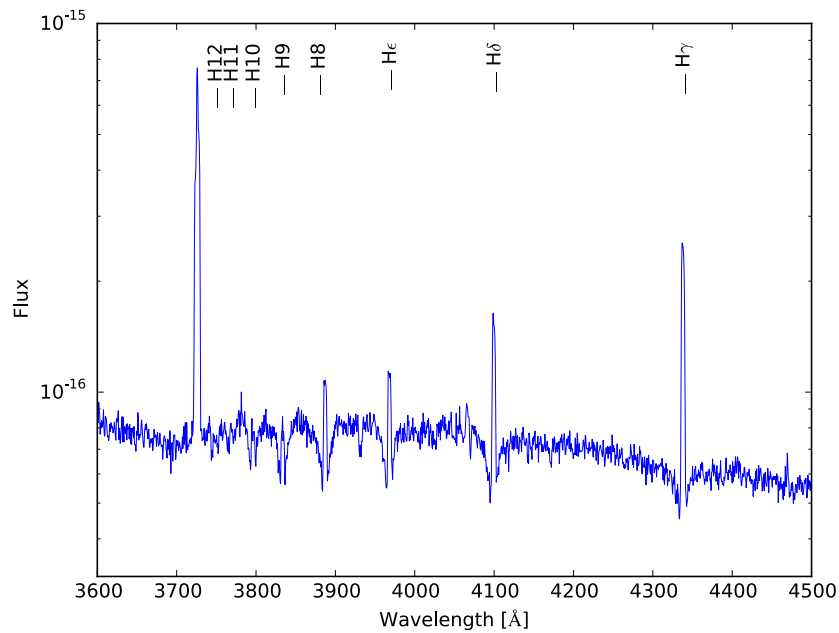
Figure 2.18 An example of hydrogen emission lines suffering from underlying stellar Balmer absorption in the H II region H101. The noticeable "dips" in flux to either side of the emission lines is the signature of an absorption line superimposed on an emission line. When the underlying absorption feature is narrow, these dips are less noticeable, making it more difficult to determine the equivalent width of the required correction.
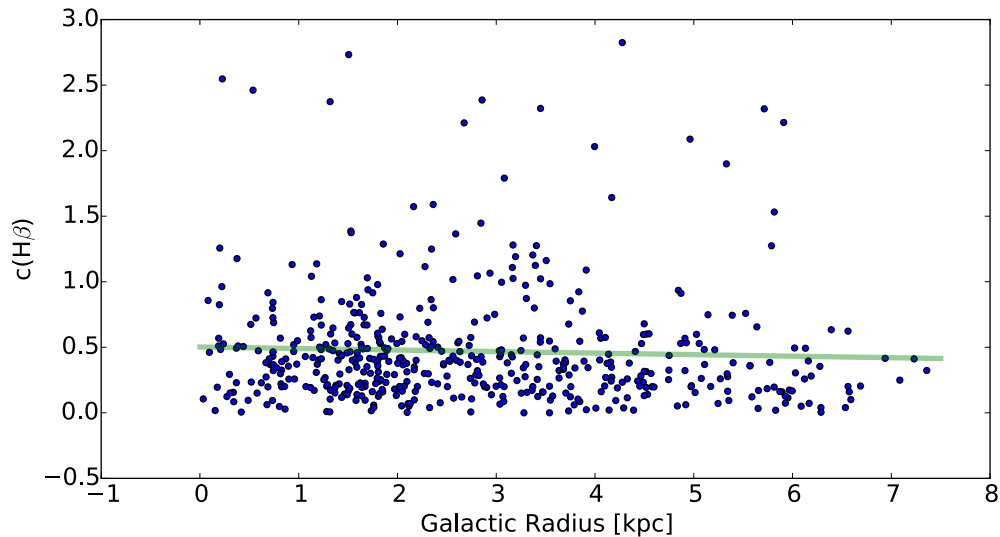
Figure 2.19 The calculated values of the extinction constant $c(H\beta)$ are plotted as a function of galactic radius. The linear gradient shown in green has a slope of -0.012 kpc^{-1} and intercept 0.011.

is therefore quite straightforward to apply the Balmer absorption correction to all Balmer lines in the spectrum once EW has been calculated from the above minimization.

$$\text{Corrected flux} = \text{Observed flux} + \text{EW} \times \text{Continuum level}$$

2.6 Interstellar reddening correction

After the Balmer absorption correction has been applied, the fluxes of all lines are corrected for interstellar reddening, or extinction. Galactic reddening is a well-known absorption effect caused by interstellar dust grains. Dust grains preferentially absorb and scatter blue light, thereby making the spectrum we observe to be redder (or technically, less blue) than what was originally emitted at the photon production site. This effect is wavelength dependent and was quantified by Cardelli et al. (1989) as follows.

Let $A(\lambda)$ be the absolute extinction at any wavelength, and $A(\lambda_{ref})$ be the absolute extinction at a reference wavelength. For historical reasons, $A(\lambda_{ref}) = A(V)$, the extinction in the V-band. Cardelli et al. (1989) then define the term "extinction law" to refer to $A(\lambda)/A(V)$.

The extinction law of Cardelli et al. (1989) depends only on $R_V \equiv A(V)/E(B-V)$, where $E(B-V)$ is the relative extinction between the B and V bands ($= A(B) - A(V)$). $A(\lambda)/A(V)$ is plotted as a function of R_V^{-1} for a sample of stars observed over a wide range of wavelengths. From this plot, an extinction law of the form

$$\langle A(\lambda)/A(V)\rangle = a(x) + b(x)/R_V \tag{2.1}$$

can be derived through least-squares fitting, where $x = 10000$ Å$/\lambda$. Note the addition of $\langle\rangle$ to denote that it is the *mean* extinction law that is being fit. This is because extinction is also dependent on the line-of-sight, but this dependence is not considered in this case.

In the wavelength regimes pertinent to the current work's data set, the final derived extinction law derived by Cardelli et al. (1989) is given by:

(i) Infrared ($\lambda \geq 9000$ Å):

$$a(x) = 0.574x^{1.61}$$
$$b(x) = -0.527x^{1.61}$$

(ii) Optical/Near-Infrared (9000 Å $\geq \lambda \geq$ 3000 Å):

$$y \equiv x - 1.82$$
$$a(x) = 1 + 0.17699y - 0.50447y^2 - 0.02427y^3 + 0.72085y^4 + 0.01979y^5 - 0.77530y^6 + 0.32999y^7$$
$$b(x) = 1.41338y + 2.28305y^2 + 1.07233y^3 - 5.38434y^4 - 0.62251y^5 + 5.30260y^6 - 2.09002y^7$$

To then apply this extinction law to the total flux values previously derived, I multiply each flux by a correction factor that depends on $a(x) + b(x)/R_V$. In detail,

$$R_V = 3.1$$
$$A(V) = R_V \times c(\text{H}\beta) \left[0.61 + 0.024c(\text{H}\beta)\right]$$
$$\text{Corrected flux} = \text{Reddened flux} \times 10^{0.4[A(\lambda)]}$$
$$= \text{Reddened flux} \times 10^{0.4[A(V)(a(x)+b(x)/R_V)]}$$

Although the value of R_V can range from 2.2 to 5.8, the mean value of 3.1 is well-constrained and used ubiquitously in the literature, so that is the value used here (Schultz and Wiemer, 1975; Cardelli et al., 1989; Fitzpatrick, 1999). Other choices for R_V are possible however, and the effect of these should be examined in future work with this data set. For example, M33 has many similarities with the Large Magellanic Cloud (LMC), which has $R_{V,\text{LMC}} = 3.4$ (Gordon et al., 2003). The expression for $A(V)$ given above in terms of $c(\text{H}\beta)$ was derived by Kaler and Lutz (1985) and is used here because $c(\text{H}\beta)$ has already been determined by the method used for the Balmer absorption correction. Then to get the corrected flux, I use a rearranged version of the well-known magnitude-flux relation.

To ensure there are no lingering inconsistencies between the three reddening-corrected spectra of each object due to unforeseen calibration effects such as uneven cloud cover during observations, the fluxes of emission lines observed from the 900/5500 and 400/8500 gratings undergo a simple correction such that the ratio of Hα to Hβ is equal to the intrinsic value of 2.86. To apply the correction, I multiply all the fluxes measured in each grating by the same factor. This factor is equal to $f = 2.86/\frac{\text{H}\alpha}{\text{H}\beta}$, where H$\alpha$ is the flux measured at 6563 Å in each red grating and Hβ is the flux measured at 4861 Å from the Blue 600/4000 grism. Typically, this factor does not introduce a large correction, as is expected since the spectra are all already dereddened—a histogram of the required f values for each red grating are presented in Figure 2.20. For those spectra that do require a large correction, or for which f is negative, rejection criteria applied later in the analysis will eliminate these from the final results (see §3.3).

As a final check of the quality of the spectra, I plot the observed Balmer ratios and compare these to the theoretical values (Figure 2.21).
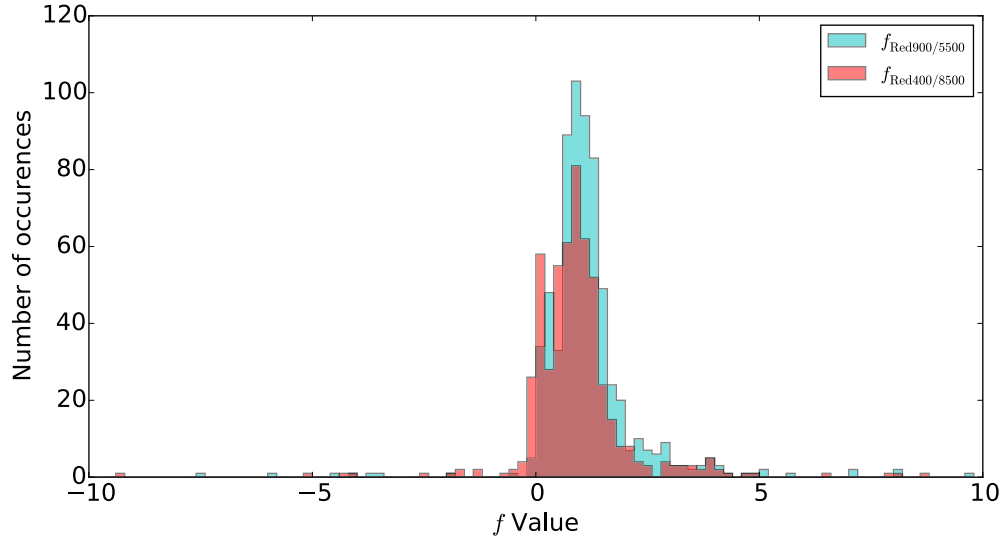
Figure 2.20 Histograms of the factors f required to adjust the spectra observed in each red grating such that $\frac{H\alpha}{H\beta}$ of each H II region is equal to its theoretical value of 2.86. Assuming the lingering inconsistencies for which this factor corrects are not significant, all values of f should be close to unity.

2.7   Signal to noise of auroral lines

I present histograms of the signal to noise ratios (SNRs) for the weak auroral lines [O III] λ4363 Å, [N II] λ5755 Å, and [S III] λ6312 Å(Figure 2.22), since it is these auroral lines that will be instrumental in calculating the temperature and density of each H II region. Recall, it is difficulty in observing these weak lines that forces most other studies to derive metallicities from the strong-line calibrations discussed in §1.5. The relatively large number of strong detections (SNR $\gtrsim$ 6.0) in this work allows us to derive metallicities based on the more accurate weak-line method.
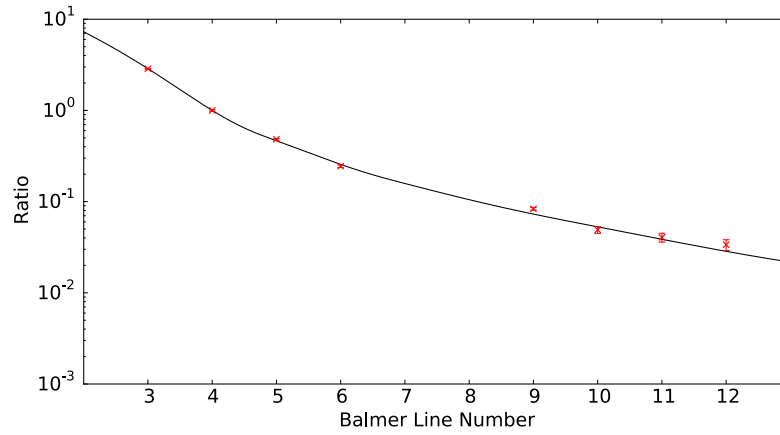
(a) H35
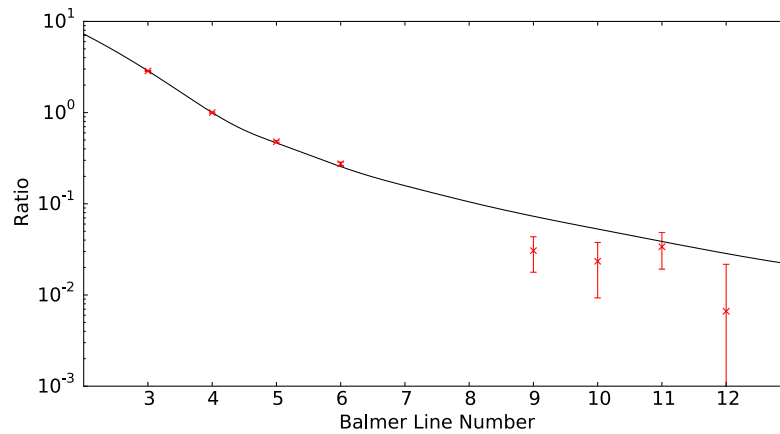
(b) H685

Figure 2.21 Typical observed Balmer ratios after all corrections have been made are shown as red × symbols. The theoretical (intrinsic) Balmer ratio values follow the solid black line. BalmerLineNumber = 3 refers to the Hγ/Hβ ratio, 4 refers to Hϵ/Hβ, etc. There is good agreement for all ratios, with the exception of the fainter Balmer lines (higher line number), which sometimes suffer from upper limits.
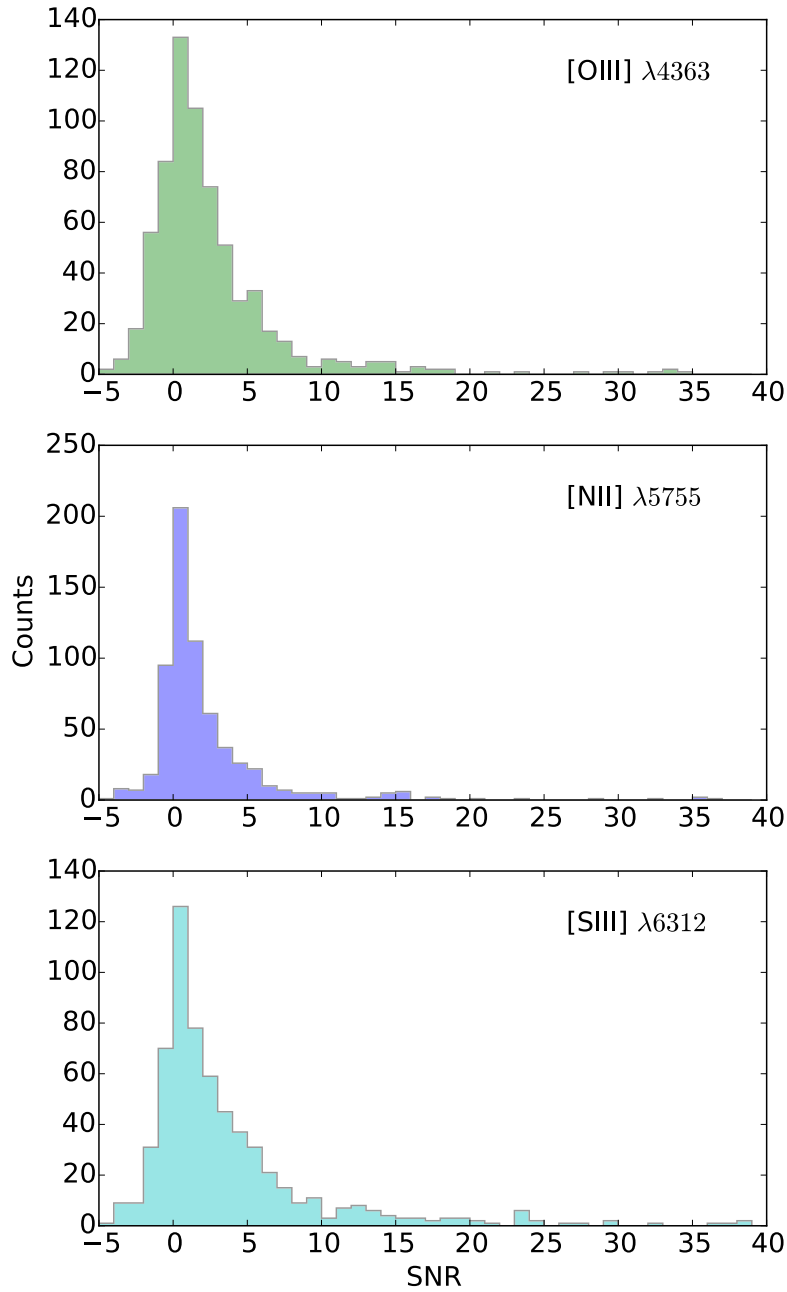
Figure 2.22 Detection rate of [O III] λ4363 Å, [N II] λ5755 Å, and [S III] λ6312 Å in this data set.

CHAPTER 3

Metallicity Determination Methods

3.1 Modelling of an H II region

The simplest model of an H II region that is still used today was first introduced by Strömgren (1939). Hydrogen being the most abundant element, Strömgren considered the extent of a fully ionized sphere of hydrogen surrounding a hot central star or cluster of stars, and embedded in a neutral hydrogen interstellar medium. He showed that the extent of the sphere of ionized hydrogen is a function of the ionizing star's temperature and absolute magnitude, and the density of the interstellar hydrogen. The equation for the radius of a so-called Strömgren Sphere is then,

$$R_S = \left(\frac{3Q_0}{4\pi n_H^2 \alpha} \right)^{1/3} \, , \tag{3.1}$$

where Q_0 is the rate of emission of hydrogen-ionizing photons, n_H is the density of interstellar hydrogen, and α is the radiative recombination coefficient of hydrogen.

Nowadays, although the extent of an H II region remains the same as defined in Strömgren (1939) and given by Equation 3.1, it is useful to model the interior of the H II region as a three zone system. These three zones are called the high-, medium- and low-ionization zones, and their names refer to the ionizing strength of the photon field in each. Thus, the high-ionization zone is infused with much more energetic photons than the low-ionization zone. Furthermore, the high-ionization zone spatially refers to the area closest to the hottest stars in the H II region, while the low-ionization zone resides at the edge of the H II region. A diagram of this three zoned system is presented in Figure 3.1.

Spatial temperature fluctuations likely arise within an individual H II region due to wide
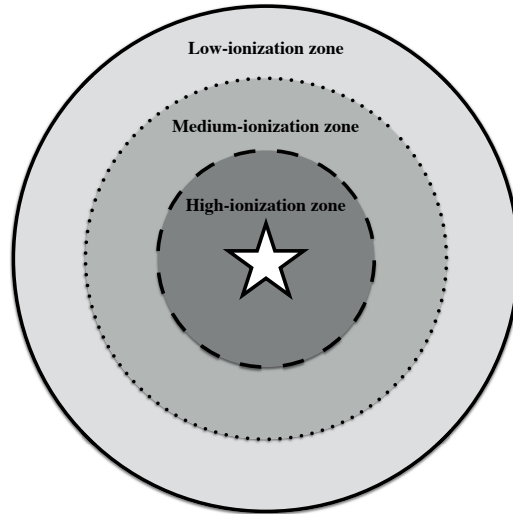
Figure 3.1 Schematic of the three ionization zones in a model of an H II region. The white star at the centre represents all the bright, hot stars that reside at the centre of the H II region, which produce the ionizing photons. The dashed and dotted lines show the transitions from high- to medium-, and medium- to low-ionization zones, respectively. The solid line represents the boundary of the H II region, marked by a relatively sharp transition from ionized hydrogen (in the low-ionization zone) to neutral hydrogen (in the surrounding ISM).

range of degrees of ionization and electron densities that are present across the different zones. The effect of these fluctuations on the temperature measured by the auroral method (described in §1.4) was investigated by Peimbert (1967). By assuming that the fluctuations are small, Peimbert expressed the measured temperature as a Taylor series about the mean (true) temperature. This revealed that when the ratio of [O III] $\lambda4363$ Å to [O III] $\lambda5007$ Å is used to measure the H II region's temperature, high-temperature regions get emphasized, leading to a temperature measurement that is biased towards values higher than the true temperature. In a model H II region, Peimbert found this effect led to a measured temperature 1350 K higher than the true value of 5500 K.

3.2 Metallicity calculation

To calculate metallicities from the observed emission line spectra, I employ two independent methods then compare the results. The first of these, PyNeb, is a Python package created for the analysis of emission lines in ionized nebulae (Luridiana et al., 2015). The second method is a Fortran package called the Nebular Empirical Analysis Tool (NEAT, Wesson et al. 2012). Both packages require the rest wavelength, total line flux, and total line flux

uncertainty of each observed emission line as input parameters. Both packages also utilize the three zone model discussed in §3.1. However, no high-ionization zone temperature or density diagnostic emission lines were observed in any of my spectra, so only the medium- and low-ionization zones will be discussed henceforth.

In general, PyNeb requires a lot of direction from the user, while NEAT operates more like a "black box". That said, NEAT uses a sophisticated Monte Carlo approach to model various SNR scenarios, which is believed to be quite effective when dealing with weak emission lines (low SNR), so I emulate this approach in PyNeb. Both PyNeb and NEAT use a list of input line fluxes to then determine the abundances of various ions. In the Monte Carlo approach developed by the writers of NEAT and emulated by me in PyNeb, the line fluxes are drawn from a given distribution and abundances are determined for n iterations. The results from these n iterations are then binned and the means and standard deviations are taken to be the abundances and their corresponding uncertainties. n is equal to 100 in both PyNeb and NEAT, unless otherwise specified.

The distribution from which the Monte Carlo line fluxes are drawn is chosen according to each line's SNR. Three distributions are available:

- **SNR > 6.0** If the given line flux is F and the given uncertainty δF, then the flux in the i-th MC iteration is given by $F_i = F + (R \times \delta F)$, where R is a random number drawn from a standard Gaussian distribution $N(0, 1)$. In other words, F_i is drawn from a Gaussian distribution with a mean equal to the given flux and a standard deviation equal to the given uncertainty.

- **1.0 < SNR < 6.0** Rola and Pelat (1994) found that measurements of weak lines are strongly biased towards overestimations, and that F_i for these lines should be drawn from a log-normal distribution: $F_i = F\, e^{-(R \times \sigma + \mu)}$, where the parameters μ and σ are functions of the SNR. The appropriate values of μ and σ for the log-normal distribution corresponding to a particular SNR were calculated in Rola and Pelat (1994), and the full equations for the values used by NEAT (and my implementation of PyNeb) are given in Wesson et al. (2012).

- **SNR < 1.0** When the given uncertainty is greater than the corresponding flux, it is reasonable to assume the given flux is an upper limit, so F_i is drawn from a folded Gaussian distribution such that $F_i = \mathrm{abs}(R) \times 0.2F$.

Of particular interest to this work, the above scheme makes NEAT superior to analytical techniques when calculating heavy element abundances and uncertainties from auroral line observations (Wesson et al., 2012).

3.2.1 PyNeb

First, I use the `getCrossTemDen` method within PyNeb's `Diagnostics` class to simulta-neously determine the electron temperature and density by fitting two line ratios (one temperature-dependent and density-independent ratio, and one density-dependent and temperature-independent ratio). This method makes an initial guess of the temperature, which I always set to 10000 K, to iteratively compute the density and temperature until a solution is found.

The temperature and density line ratios available in PyNeb and present in my spectra are presented in Table 3.1. When more than one temperature diagnostic is available for a single ion in a given ionization zone, then the average temperature is taken, e.g.,

$$T\,[\text{N II}] = \frac{T\left[\frac{\lambda 5755}{\lambda 6548}\right] + T\left[\frac{\lambda 5755}{\lambda 6548}\right]}{2} \; .$$

Similarly, the average is also taken when more than one temperature is available for a single ionization zone, e.g.,

$$T_{\text{low}} = \frac{T\,[\text{O II}] + T\,[\text{N II}] + T\,[\text{S II}]}{3} \; .$$

If only one or two of the available low-ionization zone temperature diagnostics produce acceptable temperature values, then the above equation for T_{low} is modified to only include those ions' temperatures. In this treatment of the temperatures, I assume "acceptable" temperatures lie between 5000 K and 15000 K—these are lenient bounds to place on H II regions.

If an acceptable temperature could only be found in one of the low- and medium-ionization zones, I determine a temperature in the other zone using the following relation, given by Campbell et al. (1986),

$$T_{\text{low}} = 0.7\,T_{\text{med}} + 3000 \text{ K} \; .$$

In this way, I obtain reasonable abundances in as many H II regions as possible.

I took a similar approach with the densities, however these were much simpler than the temperatures because there is only one density diagnostic and it is the same for both the low- and medium-ionization zones. Thus, whenever the density is only found in one of the ionization zones, the missing density is set equal to the known density.

After the temperature and density have been computed, the ionic abundances of O II, O III, N II, S II, S III, and Ne III relative to hydrogen are calculated using the `getIonAbundance` method within PyNeb's `Atom` class along with the appropriate ionization zone's electron temperature and density. As already mentioned, the calls to both `getCrossTemDen` and `getIonAbundance` are repeated for each of the n Monte Carlo iterations. The average values from these n iterations are then used as the final T_{low}, T_{med}, n_{low}, n_{med}, and ionic

Table 3.1.   PyNeb temperature and density diagnostics

Ionization Zone	Diagnostic	Spectral Lines
Low	N II temperature	$\frac{\lambda 5755}{\lambda 6548}, \frac{\lambda 5755}{\lambda 6584}$
	O II temperature	$\frac{\lambda 7319 + \lambda 7330}{\lambda 3726 + \lambda 3729}$
	S II temperature	$\frac{\lambda 4068 + \lambda 4076}{\lambda 6717 + \lambda 6731}$
	S II density	$\frac{\lambda 6731}{\lambda 6717}$
Medium	O III temperature	$\frac{\lambda 4363}{\lambda 5007}, \frac{\lambda 4363}{\lambda 4959 + \lambda 5007}$
	S II density	$\frac{\lambda 6731}{\lambda 6717}$

abundance values.

Lastly, to calculate the total abundances of oxygen, nitrogen, sulfur, and neon, it is necessary to sum the abundances from each ion that is present in the H II region. For oxygen, this means summing the ionic abundances of O II and O III, as given in Equation 1.2. However, for nitrogen, sulfur, and neon, not all ions that are present in the H II region are observed in the spectral data at hand. The observed ionic abundances must be multiplied by their respective ionization correction factors (ICFs) to calculate total abundances. From Izotov et al. (2006),

$$\text{ICF(N II)} = -1.476v + 1.752 + 0.688/v \ ,$$
$$\text{ICF(S II + S III)} = 0.178v + 0.610 + 0.153/v \ ,$$
$$\text{ICF(Ne III)} = -0.591w + 0.927 + 0.546/w \ ,$$

where $v = $ O II$/($O II $+$ O III$)$ and $w = $ O III$/($O II $+$ O III$)$.

All of the above steps are repeated within a Monte Carlo loop over 100 iterations. The mean and standard deviations of the Monte Carlo results are then taken to be the value and error of each quantity. Results from this approach are presented in §4.1.

3.2.2   NEAT

To compute metallicity from the input values rest wavelength, total line flux, total line flux uncertainty, NEAT follows the same rough outline as most other metallicity calculators:

1. Calculate c(Hβ) and apply the interstellar reddening correction.

2. Determine the temperature and density of the emitting medium.

Table 3.2.   NEAT temperature and density diagnostics

Ionization Zone	Diagnostic	Spectral Lines
Low	N II temperature	$\frac{\lambda 6548 + \lambda 6584}{\lambda 5755}$
	O II temperature	$\frac{\lambda 7319 + \lambda 7330}{\lambda 3726 + \lambda 3729}$
	S II temperature	$\frac{\lambda 6717 + \lambda 6731}{\lambda 4068 + \lambda 4076}$
	S II density	$\frac{\lambda 6717}{\lambda 6731}$
Medium	O III temperature	$\frac{\lambda 4959 + \lambda 5007}{\lambda 4363}$

3. Calculate the ionic abundance of each ion in the input list of rest wavelengths and total fluxes.

4. Estimate the total element abundances based on the observed ionic abundances.

As outlined in §2, I correct the total line fluxes for intrinsic Balmer absorption (§2.5) and interstellar reddening (§2.6) *before* using them as input for NEAT. NEAT already assumes there is no intrinsic Balmer absorption, so there is no issue there, however there is no need to perform the interstellar reddening correction in the first step of the above outline. NEAT allows the user to specify a value for $c(H\beta)$, so a value of 0.0 is chosen for all spectra.

Next, the temperature and density are determined. NEAT considers three zones of low, medium, and high ionization, and iteratively calculates the temperature and density in each zone (in the order listed) from traditional line diagnostics. The diagnostics commonly available from this work's line lists are given in Table 3.2, however the interested reader is referred to Wesson et al. (2012) for a full list of line diagnostics used by NEAT, along with their relative weights. If a temperature and/or density diagnostic is not available in a particular zone, the temperature and/or density is set equal to the value derived in the previous zone.

Ionic abundances are then determined from CELs, as explained in § 1.3, using the temperature and density determined for the zone appropriate to that ion's ionization potential. For example, O III would correspond to a medium ionization zone, while O II would reside in the low ionization zone.

Lastly, total element abundances are estimated by summing the abundances of all ions of the given element that were observed, then corrected according to the correction factors developed in Kingsburgh and Barlow (1994). Correction factors such as these take into account the fact that not all ions of a particular element may be observed, whether due to limitations in wavelength coverage or sensitivity.

3.3   Metallicity results

A number of key emission line fluxes along with the correction factors for Balmer absorption (EW), interstellar reddening ($c(H\beta)$), and the f factors described at the end of §2.6 are presented in Table A.1. The final metallicities calculated by PyNeb and NEAT are in Table A.2.

To eliminate any anomalous metallicity values, I applied several relatively lenient rejection criteria based on well-established criteria for H II regions. These are as follows:

- SNR > 3 for [O II] $\lambda3727$ Å, and [O III] $\lambda\lambda4959,5007$ Å

- SNR > 0 for [O III] $\lambda4363$ Å, and [S II] $\lambda\lambda6716,6730$ Å

- $0.2 < R_{23} < 1.2$

- EW < 10

- PyNeb: 8000 K $< T_{\text{low}}$, $T_{\text{med}} < 13000$ K,

- NEAT: 6000 K $< T_{\text{low}}$, $T_{\text{med}} < 15000$ K,

- $12 + \log(\text{O/H}) < 9.5$

CHAPTER 4

Results

I use both PyNeb and NEAT to independently determine densities, temperatures, and metallicities for each H II region. Thus, the results from each of these methods are presented in each section in this chapter. The two methods and their corresponding results are compared in §4.5.

4.1 PyNeb Monte Carlo parameter determination

Since I have much more control over the input and output of PyNeb, I was able to make histograms of the values obtained for several key parameters in each Monte Carlo iteration. Histograms of the low- and medium-ionization zone temperatures and densities, and the oxygen abundance from 1000 Monte Carlo iterations are presented in Figures 4.1–4.2 for the low- and medium-ionization zone temperatures and densities, and the oxygen abundance. All lines of importance in H190 have SNR > 6.0. It is evident from these figures that all the posterior parameters exhibit a symmetric Gaussian behaviour. Thus, I work under the simplifying assumption that asymmetric errors need not be calculated. The full set of results for all 701 observed Hα sources only uses 100 Monte Carlo iterations per object.
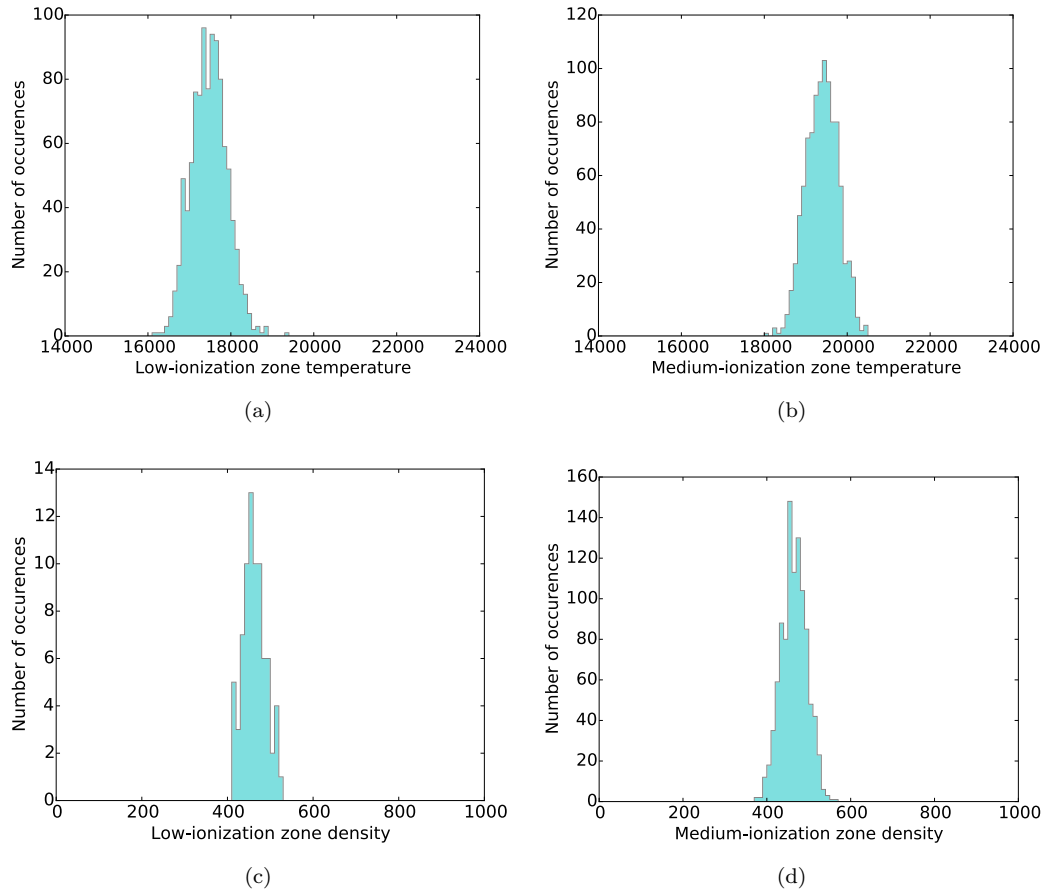
Figure 4.1 Temperature and density results in the low- and medium-ionization zones of H190 during 1000 Monte Carlo iterations in PyNeb.
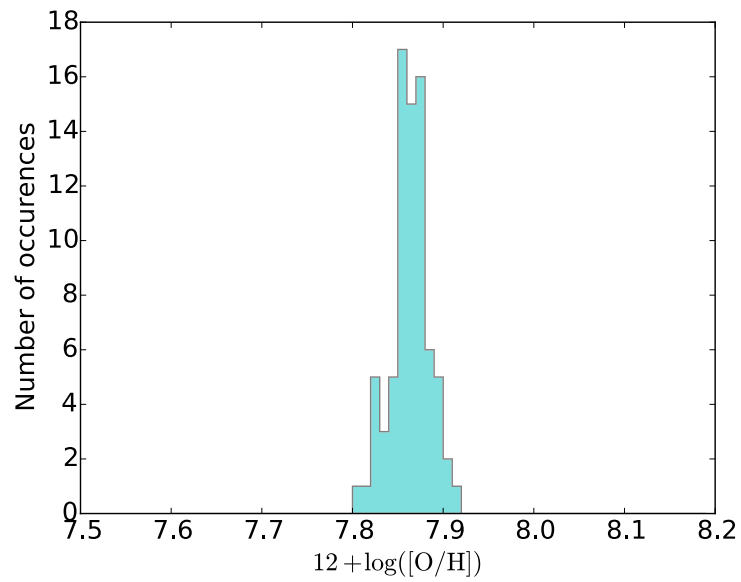
Figure 4.2 Histogram of PyNeb results for the oxygen abundance value from 1000 Monte Carlo iterations for H190.

4.2 Density and temperature distributions

The density and temperature of an H II region must be calculated before the metallicity can be derived. The unprecedented number of H II regions we have observed in the plane of M33 provides us the unique opportunity to quantify the density and temperature distributions within this spiral galaxy. I present the temperature results from both the low- and medium-ionization zones, then conduct a comparison between the two zones.

Multiple low temperature diagnostics are available to both PyNeb and NEAT from this data set. In particular, the ions O II, N II, and S II are used, as shown in Tables 3.1 and 3.2. I compare the temperatures derived from each of these indicators in Figures 4.3 and 4.4 for PyNeb and NEAT. In the PyNeb case, the N II diagnostic tends to provide a lower temperature estimate than either the O II or S II diagnostic. The O II and S II temperatures are both clustered between $\sim 10000 - 15000$ K, and there is relatively good agreement between them. For the NEAT results, I will first note that there are asymmetric error bars, and the lower valued error bars often go to 0 K. For all three diagnostic comparisons, there is a clustering of values along the 1:1 line, however in the bottom panel of Figure 4.4, there is evidence that the N II diagnostic provides a lower temperature estimate than the S II temperature, as was the case for the PyNeb results. Unlike in PyNeb however, there is no clear evidence for the N II temperatures to be significantly lower than the O II temperatures. However, it is difficult to argue whether one temperature diagnostic consistently outperforms the others, so I do not change my earlier decision to take the average of all acceptable temperatures to calculate the overall low-ionization temperature. NEAT also takes an average of acceptable temperatures to obtain the low-ionization temperature, although not all diagnostic temperatures are weighted equally (Wesson et al., 2012).

I plot my derived values of T_{med} against T_{low} to see the agreement with the relation of Campbell et al. (1986) in Figures 4.5 and 4.6 for the PyNeb and NEAT results, respectively. Both sets of results show significant scatter about this relation. There are several points in Figure 4.5 that lie directly on the Campbell et al. (1986) relation line; these are the H II regions for which one of the low- and medium-ionization zone temperatures was not available from the spectral observations, so I used the Campbell et al. (1986) relation to derive the temperature in the missing zone. Although it is difficult to discern any significant agreement with the Campbell et al. (1986) relation from these data, it does appear that the low-ionization temperatures are usually lower than the medium-ionization temperatures. Recall that I accept the PyNeb temperatures only if they lie in the range 8000–13000 K, while the NEAT temperatures can range from 6000-15000 K.

As a further comparison, the aforementioned plots of PyNeb-derived temperatures are also presented for the subset of data points whose observed SNR in [O III] $\lambda4363$ Å is greater

than 6 (Figures 4.7 and 4.8). In general, all temperatures for this subset of the data set have more reasonable values (most data points with exceptionally large error bars or values near the edge of the accepted range are removed). In particular, for the T_{med} against T_{low} plot (Figure 4.8), there is also much better agreement with the Campbell et al. (1986) relation. Also noticeable for this subset of the data is that the N II diagnostic continues to provide a lower temperature estimate than either the O II or S II diagnostic. Thus, although applying a SNR([O III] λ4363 Å) > 6 rejection criterion produces overall "better behaved" data, my goal to calculate as many abundances as possible in M33 means I will work primarily with the much larger data set given by SNR([O III] λ4363 Å) > 0, but I will periodically return to the SNR([O III] λ4363 Å) > 6 subset for comparison on notable results.

Histograms and radial gradients of the PyNeb and NEAT derived temperatures are shown in Figures 4.9–4.12. For both PyNeb and NEAT, the temperature histograms indicate that the low-ionization temperatures generally lie at slightly lower values than the medium-ionization temperatures, in agreement with the trend observed in the plots of T_{med} versus T_{low} (Figures 4.5 and 4.6). With regard to the radial gradients, both PyNeb and NEAT results show the medium-ionization zone gradient has a steeper positive slope than the low-ionization slope, although in all cases the scatter is extremely large. Both low- and medium-ionization zone temperatures from PyNeb are consistent with a flat slope. Also, these results show that the central low-ionization zone temperature is larger than the medium-ionization zone temperature, although the difference between the two central values is less than the uncertainty on the central medium-ionization zone temperature, which is relatively very large.

Histograms and radial gradients of the PyNeb and NEAT derived densities are shown in Figures 4.13 and 4.14, respectively. For both PyNeb and NEAT, densities in the low- and medium-ionization zones are approximately equal to one another, which is consistent with a single density H II region, as was originally modelled by Strömgren (1939). Nearly all of the derived densities are generally at typical H II region values of $\lesssim 500 \mathrm{cm}^{-3}$. The radial gradient slopes in both ionization zones are negative from the PyNeb results and positive from the NEAT results, however all four slopes are consistent with a flat gradient, so this is the most sensible interpretation of the results. All four gradient intercepts lie between $10^{2.21}$–$10^{2.32}$ cm^{-3}, with their average value being $\sim$180 cm^{-3}.
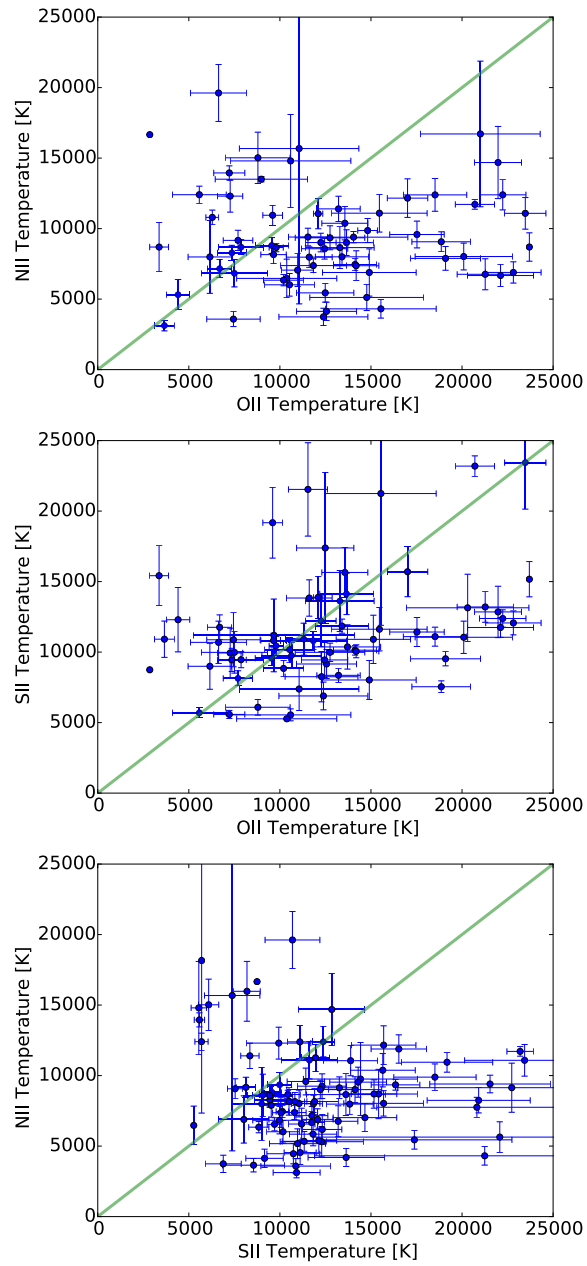
Figure 4.3 A comparison of PyNeb temperatures derived in the low-ionization zone from the three temperature diagnostics available in this data set: [O II] $\lambda\lambda3727,3729$ Å$/\lambda\lambda7319,7330$ Å, [N II] $\lambda5755$ Å$/\lambda6548$ Å and [N II] $\lambda5755$ Å$/\lambda6584$ Å, and [S II] $\lambda\lambda4068,4076$ Å$/\lambda\lambda6716,6731$ Å. The 1:1 line is shown in green.
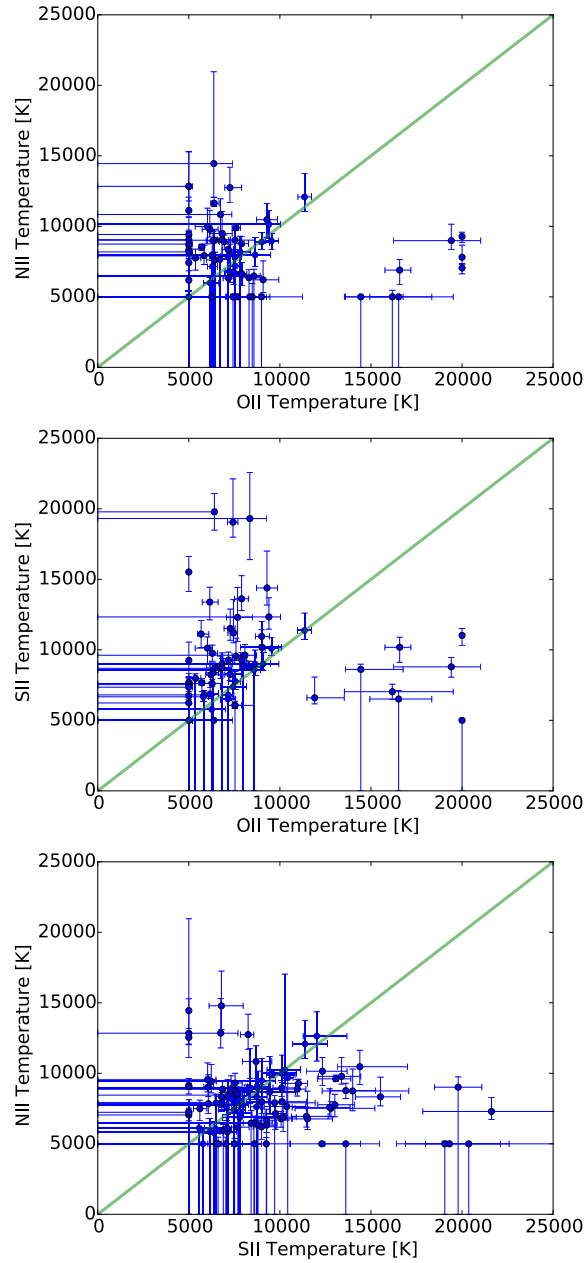
Figure 4.4 A comparison of NEAT temperatures derived in the low-ionization zone from the three temperature diagnostics available in this data set: [O II] $\lambda\lambda7319,7330$ Å$/\lambda\lambda3727,3729$ Å, [N II] $\lambda5755$ Å$/\lambda6584$ Å, [S II] $\lambda6730$ Å$/\lambda6716$ Å. The 1:1 line is shown in green.
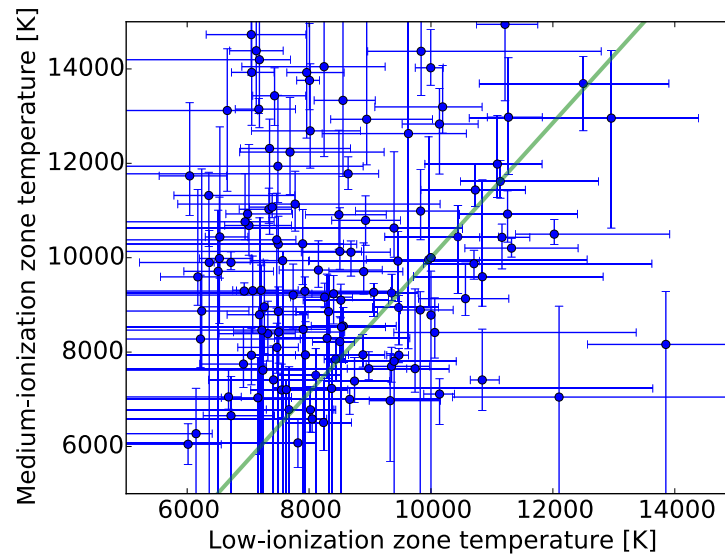
Figure 4.5 A comparison of PyNeb temperatures derived in the low- and medium-ionization zones of all observed H II regions. The solid green line marks the relation derived by Campbell et al. (1986) ($T_{\mathrm{low}} = 0.7\ T_{\mathrm{med}} + 3000$ K).
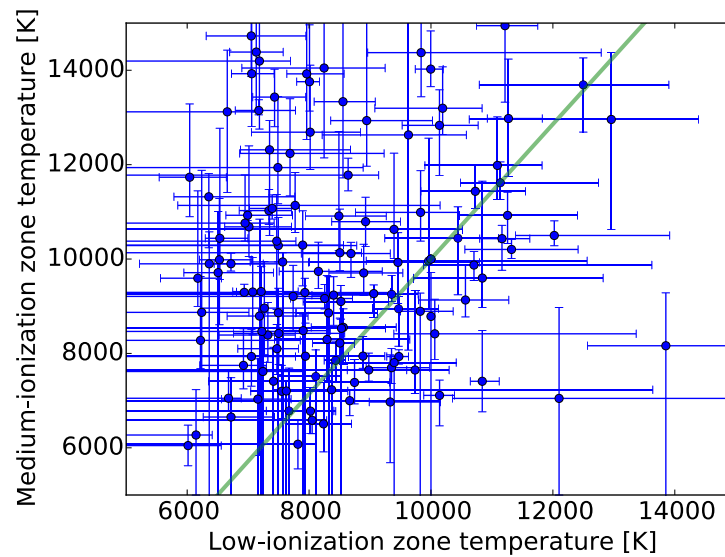
Figure 4.6 A comparison of NEAT temperatures derived in the low- and medium-ionization zones of all observed H II regions. The solid green line marks the relation derived by Campbell et al. (1986) ($T_{\mathrm{low}} = 0.7\ T_{\mathrm{med}} + 3000$ K).
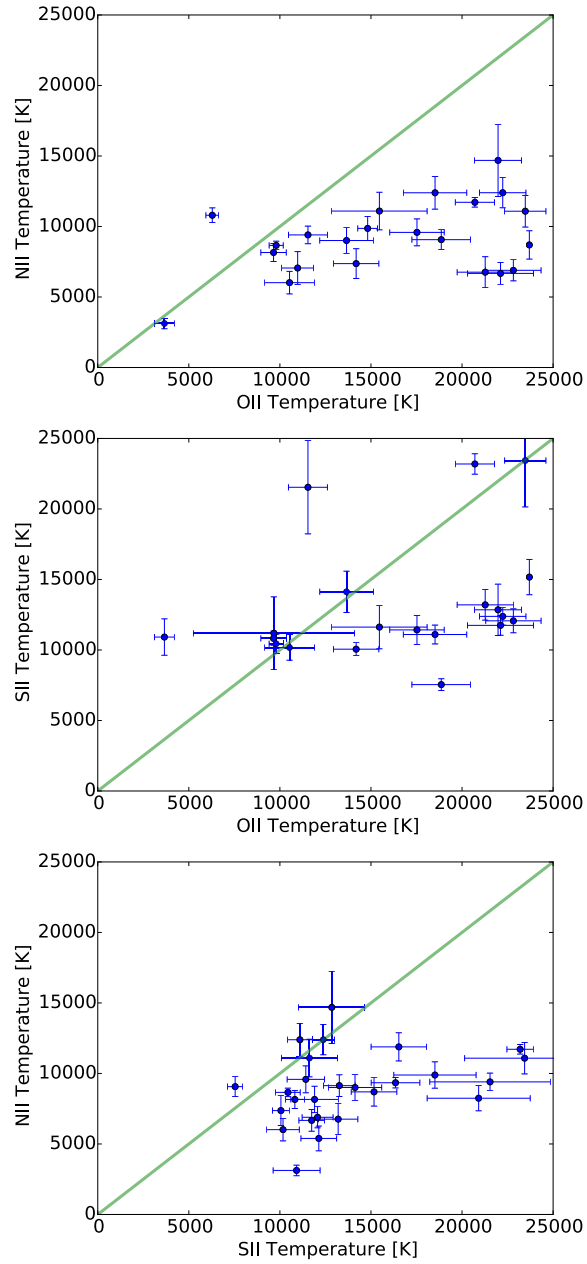
Figure 4.7 The same as Figure 4.3, but only including data points that have an observed SNR > 6 for [O III] λ4363 Å.
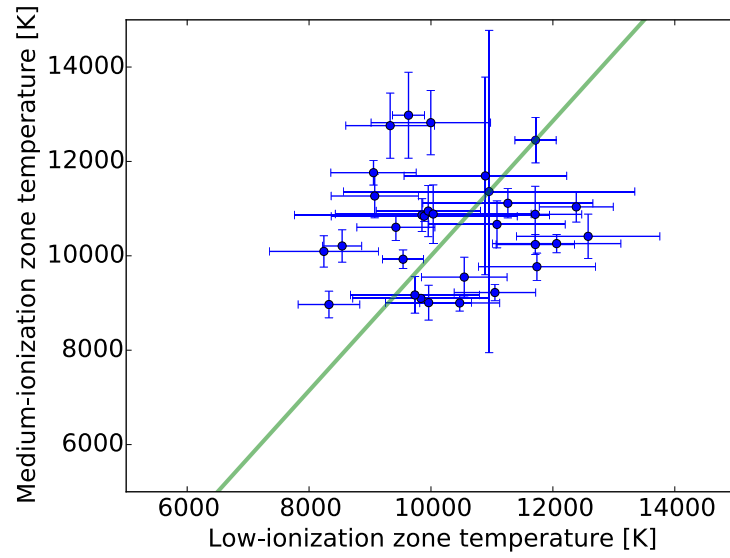
Figure 4.8 The same as Figure 4.5, but only including data points that have an observed SNR > 6 for [O III] $\lambda4363$ Å.
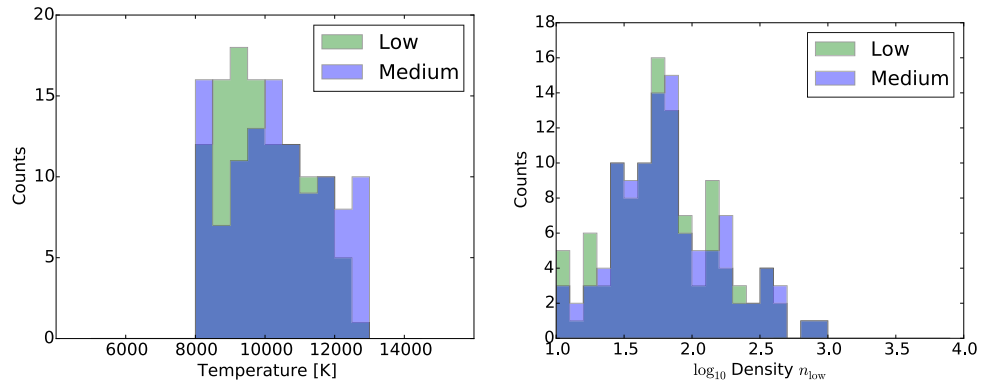
Figure 4.9 Histograms of the temperature and density results from PyNeb. The values in both the low- and medium-ionization zones are shown in each panel.
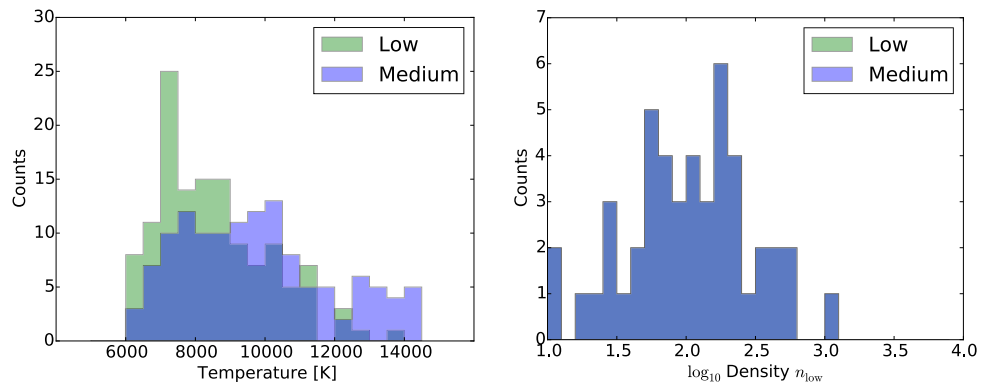
Figure 4.10 Histograms of the temperature and density results from NEAT. The values in both the low- and medium-ionization zones are shown in each panel. The density values are identical in both the ionization zones because of the way NEAT works.
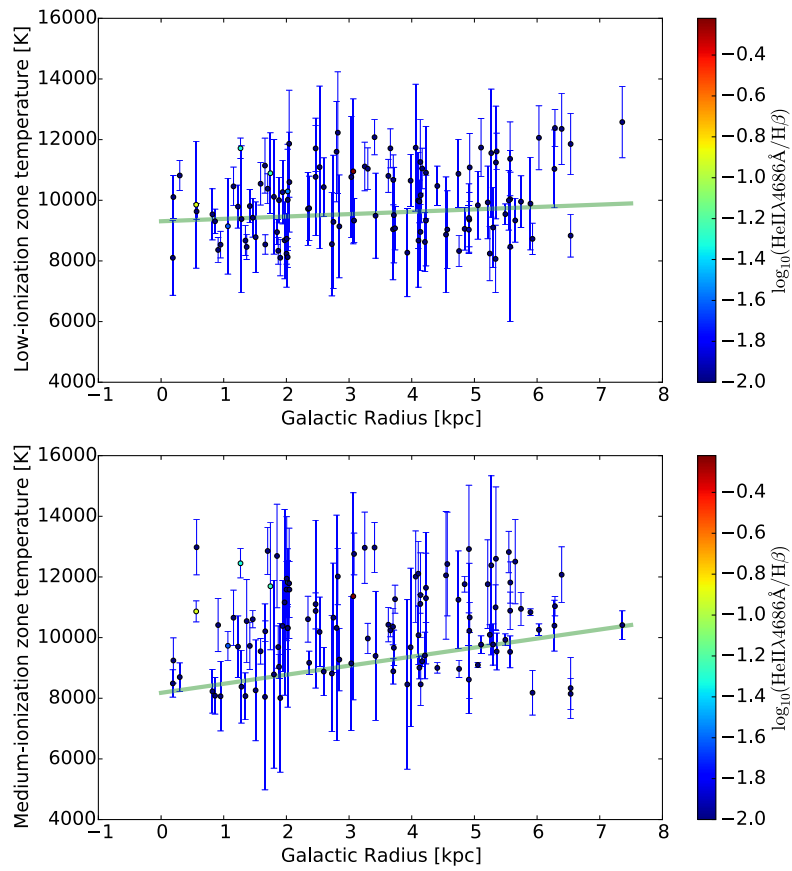
Figure 4.11 The low- and medium-ionization zone temperature radial gradients from PyNeb. The low-ionization zone gradient has slope 78 ± 105 K kpc^{-1} and intercept 9308 ± 415 K. The medium-ionization zone gradient has slope 298 ± 334 K kpc^{-1} and intercept 8179 ± 1649 K.
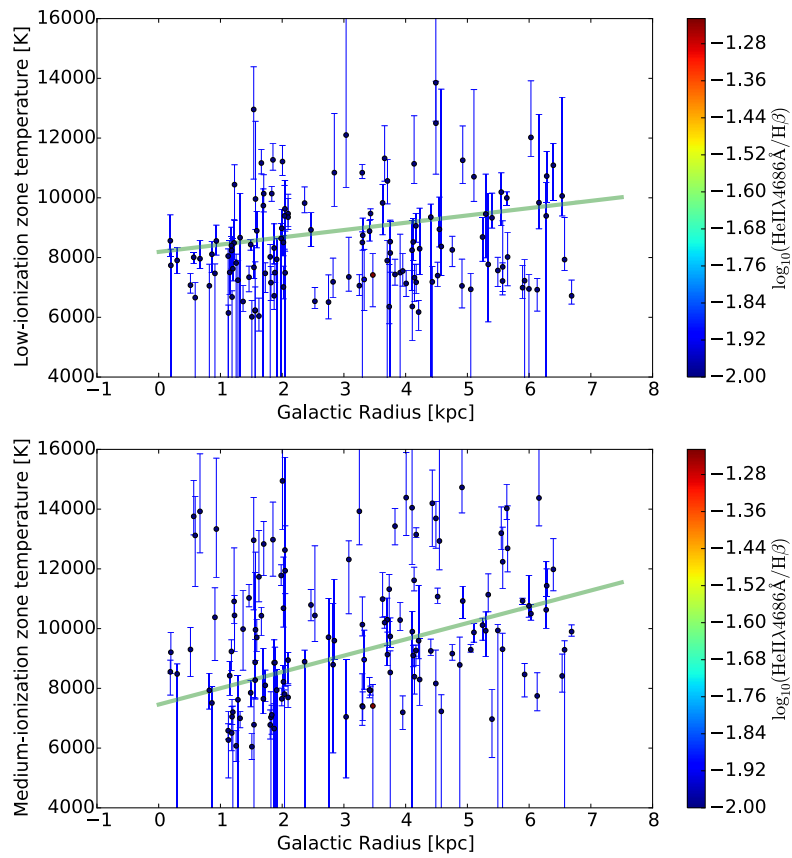
Figure 4.12 The low- and medium-ionization zone temperature radial gradients from NEAT. The low-ionization zone gradient has slope 244 ± 141 K kpc^{-1} and intercept 8190 ± 368 K. The medium-ionization zone gradient has slope 545 ± 288 K kpc^{-1} and intercept 7459 ± 1498 K.
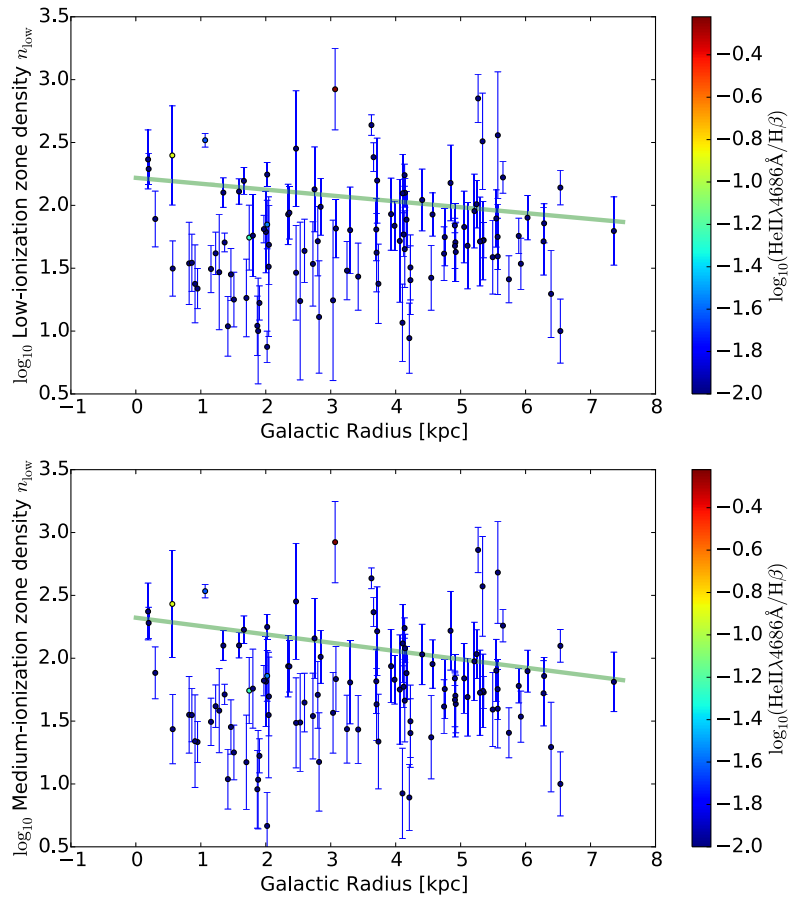
Figure 4.13 The low- and medium-ionization zone density radial gradients from PyNeb. The low-ionization zone gradient has slope -0.047 ± 0.070 dex kpc^{-1} and intercept 2.22 ± 0.29. The medium-ionization zone gradient has slope -0.066 ± 0.063 dex kpc^{-1} and intercept 2.32 ± 0.27.
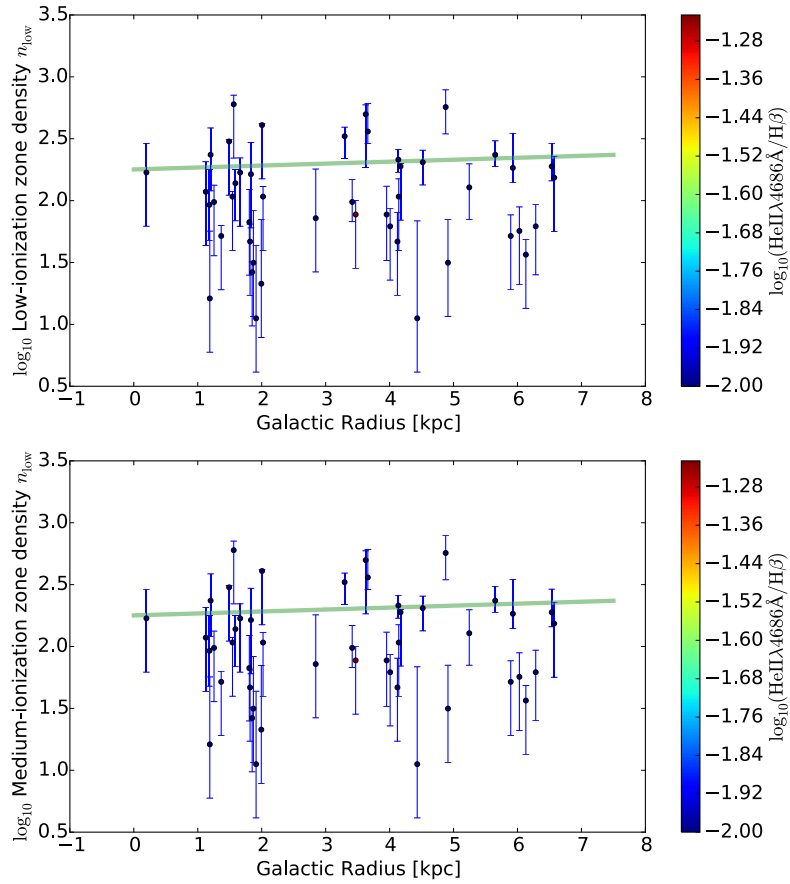
Figure 4.14 The low- and medium-ionization zone density radial gradients from NEAT. The low-ionization zone gradient has slope 0.016 ± 0.025 dex kpc^{-1} and intercept 2.25 ± 0.12. The medium-ionization zone gradient has slope 0.016 ± 0.025 dex kpc^{-1} and intercept 2.25 ± 0.12.

4.3 Metallicity comparison to strong-line indicators

As noted in §1.5, an important result of this work is the ability to improve upon the current strong-line calibrations. This is done by comparing the observed strong-line indicators $(R_{23}, N_2, O_3N_2, Ar_3O_3, S_3O_3)$ to metallicities derived from the weak-line direct method (discussed in §1.4).

I present the PyNeb and NEAT oxygen abundances as a function of R_{23} in Figures 4.15 and 4.16. Both plots also show the current strong-line calibration curve (Eq. 1.3). Similarly, the oxygen abundances plotted against the other four strong-line indicators discussed in §1.5, along with their respective calibration curves, are shown in Figures 4.17 and 4.18. In the R_{23} plots for both PyNeb and NEAT, the data agrees with the calibration curve for oxygen-rich H II regions. For all strong-line indicators, with the exception of O_3N_2, the data lie solidly on the calibration curves. For O_3N_2, there is a systematic offset, likely indicating that the objects being studied here differ from those used to perform the calibration. In all strong-line metallicity plots there is significant scatter, making it difficult to identify any further trends within either the PyNeb or NEAT data set. Improvements to the strong-line indicator calibrations must wait until further refinement of the metallicity data is accomplished in future work.
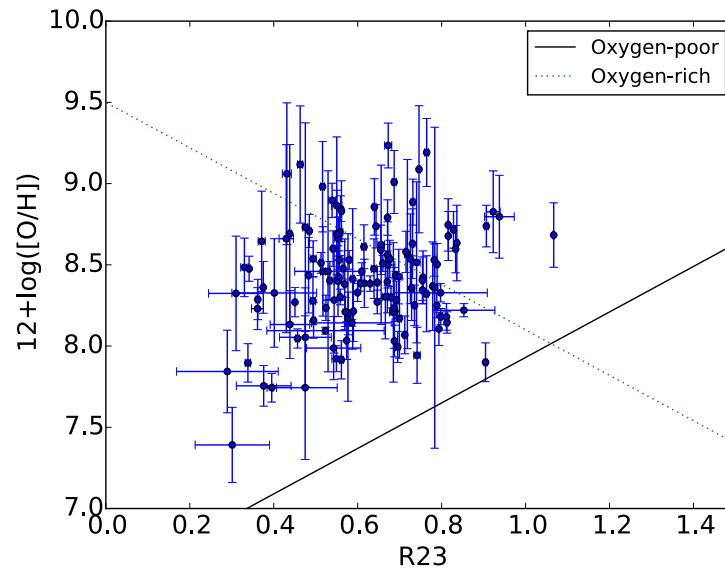
Figure 4.15 The comparison between the PyNeb metallicities derived from the weak-line method to the R_{23} strong-line metallicity diagnostic. The solid and dotted lines show the current calibration for oxygen-poor and -rich H II regions, respectively, according to Pilyugin (2000).
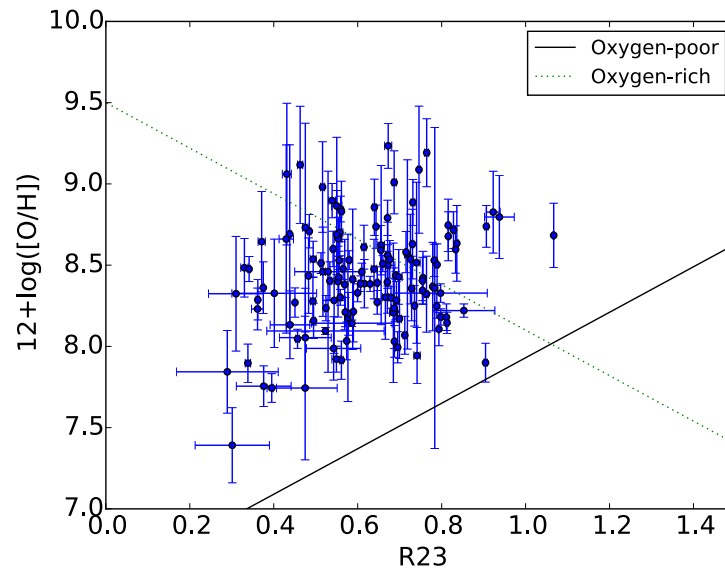
Figure 4.16 The comparison between the NEAT metallicities derived from the weak-line method to the R_{23} strong-line metallicity diagnostic. The solid and dotted lines show the current calibration for oxygen-poor and -rich H II regions, respectively, according to Pilyugin (2000).
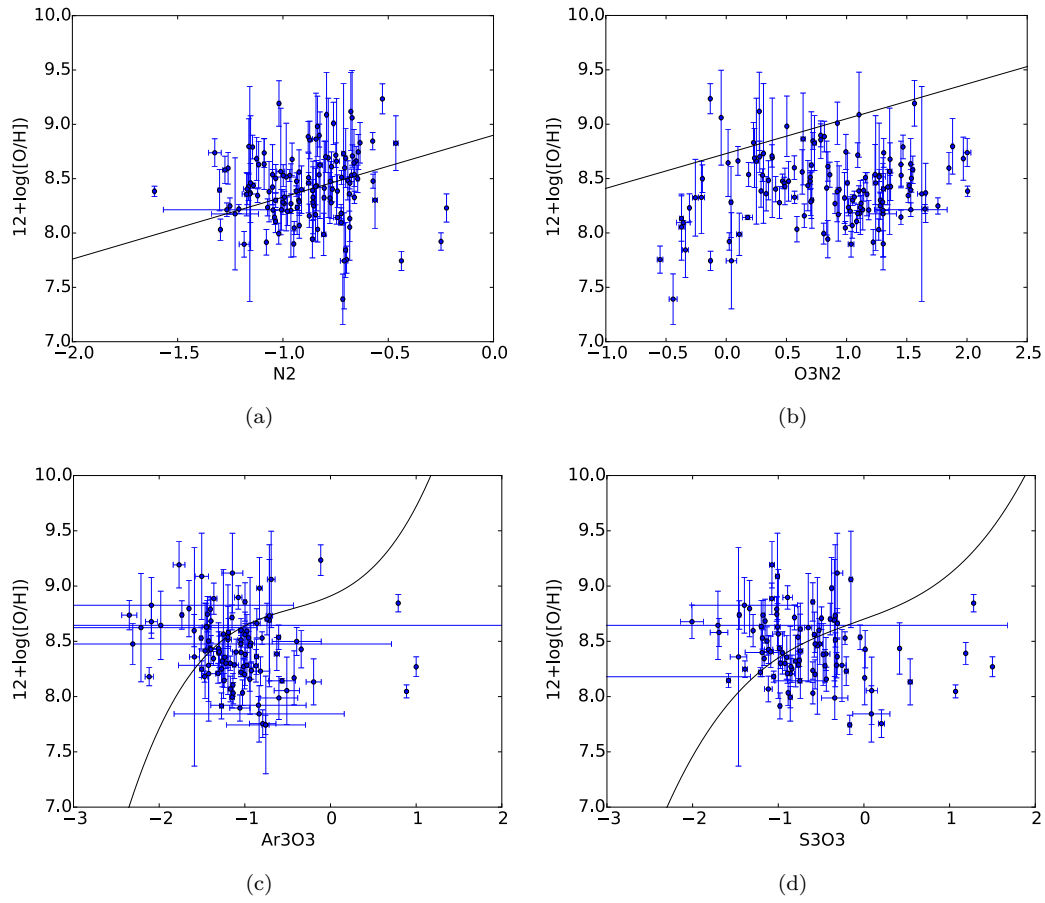
Figure 4.17 A comparison of the PyNeb metallicities derived from the weak-line method to various strong-line metallicity diagnostics. The solid lines in (a) and (b) show the current calibrations according to Pettini and Pagel (2004). The solid lines in (c) and (d) show the current calibrations according to Stasińska (2006).
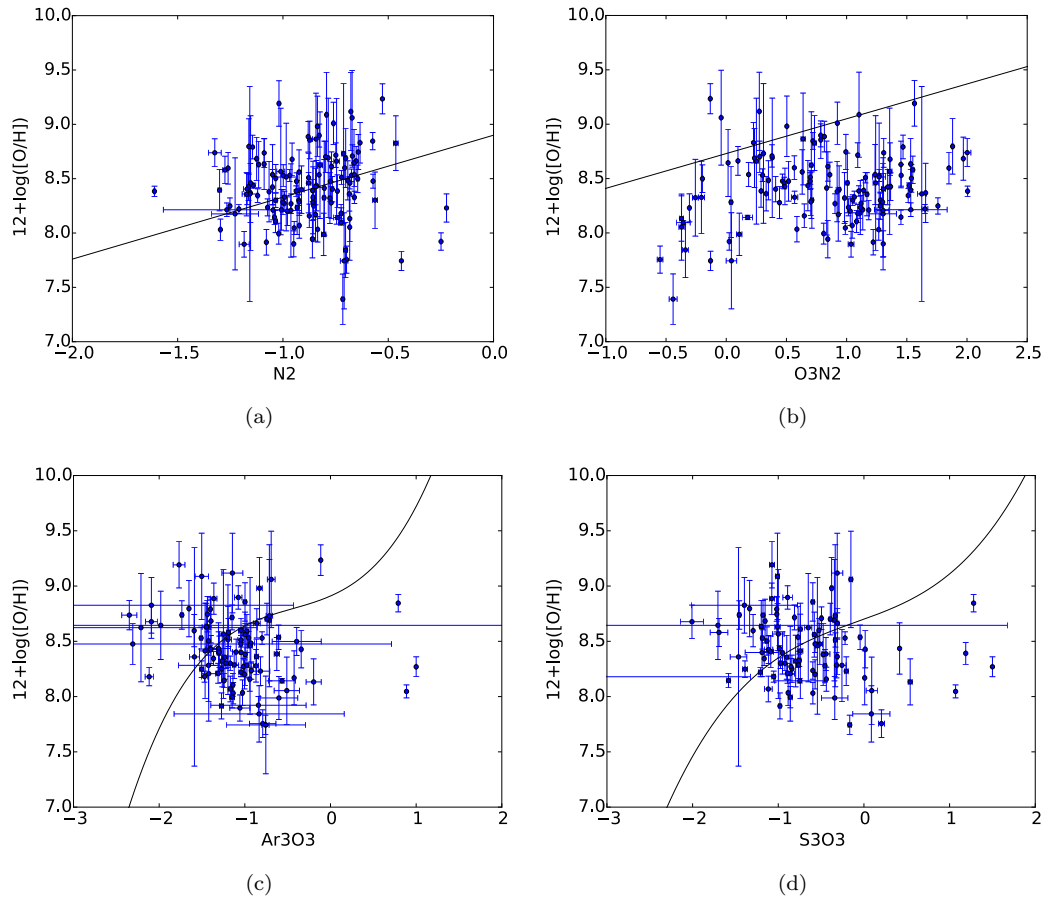
Figure 4.18 A comparison of the NEAT metallicities derived from the weak-line method to various strong-line metallicity diagnostics. The solid lines in (a) and (b) show the current calibrations according to Pettini and Pagel (2004). The solid lines in (c) and (d) show the current calibrations according to Stasińska (2006).

4.4 Metallicity gradients

The PyNeb and NEAT metallicity gradients are plotted for O/H (Figures 4.19–4.22), N/H (Figures 4.23, 4.24), N II/O II (Figures 4.25, 4.26), S/H (Figures 4.27, 4.28), S/O (Figures 4.29, 4.30), Ne/H (Figures 4.31, 4.32), and Ne/O (Figures 4.33, 4.34). Each figure shows the line of best fit in green, which I calculated by bootstrapping an inverse-uncertainty-weighted polynomial fit. Data points with exceptionally low (< 0.05) or high (> 0.4) uncertainties are excluded from the fit since I believe these values are either mis-representative of the true error, or they indicate a measurement error has likely occurred. Either way, including these data points leads to a much poorer fit. The slopes and intercepts for each line of best fit are presented in Table 4.1. Recall Table 1.5 provides information on the oxygen radial gradients derived in a number of previous M33 studies. For reference, the solar oxygen abundance is $12 + \log(\text{O/H})_{\odot} = 8.70$ (Grevesse, 2009).

The O/H radial gradients from PyNeb and NEAT are each plotted for the full data set given by SNR([O III] $\lambda 4363$ Å) > 0, as well as the subset for which SNR([O III] $\lambda 4363$ Å) > 6. I will first discuss the results given in Figures 4.19 and f:neatgradOH for the full data set. Both PyNeb and NEAT results indicate the central metallicity is around 8.47, with a negative slope that is in the same range as most previous studies have found, however the precise values of the gradients from PyNeb and NEAT are not consistent with one another. The PyNeb gradient is extremely shallow (-0.010 ± 0.019 dex kpc^{-1}), while the NEAT gradient is much steeper (-0.049 ± 0.013 dex kpc^{-1}). In looking at the plots more closely, both sets of results exhibit a large amount of scatter. For the PyNeb results, the mean residual of all data points with respect to the line of best fit is 0.21, while the average metallicity uncertainty is 0.18. For NEAT, the mean residual is 0.33 and the average uncertainty is 0.16. The implications of these values will be discussed in more detail in §4.7.

The O/H radial gradients for the SNR([O III] $\lambda 4363$ Å) > 6 subset are presented in Figures 4.21 and 4.22. The PyNeb slope is a bit steeper than for the full set, while the NEAT data set slope is a bit shallower. This, combined with the larger uncertainties, means the two slopes are now consistent with one another, although there is still quite a large difference between them. The central abundances have not changed significantly from what was calculated for the full data set ($12 + \log(\text{O/H}) \simeq 8.47$).

The nitrogen radial gradients show much less scatter than the O/H gradients in both PyNeb and NEAT. The PyNeb relations are particularly strong, with the exception of two outlier data points. Since both the N/H and N II/O II gradients are negative, this indicates that nitrogen and oxygen both become less abundant in the outskirts of the galaxy compared to the central regions, however the nitrogen drop-off occurs much faster, in agreement with the early findings of Searle (1971). Further, the N/H relations are nearly identical between

Table 4.1.   M33 metallicity gradients from this work

Element	PyNeb Gradient dex kpc^{-1}	PyNeb Intercept	NEAT Gradient dex kpc^{-1}	NEAT Intercept
O/H	-0.010 ± 0.019	8.48 ± 0.07	-0.049 ± 0.013	8.46 ± 0.05
O/H (SNR > 6)	-0.016 ± 0.030	8.52 ± 0.13	-0.041 ± 0.029	8.41 ± 0.12
N/H	-0.092 ± 0.020	7.38 ± 0.07	-0.093 ± 0.013	7.44 ± 0.05
N II/O II	-0.070 ± 0.019	-1.18 ± 0.08	-0.126 ± 0.036	-0.85 ± 0.15
S/H	0.029 ± 0.029	6.43 ± 0.13	-0.033 ± 0.078	7.53 ± 0.34
S/O	0.037 ± 0.029	-1.93 ± 0.12	-0.045 ± 0.118	-0.59 ± 0.51
Ne/H	-0.023 ± 0.030	7.63 ± 0.12	-0.039 ± 0.024	7.69 ± 0.09
Ne/O	-0.002 ± 0.024	-0.88 ± 0.11	0.036 ± 0.027	-0.83 ± 0.07

PyNeb and NEAT, and suggest the gradient is around -0.093 dex kpc^{-1} and the central N/H metallicity is approximately 7.41. The N II/O II relations are not consistent between PyNeb and NEAT, although this is expected given the differences in O/H.

There is more ambiguity in the sulfur gradients than any of the other metal gradients I examine. The PyNeb results indicate a positive gradient for both S/H and S/O, while NEAT favours a negative gradient for both. Still, the PyNeb and NEAT gradients are consistent with one another for each relation, only their intercepts differ significantly. It seems likely that the sulfur gradient is (nearly) flat.

The Ne/H and Ne/O gradients are consistent between PyNeb and NEAT, although this is due at least in part to the relatively large uncertainties on both slopes and intercepts. The PyNeb gradients for both Ne/H and Ne/O are consistent with a slope of zero, but this is not the case for the NEAT results. However, PyNeb and NEAT seem to agree that the central Ne/H abundance is roughly 7.66 and that the Ne/O slope is shallower than the Ne/H slope, thus indicating that oxygen falls off more rapidly than neon as galactic radius increases.

Lastly, I plotted R_{23} as a function of radius to derive the R_{23} radial gradient. I found the line of best fit had a positive slope of 0.041 ± 0.018 dex kpc^{-1} and intercept 0.59 ± 0.08. This is consistent with there being a negative radial gradient for $12 + \log(O/H)$, since these two quantities have an inverse relation in the oxygen-rich regime, as seen in Figures 4.15 and 4.16. Using the oxygen-rich relation between R_{23} and oxygen metallicity, I calculate that the oxygen gradient corresponding to this R_{23} gradient has a slope of -0.057 ± 0.016 and intercept $12 + \log(O/H) = 8.67 \pm 1.23$. This gradient is consistent with the NEAT-derived oxygen metallicity gradient, but not the PyNeb gradient. The intercept is consistent with both PyNeb and NEAT's $12 + \log(O/H)$ intercept, although the R_{23}-derived value has a large uncertainty.
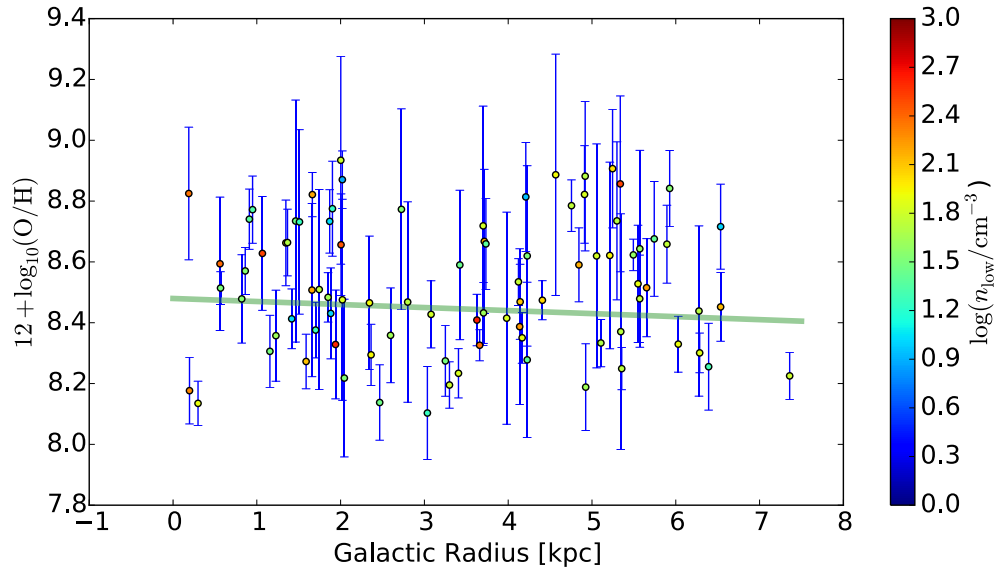
Figure 4.19 The PyNeb oxygen abundances are plotted according to their galactocentric radii to show the overall radial gradient. The slope and intercept of the line of best fit (shown in green) are -0.010 ± 0.019 dex kpc^{-1} and 8.48 ± 0.07, respectively.
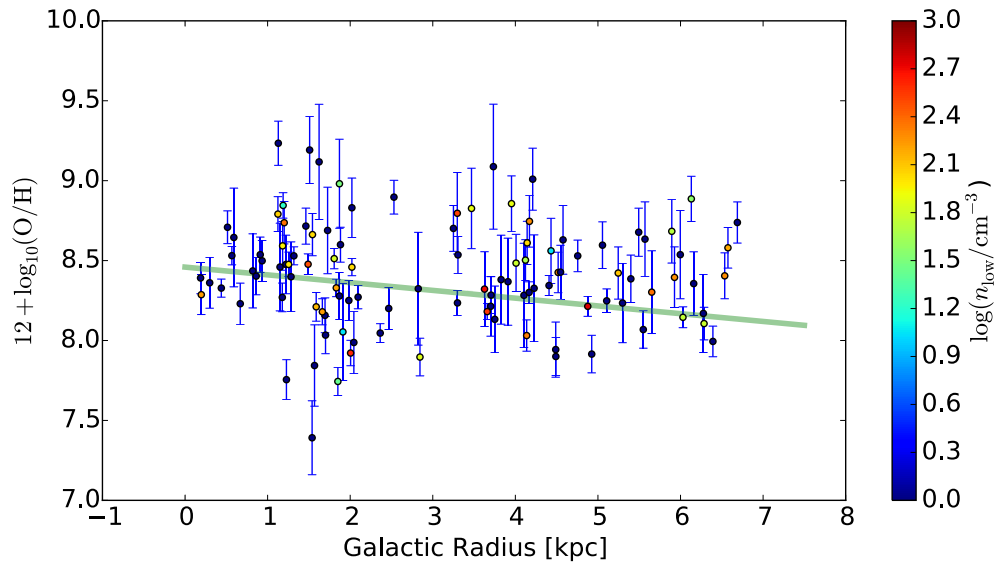
Figure 4.20 The NEAT oxygen abundances are plotted according to their galactocentric radii to show the overall radial gradient. The slope and intercept of the line of best fit (shown in green) are -0.049 ± 0.013 dex kpc^{-1} and 8.46 ± 0.05, respectively.
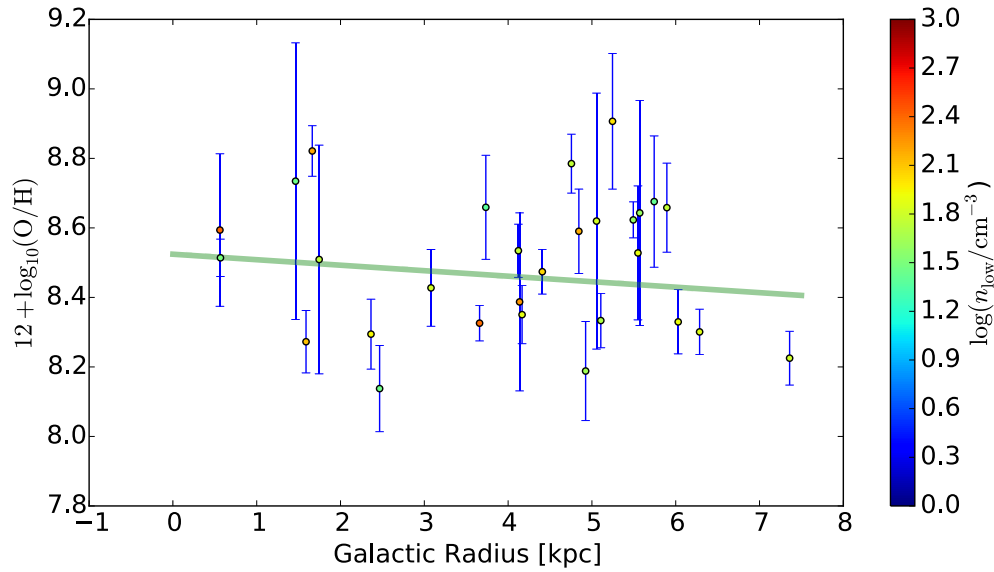
Figure 4.21 The same as Figure 4.19, but only including data points that have an observed SNR > 6 for [O III] $\lambda4363$ Å. The slope and intercept of the line of best fit (shown in green) are -0.016 ± 0.030 dex kpc^{-1} and 8.52 ± 0.13, respectively.
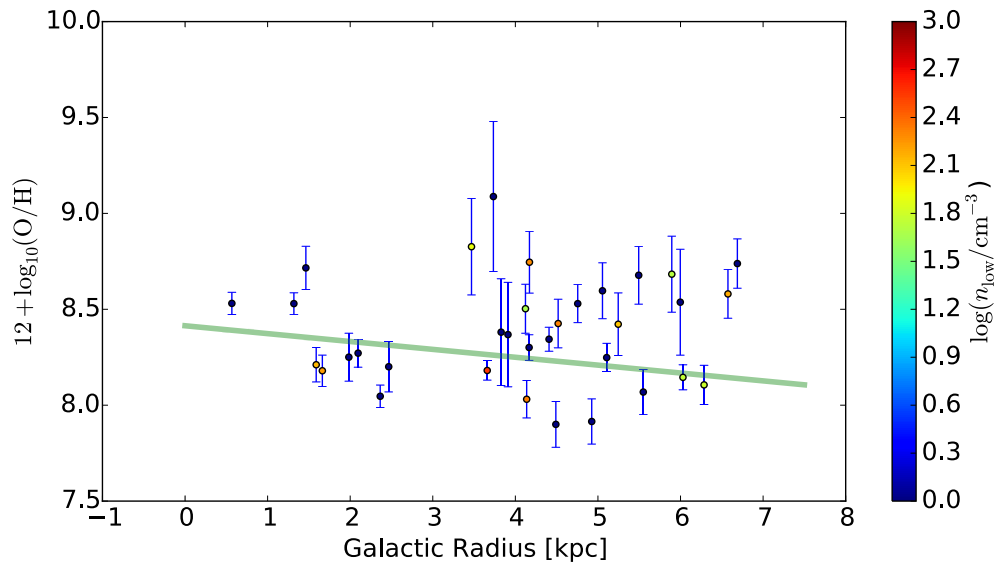
Figure 4.22 The same as Figure 4.20, but only including data points that have an observed SNR > 6 for [O III] $\lambda4363$ Å. The slope and intercept of the line of best fit (shown in green) are -0.041 ± 0.029 dex kpc^{-1} and 8.41 ± 0.12, respectively.
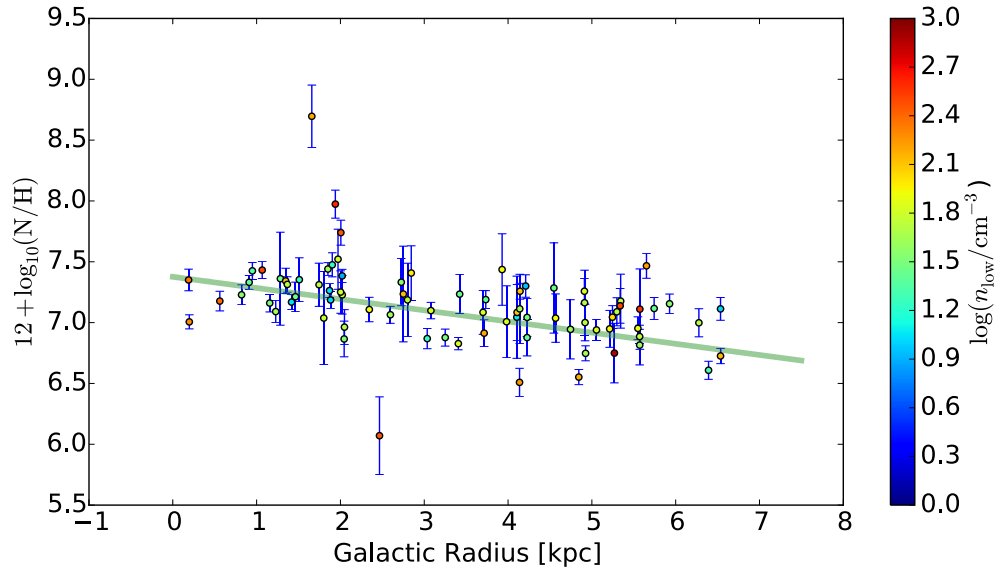
Figure 4.23 The PyNeb nitrogen abundances are plotted according to their galactocentric radii to show the overall radial gradient. The slope and intercept of the line of best fit (shown in green) are -0.092 ± 0.020 dex kpc^{-1} and 7.38 ± 0.07, respectively.
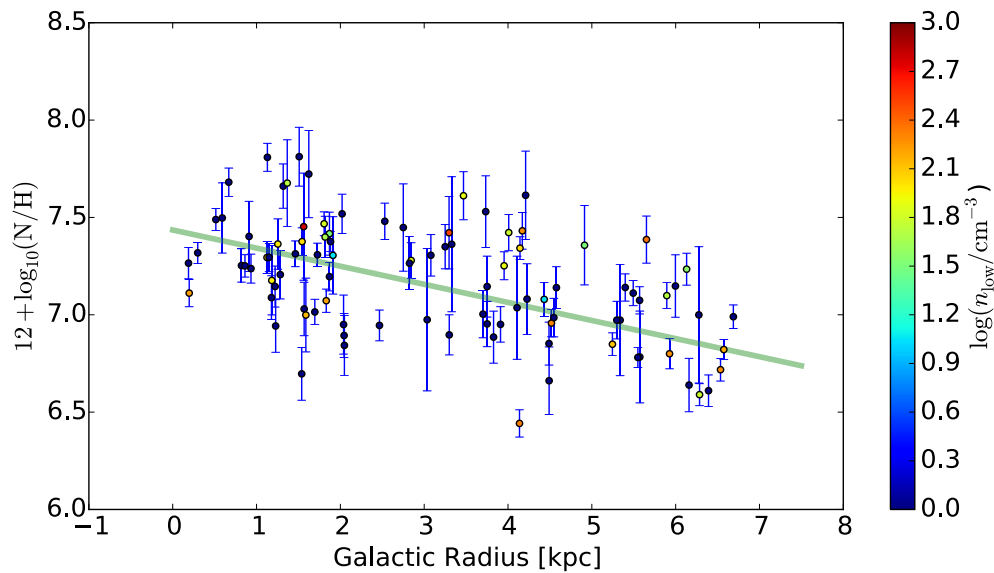
Figure 4.24 The NEAT nitrogen abundances are plotted according to their galactocentric radii to show the overall radial gradient. The slope and intercept of the line of best fit (shown in green) are -0.093 ± 0.013 dex kpc^{-1} and 7.44 ± 0.05, respectively.
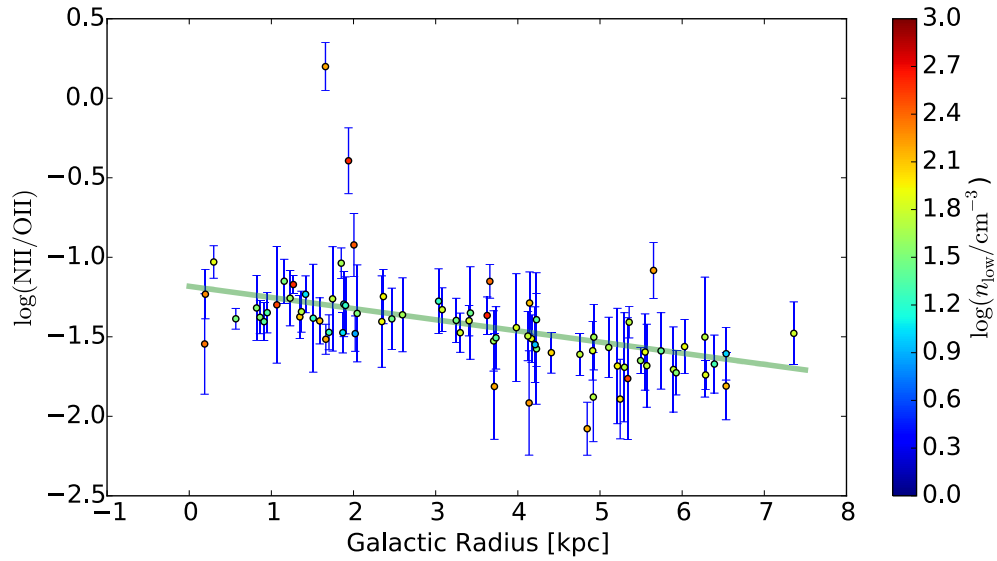
Figure 4.25 The PyNeb nitrogen to oxygen abundance ratios are plotted according to their galactocentric radii to show the overall radial gradient. The slope and intercept of the line of best fit (shown in green) are -0.070 ± 0.019 dex kpc^{-1} and -1.18 ± 0.08, respectively.
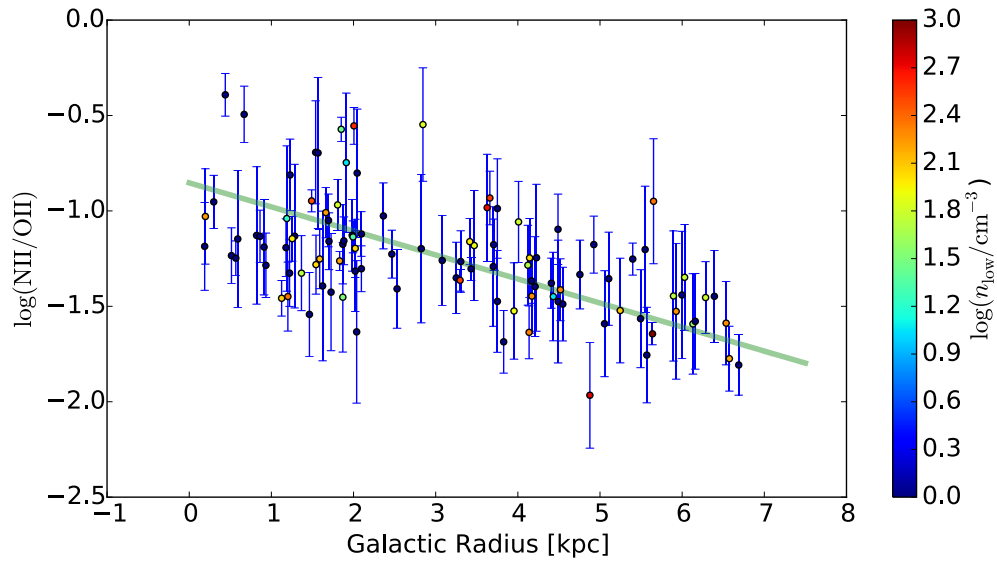
Figure 4.26 The NEAT nitrogen to oxygen abundance ratios are plotted according to their galactocentric radii to show the overall radial gradient. The slope and intercept of the line of best fit (shown in green) are -0.126 ± 0.036 dex kpc^{-1} and -0.85 ± 0.15, respectively.
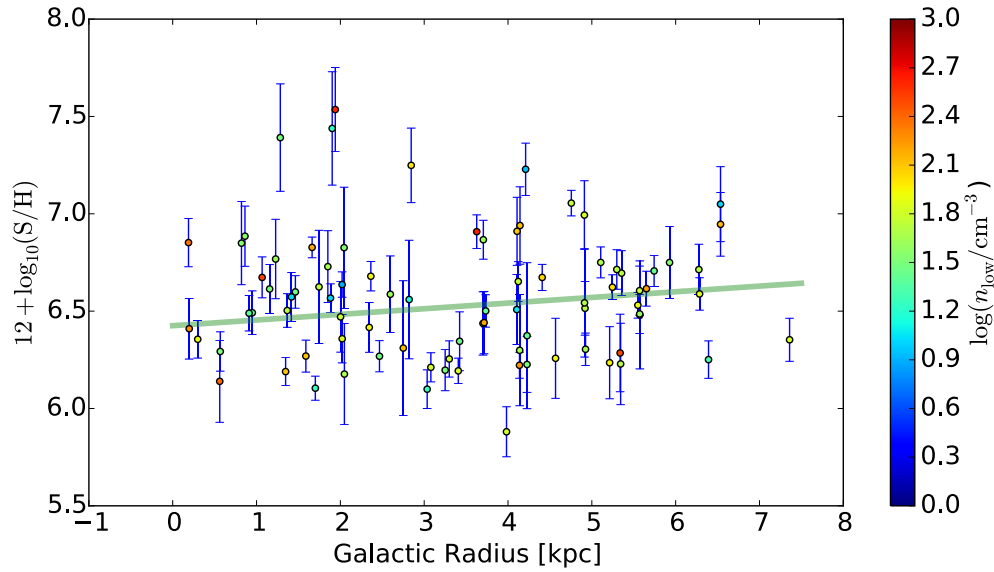
Figure 4.27 The PyNeb sulfur abundances are plotted according to their galactocentric radii to show the overall radial gradient. The slope and intercept of the line of best fit (shown in green) are 0.029 ± 0.029 dex kpc^{-1} and 6.43 ± 0.13, respectively.
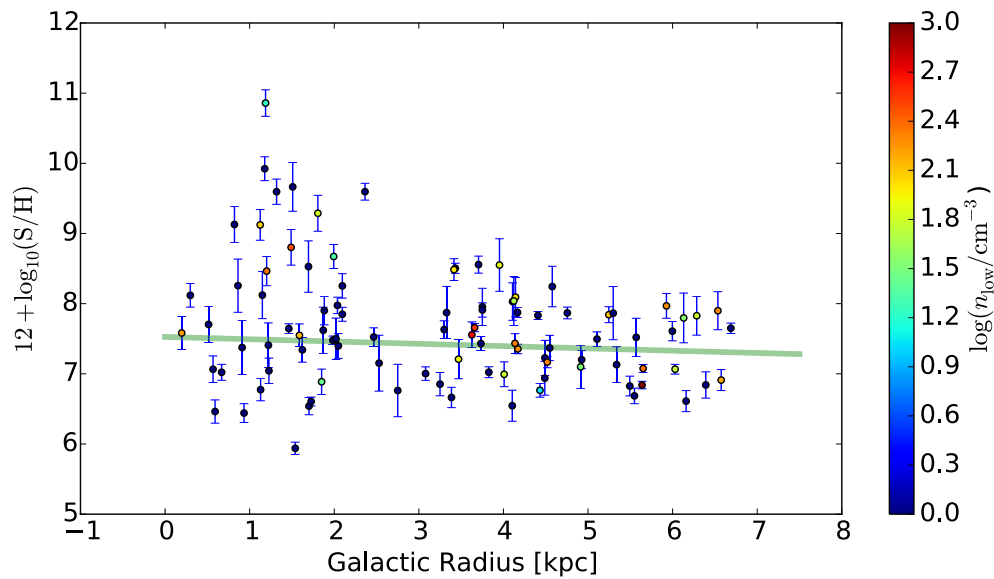
Figure 4.28 The NEAT sulfur abundances are plotted according to their galactocentric radii to show the overall radial gradient. The slope and intercept of the line of best fit (shown in green) are -0.033 ± 0.078 dex kpc^{-1} and 7.53 ± 0.34, respectively.
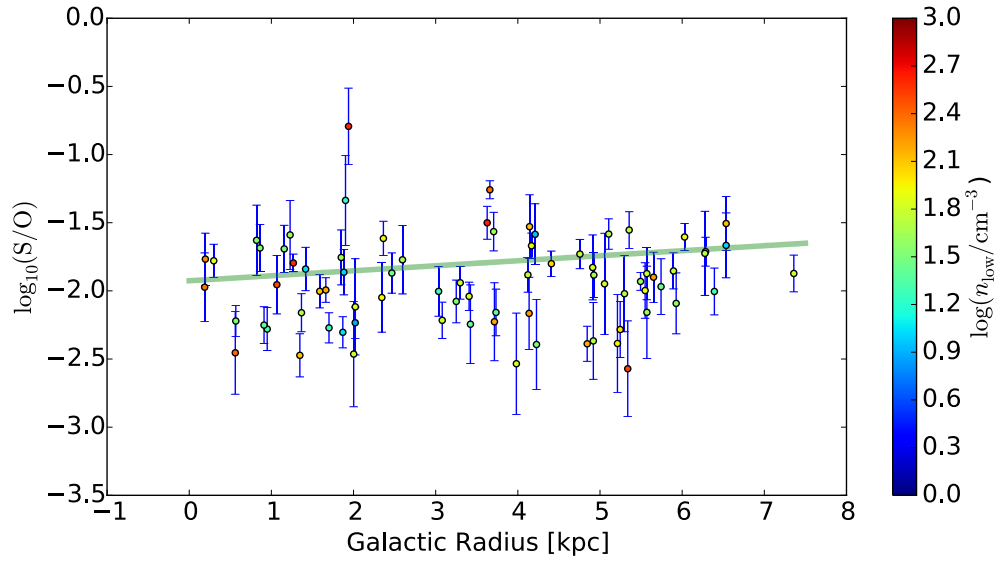
Figure 4.29 The PyNeb sulfur to oxygen abundance ratios are plotted according to their galactocentric radii to show the overall radial gradient. The slope and intercept of the line of best fit (shown in green) are 0.037 ± 0.029 dex kpc^{-1} and -1.93 ± 0.12, respectively.
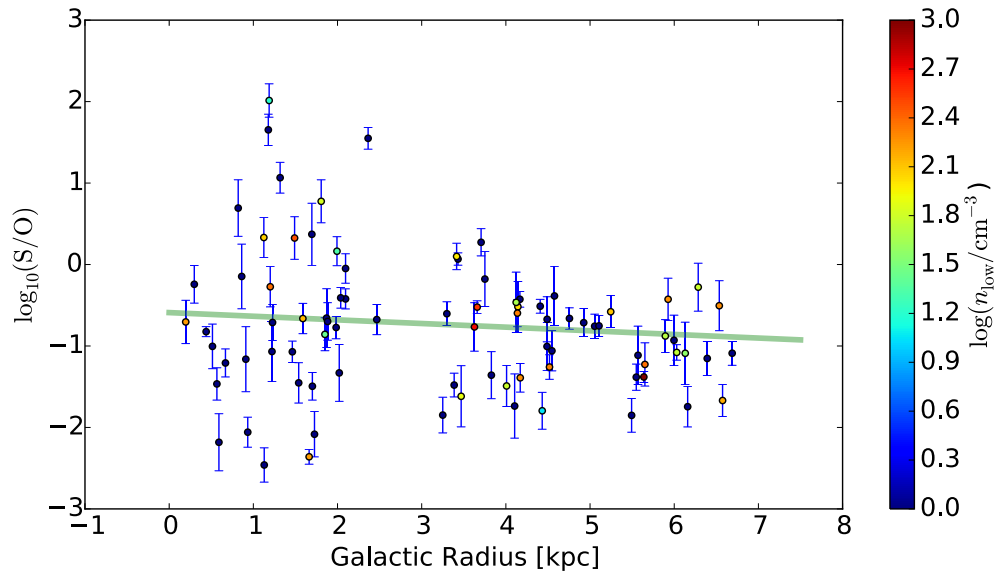
Figure 4.30 The NEAT sulfur to oxygen abundance ratios are plotted according to their galactocentric radii to show the overall radial gradient. The slope and intercept of the line of best fit (shown in green) are -0.045 ± 0.118 dex kpc^{-1} and -0.59 ± 0.51, respectively.
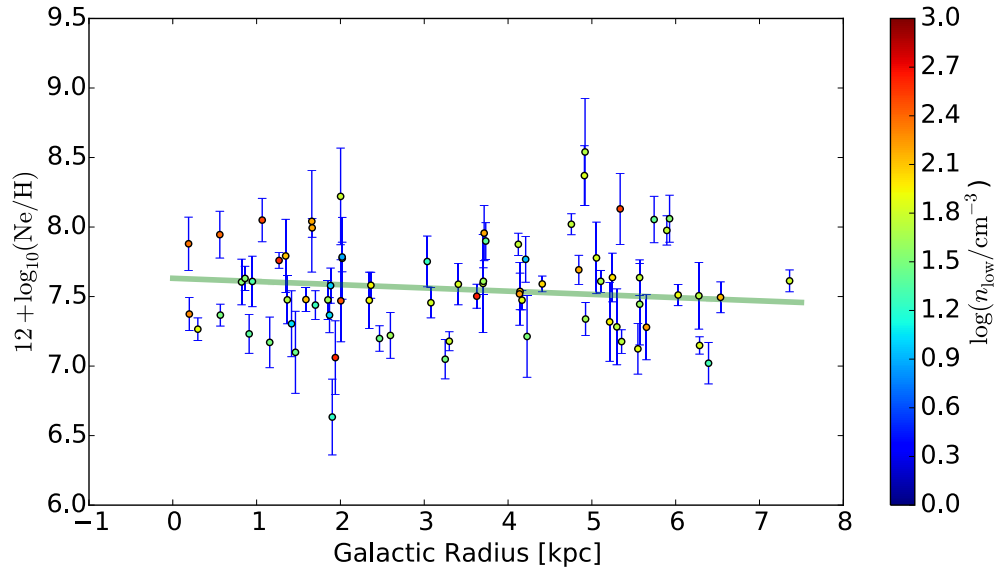
Figure 4.31 The PyNeb neon abundances are plotted according to their galactocentric radii to show the overall radial gradient. The slope and intercept of the line of best fit (shown in green) are -0.023 ± 0.030 dex kpc^{-1} and 7.63 ± 0.12, respectively.
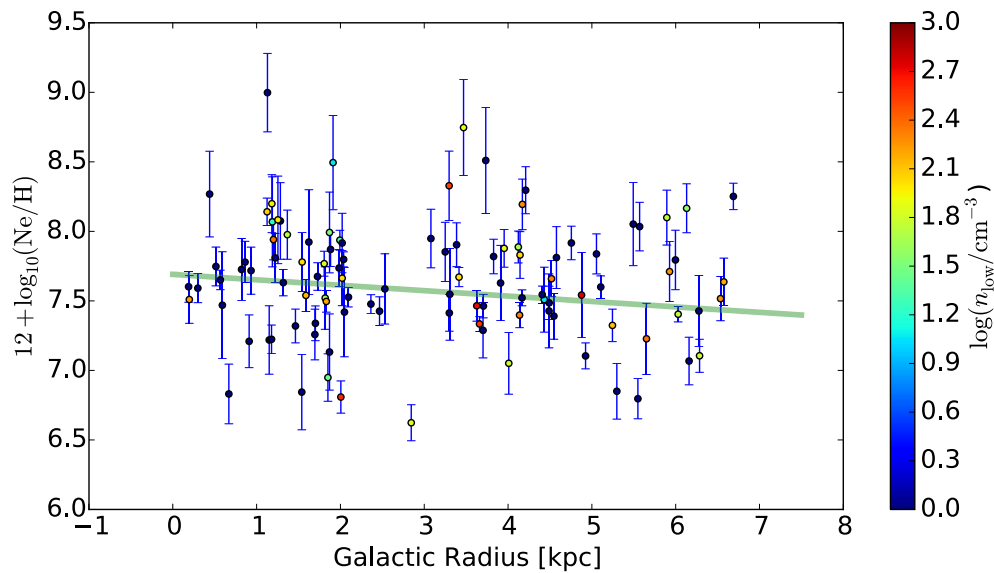
Figure 4.32 The NEAT neon abundances are plotted according to their galactocentric radii to show the overall radial gradient. The slope and intercept of the line of best fit (shown in green) are -0.039 ± 0.024 dex kpc^{-1} and 7.69 ± 0.09, respectively.
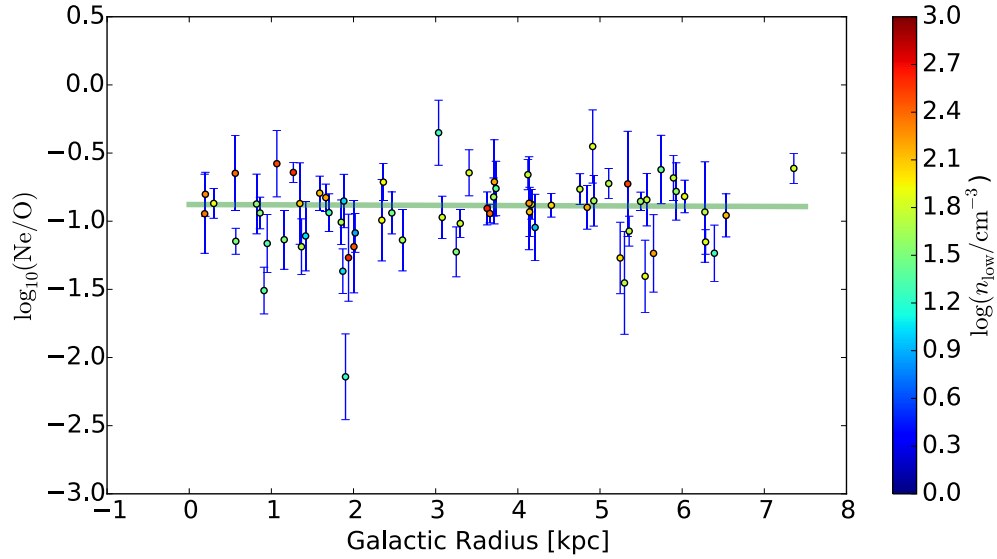
Figure 4.33 The PyNeb neon to oxygen abundance ratios are plotted according to their galactocentric radii to show the overall radial gradient. The slope and intercept of the line of best fit (shown in green) are -0.002 ± 0.024 dex kpc^{-1} and -0.88 ± 0.11, respectively.
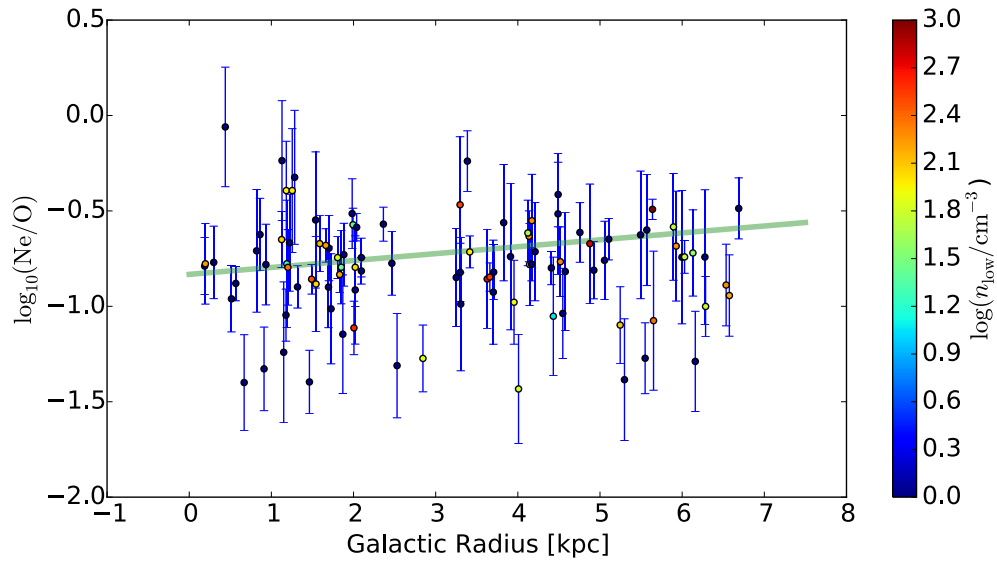
Figure 4.34 The NEAT neon to oxygen abundance ratios are plotted according to their galactocentric radii to show the overall radial gradient. The slope and intercept of the line of best fit (shown in green) are 0.036 ± 0.027 dex kpc^{-1} and -0.83 ± 0.07, respectively.
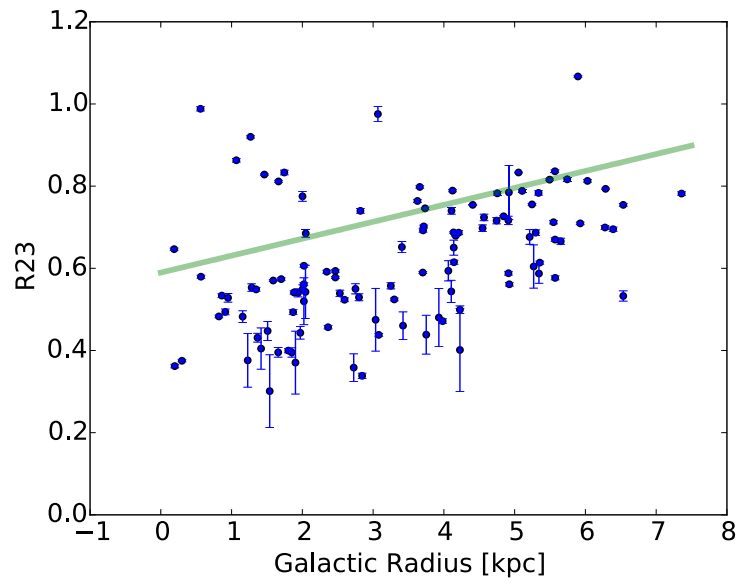
Figure 4.35 The strong-line indicator R_{23} as a function of galactic radius. The linear fit shown in green has a slope of 0.041 ± 0.018 dex kpc^{-1} and intercept 0.59 ± 0.08.

4.5 PyNeb and NEAT metallicity comparison

NEAT-derived metallicities are plotted as a function of PyNeb-derived metallicities in Figure 4.36. This plot indicates there is a fair bit of scatter about the 1:1 line, and that the NEAT-derived metallicities tend to lie at lower values than the PyNeb-derived metallicities. The correlation between PyNeb and NEAT metallicities improves when only those data points with [O III] $\lambda 4363$ Å SNR greater that 6 are plotted (see Figure 4.37), although the tendency for NEAT-derived metallicities to lie at lower values than PyNeb-derived metallicities is still present.

Since PyNeb involves much more input from the user, I understand the results much better than the metallicities given by NEAT. Additionally, NEAT was developed using H II regions in the Milky Way, and may therefore not be optimized to deal with the low-sensitivity, low-resolution data I have for the much more distant H II regions in M33. Further investigations into the capabilities of NEAT will be required in future work. Thus, I consider the PyNeb-derived metallicities to be more robust values, and I use these in the subsequent sections.
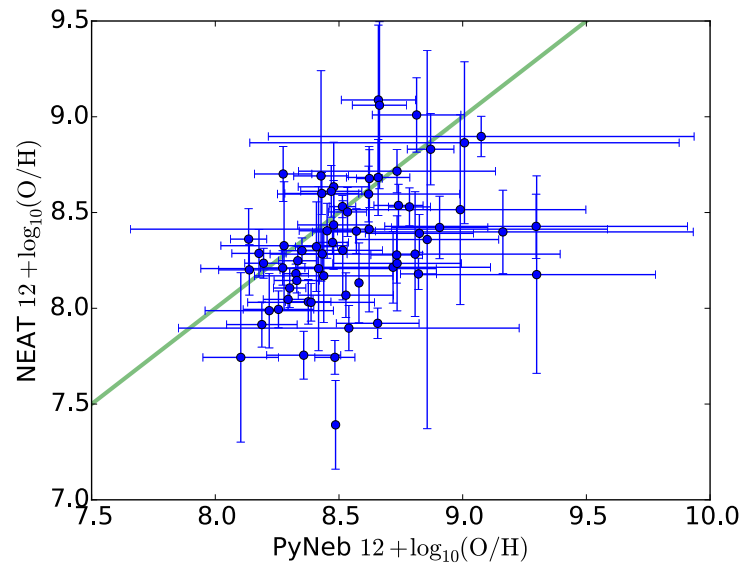
Figure 4.36 Metallicities derived from the two methods, PyNeb and NEAT, are plotted on each axis. The 1:1 line is shown in blue for comparison.
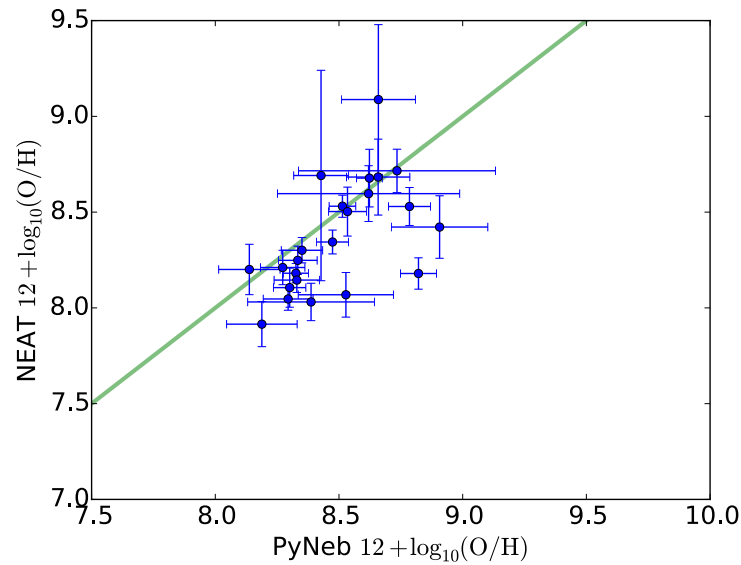
Figure 4.37 The same as Figure 4.36, but only including data points that have an observed SNR > 6 for [O III] $\lambda 4363$ Å.

4.6   High-resolution 2D metallicity map

With the PyNeb metallicities calculated in §3 and their (RA,Dec) positions within the galaxy in hand, it is a straightforward matter to create a 2D metallicity map of M33. The metallicity maps of the O/H, N/H, and N II/O II data are shown in Figures 4.38–4.40. Each map was created by plotting the best fit gradient (as given in Table 4.1) with the smoothed residuals of each H II region's metallicity as compared to the value of the best fit gradient at the corresponding galactic radius.

By comparing the O/H 2D metallicity map (Figure 4.38) to the gradient plotted in Figure 4.19, it appears that although the overall gradient is negative, there is a distinct lack of high metallicity data points near the galactic centre, which causes the colours in the map to give the impression that the centre of the galaxy has a lower oxygen abundance than the outskirts. This is likely an effect of the observational censoring that naturally occurs at high metallicities. That is to say, I am likely not observing the most oxygen abundant H II regions in the centre of the galaxy because these H II regions will have the weakest spectral lines and therefore be most difficult to detect. There is good evidence for azimuthal structure in the metallicity in addition to the radial gradient, although how much of this structure is simply due to the relatively large uncertainties associated with the oxygen abundances is unclear at this time. Future work to reduce these uncertainties should reveal the true azimuthal structure.

A similar censoring effect may be occurring in the N/H 2D abundance map (Figure 4.39), which would help explain why the peak in nitrogen abundance does not coincide with the galactic centre. Overall, the N/H map is much smoother than the O/H map, which agrees with the relative amounts of scatter seen in each gradient in Figures 4.19 and 4.23. The N II/O II abundance map (Figure 4.40) mirrors the asymmetric behaviour of the N/H map, with further azimuthal structure contributed by the O/H component.
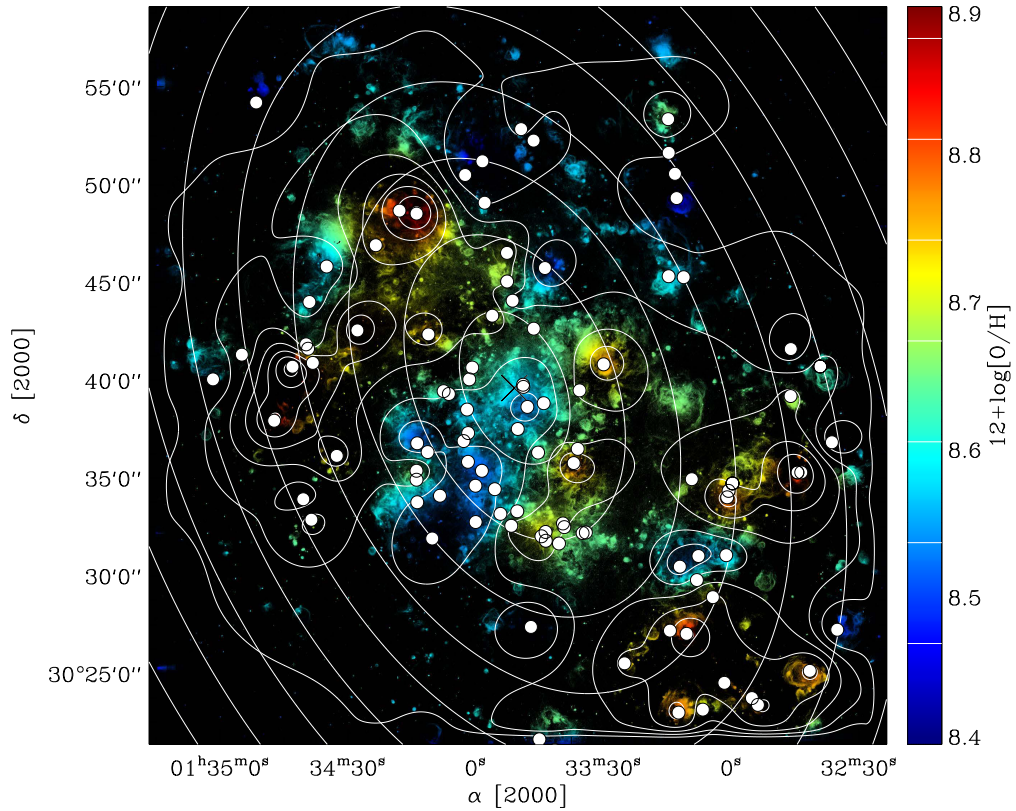
Figure 4.38 Oxygen abundances derived with PyNeb are given by both the colour scale and solid contours. These are superimposed on a continuum-subtracted Hα image of M33 produced from the survey data of Massey et al. (2006). Locations of the H II regions are marked by solid white circles. The centre of the galaxy is marked by an $\times$. Dotted contours show ellipses of constant galacto-centric radius with a spacing of 1 kpc.
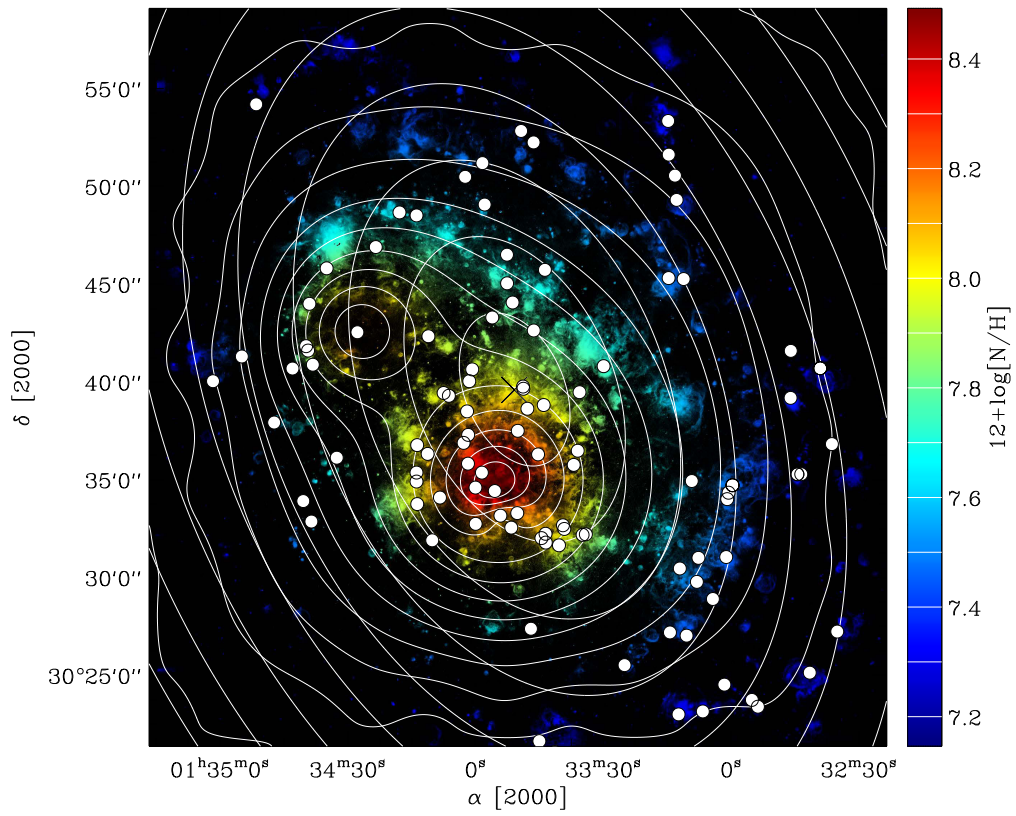
Figure 4.39 Same as Figure 4.38, except it is the PyNeb-derived nitrogen abundances that are given by both the colour scale and solid contours.
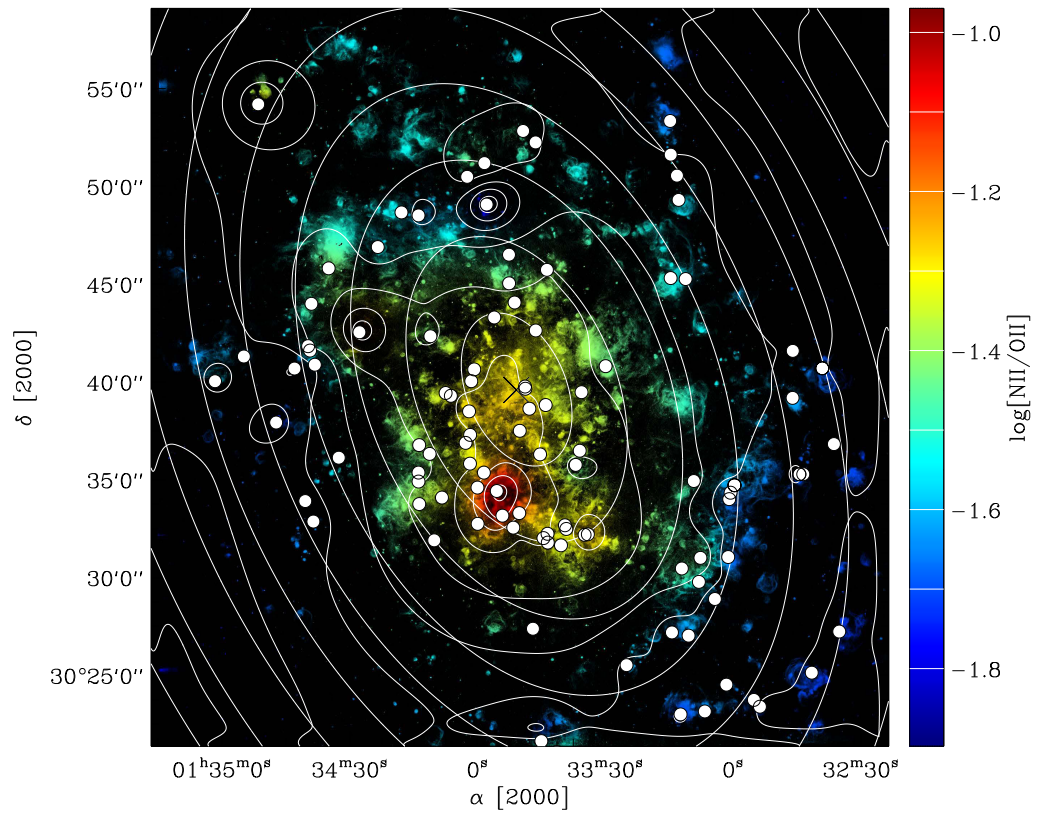
Figure 4.40 Same as Figure 4.38, except it is the PyNeb-derived N II/O II abundances that are given by both the colour scale and solid contours.

4.7 Metallicity mixing scale

Now that I have acquired the high-resolution 2D maps of metallicities across the face of M33, I can investigate characteristics of the galaxy that were simply not possible with only a radial gradient. For instance, the scale at which metallicities are or are not correlated with one another may be directly linked to how metals are mixed within a spiral galaxy. Figure 4.41 compares the difference in PyNeb O/H abundances between each pair of H II regions to their physical separation. Figure 4.42 shows the same thing for PyNeb N/H abundances. Also shown in each plot is the binned median metallicity difference, weighted inversely with the error on the metallicity difference (summed in quadrature). Both these plots suggest that except at the most extreme separations, the metallicity difference remains constant ($\sim$0.20–0.25) regardless of the separation between the two H II regions under consideration.

Additionally, in Figure 4.43 I present the same figure as Figure 4.41 for the subset of data points whose [O III] λ4363 Å observed SNR is greater than 6. There is more scatter in the binned median values compared to Figure 4.41, likely due to there being fewer data points being binned, but the overall value seems to be about the same as when the entire data set was considered (O/H difference $\sim$0.20–0.25). Thus, it seems that there is no observable trend between spatial separation and metallicity difference in the current data set.

As given in §4.4, the line of best fit residuals for the O/H radial gradient were larger than the average uncertainty on the metallicity measurements. This indicates that the scatter in data points cannot be accounted for solely by the measurement uncertainties, and the lack of a trend toward similar metallicities at small separations could be the result of many fluctuations at separations smaller than our resolution, or an indication of systematic problems. Berg et al. (2015) examine the [O III] λ4363 Å temperatures of 18 H II regions in NGC 628 and find large discrepancies in their measurements of T[O II] and T[O III] versus T[N II]. Berg et al. suggest that these temperature discrepancies may account for the large dispersions seen in their [O/H] gradient, as compared to their [N/H] gradient. I also observe a larger dispersion in the [O/H] gradient than in the [N/H] gradient in this data set.
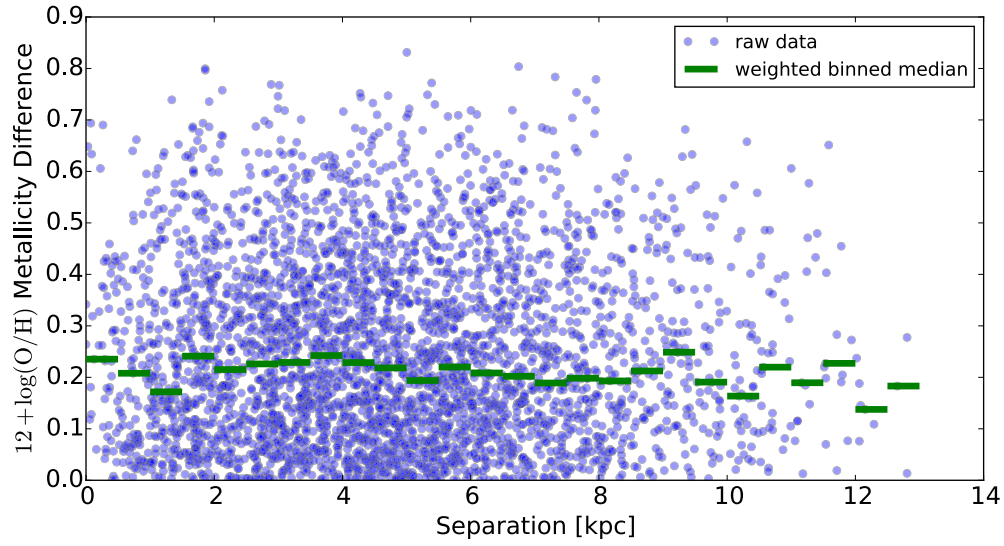
Figure 4.41 The difference in PyNeb-derived O/H abundances of any two H II regions is plotted against those two H II regions' separation within the galactic plane of M33.
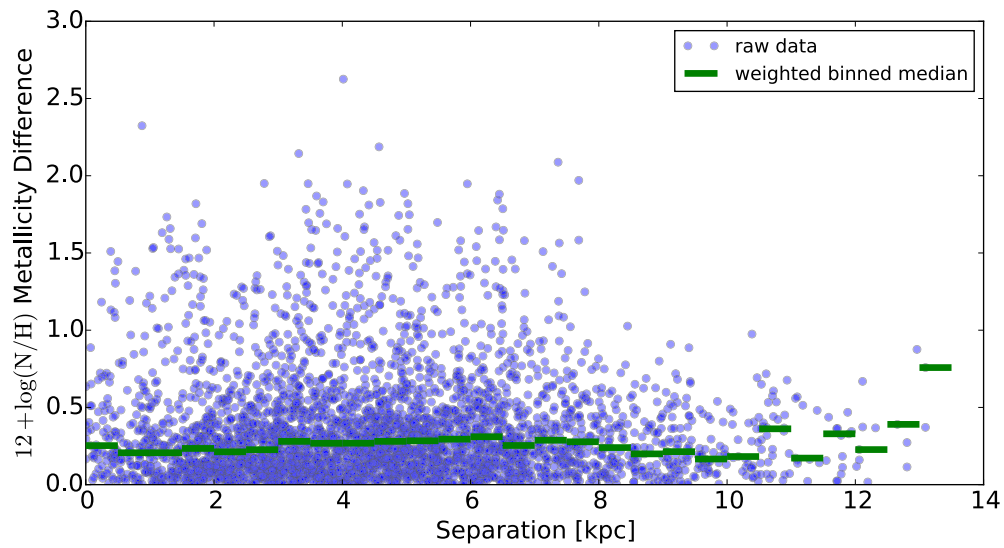
Figure 4.42 The difference in PyNeb-derived N/H abundances of any two H II regions is plotted against those two H II regions' separation within the galactic plane of M33.
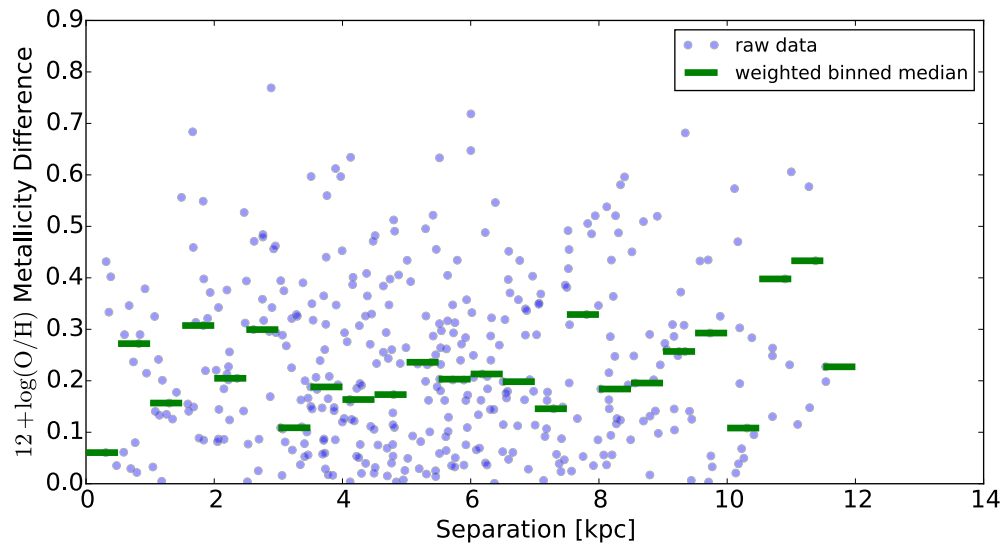
Figure 4.43 The same as Figure 4.41, but only including data points that have an observed SNR > 6 for [O III] λ4363 Å.

CHAPTER 5

Summary and Conclusions

The M33 Metallicity Project has successfully used the Keck I 10-m telescope to obtain spectroscopic observations of 701 Hα sources in the nearby face-on spiral galaxy M33. These Hα sources range in galactic radius from 0 to 7 kpc, and have a mean sampling rate of $\gtrsim 2$ measurements per square kpc. From these spectra, I have extracted oxygen metallicities using the PyNeb python package for 88 H II regions, and using NEAT for 108 H II regions. Both PyNeb and NEAT employ the direct method to calculate metallicity, which relies on the presence of the hard-to-detect auroral line [O III] λ4363 Å. This data set is far more extensive than any other data set in the literature (see Table 1.5), and as I demonstrated in §§ 1.3–1.5, the choice to use H II regions and the direct method greatly enhances the robustness of the results.

In Figure 4.19 I presented the radial oxygen abundance gradient from PyNeb, for which the line of best fit has a slope of -0.010 ± 0.019 dex kpc^{-1}. This contrasts with the radial gradient from the NEAT results which is -0.049 ± 0.013 dex kpc^{-1}. However, both sets of results agree the central oxygen abundance is $\sim$8.47. Compared to the metallicity gradients derived in previous studies (Table 1.5), the PyNeb radial gradient is consistent with the works of Crockett et al. (2006); Rosolowsky and Simon (2008); Magrini et al. (2009), and when only data points with SNR([O III] λ4363 Å) > 6 are taken into account, the resultant gradient is also consistent with Bresolin (2011). The NEAT gradient is consistent with Rosolowsky and Simon (2008); Magrini et al. (2009); U et al. (2009); Bresolin (2011).

The N/H gradient has a steeper slope (-0.093 dex kpc^{-1}) and lower central metallicity ($12 + \log(\text{N/H}) \simeq 7.41$) than the O/H gradient. This, combined with the negative slope of the N II/O II gradient plot, agrees with earlier results that show nitrogen abundances decrease more rapidly than oxygen abundances at higher galactic radii. The opposite is true for neon, for which both PyNeb and NEAT results suggest oxygen abundances decrease

more rapidly than neon abundances at higher galactic radii. The Ne/H gradients presented here (-0.023 ± 0.030 dex kpc^{-1} and -0.039 ± 0.024 dex kpc^{-1}) are both consistent with the neon gradient of -0.016 ± 0.017 dex kpc^{-1} found by Crockett et al. (2006). The central neon abundance ($12 + \log(\text{Ne/H}) \simeq 7.66$) is slightly higher than that of nitrogen. There is little evidence for a significant sulfur radial gradient, or if one does exist, then it is not very well constrained by the current data set.

The 2D high-resolution metallicity maps for [O/H], [N/H], and [N II/O II] are shown in Figures 4.38–4.40. This is the first time this type of metallicity map has ever been presented. The [O/H] map shows clear signs that there is significant azimuthal structure in the metallicities across the face of the disk, however it is currently unclear how much of this structure can be attributed to the relatively large oxygen abundance uncertainties, as opposed to true azimuthal chemical fluctuations in M33. The large uncertainties may be a result of the difficulties associated with a reliable T[O III] temperature, also experienced by Berg et al. (2015). Regardless of whether the fluctuations are real or an observational discrepancy, the large scatter in my data set of $\sim$100 H II regions helps explain why previous studies of the metallicity gradient (with less than ~ 50 H II regions) have failed to yield a consistent, well-constrained value for the slope and intercept.

The [N/H] and [N II/O II] abundance maps suggest a much smoother radial gradient with fewer azimuthal variations, although the peak in nitrogen abundance does not coincide with the centre of the galaxy. It is possible this is an observational censoring effect that prevents the robust identification of high-metallicity H II regions.

Future work with this data set will focus on further refining the XIDL spectral extraction and total flux calculation codes (especially the sky subtraction routine, Balmer absorption correction, and interstellar extinction correction), with the aim of obtaining even more useable data points. Although I have already far surpassed the number of data points used in any previous H II region metallicity study of M33, I believe the full data set should be able to yield closer to 200 metallicity measurements. Also, I expect improvements in the spectral extraction will yield oxygen metallicities with lower uncertainties, thereby allowing a better analysis of the strong-line indicator calibration curves and the metallicity map azimuthal structure. Once these have been obtained, it will be possible to compare the high-resolution metallicity map to other maps that can be found in the literature, such as the molecular gas and 21 cm maps.

Bibliography

Aller, L. H. "The Spectra of the Emission Nebulosities in Messier 33." *The Astrophysical Journal* 95 (1942): 52.

Andrews, B. H. and P. Martini. "The Mass-Metallicity Relation with the Direct Method on Stacked Spectra of SDSS Galaxies." *The Astrophysical Journal* 765 (2013).

Arnett, D. *Supernovae and nucleosynthesis : an investigation of the history of matter, from the big bang to the present.* Princeton University Press, 1996.

Arnould, M. and M. Samyn. "La physique nucléaire en astrophysique." *Astrophysique nucléaire : du microcosme au macrocosme astrophysique* (2000).

Baron, E. and J. Cooperstein. "The effect of iron core structure on supernovae." *The Astrophysical Journal* 353 (1990): 597–611.

Beasley, M. A., I. S. Roman, C. Gallart, A. Sarajedini, and A. Aparicio. "Evidence for temporal evolution in the M33 disc as traced by its star clusters." *Monthly Notices of the Royal Astronomical Society* 451 (2015): 3400–3418.

Berg, D. A., K. V. Croxall, E. D. Skillman, R. W. Pogge, J. Moustakas, and M. Groh-Johnson. "CHAOS I: Direct Chemical Abundances for HII Regions in NGC 628." *The Astrophysical Journal* 806 (2015): 16.

Binney, J. and M. Merrifield. *Galactic Astronomy.* Princeton University Press, 1998.

Boothroyd, A. I. and I.-J. Sackmann. "The CNO Isotopes: Deep Circulation in Red Giants and First and Second Dredge-up." *The Astrophysical Journal* 510 (1999): 232–250.

Bresolin, F. "The Abundance Scatter in M33 from H II Regions: Is There Any Evidence for Azimuthal Metallicity Variations?." *The Astrophysical Journal* 730 (2011).

Campbell, A., R. Terlevich, and J. Melnick. "The stellar populations and evolution of H II galaxies. I - High signal-to-noise optical spectroscopy." *Monthly Notices of the Royal Astronomical Society* 223 (1986): 811–825.

Cardelli, J. A., G. C. Clayton, and J. S. Mathis. "The relationship between infrared, optical, and ultraviolet extinction." *The Astrophysical Journal* 345 (1989): 245–256.

Cayless, A., H. Fraser, A. W. Jones, M. H Jones, R. J. A. Lambourne, S. G. Ryan, and S. Serjeant. *An Introduction to Galaxies and Cosmology.* Ed. M. H. Jones, R. J. A. Lambourne, and S. Serjeant. second edition. Cambridge University Press, 2015.

Chandrasekhar, S. "The Maximum Mass of Ideal White Dwarfs." *The Astrophysical Journal* 74 (1931): 81–82.

Corbelli, E. "Dark matter and visible baryons in M33." *Monthly Notices of the Royal Astronomical Society* 342 (2003): 199–207.

Crockett, N. R., D. R. Garnett, P. Massey, and G. Jacoby. "Neon and Oxygen Abundances in M33." *The Astrophysical Journal* 637 (2006): 741–751.

de Vaucouleurs, G., A. de Vacouleurs, H. G. Corwin, R. J. Buta, P. Fouque, and G. Paturel. *Third Reference Catalogue of Bright Galaxies.* Springer-Verlag, 1991.

Detre, L. *Non-Periodic Phenomena in Variable Stars.* Springer, 2013.

Dobbs, C.L., A. Burkert, and J. E. Pringle. "The properties of the interstellar medium in disc galaxies with stellar feedback." *Monthly Notices of the Royal Astronomical Society* 417 (2011): 1318–1334.

Draine, B. T. *Physics of the Interstellar and Intergalactic Medium.* Princeton University Press, 2011.

Ekström, S., C. Georgy, P. Eggenberger, G. Meynet, N. Mowlavi, A. Wyttenbach, A. Granada, T. Decressin, R. Hirschi, U. Frischknecht, C. Charbonnel, and A. Maeder. "Grids of stellar models with rotation. I. Models from 0.8 to 120 $M_\odot$ at solar metallicity (Z = 0.014)." *Astrononmy & Astrophysics* 537 (2012): 18.

Esteban, C., R. J. García López, A. Herrero, and F. Sánchez. *Cosmochemistry: The Melting Pot of the Elements.* Cambridge University Press, 2001.

Firmani, C. and A. V. Tutukov. "Bursting and stationary star formation in disks and nuclei of galaxies." *Astrononmy & Astrophysics* 288 (1994): 713–730.

Fitzpatrick, E. L. "Correcting for the Effects of Interstellar Extinction." *Publications of the Astronomical Society of the Pacific* 111 (1999): 63–75.

Franco, J. and D. P. Cox. "Self-regulated star formation in the galaxy." *The Astrophysical Journal* 273 (1983): 243–248.

Freedman, W. L., B. F. Madore, B. K. Gibson, L. Ferrarese, D. D. Kelson, S. Sakai, J. R. Mould, Jr. R. C. Kennicutt, H. C. Ford, J. A. Graham, J. P. Huchra, S. M. G. Hughes, G. D. Illingworth, L. M. Macri, and P. B. Stetson. "Final Results from the Hubble Space Telescope Key Project to Measure the Hubble Constant." *The Astrophysical Journal* 553 (2001): 47–72.

Gonzàlez Delgado, R. M., C. Leitherer, and T. M. Heckman. "Synthetic Spectra of H Balmer and HE I Absorption Lines. II. Evolutionary Synthesis Models for Starburst and Poststarburst Galaxies." *The Astrophysical Journal Supplement Series* 125 (1999): 489–509.

Gordon, K. D., G. C. Clayton, K. A. Misselt, A. U. Landolt, and M. J. Wolff. "A Quantitative Comparison of the Small Magellanic Cloud, Large Magellanic Cloud, and Milky Way Ultraviolet to Near-Infrared Extinction Curves." *The Astrophysical Journal* 594 (2003): 279–293.

Grevesse, N. "The solar abundance of Oxygen." *Communications in Asteroseismology* 158 (2009): 151–153.

Hansen, C. J., S. D. Kawaler, and V. Trimble. *Stellar Interiors.* second edition. Springer, 2004.

Hartwick, F. D. A. "The Chemical Evolution of the Galactic Halo." *The Astrophysical Journal* 209 (1976): 418–423.

Henry, R. B. C., M. G., and J. Köppen. "On the Cosmic Origins of Carbon and Nitrogen." *The Astrophysical Journal* 541 (2000): 660–674.

Hopkins, P. F., E. Quataert, and N. Murray. "Stellar feedback in galaxies and the origin of galaxy-scale winds." *Monthly Notices of the Royal Astronomical Society* 421 (2012): 3522–3537.

Hummer, D. G. and P. J. Storey. "Recombination-line intensities for hydrogenic ions. I - Case B calculations for H I and He II." *Monthly Notices of the Royal Astronomical Society* 224 (1987): 801–820.

Iben, I.,Jr. and J. W. Truran. "On the surface composition of thermally pulsing stars of high luminosity and on the contribution of such stars to the element enrichment of the interstellar medium." *The Astrophysical Journal* 220 (1978): 980–995.

Izotov, Y. I., G. Stasińska, G. Meynet, N. G. Guseva, and T. X. Thuan. "The chemical composition of metal-poor emission-line galaxies in the Data Release 3 of the Sloan Digital Sky Survey." *Astrononmy & Astrophysics* 448 (2006): 955–970.

Jarrett, T. H., T. Chester, R. Cutri, S. E. Schneider, and J. P. Huchra. "The 2MASS Large Galaxy Atlas." *The Astrophysical Journal* 125 (2003): 525–554.

Kaler, J. B. and J. H. Lutz. "Dust-distances to planetary nebulae." *Publications of the Astronomical Society of the Pacific* 97 (1985): 700–706.

Keck Observatory, W. M. *LRIS Detectors*. July 2015.

Kingsburgh, R. L. and M. J. Barlow. "Elemental abundances for a sample of southern galactic planetary nebulae." *Monthly Notices of the Royal Astronomical Society* 271 (1994): 257 – 299.

Kudritzki, R.-P., I.-T. Ho, A. Schruba, A. Burkert, H. J. Zahid, F. Bresolin, and G. I. Dima. "The chemical evolution of local star forming galaxies: Radial profiles of ISM metallicity, gas mass, and stellar mass and constraints on galactic accretion and winds." *Monthly Notices of the Royal Astronomical Society* 450 (2015): 342–359.

LeBlanc, F. *An Introduction to Stellar Astrophysics*. John Wiley & Sons, 2010.

Luridiana, V., C. Morisset, and R. A. Shaw. "PyNeb: a new tool for analyzing emission lines. I. Code description and validation of results." *Astrononmy & Astrophysics* 573 (2015): 14.

Magrini, L., L. Stanghellini, and E. Villaver. "The Planetary Nebula Population of M33 and its Metallicity Gradient: A Look Into the Galaxy's Distant Past." *The Astrophysical Journal* 696 (2009): 729–740.

Martins, F., D. Schaerer, and D. J. Hillier. "A new calibration of stellar parameters of Galactic O stars." *Astrononmy & Astrophysics* 436 (2005): 1049–1065.

Massey, P., K. A. G. Olsen, P. W. Hodge, S. B. Strong, G. H. Jacoby, W. Schlingman, and R. C. Smith. "A Survey of Local Group Galaxies Currently Forming Stars. I. UBVRI Photometry of Stars in M31 and M33." *The Astrophysical Journal* 131 (2006): 2478–2496.

Matteucci, F. and L. Greggio. "Relative rôles of type I and II supernovae in the chemical enrichment of the interstellar gas." *Astrononmy & Astrophysics* 154 (1986): 279–287.

Mazzali, P. A., F. K. Röpke, S. Benetti, and W. Hillebrandt. "A Common Explosion Mechanism for Type Ia Supernovae." *Science* 315 (2007): 825–828.

McKee, C. E. "Photoionization-regulated star formation and the structure of molecular clouds." *The Astrophysical Journal* 345 (1989): 782–801.

Meyer, B. S., L. R. Nittler, A. N. Nguyen, and S. Messenger. "Nucleosynthesis and Chemical Evolution of Oxygen." (2006).

NIST. *Atomic Spectroscopy.* 2007.

Oke, J. B., J. G. Cohen, M. Carr, J. Cromer, A. Dingizian, F. H. Harris, S. Labrecque, R. Lucinio, and W. Schaal. "The Keck Low-Resolution Imaging Spectrometer." *Publications of the Astronomical Society of the Pacific* 107 (April 1995): 375–385.

Olive, K. A. and E. .D. Skillman. "Uncertainties in ^{4}He abundance determinations in extragalactic H II regions." *New Astronomy* 6 (2001): 119–150.

Osterbrock, D. E. "The physics of gaseous nebulae." *Publications of the Astronomical Society of the Pacific* 100 (1988): 412–426.

Osterbrock, D. E. *Astrophysics of Gaseous Nebulae and Active Galactic Nuclei.* University Science Books, 1989.

Pagel, B. E. J., M. G. Edmunds, D. E. Blackwell, M. S. Chun, and G. Smith. "On the composition of H II regions in southern galaxies. I - NGC 300 and 1365." *Monthly Notices of the Royal Astronomical Society* 189 (1979): 95–113.

Pagel, B. E. J. and A. Kazlauskas. "Primordial helium: the third decimal place." *Monthly Notices of the Royal Astronomical Society* 256 (1992): 49P–51P.

Pagel, B. E. J., E. A. Simonson, R. J. Terlevich, and M. G. Edmunds. "The primordial helium abundance from observations of extragalactic H II regions." *Monthly Notices of the Royal Astronomical Society* 255 (1992): 325–345.

Peimbert, M. "Temperature Determinations of H II Regions." *The Astrophysical Journal* 150 (1967): 825–834.

Peimbert, M. "Chemical composition of extragalactic gaseous nebulae." *Annual review of astronomy and astrophysics* 13 (1975): 113–131.

Pettini, M. and B. E. J. Pagel. "[OIII]/[NII] as an abundance indicator at high redshift." *Monthly Notices of the Royal Astronomical Society* 348 (2004): L59–L63.

Pilyugin, L. S. "On the oxygen abundance determination in HII regions: the problem of the line intensities – oxygen abundance calibration." *Astrononmy & Astrophysics* 362 (2000): 325–332.

R. J. Talbot, Jr. and W. D. Arnett. "The Evolution of Galaxies. I. Formulation and Mathematical Behavior of the One-Zone Model." *The Astrophysical Journal* 170 (1971): 409–422.

Rola, C. and D. Pelat. "On the estimation of intensity for low S/N ratio narrow emission lines." *Astrononmy & Astrophysics* 287 (1994): 676–684.

Rosolowsky, E. and J. D. Simon. "The M33 Metallicity Project: Resolving the Abundance Gradient Discrepancies in M33." *The Astrophysical Journal* 675 (March 2008): 1213–1222.

Salaris, M. and S. Cassisi. *Evolution of Stars and Stellar Populations.* John Wiley & Sons, 2005.

Scannapieco, C., P. B. Tissera, S. D. M. White, and V. Springel. "Feedback and metal enrichment in cosmological SPH simulations - II. A multiphase model with supernova energy feedback." *Monthly Notices of the Royal Astronomical Society* 371 (2006): 1125–1139.

Schultz, G. V. and W. Wiemer. "Interstellar reddening and IR-excess of O and B stars." *Astrononmy & Astrophysics* 43 (1975): 133–139.

Searle, L. "Evidence for Composition Gradients across the Disks of Spiral Galaxies." *The Astrophysical Journal* 168 (1971): 327–342.

Springel, V. and L. Hernquist. "Cosmological smoothed particle hydrodynamics simulations: a hybrid multiphase model for star formation." *Monthly Notices of the Royal Astronomical Society* 339 (2003): 289–311.

Stasińska, G. "[Ar III]/[O III] and [S III]/[O III]: well-behaved oxygen abundance indicators for HII regions and star forming galaxies." *Astrononmy & Astrophysics* 454 (2006): L127–L130.

Strömgren, B. "The Physical State of Interstellar Hydrogen." *The Astrophysical Journal* 89 (1939): 526–547.

U, V., M. A. Urbaneja, R.-P. Kudritzki, B. A. Jacobs, F. Bresolin, and N. Przybilla. "A New Distance to M33 Using Blue Supergiants and the FGLR Method." *The Astrophysical Journal* 704 (2009): 1120–1134.

Vila-Costas, M. B. and M. G. Edmunds. "The relation between abundance gradients and the physical properties of spiral galaxies." *Monthly Notices of the Royal Astronomical Society* 259 (1992): 121–145.

Wasserburg, G. J., A. I. Boothroyd, and I.-J. Sackmann. "Deep Circulation in Red Giant Stars: A Solution to the Carbon and Oxygen Isotope Puzzles?." *The Astrophysical Journal* 447 (1995): 37–40.

Weedman, D. W. "Electron Densities in Planetary Nebulae from [S II]." *Publications of the Astronomical Society of the Pacific* 80 (1968): 314–317.

Werk, J. K., M. E. Putman, G. R. Meurer, and N. Santiago-Figueroa. "Metal Transport to the Gaseous Outskirts of Galaxies." *The Astrophysical Journal* 735 (2011).

Wesson, R., D. J. Stock, and P. Scicluna. "Understanding and reducing statistical uncertainties in nebular abundance determinations." *Monthly Notices of the Royal Astronomical Society* 422 (2012): 516–3526.

Appendices

Tables

Chart A.1: Correction factors and total line fluxes for all observed Hα sources

Object name	EW	c(Hβ)	$f_{Red900/5500}$	$f_{Red400/8500}$	[O II] λ3727 Å [F_λ]	[Ne III] λ3869 Å [F_λ]	[O III] λ4363 Å [F_λ]	[O III] λ4959 Å [F_λ]	[O III] λ5007 Å [F_λ]	[N II] λ5755 Å [F_λ]
H1	2.61	0.32	0.29	—	2827.85 ± 7.89	2.89 ± 3.01	0.0 ± 1.93	30.1 ± 1.54	80.88 ± 1.5	9.45 ± 1.35
H1	7.0	0.13	0.11	—	2175.94 ± 8.29	0.0 ± 3.95	0.0 ± 2.63	19.66 ± 2.32	56.4 ± 2.43	6.89 ± 1.63
H1	0.74	0.68	0.01	—	9104.52 ± 23.42	5.71 ± 9.88	3.25 ± 6.17	90.4 ± 4.54	234.69 ± 4.54	0.0 ± 2.85
H100	−2.0	0.0	7.08	0.94	0.0 ± 0.0	0.0 ± 3.2	0.32 ± 2.68	4.43 ± 2.39	6.3 ± 2.45	0.0 ± 0.0
H1000	0.42	0.76	0.27	0.4	3841.87 ± 12.97	24.8 ± 6.11	11.93 ± 3.18	135.43 ± 2.91	227.43 ± 2.91	16.07 ± 4.49
H1001	−1.09	0.36	1.07	0.56	1037.3 ± 3.96	13.31 ± 1.66	1.62 ± 1.0	92.31 ± 0.96	256.93 ± 1.13	4.05 ± 1.15
H1003	−2.0	0.66	1.63	0.26	52897.21 ± 98.76	7244.55 ± 27.4	899.05 ± 12.7	25891.16 ± 4162.41	49800.83 ± 2817.13	45.0 ± 3.59
H1004	9.1	0.16	0.79	0.54	735.06 ± 2.22	195.09 ± 1.0	18.73 ± 0.56	740.58 ± 1.36	2204.07 ± 1.67	0.87 ± 0.92
H1005	3.14	0.17	0.86	0.54	1226.14 ± 3.42	48.72 ± 1.42	5.91 ± 0.91	292.78 ± 1.14	896.71 ± 1.34	4.36 ± 1.1
H1009	10.0	0.11	5.19	0.67	138.41 ± 1.18	0.0 ± 0.58	0.67 ± 0.38	1.47 ± 0.37	3.89 ± 0.39	0.31 ± 2.93
H101	1.77	0.02	1.19	1.25	340.71 ± 1.88	1.4 ± 1.43	2.93 ± 0.93	2.41 ± 0.85	13.09 ± 0.87	1.11 ± 1.47
H1010	10.0	0.05	0.92	1.22	112.78 ± 0.96	3.42 ± 0.38	0.57 ± 0.28	26.33 ± 0.32	74.88 ± 0.4	0.0 ± 0.43
H1019	1.9	0.13	1.19	0.87	809.06 ± 5.38	17.06 ± 3.77	7.05 ± 2.42	32.71 ± 2.12	85.77 ± 2.04	2.68 ± 4.33
H102	3.19	0.16	0.58	0.96	980.53 ± 3.5	2.25 ± 1.39	0.0 ± 1.14	42.34 ± 1.13	125.04 ± 1.12	2.38 ± 0.77
H102	2.74	0.08	1.56	1.33	6823.57 ± 16.56	19.42 ± 6.69	4.28 ± 4.66	463.87 ± 5.6	1353.89 ± 4.97	12.13 ± 6.46
H1020	8.0	0.16	0.79	1.29	388.0 ± 3.54	24.71 ± 1.88	11.03 ± 1.47	44.17 ± 1.28	123.3 ± 1.37	1.11 ± 1.51
H1021	1.08	0.2	0.18	1.05	1650.43 ± 8.72	55.16 ± 4.66	0.45 ± 3.62	382.14 ± 3.3	1131.03 ± 3.65	0.0 ± 2.57
H1022	0.69	0.2	1.39	1.05	289.61 ± 6.1	0.57 ± 3.74	0.0 ± 2.78	4.76 ± 2.48	2.43 ± 2.44	0.0 ± 2.51
H1024	2.7	0.0	1.39	0.98	4950.8 ± 10.35	205.5 ± 7.19	20.78 ± 2.99	1319.57 ± 232.36	3549.57 ± 173.54	5.41 ± 2.49
H1026	7.97	0.06	1.34	0.83	1629.99 ± 4.28	9.38 ± 1.91	0.44 ± 1.32	26.34 ± 1.32	70.46 ± 1.31	3.89 ± 2.54
H1028	8.82	0.0	1.49	1.46	213.38 ± 2.23	0.0 ± 1.27	0.0 ± 0.94	2.12 ± 0.83	2.89 ± 0.85	1.46 ± 1.78
H1029	0.29	1.02	0.58	0.47	2549.35 ± 90.8	0.0 ± 78.63	28.02 ± 32.46	0.0 ± 20.87	201.05 ± 17.27	0.0 ± 12.57
H1029	0.46	1.28	0.75	0.5	589.58 ± 139.77	0.0 ± 129.99	106.26 ± 57.94	0.0 ± 21.33	144.59 ± 19.48	46.23 ± 24.98
H103	2.14	0.42	1.32	1.36	4641.11 ± 44.65	0.0 ± 23.37	0.0 ± 14.76	135.76 ± 12.58	315.08 ± 12.66	35.68 ± 19.09
H1030	1.09	0.57	0.89	1.29	1305.85 ± 13.0	0.79 ± 8.36	11.45 ± 4.98	6.37 ± 3.34	15.41 ± 3.28	3.25 ± 4.25
H1030	1.27	0.34	0.53	1.2	625.95 ± 7.0	8.71 ± 4.38	10.64 ± 2.86	3.85 ± 2.45	5.16 ± 2.4	0.0 ± 4.19
H1031	3.63	0.15	0.81	0.85	1522.19 ± 9.56	134.92 ± 4.53	0.0 ± 3.68	763.19 ± 5.23	2301.53 ± 5.46	6.7 ± 3.1
H1032	1.31	0.0	1.76	0.76	2040.36 ± 6.01	106.94 ± 1.78	8.57 ± 1.57	689.74 ± 5.28	1853.43 ± 5.17	3.93 ± 1.48
H1034	1.73	0.12	1.03	0.43	1818.57 ± 8.15	0.0 ± 5.17	10.46 ± 3.27	24.48 ± 2.47	61.21 ± 2.48	7.89 ± 2.84
H1034	0.22	0.85	0.7	0.58	741.47 ± 86.52	0.0 ± 46.77	15.9 ± 36.0	2.38 ± 21.57	24.62 ± 17.86	96.0 ± 13.73
H1036	4.5	0.25	1.1	1.02	3473.66 ± 10.47	14.16 ± 4.85	0.0 ± 3.9	149.88 ± 3.03	441.21 ± 3.03	6.05 ± 2.96
H1038	1.89	0.3	1.42	1.29	500.55 ± 13.7	0.0 ± 8.11	11.51 ± 5.72	14.16 ± 5.11	34.5 ± 4.78	3.02 ± 9.45
H1038	0.78	0.44	1.1	1.02	1060.15 ± 15.61	0.0 ± 9.31	14.51 ± 6.73	6.95 ± 5.24	39.59 ± 4.96	7.06 ± 7.26
H1039	0.71	0.38	0.95	1.0	2879.59 ± 12.25	32.78 ± 6.1	5.69 ± 4.55	158.87 ± 3.64	417.97 ± 3.55	9.78 ± 9.17
H104	10.0	0.2	1.21	6.53	672.36 ± 10.64	0.0 ± 6.46	2.3 ± 4.72	94.04 ± 4.15	243.76 ± 4.28	0.09 ± 5.78
H1040	0.19	0.0	4.73	223.27	0.0 ± 4.98	2.2 ± 2.94	0.0 ± 2.36	0.0 ± 2.06	2.38 ± 2.1	0.0 ± 4.49
H1040	0.52	0.0	0.91	−23.63	183.16 ± 3.88	0.0 ± 2.21	0.0 ± 1.77	5.09 ± 1.79	7.32 ± 1.71	0.0 ± 2.45
H1041	10.0	0.75	0.98	0.01	1661.03 ± 26.24	0.0 ± 16.94	0.0 ± 9.22	89.5 ± 7.12	293.45 ± 6.91	39.3 ± 28.15
H1042	10.0	1.0	0.54	0.19	5627.78 ± 81.41	1298.54 ± 43.64	100.59 ± 27.27	2568.4 ± 21.0	7344.64 ± 22.97	14.25 ± 64.07
H1042	10.0	0.48	1.07	0.31	1692.83 ± 23.0	93.47 ± 14.59	26.25 ± 8.86	218.25 ± 8.01	678.36 ± 7.93	0.0 ± 36.19
H1043	1.23	0.21	1.57	1.21	2636.59 ± 13.04	835.33 ± 9.37	66.06 ± 4.94	2935.86 ± 18.35	8840.11 ± 17.48	1.57 ± 4.7
H1045	10.0	0.0	1.77	1.85	434.24 ± 3.56	3.97 ± 1.36	0.61 ± 0.96	27.0 ± 1.01	69.39 ± 1.09	0.0 ± 2.07
H1046	2.88	0.0	0.86	1.28	1270.28 ± 5.01	0.0 ± 2.33	0.0 ± 1.67	19.67 ± 1.51	61.19 ± 1.63	4.55 ± 14.08
H1047	−1.03	0.97	0.61	0.65	225727.67 ± 714.41	44387.39 ± 258.04	1818.15 ± 1078.55	122146.77 ± 9650.62	529699.81 ± 7047.89	413.52 ± 17.69

Chart A.1 – Continued

Object name	EW	c(Hβ)	$f_{Red900/5500}$	$f_{Red400/8500}$	[O II] λ3727 Å $[F_\lambda]$	[Ne III] λ3869 Å $[F_\lambda]$	[O III] λ4363 Å $[F_\lambda]$	[O III] λ4959 Å $[F_\lambda]$	[O III] λ5007 Å $[F_\lambda]$	[N II] λ5755 Å $[F_\lambda]$
H1052	1.53	0.1	1.29	1.24	479.53 ± 4.52	7.52 ± 2.29	0.0 ± 1.76	37.3 ± 1.62	108.24 ± 1.7	2.31 ± 2.5
H1054	3.78	0.0	1.43	1.37	353.13 ± 3.27	7.25 ± 1.81	1.5 ± 1.46	10.8 ± 1.36	23.06 ± 1.34	1.48 ± 4.01
H1059	10.0	0.0	1.19	1.25	539.03 ± 3.56	3.82 ± 1.81	1.94 ± 1.51	50.19 ± 1.35	154.78 ± 1.56	5.14 ± 4.48
H106	1.46	0.86	1.3	1.07	15568.28 ± 89.92	99.91 ± 79.72	143.27 ± 38.4	407.54 ± 26.36	1289.06 ± 25.23	168.2 ± 676.91
H1060	10.0	0.0	0.71	0.86	51.99 ± 2.44	3.54 ± 1.27	1.31 ± 1.06	4.82 ± 1.02	8.39 ± 1.06	0.0 ± 1.46
H1066	0.63	0.92	0.5	0.17	0.0 ± 0.0	205.49 ± 27.39	5.21 ± 16.59	415.39 ± 11.24	1187.9 ± 12.24	112.92 ± 16.49
H1069	0.18	0.0	1.37	1.72	3124.37 ± 6.71	34.23 ± 2.14	2.93 ± 1.47	315.85 ± 2.24	792.93 ± 2.79	4.13 ± 1.72
H1073	1.26	0.16	0.65	—	197.64 ± 3.29	2.05 ± 1.67	2.47 ± 1.13	26.05 ± 1.15	60.71 ± 1.29	0.0 ± 1.16
H1074	2.35	0.74	0.18	—	786.7 ± 19.86	25.38 ± 10.56	0.0 ± 6.65	101.72 ± 5.15	285.79 ± 5.43	0.0 ± 3.89
H1075	2.23	0.28	0.07	—	236.68 ± 4.7	0.0 ± 2.19	0.0 ± 1.56	5.84 ± 1.35	17.26 ± 1.41	0.0 ± 1.4
H1077	10.0	3.0	0.17	—	63068.73 ± 20296.5	6514.0 ± 9705.54	0.0 ± 2785.43	340.31 ± 801.07	1483.98 ± 755.72	0.0 ± 382.17
H108	0.8	0.0	1.15	1.28	624.16 ± 2.62	0.19 ± 1.64	3.18 ± 1.01	20.61 ± 1.05	60.2 ± 1.03	1.12 ± 1.13
H1085	10.0	0.4	0.39	0.46	662.55 ± 12.77	25.12 ± 7.29	12.34 ± 5.04	89.45 ± 4.39	276.55 ± 4.7	12.97 ± 4.22
H1085	2.75	0.0	0.32	0.53	15.49 ± 3.31	10.72 ± 1.97	7.55 ± 1.51	85.57 ± 2.11	228.81 ± 2.07	0.08 ± 1.86
H1088	10.0	0.37	0.31	0.01	45.5 ± 4.96	1.58 ± 2.81	0.0 ± 1.89	1.03 ± 0.76	2.29 ± 1.71	0.51 ± 7.08
H109	0.38	0.0	0.36	—	128.43 ± 2.39	0.0 ± 1.23	1.06 ± 0.92	16.26 ± 1.22	27.87 ± 1.48	1.19 ± 1.28
H1093	10.0	0.0	0.41	—	50.49 ± 2.68	2.51 ± 1.53	0.0 ± 1.08	7.57 ± 3.2	14.24 ± 3.03	0.0 ± 2.93
H1094	1.29	0.57	0.4	—	577.22 ± 11.89	0.0 ± 5.81	2.09 ± 3.75	61.69 ± 1.14	165.71 ± 1.34	0.0 ± 1.0
H1096	2.18	0.0	0.23	—	210.27 ± 2.51	9.22 ± 1.37	1.82 ± 0.95	38.08 ± 1.99	35.54 ± 3.84	0.0 ± 0.98
H1097	10.0	0.0	5.0	—	60.43 ± 3.14	14.29 ± 1.59	4.13 ± 1.04	0.0 ± 1.48	0.32 ± 1.51	0.33 ± 2.14
H1098	-2.0	0.0	-1.82	—	0.0 ± 3.22	2.47 ± 2.19	0.1 ± 1.57	0.0 ± 1156.56	265.43 ± 1049.5	0.0 ± 578.23
H1098	10.0	3.0	0.27	—	0.0 ± 28381.36	0.0 ± 13260.53	0.0 ± 3954.63	0.0 ± 7.7	0.0 ± 8.09	0.0 ± 9.53
H1099	4.88	3.0	0.05	—	0.0 ± 25.34	8.86 ± 16.11	0.0 ± 9.4	7525.48 ± 847.7	16445.23 ± 1143.62	0.0 ± 350.82
H1099	10.0	3.0	0.73	—	173254.45 ± 21554.66	12883.63 ± 9626.99	66.21 ± 3000.22	0.0 ± 4.33	0.0 ± 4.11	0.0 ± 3.99
H11	2.23	0.04	1.25	0.73	0.0 ± 9.95	5.27 ± 6.92	2.18 ± 4.0	166.73 ± 2.99	520.13 ± 3.29	4.74 ± 4.73
H110	1.19	0.29	1.55	0.69	1754.59 ± 8.0	14.2 ± 4.63	11.52 ± 3.38	0.0 ± 2.82	8.13 ± 2.59	4.84 ± 3.74
H1100-MA	10.0	0.25	0.93	1.83	446.4 ± 7.45	0.0 ± 5.49	10.58 ± 3.53	27.93 ± 1.43	79.89 ± 1.57	0.56 ± 2.05
H1101	10.0	3.0	0.03	—	131.76 ± 3.99	11.62 ± 2.47	3.77 ± 1.61	0.0 ± 1384.23	0.0 ± 1291.09	7461.63 ± 602.59
H1101	-2.0	3.0	2.79	—	1587.77 ± 33817.91	13587.34 ± 18033.64	123.09 ± 4896.62	0.0 ± 10.03	0.0 ± 9.82	0.0 ± 16.59
H1101-MA	10.0	0.91	0.62	2.01	18.68 ± 1.07	2.02 ± 25.45	0.51 ± 0.52	19.12 ± 0.58	52.7 ± 0.69	1.05 ± 0.8
H112	3.53	0.22	1.02	1.03	3987.41 ± 7.21	46.7 ± 2.47	7.76 ± 1.65	408.34 ± 2.56	1194.9 ± 2.53	6.76 ± 1.85
H113	0.27	0.51	1.07	1.55	184.53 ± 4.96	1.36 ± 3.03	0.0 ± 2.21	2.56 ± 2.1	11.26 ± 2.05	7.16 ± 13.64
H113	0.19	0.0	1.27	2.12	65.13 ± 5.52	10.19 ± 3.81	2.07 ± 3.52	9.2 ± 3.47	18.76 ± 3.52	5.73 ± 4.27
H115	3.22	0.52	0.91	—	11737.46 ± 78.47	3005.82 ± 44.97	221.43 ± 29.37	10545.96 ± 32.04	31421.83 ± 43.64	38.57 ± 33.56
H116	-2.0	0.0	0.76	0.56	954.16 ± 7.29	311.2 ± 4.34	25.24 ± 3.61	1027.02 ± 5.36	3068.2 ± 5.42	5.12 ± 4.05
H116	0.62	0.16	1.01	0.74	1311.11 ± 6.45	158.12 ± 4.26	23.04 ± 3.12	353.68 ± 3.23	961.69 ± 3.3	0.13 ± 7.72
H117	1.98	0.72	0.7	1.07	12220.42 ± 24.94	82.21 ± 8.52	22.87 ± 3.77	589.08 ± 4.32	1609.87 ± 5.3	21.54 ± 2.05
H117	0.92	0.0	2.57	2.2	7534.84 ± 13.25	76.42 ± 6.56	18.78 ± 3.35	412.37 ± 3.51	1169.52 ± 4.09	48.63 ± 32.94
H1177	-2.0	1.64	0.13	—	0.0 ± 0.0	0.0 ± 0.0	272.57 ± 136.47	73.0 ± 56.07	47.9 ± 56.12	0.0 ± 0.0
H1179	10.0	0.0	-0.44	0.01	57.3 ± 3.39	9.46 ± 2.09	1.31 ± 1.6	10.85 ± 1.59	28.1 ± 1.58	0.0 ± 1.73
H1179	10.0	2.03	0.53	0.15	18069.62 ± 805.32	154.14 ± 506.29	0.0 ± 194.03	0.0 ± 87.38	0.0 ± 81.23	0.0 ± 107.46
H118	0.93	0.01	1.62	0.01	1207.11 ± 3.18	3.63 ± 2.01	4.07 ± 1.03	60.87 ± 0.95	153.15 ± 1.02	2.11 ± 0.82
H1181	1.12	0.41	0.85	0.87	3274.36 ± 14.8	22.74 ± 8.36	1.02 ± 6.11	292.12 ± 4.97	750.07 ± 5.03	0.0 ± 5.99
H1182	2.01	0.43	0.95	0.6	1002.12 ± 14.39	51.92 ± 8.7	0.0 ± 6.12	77.95 ± 4.73	236.85 ± 4.71	2.01 ± 6.05
H1182	2.84	0.0	0.7	0.95	201.59 ± 3.74	5.98 ± 2.37	0.41 ± 1.71	9.84 ± 1.46	16.46 ± 1.48	2.6 ± 1.55

Chart A.1 – Continued

Object name	EW	c(Hβ)	$f_{Red900/5500}$	$f_{Red400/8500}$	[O II] λ3727 Å [F_λ]	[Ne III] λ3869 Å [F_λ]	[O III] λ4363 Å [F_λ]	[O III] λ4959 Å [F_λ]	[O III] λ5007 Å [F_λ]	[N II] λ5755 Å [F_λ]
H1183	10.0	0.07	1.55	0.22	148.58 ± 2.55	1.78 ± 1.3	0.0 ± 0.99	2.37 ± 0.92	6.0 ± 0.93	0.82 ± 1.39
H119	0.41	1.18	3.61	8.8	15110.37 ± 286.54	0.0 ± 295.26	947.37 ± 301.03	642.16 ± 115.18	3291.15 ± 83.9	1879.92 ± 128.15
H1192	10.0	2.39	0.3	0.13	4112.88 ± 1903.04	691.63 ± 980.08	702.96 ± 342.14	2254.3 ± 159.71	6162.97 ± 193.19	0.0 ± 42.19
H1195	4.4	0.0	0.41	—	85.26 ± 1.86	0.52 ± 0.94	0.3 ± 0.72	5.7 ± 0.75	13.27 ± 0.78	0.0 ± 0.81
H1196	10.0	0.0	0.62	—	9.13 ± 1.53	0.0 ± 0.99	0.0 ± 0.78	0.41 ± 0.7	0.49 ± 0.71	0.0 ± 1.28
H1196	10.0	2.09	0.37	—	0.0 ± 1619.94	0.0 ± 952.63	0.0 ± 340.61	0.0 ± 171.0	0.0 ± 159.67	0.0 ± 186.05
H1197	10.0	0.6	0.78	1.71	384.21 ± 9.34	4.81 ± 5.09	0.0 ± 3.0	46.99 ± 2.57	145.16 ± 3.03	1.96 ± 2.52
H1198	1.11	0.0	0.94	0.88	662.6 ± 3.83	0.0 ± 2.83	3.93 ± 1.55	48.47 ± 1.57	131.35 ± 1.42	8.62 ± 1.94
H1199	10.0	0.0	0.24	0.35	50.24 ± 1.12	0.0 ± 0.63	0.0 ± 0.56	12.42 ± 0.58	22.39 ± 0.64	6.15 ± 0.75
H12	9.89	0.19	1.37	0.64	237.8 ± 3.57	50.25 ± 1.83	4.99 ± 1.32	281.97 ± 2.19	830.3 ± 2.57	1.51 ± 2.15
H120	1.36	0.82	1.09	0.97	5295.25 ± 19.45	147.41 ± 12.56	14.97 ± 5.52	717.64 ± 5.96	2131.95 ± 5.99	13.78 ± 4.03
H1201	0.97	0.48	0.79	0.33	193.94 ± 7.6	3.49 ± 4.7	9.75 ± 3.12	4.06 ± 2.81	5.63 ± 2.66	0.0 ± 3.01
H1202	0.22	0.0	0.86	-0.4	297.74 ± 2.34	0.0 ± 1.17	1.69 ± 0.91	8.11 ± 1.01	26.41 ± 1.0	0.54 ± 1.32
H1203	2.65	0.0	1.05	1.59	136.63 ± 3.93	16.12 ± 2.64	7.29 ± 1.79	45.1 ± 1.93	131.74 ± 1.96	0.0 ± 2.41
H1203	6.48	0.26	2.09	0.99	56.85 ± 2.71	3.47 ± 1.57	0.0 ± 1.31	0.0 ± 1.11	0.0 ± 1.14	0.37 ± 2.38
H1208	2.16	1.29	1.12	0.45	2795.17 ± 50.03	69.07 ± 25.81	3.01 ± 14.28	253.82 ± 9.21	812.93 ± 10.22	17.87 ± 49.35
H1209	1.14	0.0	11.15	3.29	0.0 ± 2.63	0.0 ± 2.18	0.0 ± 1.35	0.0 ± 1.52	0.0 ± 1.49	1.32 ± 12.85
H1209	3.23	0.51	0.96	0.01	26.91 ± 2.82	5.9 ± 1.83	1.99 ± 1.5	0.0 ± 1.54	4.61 ± 1.48	0.0 ± 2.49
H121	1.34	0.43	1.63	1.29	2564.17 ± 8.77	122.65 ± 4.27	11.24 ± 2.69	864.52 ± 3.9	2610.31 ± 4.16	5.24 ± 2.19
H1210	3.15	0.0	1.29	2.38	364.34 ± 5.86	8.2 ± 2.83	1.49 ± 2.18	37.09 ± 2.0	109.7 ± 2.2	1.5 ± 7.04
H1211	10.0	0.47	1.24	—	93.72 ± 1.69	1.45 ± 1.08	0.96 ± 0.92	0.03 ± 0.83	1.79 ± 0.83	0.26 ± 0.81
H122	10.0	0.0	1.06	3.8	3264.34 ± 64.24	76.97 ± 35.82	0.0 ± 28.61	855.88 ± 23.28	2561.13 ± 23.83	0.84 ± 3.09
H124	10.0	0.0	3.87	0.47	565.01 ± 2.28	9.96 ± 1.05	0.0 ± 0.98	75.93 ± 1.07	191.08 ± 1.06	0.0 ± 0.0
H125	0.64	0.0	2.55	1.45	0.0 ± 0.0	67.46 ± 15.31	48.79 ± 8.96	944.25 ± 10.56	3420.71 ± 12.65	24.62 ± 9.7
H126	2.04	0.29	1.5	0.69	45510.02 ± 75.82	709.45 ± 24.31	52.22 ± 11.1	4679.01 ± 26.9	11543.43 ± 14.14	145.43 ± 40.56
H127	-2.0	0.27	2.04	1.01	1836.77 ± 19.45	291.28 ± 11.3	4.75 ± 9.16	724.44 ± 8.52	1401.93 ± 9.7	2.02 ± 9.8
H127	10.0	0.88	0.75	—	2603.68 ± 40.27	328.05 ± 28.99	23.25 ± 18.1	816.94 ± 16.49	4223.07 ± 25.2	13.41 ± 3.38
H128	8.38	0.27	0.75	-0.13	3948.71 ± 22.99	16.59 ± 6.35	0.0 ± 5.32	69.58 ± 4.75	184.13 ± 5.08	8.78 ± 5.93
H129	3.23	0.58	1.34	0.85	5770.06 ± 102.1	181.35 ± 58.94	71.77 ± 34.48	706.2 ± 28.95	2036.23 ± 30.94	21.3 ± 40.16
H130	1.22	0.23	1.03	1.39	1420.51 ± 4.97	13.65 ± 3.06	7.04 ± 1.61	42.54 ± 1.57	129.88 ± 1.64	1.55 ± 1.82
H131	1.3	0.41	1.26	-0.0	861.2 ± 7.94	33.98 ± 4.29	3.01 ± 2.88	117.79 ± 2.69	346.9 ± 3.12	0.36 ± 6.36
H132	1.22	0.37	1.5	—	12391.86 ± 31.65	257.84 ± 13.74	34.16 ± 5.8	2236.54 ± 14.65	5188.09 ± 13.85	18.3 ± 4.17
H134	1.57	0.53	1.77	—	0.0 ± 0.0	0.0 ± 0.0	15.72 ± 15.0	2.66 ± 12.94	55.81 ± 12.58	0.0 ± 19.07
H134	2.29	0.43	3.98	—	681.73 ± 39.27	28.6 ± 23.55	25.39 ± 19.35	0.0 ± 13.06	16.67 ± 13.46	0.0 ± 16.76
H138	10.0	0.46	488.96	0.86	4209.83 ± 14.06	99.77 ± 4.55	0.0 ± 3.69	599.78 ± 7.43	16565.15 ± 10.76	1.17 ± 253.79
H138	10.0	0.43	1.32	0.95	67325.66 ± 95.39	693.2 ± 19.51	62.96 ± 10.57	9862.9 ± 27.4	31542.72 ± 22.22	172.21 ± 19.29
H138	10.0	0.84	2291.66	0.4	333.24 ± 19.22	25.88 ± 9.11	0.0 ± 5.55	53.72 ± 4.44	158.73 ± 4.74	0.0 ± 5054.06
H139	-0.87	0.23	1.29	—	8704.98 ± 54.3	80.51 ± 27.42	0.0 ± 21.8	1180.01 ± 21.14	2507.64 ± 21.82	13.69 ± 23.49
H14	10.0	0.0	9.6	1.08	2642.13 ± 12.59	562.75 ± 5.89	65.52 ± 4.42	1362.01 ± 4.95	3909.33 ± 6.1	16.23 ± 98.92
H140	-0.18	0.93	2.27	2.23	87025.78 ± 247.4	5458.81 ± 94.31	756.83 ± 47.82	28564.02 ± 72.46	68392.01 ± 75.79	49.09 ± 37.02
H141	2.97	0.33	298.29	-0.12	59.98 ± 2.91	0.0 ± 1.65	0.0 ± 1.54	4.0 ± 1.76	4.27 ± 1.5	0.0 ± 199.24
H143	2.45	0.21	1.13	1.34	3345.19 ± 15.18	31.38 ± 7.5	1.96 ± 6.12	388.46 ± 5.46	1057.42 ± 5.47	10.34 ± 5.81
H144	4.91	0.32	1.27	-0.05	808.76 ± 4.77	4.62 ± 2.41	0.0 ± 1.85	71.07 ± 2.08	219.31 ± 2.09	4.75 ± 3.24
H145	3.38	0.0	2.96	3.17	892.26 ± 7.5	379.91 ± 4.26	33.81 ± 3.38	1261.46 ± 5.18	4109.7 ± 7.15	0.0 ± 19.42
H147	3.86	0.05	1.57	1.07	12939.65 ± 21.93	130.35 ± 9.47	0.0 ± 4.42	1622.75 ± 6.61	5138.64 ± 5.68	53.29 ± 26.86
H148	8.25	0.2	2.67	0.15	1092.34 ± 3.76	22.56 ± 1.18	0.0 ± 1.17	195.38 ± 1.76	559.08 ± 1.79	2.83 ± 0.92

Chart A.1 – Continued

Object name	EW	c(Hβ)	$f_{Red900/5500}$	$f_{Red400/8500}$	[O II] λ3727 Å $[F_\lambda]$	[Ne III] λ3869 Å $[F_\lambda]$	[O III] λ4363 Å $[F_\lambda]$	[O III] λ4959 Å $[F_\lambda]$	[O III] λ5007 Å $[F_\lambda]$	[N II] λ5755 Å $[F_\lambda]$
H149	1.07	0.0	1.71	1.36	1088.7 ± 2.92	1.55 ± 1.27	0.0 ± 0.86	32.86 ± 0.86	108.99 ± 0.86	2.45 ± 1.07
H15	10.0	0.0	2.36	64.59	1126.92 ± 8.38	123.97 ± 4.12	10.85 ± 3.03	232.29 ± 3.05	560.47 ± 4.53	5.93 ± 5.08
H15	3.47	0.98	1.47	2.08	6302.12 ± 165.62	1241.84 ± 70.78	124.54 ± 34.47	3153.93 ± 37.52	4357.17 ± 51.88	23.08 ± 27.79
H150	10.0	0.38	1.21	—	8522.44 ± 62.79	2219.79 ± 36.28	120.57 ± 26.62	8616.83 ± 29.77	26732.99 ± 37.97	0.0 ± 0.0
H151	1.85	0.32	1.07	0.77	1873.23 ± 9.82	0.06 ± 5.04	0.0 ± 3.59	7.55 ± 3.14	57.21 ± 2.93	2.73 ± 3.4
H153	10.0	0.8	1.12	0.35	970.91 ± 13.98	7.76 ± 8.61	0.0 ± 5.84	4.49 ± 4.17	2.7 ± 3.93	8.64 ± 7.27
H153	1.7	0.09	2.08	-1.93	156.39 ± 2.25	0.0 ± 1.29	0.09 ± 1.09	4.66 ± 1.19	13.68 ± 1.1	2.41 ± 4.78
H154	1.73	0.35	1.18	-0.12	554.71 ± 5.79	2.0 ± 3.44	0.0 ± 2.54	6.45 ± 2.29	8.7 ± 2.25	0.0 ± 2.36
H155	0.92	1.03	0.62		117272.0 ± 865.15	2711.95 ± 381.49	150.37 ± 177.55	12223.54 ± 109.07	40176.52 ± 126.73	382.05 ± 138.68
H155	1.3	0.49	0.62	0.65	7144.77 ± 15.95	50.65 ± 6.89	6.58 ± 3.38	595.86 ± 4.52	1815.88 ± 4.59	12.2 ± 1.77
H156	2.83	0.37	0.98	0.04	582.46 ± 4.39	7.92 ± 2.95	0.04 ± 1.99	30.07 ± 1.72	81.31 ± 1.91	2.96 ± 2.02
H157	7.99	0.32	1.77	1.47	7219.41 ± 22.17	216.78 ± 11.48	47.93 ± 9.29	510.79 ± 10.65	1172.01 ± 10.65	16.44 ± 16.32
H159	0.22	0.28	0.95	0.18	10368.33 ± 36.8	191.14 ± 18.47	8.41 ± 14.02	1388.78 ± 13.02	4060.86 ± 14.16	0.0 ± 14.19
H16	-0.88	0.0	1.21	1.56	5168.43 ± 24.94	0.0 ± 10.17	11.41 ± 6.86	388.42 ± 6.29	1126.85 ± 6.23	13.25 ± 12.52
H160	2.1	0.0	3.8		303.42 ± 17.15	4.32 ± 10.3	0.0 ± 8.74	16.99 ± 7.69	24.8 ± 8.22	0.0 ± 60.43
H162	10.0	0.07	3.84		1651.27 ± 20.98	137.17 ± 11.82	10.93 ± 9.22	516.23 ± 9.45	1587.36 ± 11.72	0.0 ± 15.36
H163	0.72	0.53	1.49	0.98	25379.91 ± 76.57	855.14 ± 36.53	128.52 ± 19.49	2447.86 ± 22.01	17121.1 ± 25.84	65.35 ± 20.23
H164	1.47	0.26	2.26		323.06 ± 3.14	7.78 ± 1.5	1.77 ± 1.15	69.48 ± 1.08	205.36 ± 1.2	0.52 ± 2.98
H165	2.53	0.4	2.31	-0.07	8283.38 ± 13.55	246.75 ± 3.69	12.62 ± 2.3	2247.08 ± 7.03	6346.09 ± 7.41	8.17 ± 3.41
H167	-0.26	0.0	1.64	3.99	59.85 ± 0.99	2.0 ± 0.61	1.23 ± 0.48	6.28 ± 0.51	14.46 ± 0.52	0.69 ± 0.7
H168	10.0	0.0	2.55	2.52	3959.81 ± 16.38	50.51 ± 7.32	21.72 ± 5.61	381.54 ± 5.1	1438.72 ± 5.79	2.28 ± 15.08
H169	0.83	0.0	2.0	1.4	2599.25 ± 23.89	50.41 ± 16.81	13.81 ± 12.01	65.12 ± 8.93	143.11 ± 8.5	17.48 ± 15.82
H169	0.49	0.06	1.05	1.05	1955.61 ± 19.95	64.99 ± 11.62	12.38 ± 10.14	244.73 ± 8.25	678.68 ± 8.1	20.65 ± 10.91
H17	1.79	0.0	2.16	-0.48	945.78 ± 8.02	2.6 ± 4.89	7.24 ± 3.95	0.0 ± 3.26	1.36 ± 3.31	4.07 ± 6.12
H170	-2.0	1.13	1.59	1.33	89006.39 ± 338.07	295.96 ± 92.02	87.15 ± 43.86	1036.73 ± 38.89	2840.92 ± 33.07	119.9 ± 40.09
H171	0.97	0.0	1.81	1.71	3704.18 ± 16.74	108.92 ± 11.71	37.14 ± 5.52	980.09 ± 4.62	2380.7 ± 4.65	0.0 ± 35.23
H174	1.64	0.15	1.09	0.77	3694.22 ± 7.46	16.13 ± 3.97	3.47 ± 2.32	179.62 ± 2.41	591.46 ± 2.68	8.11 ± 3.06
H176	4.39	0.0	1.15	1.11	2027.28 ± 12.19	15.21 ± 6.98	15.99 ± 5.23	6.65 ± 4.5	22.69 ± 4.63	9.67 ± 8.76
H179	0.43	0.0	3.37	8.12	241.42 ± 1.38	6.11 ± 0.62	1.37 ± 0.49	102.63 ± 1.02	237.67 ± 1.09	1.12 ± 0.56
H18	-0.09	0.17	1.51	4.38	11132.07 ± 34.83	141.85 ± 13.49	0.55 ± 9.93	1301.36 ± 11.36	2876.07 ± 10.82	21.23 ± 12.16
H181	0.77	0.0	4.02		2197.88 ± 21.17	46.43 ± 15.32	19.75 ± 9.96	190.62 ± 8.58	418.17 ± 9.0	7.76 ± 15.29
H184	1.04	0.0	1.93	1.54	3417.44 ± 12.15	109.55 ± 6.2	27.04 ± 4.66	568.26 ± 4.73	1527.03 ± 5.41	9.25 ± 8.97
H185	0.87	0.2	0.96	0.8	4846.36 ± 39.2	323.03 ± 32.69	21.72 ± 15.5	826.5 ± 14.17	2399.1 ± 14.69	9.3 ± 17.3
H185	2.82	0.01	1.27	1.27	2203.33 ± 8.13	51.97 ± 5.55	9.47 ± 3.98	203.48 ± 3.64	566.03 ± 3.74	0.24 ± 6.87
H186	0.65	0.74	0.81	0.33	1328.82 ± 14.72	156.58 ± 8.06	72.96 ± 4.16	234.82 ± 8.72	421.44 ± 8.33	4.0 ± 2.56
H187	2.5	0.53	1.39	0.98	69482.2 ± 116.39	7228.51 ± 45.7	676.54 ± 22.07	39927.33 ± 45.97	145218.41 ± 61.6	74.5 ± 58.28
H189	-2.0	0.0	2.85	3.59	967.47 ± 2.75	15.01 ± 1.16	2.01 ± 0.74	79.39 ± 1.01	152.24 ± 0.95	1.48 ± 0.74
H19	1.41	0.16	2.2	1.85	842.59 ± 12.38	0.0 ± 7.91	15.03 ± 5.35	13.65 ± 4.84	37.4 ± 4.78	1.02 ± 12.19
H190	5.24	0.27	1.53	1.17	52128.23 ± 63.21	2910.57 ± 30.62	754.65 ± 25.69	7762.83 ± 41.55	23334.12 ± 39.11	217.46 ± 13.86
H192	1.84	0.65	1.68	1.44	7559.9 ± 21.01	164.42 ± 5.61	1.5 ± 4.31	1146.01 ± 9.38	3054.97 ± 9.0	16.67 ± 2.94
H193	1.16	0.21	0.94		261.36 ± 2.59	2.85 ± 1.33	1.74 ± 1.03	19.01 ± 1.01	62.82 ± 1.08	0.81 ± 1.39
H194	0.4	0.0	4.01		1777.59 ± 23.05	17.46 ± 14.11	22.14 ± 10.64	18.5 ± 8.56	90.85 ± 8.89	5.97 ± 20.04
H195	10.0	0.0	2.75		1280.22 ± 17.11	13.55 ± 10.43	5.61 ± 8.48	92.04 ± 8.02	176.79 ± 7.99	0.0 ± 10.72
H196	1.48	0.6	1.83	1.42	13247.26 ± 40.77	103.67 ± 18.34	6.19 ± 11.72	788.08 ± 10.6	1880.83 ± 11.04	25.11 ± 15.45
H197	0.66	0.0	0.19	1.76	650.45 ± 5.43	7.41 ± 2.31	3.2 ± 1.3	52.32 ± 1.07	142.31 ± 1.3	9.48 ± 0.84
H198	8.74	0.1	2.44	0.57	11555.51 ± 30.39	823.22 ± 11.66	46.12 ± 6.99	10297.41 ± 17.27	27590.79 ± 12.93	37.35 ± 7.91

Chart A.1 – Continued

Object name	EW	c(Hβ)	$f_{Red900/5500}$	$f_{Red400/8500}$	[O II] $\lambda3727$ Å $[F_\lambda]$	[Ne III] $\lambda3869$ Å $[F_\lambda]$	[O III] $\lambda4363$ Å $[F_\lambda]$	[O III] $\lambda4959$ Å $[F_\lambda]$	[O III] $\lambda5007$ Å $[F_\lambda]$	[N II] $\lambda5755$ Å $[F_\lambda]$
H200	10.0	0.45	3.21	0.0	0.0 ± 0.0	14.94 ± 12.05	0.0 ± 8.55	158.6 ± 7.68	486.08 ± 7.88	0.0 ± 1697.99
H201	1.5	0.18	1.8	—	21405.92 ± 57.96	1009.45 ± 21.97	89.96 ± 15.41	2760.5 ± 16.58	8543.6 ± 18.52	35.84 ± 50.19
H202	10.0	0.0	2.24	1.82	2506.36 ± 10.14	24.8 ± 4.35	0.0 ± 3.8	342.24 ± 3.66	767.92 ± 4.13	1.79 ± 5.96
H203	0.58	0.4	1.59	0.16	10617.1 ± 30.44	119.27 ± 13.02	8.99 ± 9.78	863.46 ± 8.04	2422.76 ± 7.88	10.58 ± 19.31
H207	10.0	0.0	1.25	1.27	4368.21 ± 13.19	94.69 ± 5.65	10.9 ± 5.0	681.05 ± 4.98	2230.04 ± 5.88	2.44 ± 4.13
H208	2.38	0.14	0.31	—	4062.67 ± 5.72	45.91 ± 2.27	4.0 ± 1.05	339.97 ± 2.2	1196.25 ± 2.56	15.45 ± 1.05
H210	0.76	0.0	1.56	1.62	351.69 ± 1.95	0.74 ± 0.89	0.71 ± 0.68	17.42 ± 0.64	49.85 ± 0.67	1.3 ± 1.06
H211	10.0	0.42	0.84	—	1238.93 ± 4.81	7.05 ± 2.24	1.27 ± 1.41	90.89 ± 1.57	267.96 ± 1.63	1.15 ± 1.36
H214	10.0	0.0	1.49	1.27	12741.3 ± 19.53	557.44 ± 7.65	48.0 ± 4.67	2556.81 ± 7.33	6549.23 ± 8.11	11.91 ± 5.48
H216	1.63	0.55	1.03	-1.35	4999.96 ± 15.27	13.99 ± 6.56	0.0 ± 3.83	207.66 ± 3.45	546.71 ± 3.63	0.0 ± 412.43
H217	1.49	0.2	0.9	—	9906.23 ± 12.29	58.51 ± 6.08	11.45 ± 3.18	403.12 ± 3.13	1241.92 ± 3.09	12.64 ± 5.06
H218	2.55	0.42	0.71	0.71	10604.69 ± 13.54	78.61 ± 3.81	7.18 ± 1.84	703.65 ± 2.83	2071.4 ± 2.72	20.82 ± 2.82
H219	0.23	0.0	3.1	3.26	803.89 ± 7.51	11.58 ± 4.88	12.91 ± 3.81	83.34 ± 3.32	156.78 ± 3.4	1.18 ± 4.55
H220	0.99	0.0	2.64	2.04	2822.65 ± 11.19	91.57 ± 6.0	34.87 ± 3.89	831.35 ± 4.08	2252.67 ± 5.01	0.6 ± 4.74
H221	10.0	0.0	5.08	—	590.21 ± 13.14	0.0 ± 7.23	0.0 ± 6.43	75.47 ± 5.78	98.47 ± 5.69	1.71 ± 9.92
H222	1.03	0.0	1.3	1.26	1501.76 ± 12.65	5.15 ± 8.75	3.73 ± 6.28	42.81 ± 5.49	134.74 ± 5.5	1.9 ± 6.96
H224	4.66	0.42	2.84	—	7168.85 ± 21.3	1333.49 ± 7.92	52.8 ± 3.94	6833.08 ± 12.8	19526.72 ± 10.81	5.24 ± 2.51
H225	10.0	0.57	0.93	—	49572.74 ± 161.19	7524.12 ± 76.14	521.18 ± 45.14	24706.38 ± 52.87	72161.38 ± 70.82	185.93 ± 32.7
H226	0.44	0.4	0.48	—	2881.46 ± 6.75	11.88 ± 2.35	2.51 ± 1.65	162.6 ± 1.54	471.3 ± 1.67	1.9 ± 2.0
H228	0.35	0.37	0.21	—	3008.73 ± 24.82	70.42 ± 26.01	0.0 ± 12.08	52.76 ± 10.14	208.43 ± 5.65	30.45 ± 18.54
H229	0.89	0.05	0.71	—	497.96 ± 2.54	0.63 ± 1.09	1.93 ± 0.73	26.58 ± 0.7	68.15 ± 0.76	3.09 ± 0.78
H23	1.24	0.38	1.26	—	17236.88 ± 50.45	438.7 ± 24.55	81.98 ± 15.27	3475.46 ± 14.71	10869.62 ± 17.97	35.32 ± 18.19
H230	3.51	0.0	1.63	—	2264.04 ± 22.47	10.81 ± 12.7	10.66 ± 13.27	95.25 ± 8.98	265.82 ± 9.55	0.0 ± 11.65
H232	0.29	0.0	32.16	4.18	159.75 ± 9.69	11.07 ± 6.41	0.0 ± 5.12	8.71 ± 4.01	20.35 ± 4.09	0.0 ± 347.6
H233	10.0	0.0	0.22	—	392.24 ± 16.18	66.3 ± 4.99	25.2 ± 3.48	114.29 ± 4.21	148.05 ± 6.5	48.17 ± 6.34
H234	10.0	1.37	1.23	—	121433.99 ± 893.81	6256.82 ± 398.36	833.95 ± 200.22	15560.24 ± 154.93	106554.19 ± 223.9	413.25 ± 97.96
H235	10.0	0.0	1.25	—	178.17 ± 11.67	46.13 ± 4.15	31.92 ± 3.04	79.35 ± 3.3	92.33 ± 5.5	1.12 ± 33.1
H236	0.84	0.11	10.74	13.97	5.57 ± 1.32	0.0 ± 0.85	0.82 ± 0.63	0.53 ± 0.6	0.0 ± 0.6	0.0 ± 1.0
H237	1.4	0.01	1.37	—	562.39 ± 9.65	0.0 ± 5.44	7.83 ± 3.73	8.34 ± 3.64	12.17 ± 3.67	16.38 ± 9.5
H238	7.57	0.0	0.92	—	0.0 ± 11.68	0.0 ± 7.39	8.55 ± 6.19	0.0 ± 5.38	0.0 ± 5.63	16.67 ± 22.26
H239	2.12	0.12	1.85	—	1624.88 ± 27.03	0.0 ± 15.12	21.62 ± 11.75	11.93 ± 10.79	7.35 ± 10.72	0.0 ± 19.52
H241	0.95	0.36	0.99	0.8	11216.46 ± 41.12	510.36 ± 19.72	59.29 ± 13.82	2827.16 ± 12.81	9520.27 ± 16.25	0.0 ± 0.0
H242	1.99	0.26	1.36	—	4954.83 ± 60.12	44.89 ± 26.95	5.32 ± 19.68	199.34 ± 16.19	535.76 ± 16.35	6.81 ± 17.89
H243	5.12	0.0	3.87	13.1	2.48 ± 1.04	0.0 ± 0.65	1.23 ± 0.52	1.37 ± 0.53	2.37 ± 0.53	0.08 ± 0.66
H245	0.18	0.29	0.59	—	388.07 ± 2.92	1.58 ± 1.47	0.59 ± 1.16	6.8 ± 0.96	17.54 ± 0.92	0.0 ± 1.19
H248	10.0	0.0	14.82	-40.59	2.95 ± 0.58	0.0 ± 0.35	0.29 ± 0.29	0.0 ± 0.29	0.0 ± 0.3	0.0 ± 0.87
H248	10.0	0.0	0.12	1.14	211.79 ± 28.62	29.79 ± 8.01	5.21 ± 5.99	98.4 ± 6.01	88.25 ± 8.64	136.8 ± 10.51
H249	0.77	0.04	1.37	—	176.07 ± 2.87	0.0 ± 1.51	1.23 ± 1.22	0.0 ± 1.11	0.0 ± 1.12	0.0 ± 1.92
H250	-2.0	0.0	2.86	—	4499.57 ± 15.5	244.69 ± 6.11	16.61 ± 3.74	938.71 ± 4.91	2412.85 ± 6.12	3.57 ± 6.71
H253	10.0	0.0	0.58	0.48	140.18 ± 0.89	3.33 ± 0.41	0.0 ± 0.32	17.46 ± 0.46	40.65 ± 0.54	0.0 ± 0.35
H255	10.0	0.0	1.14	0.86	1312.01 ± 2.22	54.8 ± 1.18	5.88 ± 0.53	337.2 ± 1.31	839.97 ± 1.52	2.06 ± 0.63
H257	2.83	0.87	1.08	—	8060.2 ± 18.96	59.49 ± 5.94	8.14 ± 3.51	865.34 ± 4.97	2616.91 ± 5.4	12.51 ± 3.41
H259	3.35	0.0	1.33	2.13	182.95 ± 1.92	1.68 ± 1.07	0.0 ± 0.82	12.57 ± 0.77	33.47 ± 0.78	0.95 ± 1.17
	8.89	0.0	1.54	—	801.04 ± 9.47	26.09 ± 5.1	0.0 ± 3.76	138.23 ± 3.7	408.69 ± 4.48	3.67 ± 9.9
	1.33	1.28	0.34	0.46	18708.97 ± 56.19	137.78 ± 39.25	73.9 ± 14.63	236.04 ± 6.95	735.51 ± 6.87	46.44 ± 11.41
	2.07	0.44	0.67	—	14556.45 ± 20.94	456.88 ± 8.41	25.66 ± 3.43	3341.56 ± 13.28	10097.65 ± 12.52	24.47 ± 2.65

Chart A.1 – Continued

Object name	EW	c(Hβ)	$f_{Red900/5500}$	$f_{Red400/8500}$	[O II] λ3727 Å $[F_\lambda]$	[Ne III] λ3869 Å $[F_\lambda]$	[O III] λ4363 Å $[F_\lambda]$	[O III] λ4959 Å $[F_\lambda]$	[O III] λ5007 Å $[F_\lambda]$	[N II] λ5755 Å $[F_\lambda]$
H26	10.0	1.11	0.65	1.3	65755.25 ± 337.86	488.99 ± 173.55	151.16 ± 95.46	3744.55 ± 53.74	12522.93 ± 62.19	47.89 ± 196.26
H262	10.0	0.34	1.33	1.48	1624.57 ± 5.69	155.99 ± 1.75	8.43 ± 1.48	1110.59 ± 8.78	2930.81 ± 8.81	4.24 ± 0.8
H264	1.63	0.34	1.45	—	1304.34 ± 22.06	33.19 ± 12.82	11.98 ± 8.81	48.09 ± 7.15	120.87 ± 7.55	0.0 ± 11.18
H266	0.9	1.09	1.96	—	38412.14 ± 238.16	3742.39 ± 108.93	415.74 ± 56.45	19633.56 ± 63.72	65028.65 ± 86.95	62.9 ± 57.39
H269	−2.0	0.0	1.32	4.82	2377.64 ± 9.58	6.88 ± 4.09	6.16 ± 2.86	35.61 ± 2.54	92.53 ± 2.67	4.07 ± 3.94
H27	10.0	0.0	1.27	—	315.87 ± 9.51	0.0 ± 5.03	0.09 ± 4.02	0.0 ± 3.56	0.0 ± 3.94	4.02 ± 11.25
H270	10.0	0.0	2.86	—	294.39 ± 13.04	12.85 ± 7.48	0.0 ± 5.37	7.94 ± 5.34	42.58 ± 5.65	0.0 ± 9.91
H270	10.0	0.0	0.26	1.07	342.73 ± 13.48	10.11 ± 7.45	3.37 ± 5.37	12.49 ± 5.63	0.71 ± 5.24	0.0 ± 8.86
H271	1.39	0.68	0.88	3.99	2620.58 ± 9.03	181.49 ± 5.54	18.36 ± 2.65	624.42 ± 3.17	1876.93 ± 3.72	4.8 ± 4.59
H272	−1.82	0.0	0.68	0.59	1204.18 ± 3.55	54.33 ± 1.36	7.69 ± 0.54	446.4 ± 1.81	1045.93 ± 1.98	6.27 ± 1.11
H274	10.0	0.44	1.83	1.43	726.74 ± 7.7	15.49 ± 3.67	2.22 ± 2.75	124.66 ± 2.35	361.87 ± 2.76	1.27 ± 6.79
H275	−2.0	0.0	1.28	—	540.67 ± 7.45	0.0 ± 3.8	2.92 ± 2.96	20.04 ± 2.72	42.87 ± 2.81	1.89 ± 5.09
H279	0.91	0.39	0.54	3.24	365.25 ± 3.11	3.2 ± 2.06	4.61 ± 1.18	6.73 ± 0.92	20.74 ± 0.91	2.92 ± 1.44
H28	7.93	0.14	1.78	0.99	1251.72 ± 11.18	0.77 ± 4.58	0.0 ± 3.77	60.31 ± 3.59	32.96 ± 3.72	268.7 ± 368.82
H280	1.33	0.1	1.41	1.06	1832.19 ± 3.17	33.2 ± 1.74	7.17 ± 0.83	195.48 ± 0.87	485.83 ± 1.09	1.6 ± 1.54
H282	4.07	0.16	1.24	1.31	872.17 ± 14.79	0.0 ± 8.85	9.46 ± 5.79	112.91 ± 5.42	338.09 ± 6.02	10.31 ± 8.25
H285	2.24	0.0	0.98	—	446.38 ± 3.06	14.87 ± 1.65	0.99 ± 1.27	39.35 ± 1.19	119.09 ± 1.29	1.53 ± 1.59
H286	1.85	0.32	0.99	1.66	1642.09 ± 9.73	259.41 ± 5.04	21.42 ± 2.92	918.26 ± 5.77	2789.43 ± 6.37	7.86 ± 3.07
H287	10.0	0.0	4.24	0.92	339.09 ± 8.17	10.2 ± 4.21	3.01 ± 3.4	9.87 ± 3.07	22.8 ± 3.14	0.0 ± 0.0
H288	0.99	0.0	1.97	0.84	3066.59 ± 12.36	33.76 ± 8.14	35.58 ± 4.92	451.97 ± 3.49	1344.93 ± 4.01	4.63 ± 6.74
H288	10.0	0.0	1.79	1.25	3104.47 ± 18.9	49.1 ± 9.34	5.75 ± 6.97	530.54 ± 6.46	1398.79 ± 7.04	20.86 ± 17.04
H290	−0.06	0.0	0.8	1.26	2959.26 ± 7.04	277.25 ± 2.13	17.27 ± 2.08	1358.2 ± 10.82	3829.01 ± 10.07	6.0 ± 1.97
H292	0.48	0.45	1.4	1.19	9984.19 ± 17.13	198.65 ± 6.37	23.88 ± 1.94	892.47 ± 3.29	2577.75 ± 3.5	8.02 ± 2.5
H294	0.35	0.27	1.33	1.22	435.39 ± 3.54	14.61 ± 1.67	2.92 ± 1.13	91.15 ± 1.25	284.95 ± 1.52	1.31 ± 1.75
H295	0.7	0.0	0.87	1.47	2372.25 ± 3.64	152.86 ± 1.4	20.96 ± 0.63	495.12 ± 1.94	1499.77 ± 2.19	4.11 ± 1.58
H296	0.91	0.0	1.28	—	348.13 ± 1.99	3.19 ± 0.91	1.18 ± 0.7	18.68 ± 0.69	51.85 ± 0.88	0.08 ± 0.84
H299	0.77	0.0	1.19	—	4856.63 ± 14.75	22.96 ± 7.52	11.77 ± 5.03	241.53 ± 4.69	671.82 ± 4.85	7.3 ± 6.93
H299	4.12	0.19	1.22	1.25	7306.93 ± 43.33	26.01 ± 24.13	55.29 ± 17.91	68.27 ± 15.38	261.91 ± 14.73	0.0 ± 26.55
H301	0.93	0.0	1.47	—	2266.91 ± 9.76	1.92 ± 5.29	0.0 ± 3.5	33.85 ± 3.14	81.27 ± 3.32	0.0 ± 6.67
H303	1.42	0.23	0.64	—	3626.28 ± 16.75	65.14 ± 6.17	7.41 ± 4.15	315.56 ± 4.51	833.83 ± 5.36	12.58 ± 3.43
H306	0.83	0.24	0.97	1.25	2425.11 ± 4.3	9.97 ± 1.94	5.78 ± 1.0	99.3 ± 0.89	307.86 ± 1.02	2.27 ± 1.07
H307	−2.0	0.0	0.63	—	363.98 ± 3.14	35.08 ± 1.37	25.64 ± 4.03	265.3 ± 4.86	375.52 ± 5.93	30.41 ± 5.94
H307	1.91	0.0	1.11	1.58	0.0 ± 0.0	0.0 ± 0.0	2.6 ± 1.03	159.07 ± 2.97	323.47 ± 3.44	0.95 ± 1.04
H309	−2.0	0.6	7.11	—	0.0 ± 0.0	0.0 ± 0.0	108.26 ± 12.55	3792.53 ± 15.08	11404.87 ± 17.89	2.2 ± 11.96
H309	1.2	0.31	0.94	1.23	3084.04 ± 10.19	219.59 ± 8.07	31.87 ± 2.32	1399.8 ± 3.16	3570.44 ± 3.46	3.72 ± 5.49
H31	2.93	0.11	2.06	−1.23	3169.81 ± 15.21	22.2 ± 12.17	13.81 ± 8.51	294.71 ± 7.58	739.26 ± 7.2	6.97 ± 11.29
H312	1.87	0.3	1.13	0.81	1452.63 ± 10.22	203.62 ± 5.71	19.12 ± 4.14	667.29 ± 5.19	1973.42 ± 5.31	8.86 ± 10.24
H314	0.22	0.53	0.64	—	19081.54 ± 53.56	728.08 ± 20.4	64.35 ± 12.64	2432.39 ± 11.96	5982.68 ± 17.34	16.79 ± 18.81
H316	8.87	0.0	1.72	—	0.0 ± 0.0	0.0 ± 3.74	0.0 ± 2.81	46.27 ± 3.27	151.04 ± 3.23	1.23 ± 6.13
H318	2.17	0.12	1.74	0.71	971.92 ± 5.05	0.0 ± 2.24	0.56 ± 1.69	11.57 ± 1.75	36.68 ± 1.68	0.0 ± 2.7
H319	0.77	0.18	0.78	0.9	3807.6 ± 7.12	175.19 ± 2.83	11.38 ± 1.61	436.49 ± 3.34	1288.7 ± 5.77	6.24 ± 4.12
H32	4.79	0.0	1.5	7.81	1549.43 ± 11.35	22.9 ± 5.46	9.46 ± 4.55	499.84 ± 5.37	994.69 ± 5.81	19.06 ± 7.55
H32	10.0	1.45	0.86	2.27	146561.62 ± 1364.84	2549.75 ± 689.89	985.42 ± 323.07	14294.92 ± 230.41	43777.67 ± 219.1	42.52 ± 212.95
H320	10.0	0.0	1.02	—	2478.11 ± 14.11	424.91 ± 6.32	37.58 ± 4.23	2029.49 ± 5.66	6661.67 ± 8.93	7.5 ± 5.72
H320	10.0	0.0	0.88	—	16449.83 ± 134.84	19846.22 ± 56.02	3928.28 ± 28.27	52857.52 ± 92.27	152535.41 ± 66.76	92.69 ± 13.73
H321	10.0	0.28	0.61	0.04	0.0 ± 0.0	78.74 ± 0.81	10.6 ± 0.58	435.36 ± 1.75	1278.3 ± 2.02	2.17 ± 0.52

Chart A.1 – Continued

Object name	EW	c(Hβ)	$f_{Red900/5500}$	$f_{Red400/8500}$	[O II] λ3727 Å [F_λ]	[Ne III] λ3869 Å [F_λ]	[O III] λ4363 Å [F_λ]	[O III] λ4959 Å [F_λ]	[O III] λ5007 Å [F_λ]	[N II] λ5755 Å [F_λ]
H322	4.37	1.53	0.32	—	1244102.88 ± 2045.97	91652.74 ± 570.85	6528.62 ± 189.09	252622.84 ± 334.16	914083.0 ± 436.06	775.29 ± 74.94
H323	−1.11	0.0	5.69	—	1158.68 ± 9.58	0.0 ± 6.64	19.64 ± 4.6	93.77 ± 3.8	258.65 ± 3.99	1.69 ± 5.3
H324	0.65	0.0	8.06	—	2293.9 ± 9.82	18.82 ± 4.18	14.73 ± 3.02	499.03 ± 4.05	1286.78 ± 5.45	2.9 ± 14.41
H324	1.17	0.0	1.37	1.44	3236.43 ± 5.8	33.06 ± 2.01	7.9 ± 1.27	299.35 ± 2.48	890.83 ± 2.8	3.97 ± 1.95
H325	1.33	0.0	1.89	—	969.61 ± 6.78	0.0 ± 3.26	0.0 ± 2.3	15.4 ± 2.06	48.53 ± 2.08	2.03 ± 2.8
H325	1.34	0.17	0.99	1.04	4026.4 ± 9.22	10.56 ± 4.88	1.17 ± 2.73	101.14 ± 2.37	248.27 ± 2.44	2.45 ± 2.44
H327	−1.42	0.03	1.08	—	838.06 ± 6.66	20.35 ± 3.12	8.59 ± 2.38	249.03 ± 2.67	474.46 ± 3.05	5.25 ± 2.96
H328	1.16	0.4	1.21	1.01	3892.13 ± 9.83	26.59 ± 4.3	17.26 ± 3.02	365.73 ± 2.69	968.98 ± 3.17	4.45 ± 2.39
H329	1.67	0.04	1.33	0.85	312.93 ± 1.22	3.58 ± 0.54	1.52 ± 0.42	18.43 ± 0.41	54.23 ± 0.43	0.54 ± 0.51
H33	1.26	0.37	0.99	0.78	2000.16 ± 5.4	61.81 ± 2.15	9.13 ± 1.42	414.18 ± 1.79	1023.56 ± 2.02	3.68 ± 1.06
H331	−0.92	0.26	2.54	0.57	1911.74 ± 4.01	110.61 ± 1.27	11.21 ± 0.68	401.31 ± 2.98	2120.64 ± 3.26	1.1 ± 0.6
H334	1.84	0.0	0.07	1.04	575.28 ± 1.43	1.62 ± 0.51	1.07 ± 0.34	33.49 ± 0.41	81.9 ± 0.45	16.52 ± 0.47
H335	6.5	0.13	0.84	0.98	2519.82 ± 4.44	51.4 ± 1.92	0.13 ± 1.19	250.81 ± 1.52	734.76 ± 1.5	3.6 ± 1.84
H335	1.31	0.07	1.01	0.97	1234.33 ± 2.79	52.3 ± 1.37	3.67 ± 0.82	300.23 ± 1.18	878.98 ± 1.31	1.47 ± 1.3
H337	1.37	0.49	0.96	0.58	4245.38 ± 10.1	53.52 ± 3.4	14.3 ± 1.47	369.85 ± 2.52	1219.59 ± 3.03	7.03 ± 1.6
H34	6.45	0.2	1.91	1.7	21688.37 ± 38.21	335.82 ± 14.34	55.63 ± 8.62	1853.02 ± 12.0	3970.4 ± 8.6	40.95 ± 23.64
H340	1.79	0.0	1.12	1.38	3659.38 ± 8.44	0.0 ± 3.3	0.11 ± 3.04	96.92 ± 2.58	281.34 ± 2.56	9.96 ± 5.12
H340	1.07	0.04	1.04	1.26	3603.35 ± 6.97	48.87 ± 2.44	5.31 ± 1.72	433.57 ± 2.66	1279.27 ± 2.91	4.43 ± 1.82
H341	0.56	0.07	1.41	0.48	1167.22 ± 3.06	8.15 ± 1.64	0.0 ± 1.16	18.48 ± 1.04	53.44 ± 1.07	0.82 ± 1.7
H343	1.42	0.0	0.97	1.06	3011.58 ± 2.99	26.84 ± 1.15	6.51 ± 0.59	243.09 ± 0.81	711.43 ± 0.91	3.69 ± 0.59
H345	10.0	0.0	1.49	1.59	0.0 ± 32.07	39.21 ± 1.78	7.61 ± 0.55	218.24 ± 0.86	542.75 ± 0.93	2.17 ± 0.57
H347	2.38	0.2	0.96	1.3	4020.83 ± 14.15	839.29 ± 4.7	64.8 ± 3.9	3578.59 ± 26.06	10982.54 ± 24.5	2.34 ± 2.17
H35	−0.69	0.43	3.1	3.19	24965.94 ± 70.32	738.87 ± 27.66	0.0 ± 152.17	3131.03 ± 179.21	8051.35 ± 128.76	29.04 ± 86.11
H350	1.33	0.42	1.49	0.26	1830.89 ± 10.64	36.23 ± 8.66	24.72 ± 3.98	373.97 ± 4.02	1101.09 ± 4.13	0.0 ± 4.44
H358	10.0	0.55	0.67	0.6	20982.96 ± 39.19	599.3 ± 10.32	27.05 ± 4.41	5376.05 ± 8.49	13895.28 ± 7.58	16.44 ± 1.83
H360	0.94	0.0	3.07	1.16	162.1 ± 1.75	0.59 ± 0.93	0.0 ± 0.73	4.47 ± 0.75	14.04 ± 0.77	0.84 ± 1.36
H361	0.84	0.04	2.19	1.59	150.02 ± 2.02	0.64 ± 1.18	0.0 ± 0.93	0.99 ± 0.89	2.67 ± 0.93	1.14 ± 1.43
H362	10.0	3.0	10.28	−1.7	46944.38 ± 17589.02	12510.98 ± 9739.25	1408.43 ± 2878.65	7108.75 ± 851.61	18137.74 ± 814.54	0.0 ± 840.29
H362	0.81	0.53	1.64	0.2	514.85 ± 12.44	2.08 ± 7.09	1.12 ± 4.74	26.34 ± 3.89	58.95 ± 3.96	0.01 ± 6.19
H363	0.91	0.43	1.42	0.37	199.41 ± 8.32	2.48 ± 5.27	6.01 ± 3.62	6.4 ± 2.93	21.67 ± 3.0	2.6 ± 3.69
H363	4.09	1.02	1.21	0.53	0.0 ± 65.85	0.0 ± 43.69	0.0 ± 22.75	161.14 ± 14.13	516.4 ± 13.9	0.0 ± 23.48
H364	−2.0	1.14	0.31	0.7	22740.9 ± 59.08	299.08 ± 20.47	13.31 ± 10.08	1609.63 ± 9.95	4335.64 ± 9.5	22.74 ± 4.19
H365	10.0	0.15	1.01	0.33	386.71 ± 1.79	101.63 ± 1.04	4.99 ± 0.89	356.01 ± 1.5	1038.81 ± 1.86	3.45 ± 0.92
H366	10.0	0.0	3.38	−5.03	26.97 ± 1.85	0.79 ± 1.23	0.12 ± 1.06	1.67 ± 0.99	8.87 ± 0.99	0.63 ± 2.69
H368	0.94	0.46	0.97	0.2	275.98 ± 5.66	0.75 ± 4.1	6.28 ± 2.32	12.12 ± 2.36	27.37 ± 2.25	2.89 ± 2.22
H369	1.18	0.48	1.39	−0.06	2298.66 ± 11.05	87.19 ± 9.0	24.54 ± 4.33	537.82 ± 4.79	1603.49 ± 5.22	10.3 ± 3.56
H37	1.47	0.39	0.82	0.69	741.55 ± 4.4	12.65 ± 4.51	10.74 ± 1.88	9.01 ± 1.2	22.85 ± 1.1	0.0 ± 1.51
H370	0.66	0.15	1.02	0.51	1248.75 ± 4.44	0.0 ± 2.4	0.0 ± 1.94	79.3 ± 1.95	238.85 ± 2.08	7.33 ± 1.55
H371	−0.16	0.53	3.42	2.84	676.94 ± 14.58	0.0 ± 7.34	11.67 ± 3.59	75.3 ± 2.83	0.0 ± 3.72	2.15 ± 3.63
H373	1.11	3.0	0.13	0.02	824743.62 ± 130154.14	121040.82 ± 90642.52	56127.97 ± 22844.32	31993.0 ± 6162.24	126619.31 ± 5413.68	40318.95 ± 2901.22
H373	1.13	0.51	0.88	−0.02	1853.19 ± 13.74	45.58 ± 12.61	24.6 ± 6.17	226.72 ± 4.45	666.15 ± 4.46	4.51 ± 9.4
H374	5.18	0.47	0.9	1.26	6074.8 ± 11.49	34.96 ± 8.23	12.38 ± 4.25	154.24 ± 2.92	660.41 ± 3.23	16.26 ± 7.63
H375	0.74	1.26	0.36	0.06	2472.83 ± 53.12	45.6 ± 27.75	6.04 ± 15.91	0.06 ± 9.62	72.09 ± 9.31	0.0 ± 586.72
H376	1.7	0.38	0.13	0.94	1192.75 ± 4.84	5.56 ± 3.17	4.88 ± 2.0	57.68 ± 1.8	184.76 ± 1.95	11.44 ± 1.63
H377	1.35	0.41	22.2	0.83	3023.02 ± 10.09	253.75 ± 4.57	4.45 ± 3.18	1556.41 ± 6.83	4639.26 ± 6.79	0.51 ± 5.98
H377	7.28	0.09	0.05	1.15	1197.88 ± 4.71	121.24 ± 2.6	3.11 ± 1.84	914.66 ± 4.12	2794.46 ± 4.36	45.08 ± 2.22

Chart A.1 – Continued

Object name	EW	c(Hβ)	$f_{Red900/5500}$	$f_{Red400/8500}$	[O II] λ3727 Å $[F_\lambda]$	[Ne III] λ3869 Å $[F_\lambda]$	[O III] λ4363 Å $[F_\lambda]$	[O III] λ4959 Å $[F_\lambda]$	[O III] λ5007 Å $[F_\lambda]$	[N II] λ5755 Å $[F_\lambda]$
H378	1.02	0.23	1.1	1.06	2309.51 ± 5.25	45.32 ± 2.22	4.13 ± 1.32	244.72 ± 1.9	669.76 ± 1.94	3.98 ± 1.01
H38	5.5	0.47	0.67	0.7	3874.43 ± 9.01	80.43 ± 2.79	4.56 ± 1.88	647.95 ± 2.59	1956.67 ± 3.37	6.82 ± 1.48
H380	6.44	0.77	0.67	0.76	14546.96 ± 37.2	330.89 ± 18.47	0.0 ± 13.01	2901.66 ± 13.7	9050.73 ± 14.25	21.26 ± 3.73
H381	−0.28	0.76	0.83	—	74353.86 ± 132.17	1273.65 ± 34.57	71.35 ± 15.81	11132.96 ± 33.24	35932.61 ± 20.06	114.79 ± 7.1
H382	10.0	0.92	0.94	−0.0	8771.89 ± 36.75	88.68 ± 14.21	3.4 ± 7.85	1603.16 ± 9.51	4891.79 ± 10.53	14.05 ± 5.44
H382	10.0	0.0	1.45	0.01	2386.23 ± 3.3	5.53 ± 1.08	0.0 ± 0.87	59.79 ± 1.14	124.26 ± 1.43	5.15 ± 1.0
H384	1.47	0.22	0.82	—	14351.17 ± 19.55	107.31 ± 5.37	0.0 ± 3.27	1493.6 ± 5.9	4412.49 ± 3.46	27.54 ± 1.68
H386	0.98	0.41	1.29	−0.03	630.07 ± 5.22	0.0 ± 2.96	0.0 ± 2.14	48.55 ± 1.64	93.95 ± 1.79	0.0 ± 2.25
H387	2.14	0.13	1.14	−0.16	2190.87 ± 4.76	48.63 ± 1.64	2.58 ± 1.13	386.83 ± 2.63	1057.32 ± 2.44	5.66 ± 1.02
H387	2.42	0.31	1.07	0.77	3102.5 ± 11.94	57.31 ± 4.11	0.0 ± 3.67	461.45 ± 4.5	1092.9 ± 4.67	4.96 ± 3.01
H388	0.34	0.33	1.15	−0.2	768.65 ± 5.63	145.26 ± 2.46	3.2 ± 1.68	662.77 ± 4.26	2176.96 ± 4.54	2.02 ± 1.45
H389	1.26	0.64	1.38	−0.06	1837.3 ± 8.48	8.73 ± 4.24	1.06 ± 2.25	56.59 ± 1.93	198.93 ± 2.18	2.46 ± 1.96
H389	2.6	0.18	1.07	0.97	410.21 ± 4.3	4.1 ± 2.02	0.0 ± 1.49	35.23 ± 1.39	106.71 ± 1.53	0.67 ± 1.29
H390	1.1	0.3	0.85	—	7058.44 ± 10.36	24.94 ± 2.38	3.66 ± 1.37	264.51 ± 2.17	778.04 ± 1.89	9.85 ± 2.14
H393	1.2	0.38	1.11	0.53	665.9 ± 8.35	62.35 ± 5.3	8.42 ± 3.51	173.42 ± 3.2	566.74 ± 3.9	1.7 ± 6.74
H394	1.54	0.38	0.86	−0.01	211.86 ± 2.91	1.23 ± 1.69	2.81 ± 1.23	0.71 ± 1.07	8.51 ± 1.06	0.0 ± 0.94
H396	7.0	0.04	1.59	1.14	217.42 ± 2.19	2.24 ± 1.19	0.0 ± 1.1	16.97 ± 1.11	52.01 ± 1.16	0.2 ± 2.87
H398	−0.25	0.54	0.84	0.56	537.76 ± 8.73	0.0 ± 4.57	3.65 ± 3.16	0.0 ± 2.56	0.0 ± 2.54	3.26 ± 6.0
H399	0.82	0.53	0.92	0.8	301.62 ± 8.74	6.96 ± 4.31	0.0 ± 3.18	22.37 ± 2.53	61.01 ± 2.74	3.0 ± 3.54
H4	0.4	0.09	0.33	—	699.85 ± 2.91	15.12 ± 1.28	2.41 ± 0.88	109.69 ± 0.97	346.03 ± 1.1	0.0 ± 0.62
H40	0.77	1.25	1.39	−64.27	77640.81 ± 406.36	2192.81 ± 184.09	387.1 ± 103.43	13599.23 ± 79.15	43243.13 ± 81.58	0.0 ± 442.09
H400	1.1	0.0	0.38	1.12	136.56 ± 1.32	0.0 ± 0.79	0.52 ± 0.6	1.78 ± 0.6	6.05 ± 0.62	0.0 ± 0.21
H412	1.21	0.38	0.86	1.13	2304.4 ± 11.25	13.69 ± 6.28	1.48 ± 4.18	72.35 ± 3.37	192.33 ± 3.54	2.52 ± 4.52
H412	10.0	0.34	1.11	0.5	3729.08 ± 20.32	112.02 ± 12.1	0.0 ± 9.31	320.9 ± 6.91	863.06 ± 7.42	0.0 ± 8.12
H412	10.0	0.33	1.06	0.99	3438.02 ± 36.01	124.18 ± 20.16	20.01 ± 15.04	402.21 ± 12.26	1116.88 ± 12.41	0.0 ± 17.81
H416	−0.67	0.28	1.06	0.73	3459.56 ± 11.26	10.04 ± 4.02	0.0 ± 3.23	141.91 ± 2.95	440.71 ± 3.3	7.99 ± 3.23
H419	1.07	0.23	1.72	1.65	509.23 ± 9.12	6.46 ± 6.68	9.57 ± 3.57	5.07 ± 2.74	8.44 ± 2.83	4.67 ± 4.53
H42	0.15	2.21	0.65	1.5	50874.64 ± 5327.68	0.0 ± 3313.72	5127.49 ± 2403.84	0.0 ± 752.49	5723.19 ± 669.78	0.0 ± 4390.05
H420	10.0	0.0	0.71	0.36	67.72 ± 1.61	12.9 ± 1.01	1.31 ± 0.84	26.55 ± 0.8	70.47 ± 0.92	0.87 ± 0.92
H421	3.55	0.0	1.92	1.56	24.67 ± 1.56	0.55 ± 0.94	1.83 ± 0.9	1.37 ± 0.8	3.06 ± 0.82	0.09 ± 2.5
H422	2.73	0.28	1.49	2.13	190.48 ± 3.26	2.16 ± 1.62	1.74 ± 1.36	13.57 ± 1.28	42.85 ± 1.34	0.91 ± 1.74
H425	0.84	0.6	1.0	0.64	1791.63 ± 24.23	20.48 ± 16.73	28.86 ± 8.47	24.11 ± 6.02	53.23 ± 5.67	7.48 ± 9.06
H429	10.0	0.09	1.37	1.39	123.37 ± 1.41	0.63 ± 0.76	0.0 ± 0.56	3.83 ± 0.61	9.85 ± 0.6	0.0 ± 0.87
H43	−2.0	0.0	17.22	2.01	4180.69 ± 4.72	12.24 ± 1.01	0.48 ± 0.59	329.83 ± 1.63	1430.52 ± 1.76	0.0 ± 25.62
H431	1.33	0.36	1.36	1.15	1361.95 ± 6.32	18.37 ± 3.0	1.01 ± 2.11	250.32 ± 2.54	800.41 ± 2.77	1.35 ± 1.32
H432	1.34	0.49	0.86	0.68	549.89 ± 5.0	0.91 ± 2.83	3.54 ± 2.12	10.5 ± 1.78	37.42 ± 1.79	2.09 ± 1.76
H433	1.38	0.35	1.12	0.5	546.46 ± 6.43	8.2 ± 3.89	0.0 ± 3.01	4.96 ± 2.53	0.0 ± 2.33	3.08 ± 3.12
H433	1.47	0.67	0.62	0.58	1327.06 ± 9.81	7.93 ± 7.26	9.65 ± 3.76	0.0 ± 2.77	6.56 ± 2.54	7.04 ± 1.97
H434	2.29	0.17	1.37	0.83	366.85 ± 3.97	32.19 ± 2.13	5.7 ± 1.77	141.09 ± 1.94	418.5 ± 2.32	2.49 ± 2.31
H435	2.8	0.16	0.22	1.1	1280.56 ± 3.92	10.71 ± 1.94	3.39 ± 1.17	55.2 ± 1.34	163.23 ± 1.35	17.11 ± 1.18
H437	0.35	0.03	1.28	2.52	1771.02 ± 3.86	16.69 ± 1.17	1.52 ± 0.72	134.46 ± 1.19	282.76 ± 1.16	3.62 ± 0.6
H438	0.98	0.39	0.97	—	2776.24 ± 6.61	2.81 ± 4.17	1.95 ± 2.29	75.64 ± 1.87	215.11 ± 2.02	1.36 ± 2.85
H44	10.0	0.0	1.74	0.02	0.0 ± 0.0	0.0 ± 0.0	3.29 ± 4.03	80.24 ± 3.81	166.28 ± 3.92	2.25 ± 9.05
H44	1.03	0.48	1.07	0.9	20801.51 ± 48.56	103.57 ± 27.01	43.4 ± 14.96	762.36 ± 11.98	1974.33 ± 13.04	0.0 ± 0.0
H445	1.09	0.26	0.81	1.06	1268.71 ± 5.59	10.52 ± 3.79	0.44 ± 2.02	67.43 ± 1.62	184.62 ± 1.75	1.5 ± 0.97
H448	1.14	0.2	0.78	0.76	839.76 ± 4.0	8.47 ± 1.82	0.0 ± 1.49	71.36 ± 1.62	196.93 ± 1.79	3.26 ± 1.09

Continued on Next Page. . .

Chart A.1 – Continued

Object name	EW	c(Hβ)	$f_{Red900/5500}$	$f_{Red400/8500}$	[O II] λ3727 Å [F_λ]	[Ne III] λ3869 Å [F_λ]	[O III] λ4363 Å [F_λ]	[O III] λ4959 Å [F_λ]	[O III] λ5007 Å [F_λ]	[N II] λ5755 Å [F_λ]
H448	10.0	0.92	0.75	0.77	3323.27 ± 50.98	0.0 ± 34.16	0.0 ± 21.38	418.52 ± 16.55	1254.5 ± 17.44	0.0 ± 9.84
H450	1.73	0.47	0.86	—	2475.38 ± 8.28	12.92 ± 4.52	2.29 ± 2.18	50.05 ± 1.92	148.62 ± 1.95	3.24 ± 2.1
H452	1.36	0.19	0.95	—	574.43 ± 6.58	0.0 ± 4.56	1.39 ± 3.55	20.72 ± 3.59	73.94 ± 3.57	0.63 ± 5.13
H452	10.0	0.63	0.61	—	1248.28 ± 10.34	0.0 ± 6.27	0.0 ± 4.53	65.35 ± 3.21	209.46 ± 3.11	5.62 ± 3.11
H459	0.08	0.44	0.34	—	814.7 ± 5.56	4.32 ± 2.96	0.0 ± 2.2	11.88 ± 1.8	29.74 ± 1.78	3.15 ± 4.4
H459	10.0	0.85	0.23	—	786.55 ± 35.19	20.26 ± 21.1	0.0 ± 15.49	0.0 ± 15.14	0.0 ± 15.17	0.0 ± 14.75
H46	1.45	0.12	0.74	—	500.85 ± 3.79	2.02 ± 2.11	0.0 ± 1.69	1.67 ± 1.68	9.81 ± 1.6	5.53 ± 2.73
H460	0.11	0.39	0.46	3.82	3171.45 ± 31.49	107.83 ± 16.55	9.42 ± 11.55	824.77 ± 10.34	1982.28 ± 12.58	28.34 ± 13.63
H460	10.0	0.0	1.32	—	0.0 ± 0.0	0.0 ± 0.0	1.53 ± 0.77	24.66 ± 0.94	70.98 ± 0.99	0.0 ± 0.0
H460	10.0	0.0	0.07	—	0.0 ± 0.0	0.0 ± 0.0	7.37 ± 2.67	106.91 ± 2.89	318.36 ± 3.03	0.0 ± 0.0
H460	10.0	0.0	0.91	—	0.0 ± 0.0	0.0 ± 0.0	4.23 ± 1.37	158.6 ± 1.49	471.97 ± 1.55	0.0 ± 0.0
H465	2.4	0.55	1.05	-0.03	609.16 ± 6.73	10.89 ± 4.34	4.41 ± 3.09	0.0 ± 2.58	10.03 ± 2.54	1.59 ± 2.88
H466	1.26	0.23	1.3	-0.41	1042.05 ± 3.12	5.43 ± 1.31	2.65 ± 0.87	82.38 ± 1.04	177.38 ± 1.11	1.6 ± 1.1
H467	0.61	0.23	1.2	1.18	1228.41 ± 3.49	3.4 ± 1.3	0.96 ± 0.99	51.38 ± 1.02	123.95 ± 1.03	0.0 ± 8.16
H468	1.23	0.06	1.16	1.32	800.0 ± 2.67	4.86 ± 1.7	3.76 ± 0.99	25.67 ± 0.86	64.91 ± 0.89	1.32 ± 0.91
H469	2.22	0.1	1.2	1.28	2013.05 ± 4.71	13.1 ± 1.36	0.0 ± 1.22	189.03 ± 1.56	596.36 ± 1.49	4.9 ± 1.23
H47	0.78	0.4	0.97	1.2	16470.27 ± 60.04	183.13 ± 32.28	43.83 ± 20.17	2093.15 ± 17.99	5625.53 ± 21.68	10.51 ± 19.04
H470	-0.1	2.46	0.33	0.01	119072.23 ± 11270.71	0.0 ± 5659.15	0.0 ± 2593.08	0.0 ± 1258.21	1894.44 ± 358.79	828.64 ± 103.68
H473	2.13	0.69	0.74	1.21	2698.7 ± 9.61	63.98 ± 4.92	0.0 ± 3.11	323.04 ± 3.05	982.46 ± 3.36	7.35 ± 2.73
H475	1.91	0.2	1.08	—	263.82 ± 2.39	1.61 ± 1.41	1.37 ± 1.06	2.34 ± 0.95	1.76 ± 0.95	0.0 ± 2.13
H476	6.13	0.0	12.84	—	380.24 ± 1.51	0.62 ± 0.61	1.03 ± 0.48	1.9 ± 0.51	5.01 ± 0.51	0.0 ± 9.4
H477	1.17	0.46	0.71	—	337.67 ± 3.43	1.14 ± 1.72	3.51 ± 1.21	3.7 ± 1.09	8.71 ± 1.12	0.0 ± 2.16
H478	1.12	0.53	0.67	—	11514.38 ± 21.95	729.12 ± 7.05	25.62 ± 4.52	3611.23 ± 7.11	10748.36 ± 6.86	23.25 ± 2.93
H48	1.69	0.22	1.83	0.0	273.23 ± 4.17	0.0 ± 2.84	0.05 ± 2.06	1.71 ± 1.6	5.28 ± 1.68	1.05 ± 4.97
H482	0.42	0.3	1.15	—	62.74 ± 1.18	0.0 ± 0.65	0.0 ± 0.48	1.55 ± 0.52	4.45 ± 0.48	1.01 ± 1.16
H483	0.32	0.3	1.82	—	167.78 ± 2.93	1.42 ± 1.54	1.11 ± 1.13	0.0 ± 0.98	0.39 ± 1.0	0.69 ± 1.92
H490	0.69	0.43	0.7	—	444.01 ± 4.15	8.96 ± 2.36	2.15 ± 1.52	9.1 ± 1.26	31.14 ± 1.41	1.11 ± 2.3
H497	10.0	0.0	0.75	0.85	0.0 ± 0.0	0.0 ± 0.0	1.33 ± 0.61	0.13 ± 0.66	0.52 ± 0.67	23.09 ± 1.35
H497	-2.0	0.0	56.44	4.69	0.0 ± 0.0	0.0 ± 0.9	0.0 ± 0.77	0.75 ± 0.79	1.1 ± 0.74	1.8 ± 3.8
H5	0.95	0.12	1.18	0.55	1907.02 ± 5.47	13.4 ± 3.54	0.86 ± 1.87	136.82 ± 1.96	389.0 ± 2.1	1.47 ± 2.47
H50	0.96	0.0	0.23	1.3	535.61 ± 2.02	1.42 ± 1.05	2.77 ± 0.75	13.49 ± 0.68	41.11 ± 0.73	5.98 ± 0.74
H509	3.84	0.73	0.64	0.0	0.0 ± 0.0	0.0 ± 0.0	0.0 ± 2.15	18.84 ± 1.76	59.25 ± 1.88	0.39 ± 1.13
H510	10.0	0.13	0.33	1.16	426.94 ± 2.29	4.0 ± 0.8	0.26 ± 0.7	11.4 ± 0.66	30.52 ± 0.7	16.92 ± 3.26
H511	10.0	0.46	0.02	0.75	1675.26 ± 7.2	1.62 ± 3.76	3.6 ± 2.78	30.42 ± 3.02	101.34 ± 2.93	1.24 ± 1.25
H512	10.0	0.0	0.04	1.17	1272.85 ± 3.22	3.33 ± 1.2	0.0 ± 0.87	43.25 ± 1.01	116.16 ± 1.01	49.13 ± 0.34
H515	1.31	0.17	0.91	1.26	725.61 ± 5.97	32.41 ± 4.52	8.06 ± 2.65	200.42 ± 2.56	613.81 ± 2.55	1.37 ± 3.19
H515	0.61	0.0	1.15	1.04	694.06 ± 2.21	3.52 ± 0.98	0.02 ± 0.66	21.64 ± 0.67	74.93 ± 0.72	2.94 ± 0.84
H517	3.78	0.0	0.21	0.93	58.52 ± 1.13	0.0 ± 0.71	0.0 ± 0.56	0.42 ± 0.52	0.4 ± 0.54	2.41 ± 0.39
H521	0.64	0.3	1.04	0.38	1191.07 ± 3.36	2.05 ± 1.22	1.85 ± 0.9	7.82 ± 0.85	22.02 ± 0.86	2.62 ± 0.94
H523	4.15	0.0	1.2	0.92	0.0 ± 2.12	0.0 ± 1.27	0.0 ± 0.93	0.0 ± 0.96	0.0 ± 1.04	0.0 ± 1.09
H524	10.0	3.0	0.0	0.04	2409902.0 ± 36351.58	7525.3 ± 10533.03	0.0 ± 3765.62	26186.62 ± 1111.68	29848.5 ± 1080.98	547898.94 ± 82.04
H525	1.96	0.02	1.2	0.45	244.64 ± 3.01	86.96 ± 1.94	7.98 ± 1.5	277.59 ± 2.09	777.98 ± 2.38	1.32 ± 2.05
H526	5.66	0.19	1.38	0.79	144.83 ± 2.48	4.38 ± 1.23	0.0 ± 1.01	17.49 ± 0.99	54.57 ± 1.08	0.17 ± 1.66
H527	10.0	0.5	-11.16	-1.73	0.0 ± 7.35	0.95 ± 4.69	0.0 ± 4.05	6.45 ± 3.39	3.55 ± 2.14	0.0 ± 4.4
H53	1.93	0.22	0.52	1.54	3078.92 ± 18.85	1655.62 ± 11.22	132.42 ± 7.57	6670.71 ± 10.18	20377.72 ± 14.4	4408.15 ± 1230.67
H540	0.69	0.21	0.09	1.17	194.97 ± 2.6	21.68 ± 1.4	0.0 ± 0.95	80.35 ± 1.13	270.67 ± 1.35	0.0 ± 0.45

Continued on Next Page...

Chart A.1 – Continued

Object name	EW	c(Hβ)	$f_{\text{Red900/5500}}$	$f_{\text{Red400/8500}}$	[O II] $\lambda 3727$ Å $[F_\lambda]$	[Ne III] $\lambda 3869$ Å $[F_\lambda]$	[O III] $\lambda 4363$ Å $[F_\lambda]$	[O III] $\lambda 4959$ Å $[F_\lambda]$	[O III] $\lambda 5007$ Å $[F_\lambda]$	[N II] $\lambda 5755$ Å $[F_\lambda]$
H542	0.69	0.0	2286.54	1.11	103.24 ± 1.21	0.15 ± 0.7	0.01 ± 0.54	1.09 ± 0.56	3.2 ± 0.56	0.1 ± 385.17
H543	10.0	0.5	0.92	0.68	268.78 ± 4.17	11.84 ± 2.46	0.0 ± 2.06	11.46 ± 1.63	39.01 ± 1.69	0.47 ± 1.09
H545	10.0	0.0	4.02	—	41.14 ± 0.95	0.28 ± 0.48	0.21 ± 0.38	2.75 ± 0.36	10.23 ± 0.39	0.02 ± 1.21
H549	4.48	0.06	1.59	—	323.98 ± 2.12	3.38 ± 1.14	0.17 ± 0.92	21.48 ± 0.91	61.23 ± 0.96	2.42 ± 1.5
H55	10.0	0.0	1.01	1.6	428.8 ± 8.28	0.0 ± 4.35	0.61 ± 3.79	30.7 ± 3.57	89.16 ± 3.76	4.9 ± 5.2
H55	3.44	0.0	0.51	1.28	2234.76 ± 21.1	208.49 ± 15.3	15.63 ± 11.96	723.61 ± 10.66	2026.25 ± 11.06	7.55 ± 15.22
H551	1.0	0.2	38.39	48.48	61.09 ± 2.63	0.0 ± 1.47	0.0 ± 1.59	0.14 ± 0.49	1.74 ± 1.02	0.05 ± 1.22
H552	1.32	0.4	2.24	0.52	188.6 ± 3.28	0.0 ± 1.66	0.89 ± 1.32	10.35 ± 1.12	27.77 ± 1.15	0.0 ± 4.35
H552	10.0	0.58	0.25	0.11	532.36 ± 16.61	0.0 ± 11.35	1.8 ± 6.89	4.69 ± 5.52	25.81 ± 5.42	0.0 ± 24.59
H553	10.0	0.33	12.03	1.15	9.94 ± 1.8	0.0 ± 1.05	0.77 ± 0.73	11.07 ± 0.7	22.54 ± 0.78	0.73 ± 42.27
H554	1.0	0.0	2.81	1.9	76.41 ± 1.7	1.11 ± 0.97	0.21 ± 0.83	16.05 ± 0.85	45.82 ± 1.03	1.37 ± 2.13
H558	10.0	0.07	1.69	0.24	82.87 ± 4.27	1.93 ± 2.84	0.0 ± 2.24	30.6 ± 2.4	90.8 ± 2.34	1.63 ± 5.67
H558	7.79	0.0	1.3	0.15	101.54 ± 1.79	1.49 ± 1.02	0.39 ± 0.89	18.52 ± 0.94	52.95 ± 0.99	0.0 ± 1.57
H559	10.0	1.57	0.59	0.65	2277.68 ± 99.92	0.0 ± 51.43	0.0 ± 27.73	0.0 ± 15.36	0.0 ± 15.46	0.0 ± 22.01
H56	1.63	0.6	1.1	-2.56	6269.81 ± 51.89	68.66 ± 32.35	90.55 ± 22.87	90.53 ± 17.15	229.4 ± 17.17	70.81 ± 20.55
H565	0.37	3.0	-0.15	-0.19	83405.62 ± 14712.38	0.0 ± 8098.38	0.0 ± 2411.88	0.0 ± 633.53	0.0 ± 617.77	459.85 ± 287.71
H565	10.0	0.0	-0.0	-0.38	0.0 ± 2.47	0.0 ± 1.8	0.0 ± 1.66	0.0 ± 2.02	2.64 ± 2.02	0.0 ± 1.81
H565	5.09	0.0	-3.53	-4.09	0.0 ± 0.95	0.15 ± 0.6	0.7 ± 0.48	0.0 ± 0.49	0.0 ± 0.48	0.0 ± 1.39
H57	1.46	0.31	0.9	0.01	5831.99 ± 12.15	85.82 ± 6.32	15.46 ± 2.61	1042.38 ± 3.06	3087.05 ± 3.02	8.1 ± 1.85
H576	3.16	0.05	1.27	0.43	191.45 ± 4.63	9.54 ± 2.68	0.0 ± 2.23	49.86 ± 2.19	146.31 ± 2.35	2.83 ± 6.34
H576	2.65	0.0	1.1	0.61	144.74 ± 3.14	4.77 ± 1.69	0.68 ± 1.46	26.45 ± 1.53	74.57 ± 1.65	0.96 ± 3.98
H577	1.93	3.0	1.35	0.58	404068.22 ± 21141.04	44211.12 ± 13542.11	5637.22 ± 3293.22	2172.22 ± 930.2	6302.27 ± 779.94	506.13 ± 530.53
H58	1.42	0.0	0.72	—	1957.63 ± 10.19	15.04 ± 4.81	0.0 ± 3.53	88.24 ± 2.95	238.66 ± 2.95	2.78 ± 2.3
H580	2.15	0.16	1.2	-0.03	265.6 ± 3.02	3.81 ± 1.96	3.84 ± 1.47	23.78 ± 1.36	63.79 ± 1.39	0.0 ± 3.28
H582	1.87	0.0	0.78	1.07	13.38 ± 2.86	0.31 ± 1.72	0.03 ± 1.35	0.0 ± 1.25	0.0 ± 1.31	0.15 ± 1.23
H585	10.0	0.0	33.96	20.28	0.0 ± 8.28	0.0 ± 6.23	5.39 ± 4.64	1.12 ± 4.37	0.0 ± 4.35	0.57 ± 10.94
H585	0.76	0.32	1.01	1.1	378.93 ± 8.47	1.79 ± 5.05	4.1 ± 3.39	6.96 ± 2.89	11.73 ± 2.89	0.15 ± 4.31
H585	1.72	1.04	0.75	0.5	892.61 ± 213.11	0.0 ± 142.41	363.06 ± 108.64	0.0 ± 68.7	0.0 ± 59.84	0.0 ± 72.2
H586	5.61	3.0	0.27	0.46	500383.25 ± 13488.23	0.0 ± 6510.95	0.0 ± 2109.81	3628.26 ± 639.86	6235.53 ± 624.29	717.81 ± 239.37
H587	10.0	0.5	0.35	0.01	157.48 ± 3.64	2.28 ± 1.96	3.02 ± 1.47	3.0 ± 1.25	2.19 ± 1.29	0.0 ± 1.17
H589	1.61	1.07	1.67	1.15	712.66 ± 40.13	0.0 ± 27.44	0.0 ± 15.33	2.04 ± 9.88	28.58 ± 9.78	11.67 ± 11.16
H59	10.0	3.0	0.01	0.06	26264688.0 ± 54829.0	76995.05 ± 13806.86	4225.87 ± 3547.54	273329.69 ± 7931.56	122078.43 ± 110547.89	141538.11 ± 564.97
H593	1.79	0.86	22.63	—	10443.13 ± 30.68	259.49 ± 12.57	6.51 ± 6.12	1995.4 ± 8.25	6295.6 ± 8.47	0.0 ± 30.23
H593	-1.19	0.5	2.86	0.01	7292.7 ± 11.75	80.22 ± 3.97	0.0 ± 2.45	601.57 ± 3.51	1669.91 ± 3.11	32.01 ± 21.65
H596	1.63	0.67	0.77	0.92	1004.43 ± 14.45	27.38 ± 12.6	28.42 ± 6.6	1.15 ± 4.54	0.28 ± 4.36	7.81 ± 5.66
H597	5.23	0.31	0.05	1.13	279.33 ± 3.89	12.2 ± 1.59	0.38 ± 1.16	54.5 ± 1.1	163.62 ± 1.33	40.78 ± 1.14
H598	9.0	2.32	0.65	1.31	12674.76 ± 1223.8	0.0 ± 678.65	257.79 ± 231.46	0.0 ± 95.66	417.64 ± 91.83	335.59 ± 142.85
H598	3.76	1.02	0.97	1.64	460.2 ± 21.5	3.16 ± 12.68	2.54 ± 6.72	0.0 ± 4.92	2.27 ± 4.96	0.0 ± 6.95
H598	1.67	0.0	0.77	0.7	0.0 ± 3.8	0.0 ± 3.07	0.0 ± 3.06	1.74 ± 2.71	0.0 ± 2.7	0.0 ± 2.77
H598	10.0	3.0	0.42	1.15	107633.45 ± 11411.04	0.0 ± 5694.45	0.0 ± 1676.34	0.0 ± 509.39	1273.38 ± 468.95	944.94 ± 406.4
H599	10.0	0.0	0.23	0.32	0.0 ± 1.88	0.0 ± 1.14	0.0 ± 0.85	0.0 ± 0.85	0.0 ± 0.94	7.71 ± 1.93
H599	0.62	1.2	0.52	1.05	450.55 ± 40.37	3.76 ± 23.59	7.02 ± 12.35	9.98 ± 7.65	19.65 ± 7.47	0.0 ± 6.93
H6	-1.06	0.27	1.08	0.6	587.22 ± 4.35	3.76 ± 2.35	0.91 ± 1.64	43.4 ± 1.64	131.43 ± 1.77	2.19 ± 12.52
H60	10.0	0.83	1.84	0.81	7759.4 ± 24.11	27.67 ± 7.01	0.0 ± 4.57	216.34 ± 4.48	656.17 ± 4.78	15.14 ± 13.86
H601	1.61	0.55	0.92	1.09	145.41 ± 14.84	0.0 ± 9.22	11.94 ± 5.96	3.46 ± 5.13	3.93 ± 4.84	4.0 ± 4.72
H601	2.29	0.0	1.93	3.67	2.59 ± 1.16	0.0 ± 0.67	0.0 ± 0.59	0.0 ± 0.61	0.16 ± 0.57	1.71 ± 1.45

Chart A.1 – Continued

Object name	EW	c(Hβ)	$f_{Red900/5500}$	$f_{Red400/8500}$	[O II] λ3727 Å [F_λ]	[Ne III] λ3869 Å [F_λ]	[O III] λ4363 Å [F_λ]	[O III] λ4959 Å [F_λ]	[O III] λ5007 Å [F_λ]	[N II] λ5755 Å [F_λ]
H606	10.0	3.0	−7.48	−9.37	0.0 ± 7958.4	0.0 ± 4263.58	0.0 ± 1137.48	0.0 ± 344.59	0.0 ± 331.74	0.0 ± 357.24
H612	2.65	0.29	0.66	0.94	367.21 ± 2.26	0.46 ± 1.06	1.31 ± 0.68	0.54 ± 0.61	4.35 ± 0.65	0.0 ± 0.7
H614	1.72	0.63	1.07	0.9	8529.55 ± 22.1	52.55 ± 8.33	18.06 ± 4.47	528.98 ± 5.38	1285.73 ± 5.54	13.9 ± 3.15
H62	1.06	0.94	0.77	0.88	82951.02 ± 187.06	1273.19 ± 100.25	227.82 ± 44.0	6028.25 ± 34.68	15781.86 ± 35.91	214.37 ± 43.59
H621	0.96	0.6	0.68	−0.12	2925.95 ± 8.31	176.3 ± 4.27	18.48 ± 1.92	273.73 ± 1.76	1259.4 ± 2.37	5.84 ± 1.64
H627	1.3	1.16	0.39	0.46	17555.15 ± 47.18	177.3 ± 15.17	32.33 ± 7.6	409.94 ± 4.92	769.2 ± 7.29	10.18 ± 4.74
H63	1.42	0.19	0.74	0.72	2009.68 ± 4.87	7.9 ± 2.27	2.53 ± 1.35	56.96 ± 1.31	159.46 ± 1.31	2.51 ± 0.89
H63	1.67	0.15	1.9	0.93	1748.1 ± 4.26	8.22 ± 2.07	2.9 ± 1.11	41.66 ± 1.02	129.0 ± 1.08	1.21 ± 1.27
H63	0.99	0.53	1.46	0.4	7369.41 ± 51.21	0.0 ± 29.09	65.95 ± 19.13	646.02 ± 14.13	1829.96 ± 14.26	22.13 ± 54.22
H631	10.0	0.27	1.09	1.22	238.19 ± 1.81	0.96 ± 0.93	0.64 ± 0.68	19.55 ± 0.7	60.73 ± 0.73	0.0 ± 0.86
H64	1.91	0.0	1.18	1.0	1586.3 ± 2.83	4.66 ± 1.25	2.37 ± 0.9	68.94 ± 1.05	198.99 ± 0.94	3.56 ± 0.87
H643	1.41	0.2	0.51	1.27	895.18 ± 4.35	1.71 ± 2.04	0.0 ± 1.61	22.82 ± 1.53	67.9 ± 1.59	4.05 ± 1.86
H644	0.9	0.3	0.84	0.67	1945.07 ± 7.7	3.58 ± 4.07	8.26 ± 2.86	165.3 ± 2.53	408.98 ± 2.95	0.21 ± 4.22
H645	1.52	0.48	1.1	0.85	1193.05 ± 9.35	11.83 ± 4.97	6.39 ± 3.64	84.78 ± 3.09	220.83 ± 3.08	0.0 ± 6.32
H646	1.16	0.25	0.87	0.8	2339.5 ± 8.5	34.17 ± 5.74	20.21 ± 3.57	166.0 ± 2.67	495.23 ± 2.82	6.42 ± 4.38
H647	1.56	0.2	1.1	0.86	3126.49 ± 9.31	100.56 ± 4.14	8.84 ± 3.12	788.81 ± 4.34	2641.87 ± 4.78	5.95 ± 3.66
H649	0.28	0.0	0.52	0.24	265.03 ± 2.41	0.0 ± 1.26	0.12 ± 0.94	0.99 ± 1.0	2.94 ± 1.03	0.0 ± 1.48
H65	1.35	0.19	0.79	0.84	2688.42 ± 5.92	20.1 ± 3.35	9.12 ± 1.63	177.01 ± 1.51	518.28 ± 1.66	4.41 ± 0.87
H65	0.82	0.83	1.34	1.43	31114.99 ± 184.94	18.22 ± 99.28	46.51 ± 63.54	1374.13 ± 43.49	3515.87 ± 48.56	40.42 ± 68.03
H650	0.91	0.14	1.01	0.17	587.13 ± 6.99	8.91 ± 3.32	3.58 ± 2.53	238.9 ± 2.76	705.52 ± 3.44	0.89 ± 3.67
H655	2.14	0.41	0.81	1.43	231.59 ± 7.68	5.32 ± 4.11	3.97 ± 3.0	6.58 ± 2.39	15.89 ± 2.37	0.8 ± 2.6
H656	−1.38	2.22	0.28	0.0	0.0 ± 0.0	0.0 ± 0.0	449.82 ± 480.57	539.63 ± 194.71	1089.17 ± 174.01	0.0 ± 0.0
H657	2.75	0.49	0.76	1.19	2249.83 ± 5.01	24.23 ± 1.78	2.18 ± 1.19	160.47 ± 1.41	458.47 ± 1.51	1.66 ± 0.88
H659	1.15	0.17	0.94	0.9	1576.16 ± 3.2	32.89 ± 1.55	5.91 ± 0.82	294.6 ± 1.1	761.76 ± 1.34	1.22 ± 0.86
H66	2.33	0.41	1.27	0.57	250.95 ± 2.95	0.0 ± 1.8	0.0 ± 1.31	20.75 ± 1.42	63.46 ± 1.35	2.57 ± 2.05
H662	10.0	0.0	0.69	0.99	732.98 ± 1.62	11.06 ± 0.65	1.61 ± 0.49	54.17 ± 0.51	149.76 ± 0.52	1.56 ± 0.47
H664	4.15	0.2	1.32	0.95	512.3 ± 4.03	1.75 ± 2.01	0.0 ± 1.52	9.37 ± 1.45	26.16 ± 1.47	0.6 ± 2.58
H666	−0.17	0.98	0.77	0.72	104770.36 ± 247.98	2457.76 ± 72.28	0.0 ± 737.0	15693.73 ± 106.97	42870.12 ± 93.11	207.89 ± 13.79
H666	1.48	0.61	0.75	0.07	10887.63 ± 34.5	289.64 ± 11.59	0.0 ± 9.3	1860.13 ± 16.49	5130.43 ± 15.88	40.21 ± 9.04
H67	1.32	0.22	1.31	0.22	1576.38 ± 4.27	34.59 ± 1.84	2.87 ± 1.16	272.1 ± 1.55	540.17 ± 1.73	4.74 ± 2.42
H670	0.73	0.4	0.87	1.26	2834.01 ± 6.67	10.05 ± 2.6	2.29 ± 1.98	93.78 ± 1.7	247.08 ± 1.79	5.67 ± 1.68
H672	2.96	0.14	1.12	0.84	2891.93 ± 3.89	20.53 ± 2.27	13.09 ± 1.16	545.6 ± 1.55	1674.22 ± 1.85	3.36 ± 1.6
H673	−0.27	0.17	1.95	1.68	16244.43 ± 19.81	269.88 ± 7.96	0.0 ± 166.34	1153.69 ± 293.37	3063.71 ± 254.98	20.13 ± 3.75
H676	3.47	0.21	1.55	0.96	3914.69 ± 5.79	11.38 ± 1.76	0.0 ± 1.19	143.91 ± 1.52	449.92 ± 1.3	3.55 ± 1.52
H678	3.31	0.57	1.52	1.22	12590.71 ± 24.53	696.75 ± 7.19	19.83 ± 4.67	4548.08 ± 12.26	14014.48 ± 11.6	10.23 ± 1.76
H679	1.0	0.86	0.71	0.83	2521.4 ± 17.76	14.11 ± 14.35	30.31 ± 5.77	24.43 ± 3.41	62.05 ± 3.37	15.94 ± 3.98
H679	1.3	0.67	27.31	0.83	1689.14 ± 9.93	7.23 ± 6.77	6.67 ± 3.44	9.39 ± 2.31	27.19 ± 2.24	0.0 ± 32.28
H680	2.62	0.49	0.75	0.76	2661.67 ± 8.67	28.31 ± 3.06	0.0 ± 2.15	517.41 ± 2.76	1601.18 ± 3.14	6.13 ± 2.36
H681	0.03	1.04	0.65	−0.01	17168.64 ± 42.51	116.47 ± 17.26	7.79 ± 9.43	392.26 ± 6.8	855.94 ± 7.14	16.69 ± 5.37
H682	1.47	0.47	1.1	2.0	2062.72 ± 4.96	6.59 ± 2.3	5.21 ± 1.2	53.57 ± 1.18	130.93 ± 1.2	4.59 ± 1.94
H682	2.51	0.52	0.74	1.06	3148.84 ± 7.5	6.11 ± 3.39	1.2 ± 1.87	75.33 ± 1.67	203.05 ± 1.65	10.34 ± 1.98
H685	5.14	0.36	1.24	0.61	201.93 ± 2.29	0.0 ± 1.13	0.0 ± 0.84	0.0 ± 0.79	1.3 ± 0.77	1.4 ± 1.3
H686	2.22	0.37	0.95	1.05	9682.7 ± 16.7	109.64 ± 4.79	0.0 ± 3.54	1147.67 ± 6.25	3593.88 ± 5.01	19.22 ± 2.0
H688	2.59	0.57	1.55	0.83	1719.74 ± 7.33	22.63 ± 3.76	1.17 ± 2.21	253.27 ± 2.14	779.31 ± 2.42	1.23 ± 1.92
H689	1.37	0.3	0.89	0.93	1109.55 ± 3.53	5.7 ± 2.32	4.99 ± 1.19	27.28 ± 1.06	82.29 ± 1.17	0.83 ± 1.75
H69	2.9	0.0	1.94	1.35	4295.96 ± 12.53	721.97 ± 6.98	67.84 ± 5.18	2336.81 ± 7.23	6359.08 ± 8.82	0.0 ± 0.0

Chart A.1 – Continued

Object name	EW	c(Hβ)	$f_{Red900/5500}$	$f_{Red400/8500}$	[O II] λ3727 Å [F_λ]	[Ne III] λ3869 Å [F_λ]	[O III] λ4363 Å [F_λ]	[O III] λ4959 Å [F_λ]	[O III] λ5007 Å [F_λ]	[N II] λ5755 Å [F_λ]
H690	2.31	0.43	0.46	0.0	554.3 ± 4.52	164.95 ± 3.09	9.93 ± 1.74	486.63 ± 1.63	1666.83 ± 2.32	6.69 ± 1.86
H691	1.67	0.76	0.52	0.51	13002.33 ± 72.84	121.44 ± 37.6	0.0 ± 21.39	2999.53 ± 348.39	7312.4 ± 266.44	85.69 ± 28.63
H692	0.56	0.54	0.93	0.86	1647.19 ± 14.26	0.0 ± 8.13	5.91 ± 5.12	31.24 ± 4.44	102.27 ± 4.51	0.0 ± 4.14
H694	4.79	0.8	0.15	0.24	888.02 ± 18.78	11.42 ± 9.91	0.33 ± 6.46	26.82 ± 4.48	75.0 ± 4.84	367.68 ± 75.96
H695	0.83	0.1	1.27	1.15	638.35 ± 2.23	20.75 ± 0.88	0.0 ± 0.74	158.56 ± 0.95	507.75 ± 1.05	2.02 ± 3.08
H696	10.0	0.2	0.56	0.93	1269.58 ± 3.61	35.03 ± 1.35	0.89 ± 1.04	278.4 ± 1.28	849.47 ± 1.44	2.96 ± 0.89
H696	2.23	0.58	0.93	1.06	1159.11 ± 8.71	42.23 ± 6.05	17.9 ± 3.87	264.29 ± 2.83	843.44 ± 3.08	0.0 ± 2.91
H697	0.91	0.14	1.0	1.45	723.4 ± 3.46	6.9 ± 2.17	8.0 ± 1.57	60.53 ± 1.53	179.61 ± 1.56	0.0 ± 1.66
H7	1.01	0.76	0.79	0.7	3315.31 ± 32.08	44.21 ± 23.01	50.73 ± 11.3	30.31 ± 8.32	163.86 ± 8.3	19.47 ± 7.54
H700	0.36	0.48	1.07	0.5	929.88 ± 7.52	129.09 ± 4.24	4.54 ± 2.76	380.03 ± 3.44	1131.3 ± 3.69	0.67 ± 3.36
H701	2.59	0.25	0.79	0.65	2574.25 ± 6.27	74.09 ± 2.95	2.07 ± 1.37	347.59 ± 1.9	1045.36 ± 1.71	6.02 ± 1.1
H71	-1.85	0.73	1.05	2.97	6774.88 ± 19.89	310.96 ± 9.51	30.93 ± 3.6	1163.35 ± 5.34	4475.06 ± 6.72	19.17 ± 2.01
H712	1.56	0.0	2.9	3.56	0.0 ± 0.0	52.36 ± 10.94	34.3 ± 6.7	243.38 ± 4.78	759.24 ± 5.09	0.0 ± 0.0
H713	5.4	0.37	0.64	0.01	6216.52 ± 11.61	181.76 ± 3.61	8.53 ± 2.17	1671.77 ± 4.8	4959.04 ± 3.98	15.04 ± 2.18
H714	2.59	0.73	-0.03	0.01	1409.26 ± 9.88	14.24 ± 5.43	5.51 ± 3.29	77.46 ± 2.28	225.01 ± 2.38	0.0 ± 1.96
H715	1.2	0.48	1.06	0.96	1868.28 ± 5.59	23.45 ± 2.69	2.97 ± 1.39	216.28 ± 1.5	652.6 ± 1.61	1.51 ± 1.38
H716	0.57	0.46	1.29	1.31	1277.67 ± 5.58	7.48 ± 2.56	3.31 ± 1.69	40.77 ± 1.41	94.06 ± 1.47	3.16 ± 1.51
H72	1.42	0.42	0.97	0.3	771.35 ± 3.51	0.53 ± 2.38	4.11 ± 1.41	6.76 ± 1.14	21.95 ± 1.05	0.51 ± 0.87
H72	10.0	1.59	0.6	0.02	8590.25 ± 32.3	18049.99 ± 521.51	1219.53 ± 222.07	170655.08 ± 404.49	514101.78 ± 465.35	878.04 ± 96.85
H720	1.21	0.8	0.94	0.01	1856.35 ± 4.98	610.26 ± 9.29	35.39 ± 5.45	2849.79 ± 22.53	7178.06 ± 21.41	26.03 ± 2.55
H721	1.34	0.17	0.92	0.94	837.47 ± 4.48	10.26 ± 1.83	0.0 ± 1.28	98.66 ± 1.39	278.69 ± 1.12	1.1 ± 1.21
H726	1.27	0.01	0.5	0.01	2153.37 ± 5.88	20.99 ± 1.35	0.0 ± 1.29	124.91 ± 1.77	357.14 ± 1.39	0.0 ± 0.0
H727	0.9	0.4	0.78	0.93	2269.24 ± 6.62	7.44 ± 2.32	0.0 ± 1.8	78.77 ± 1.51	247.06 ± 1.5	0.01 ± 1.49
H727	5.8	0.43	0.69	0.89	2255.2 ± 4.88	12.2 ± 2.43	2.03 ± 1.63	156.33 ± 1.56	380.77 ± 1.64	3.01 ± 1.57
H728	2.41	0.5	1.33	0.86	4056.01 ± 6.86	11.31 ± 2.48	4.23 ± 1.83	144.93 ± 1.81	428.8 ± 1.93	6.33 ± 1.81
H728	1.3	0.24	0.99	0.95	788.61 ± 5.56	65.86 ± 1.78	4.09 ± 0.85	536.32 ± 2.1	1633.25 ± 2.13	4.64 ± 0.99
H729	0.32	0.31	1.08	0.55	308265.91 ± 31176.36	99.59 ± 2.62	8.92 ± 1.17	608.95 ± 1.97	2011.11 ± 1.94	4.9 ± 1.12
H73	1.13	0.57	0.57	0.91	1178.6 ± 9.39	0.0 ± 2.95	1.11 ± 2.12	68.4 ± 1.79	206.61 ± 1.95	0.0 ± 4.59
H73	10.0	2.73	0.88	-0.28	0.0 ± 0.0	28532.89 ± 13547.12	0.0 ± 5503.26	160774.2 ± 1813.89	485618.16 ± 2411.88	418.24 ± 1420.95
H730	-0.28	0.65	1.43	1.12	693.67 ± 6.49	33.26 ± 4.66	0.0 ± 3.09	351.19 ± 3.88	964.37 ± 4.23	5.85 ± 2.62
H730	2.04	1.21	0.27	0.01	2075.28 ± 8.11	1.99 ± 12.22	0.0 ± 6.57	78.44 ± 4.45	211.36 ± 4.41	0.0 ± 0.0
H732	2.28	0.73	1.34	0.7	3703.67 ± 9.03	0.0 ± 3.53	0.0 ± 2.32	28.65 ± 1.7	73.56 ± 1.75	1.08 ± 2.54
H733	0.16	0.69	1.13	1.15	2925.93 ± 6.09	20.89 ± 3.41	3.28 ± 2.3	196.12 ± 2.2	571.08 ± 2.38	237.34 ± 58.66
H735	2.67	0.54	1.61	0.9	376.97 ± 9.66	1.23 ± 2.73	0.0 ± 2.32	103.71 ± 1.82	307.37 ± 1.82	6.19 ± 2.46
H737	1.32	0.37	1.74	-4.27	4283.83 ± 31.3	41.75 ± 1.75	0.06 ± 1.27	403.94 ± 2.39	1328.58 ± 2.35	684.24 ± 415.59
H74	2.05	0.4	1.46	-0.0	0.0 ± 0.0	3.06 ± 8.3	5.93 ± 5.33	5.31 ± 5.15	37.34 ± 4.99	6.69 ± 22.66
H740	-1.31	0.24	0.65	1.88	1553.76 ± 17.22	40.41 ± 16.88	11.48 ± 16.86	693.55 ± 12.34	1706.09 ± 13.76	0.82 ± 17.55
H746	0.64	0.47	0.73	0.45	22651.63 ± 90.24	0.0 ± 0.0	1.3 ± 4.69	15.34 ± 4.67	140.3 ± 3.51	0.0 ± 0.0
H747	1.35	0.52	1.11	0.67	640.71 ± 2.55	5.44 ± 9.26	9.83 ± 6.0	71.36 ± 4.41	71.36 ± 4.41	9.44 ± 4.57
H75	3.01	1.12	1.16	1.91	5193.02 ± 12.14	1678.55 ± 35.76	62.26 ± 23.76	10859.6 ± 52.38	33435.57 ± 51.13	20.41 ± 11.77
H750	5.05	0.37	1.06	0.11	6039.62 ± 10.62	16.42 ± 1.14	0.48 ± 0.98	98.85 ± 1.12	299.52 ± 1.1	2.29 ± 1.36
H750	10.0	0.0	0.91	-0.7	2373.66 ± 7.67	56.76 ± 2.25	0.0 ± 2.92	827.7 ± 5.11	2423.32 ± 4.45	17.89 ± 1.86
H752	2.94	0.08	0.87	0.55	634.09 ± 7.34	103.86 ± 2.33	0.0 ± 3.11	1694.18 ± 6.61	4420.01 ± 6.12	16.46 ± 1.53
H753	1.09	0.51	0.93	1.0	3378.91 ± 18.28	167.46 ± 1.96	2.35 ± 2.4	1341.94 ± 7.97	3771.91 ± 7.62	5.31 ± 2.23
H754	1.67	0.72	0.69	-0.37	—	0.83 ± 3.95	0.0 ± 5.0	30.5 ± 2.13	79.52 ± 2.4	0.25 ± 1.92

Chart A.1 – Continued

Object name	EW	c(Hβ)	$f_{Red900/5500}$	$f_{Red400/8500}$	[O II] λ3727 Å [F_λ]	[Ne II] λ3869 Å [F_λ]	[O III] λ4363 Å [F_λ]	[O III] λ4959 Å [F_λ]	[O III] λ5007 Å [F_λ]	[N II] λ5755 Å [F_λ]
H755	10.0	0.0	0.26	0.68	180.77 ± 3.07	1.52 ± 1.23	0.0 ± 0.87	19.85 ± 0.98	73.42 ± 1.22	0.0 ± 0.47
H757	4.1	0.29	1.0	0.9	244.43 ± 3.39	2.03 ± 1.74	2.23 ± 1.19	0.42 ± 1.11	8.38 ± 1.13	2.84 ± 1.07
H76	10.0	1.39	0.72	0.86	535609.25 ± 2102.06	13284.07 ± 1325.39	24.19 ± 1052.05	111546.42 ± 664.87	324199.56 ± 604.24	1694.81 ± 383.35
H76	5.37	0.67	1.47	1.92	52466.48 ± 154.57	892.29 ± 77.33	52.36 ± 50.75	8966.4 ± 61.5	26035.78 ± 63.11	144.58 ± 46.94
H760	3.58	0.49	0.63	0.01	0.0 ± 0.0	4.72 ± 4.17	1.26 ± 2.7	49.32 ± 2.48	129.92 ± 2.69	0.0 ± 0.0
H763	−2.0	0.43	0.73	0.02	0.0 ± 0.0	46.77 ± 2.88	5.84 ± 1.56	440.85 ± 1.94	1256.97 ± 2.02	0.0 ± 0.0
H766	−2.0	0.0	3.79	4.11	103.99 ± 1.01	0.67 ± 0.51	0.0 ± 0.39	9.68 ± 0.41	10.87 ± 0.44	0.31 ± 0.68
H77	6.06	0.38	1.03	0.71	7395.13 ± 18.22	0.0 ± 9.55	0.0 ± 6.35	85.39 ± 5.78	251.64 ± 5.45	27.3 ± 12.58
H770	10.0	0.0	0.28	0.73	75.96 ± 2.64	0.86 ± 1.43	0.0 ± 0.99	1.67 ± 0.99	4.33 ± 0.96	0.28 ± 0.55
H770	2.3	0.0	0.01	1.26	0.0 ± 6.58	0.0 ± 3.56	0.0 ± 2.61	0.0 ± 2.87	0.0 ± 2.81	0.0 ± 1.74
H772	−2.0	0.57	0.11	0.69	168.45 ± 10.26	1.8 ± 5.87	0.0 ± 3.36	1.54 ± 2.67	0.0 ± 2.7	0.0 ± 1.6
H772	0.73	0.01	0.07	0.99	28.36 ± 3.82	0.0 ± 2.69	0.0 ± 2.05	1.26 ± 2.07	1.39 ± 2.2	0.0 ± 2.06
H774	−2.0	0.49	1.47	0.63	219.98 ± 2.87	0.0 ± 1.51	0.0 ± 1.16	1.42 ± 0.94	4.94 ± 0.92	0.0 ± 2.56
H779	1.96	0.39	1.25	1.06	997.82 ± 6.06	10.61 ± 3.57	4.43 ± 1.96	124.21 ± 1.91	398.13 ± 2.17	0.8 ± 1.7
H78	1.0	0.35	0.93	0.77	4486.37 ± 12.65	221.06 ± 5.5	18.45 ± 2.68	1166.39 ± 3.33	3294.42 ± 3.85	10.18 ± 3.08
H781	1.08	0.48	0.91	0.9	2223.96 ± 7.73	272.1 ± 3.82	23.55 ± 2.3	1310.21 ± 6.65	3865.81 ± 6.66	5.71 ± 2.26
H782	2.67	0.15	0.76	0.71	526.15 ± 2.78	41.86 ± 1.44	4.4 ± 0.97	160.44 ± 1.36	468.39 ± 1.48	1.03 ± 0.95
H783	10.0	0.26	0.92	0.71	194.63 ± 1.92	42.63 ± 1.09	3.47 ± 0.65	145.74 ± 1.0	425.27 ± 1.12	2.47 ± 0.86
H785	2.28	0.02	0.86	0.46	265.38 ± 3.03	3.44 ± 1.98	1.17 ± 1.25	25.35 ± 1.39	90.06 ± 1.41	0.75 ± 1.8
H786	1.64	0.57	1.3	0.7	854.05 ± 13.73	0.0 ± 7.79	0.41 ± 5.0	16.44 ± 3.43	43.85 ± 3.47	1.14 ± 5.09
H787	0.46	0.0	1.04	1.41	1009.38 ± 5.48	56.83 ± 3.14	1.28 ± 1.86	400.1 ± 2.56	1240.13 ± 2.73	0.59 ± 1.55
H787	0.39	0.0	1.3	14.22	634.66 ± 3.97	48.83 ± 2.28	3.67 ± 1.39	308.17 ± 1.98	861.1 ± 2.19	1.53 ± 2.82
H788a	0.32	0.47	0.96	0.76	19648.18 ± 38.43	928.12 ± 11.93	90.58 ± 6.65	6255.75 ± 18.53	19814.23 ± 18.84	25.71 ± 5.81
H79	3.24	0.22	1.6	0.95	520.2 ± 4.88	3.49 ± 2.39	1.83 ± 1.87	3.87 ± 1.62	15.53 ± 1.69	5.41 ± 3.18
H790	0.56	0.4	0.73	0.0	1555.25 ± 8.51	1.69 ± 4.34	1.21 ± 2.8	33.47 ± 2.33	92.41 ± 2.53	9.0 ± 3.57
H791	10.0	2.82	0.19	0.1	3404594.0 ± 28289.04	1086961.75 ± 15375.65	13108.56 ± 3726.58	415110.31 ± 1919.55	1237094.5 ± 2054.82	0.0 ± 765.42
H791	0.57	0.23	0.81	0.79	1092.78 ± 9.65	219.75 ± 6.62	34.06 ± 2.93	319.65 ± 3.77	824.06 ± 4.26	7.04 ± 3.22
H792	3.84	0.38	0.76	0.63	3333.14 ± 13.13	427.27 ± 5.9	25.15 ± 3.71	1796.68 ± 7.04	5521.81 ± 8.6	6.54 ± 3.12
H795	−0.33	0.38	1.02	1.29	15977.87 ± 25.21	111.79 ± 6.13	0.0 ± 5.01	757.42 ± 5.41	1844.02 ± 5.62	15.62 ± 3.13
H796	1.46	0.25	0.74	1.12	453.48 ± 6.8	0.0 ± 4.34	2.79 ± 2.97	3.92 ± 2.37	1.67 ± 2.26	1.79 ± 3.29
H80	−0.16	0.0	2.54	1.42	1673.7 ± 16.67	61.81 ± 6.97	10.67 ± 6.31	563.79 ± 5.52	1655.7 ± 6.39	7.83 ± 9.04
H803	1.72	0.2	0.05	—	3642.79 ± 8.88	75.01 ± 2.23	0.15 ± 2.02	485.28 ± 3.74	1082.18 ± 3.91	0.0 ± 3.3
H803	−2.0	3.0	106.67	0.57	36501.25 ± 14193.17	7614.66 ± 6536.45	1323.75 ± 1715.58	0.0 ± 623.99	0.0 ± 601.06	0.0 ± 951.49
H807	0.43	0.3	0.93	−0.08	5080.43 ± 13.1	251.46 ± 3.9	29.76 ± 1.99	1264.28 ± 6.43	4169.98 ± 8.0	9.54 ± 1.74
H809	0.18	0.1	0.26	0.67	0.0 ± 14.92	80.26 ± 19.24	0.0 ± 9.0	10.27 ± 8.47	0.0 ± 5.09	22.61 ± 12.3
H809	0.94	0.67	1.15	1.19	851.75 ± 4.71	5.48 ± 2.09	1.43 ± 1.68	52.02 ± 1.59	178.6 ± 1.95	2.33 ± 2.29
H81	0.56	0.67	0.99	0.03	5899.52 ± 15.49	54.14 ± 5.58	10.1 ± 3.49	501.53 ± 3.9	1292.01 ± 3.74	11.44 ± 2.83
H811	10.0	1.27	0.96	0.09	70521.29 ± 321.33	5531.81 ± 130.75	270.47 ± 58.59	22905.53 ± 84.88	85845.19 ± 134.52	136.87 ± 156.11
H811	10.0	0.0	1.08	0.01	7050.33 ± 15.38	1322.26 ± 5.52	116.34 ± 4.27	4835.92 ± 21.6	14296.95 ± 20.35	15.49 ± 8.84
H82	10.0	0.0	1.48	—	622.87 ± 1.78	0.0 ± 0.0	0.0 ± 0.6	9.85 ± 0.61	29.16 ± 0.62	1.31 ± 0.8
H822	1.15	0.0	1.13	1.08	367.07 ± 2.7	7.66 ± 1.55	0.04 ± 0.89	95.13 ± 1.0	351.35 ± 1.14	0.0 ± 1.62
H824	1.34	0.16	3910.48	1.03	1519.57 ± 10.75	1.87 ± 6.22	11.0 ± 3.45	10.65 ± 3.18	26.83 ± 3.12	2.46 ± 3.26
H825	1.53	0.45	0.7	0.79	274.13 ± 3.63	0.47 ± 1.59	0.4 ± 1.11	22.06 ± 1.14	70.49 ± 1.21	1.01 ± 1.36
H828	8.74	0.1	0.98	0.6	719.86 ± 3.63	14.6 ± 1.88	0.87 ± 1.17	58.3 ± 1.25	161.57 ± 1.32	1.3 ± 0.94
H83	2.06	0.25	0.74		246.34 ± 15.6	0.0 ± 9.38	9.43 ± 5.59	1.23 ± 4.77	2.0 ± 4.54	7.08 ± 3.69
H830	0.86	0.69	0.67							

Continued on Next Page...

Chart A.1 – Continued

Object name	EW	c(Hβ)	$f_{Red900/5500}$	$f_{Red400/8500}$	[O II] λ3727 Å $[F_\lambda]$	[Ne III] λ3869 Å $[F_\lambda]$	[O III] λ4363 Å $[F_\lambda]$	[O III] λ4959 Å $[F_\lambda]$	[O III] λ5007 Å $[F_\lambda]$	[N II] λ5755 Å $[F_\lambda]$
H831	9.69	1.79	0.27	0.31	4306.25 ± 235.47	0.0 ± 125.21	12.23 ± 50.95	34.77 ± 24.47	3.71 ± 24.24	99.48 ± 27.1
H836	0.74	0.39	1.15	0.79	709.69 ± 6.86	54.38 ± 5.17	2.56 ± 3.52	252.83 ± 3.05	738.55 ± 3.22	0.71 ± 2.34
H837	1.77	0.55	1.11	1.26	158959.27 ± 457.15	4419.02 ± 655.36	0.0 ± 1629.1	28198.82 ± 10663.69	129331.95 ± 7510.36	105.44 ± 6.67
H837	1.45	0.09	1.84	1.67	32749.79 ± 142.37	1406.34 ± 230.85	0.0 ± 605.69	13839.65 ± 3327.47	33763.46 ± 2588.38	27.04 ± 3.74
H843	2.17	0.35	0.97	1.13	28235.88 ± 55.78	1815.96 ± 15.77	98.26 ± 8.17	12093.79 ± 23.32	38298.02 ± 19.55	47.28 ± 2.57
H847	3.64	0.44	0.65	0.0	1465.02 ± 11.86	9.07 ± 4.42	0.0 ± 2.92	72.25 ± 2.95	224.17 ± 3.55	0.0 ± 1.76
H848	1.33	0.29	0.78	0.01	1143.8 ± 5.8	74.21 ± 3.08	7.94 ± 2.14	199.93 ± 2.02	581.68 ± 2.27	0.67 ± 1.63
H850	4.31	0.47	0.81	0.93	1072.73 ± 7.79	8.45 ± 3.81	0.02 ± 2.42	26.97 ± 2.08	74.41 ± 2.09	2.6 ± 1.71
H855	−2.0	0.0	0.86	2.88	1051.52 ± 3.18	28.41 ± 1.01	3.53 ± 0.64	165.43 ± 1.03	465.14 ± 1.34	3.14 ± 0.61
H856	2.16	0.0	1.53	0.15	17.13 ± 1.66	0.52 ± 0.93	1.08 ± 0.81	1.82 ± 0.77	6.97 ± 0.83	0.58 ± 1.35
H859	1.38	0.0	1.35	1.64	5309.07 ± 14.32	37.4 ± 5.54	1.75 ± 3.25	480.02 ± 3.87	1474.74 ± 3.87	7.65 ± 2.75
H86	8.45	0.18	1.08	0.5	29264.21 ± 73.7	1244.87 ± 30.24	446.33 ± 18.68	2428.6 ± 22.19	6814.36 ± 21.01	0.0 ± 1784.5
H860	10.0	0.78	0.5	0.43	3860.02 ± 27.11	12.04 ± 8.87	1.13 ± 5.01	163.0 ± 4.14	528.29 ± 5.53	4.14 ± 2.58
H861	2.58	0.24	1.2	1.16	8026.65 ± 15.88	97.03 ± 4.31	0.0 ± 4.21	800.73 ± 6.1	2183.19 ± 5.8	19.93 ± 3.21
H862	2.42	0.35	1.23	0.42	12377.78 ± 19.1	458.6 ± 6.25	45.22 ± 3.11	2980.72 ± 11.51	8964.42 ± 11.41	15.62 ± 3.07
H864	0.73	0.57	0.88	0.35	4310.05 ± 15.82	6.34 ± 7.66	7.81 ± 5.3	64.9 ± 3.82	198.97 ± 3.89	9.31 ± 5.19
H865	2.93	0.27	1.29	0.42	1754.54 ± 6.87	26.31 ± 2.87	2.87 ± 2.21	224.79 ± 2.4	678.26 ± 2.75	0.0 ± 2.87
H866	9.14	0.02	2.76	3.94	101.52 ± 5.65	0.0 ± 1.83	0.62 ± 1.5	0.0 ± 1.28	0.2 ± 1.26	0.44 ± 1.5
H867	1.26	0.6	1.33	0.16	5004.86 ± 16.8	23.6 ± 6.5	10.24 ± 3.99	199.95 ± 3.17	502.69 ± 3.55	5.6 ± 3.83
H869	0.66	1.12	0.87	0.23	19757.8 ± 74.17	132.09 ± 27.65	5.89 ± 14.64	751.48 ± 11.31	2306.34 ± 12.55	24.15 ± 15.22
H870	0.92	0.15	1.59	0.86	1080.37 ± 4.09	1.73 ± 1.33	0.0 ± 1.03	39.43 ± 1.06	94.69 ± 1.21	1.31 ± 1.63
H872	10.0	0.39	2.37	0.64	730.04 ± 5.08	97.35 ± 2.27	6.4 ± 1.42	302.76 ± 2.25	863.32 ± 3.27	7.89 ± 11.86
H873	2.56	0.02	1.28	0.56	964.07 ± 3.69	19.86 ± 1.62	2.65 ± 1.21	144.76 ± 1.37	449.31 ± 1.58	0.0 ± 1.92
H874	10.0	0.05	1.48	—	3300.67 ± 6.14	111.06 ± 1.65	15.43 ± 1.1	776.32 ± 3.33	2332.89 ± 3.5	3.5 ± 0.64
H876	0.7	0.75	0.64	0.64	8221.19 ± 19.37	7.96 ± 8.21	2.0 ± 4.5	103.03 ± 3.14	279.03 ± 3.09	7.89 ± 2.29
H877	0.51	0.07	1.94	1.94	1578.26 ± 3.4	28.63 ± 1.13	6.71 ± 0.65	330.96 ± 1.13	999.09 ± 1.46	2.0 ± 1.0
H878	10.0	1.19	0.31	0.15	1948.22 ± 35.16	61.3 ± 18.95	16.12 ± 11.1	202.5 ± 7.82	643.45 ± 8.67	31.59 ± 19.2
H879	1.69	0.26	0.23	—	248.67 ± 2.51	0.67 ± 1.46	1.87 ± 1.0	7.53 ± 0.87	24.7 ± 0.84	0.0 ± 0.63
H881	10.0	0.26	3.42	—	0.0 ± 3.32	0.77 ± 2.06	1.71 ± 1.41	5.31 ± 1.39	3.09 ± 1.3	0.09 ± 1.33
H881	0.76	0.11	0.57	—	66.53 ± 2.42	0.25 ± 1.43	3.6 ± 1.05	0.51 ± 0.99	0.95 ± 0.96	0.0 ± 0.7
H884	0.76	0.16	1.07	0.73	4070.94 ± 9.92	88.48 ± 3.85	15.47 ± 2.01	1016.75 ± 3.54	2891.21 ± 3.97	0.99 ± 1.86
H886	0.42	0.0	2.26	0.93	1832.39 ± 5.3	18.45 ± 2.91	10.09 ± 1.33	255.75 ± 1.93	725.9 ± 2.02	3.82 ± 1.27
H887	−1.41	0.35	1.43	0.15	1788.64 ± 8.26	43.17 ± 3.22	6.74 ± 2.17	277.71 ± 2.28	664.28 ± 2.77	4.93 ± 2.21
H89	0.75	1.37	0.57	0.62	90941.12 ± 730.66	382.36 ± 371.85	315.39 ± 181.16	1934.23 ± 98.15	5391.77 ± 104.62	569.34 ± 166.9
H899	0.94	0.38	1.21	—	3077.91 ± 7.42	63.62 ± 2.36	0.39 ± 1.96	396.6 ± 3.35	513.91 ± 4.08	0.33 ± 1.1
H9	10.0	0.0	2.92	3.84	208.81 ± 5.62	46.33 ± 2.8	1.19 ± 2.3	226.21 ± 2.4	691.87 ± 3.08	0.67 ± 4.0
H90	0.54	0.56	0.19	0.87	11510.98 ± 74.49	114.88 ± 36.46	125.01 ± 25.56	1038.51 ± 20.35	3758.09 ± 29.31	216.77 ± 26.44
H900	10.0	0.02	0.88	—	685.79 ± 2.85	55.79 ± 1.34	2.8 ± 1.04	420.02 ± 2.64	1353.17 ± 2.72	1.57 ± 0.72
H901	10.0	0.16	−0.17	—	154.12 ± 2.07	2.86 ± 1.09	1.15 ± 0.65	29.11 ± 0.76	91.17 ± 0.87	6.26 ± 0.39
H903	0.41	1.9	−0.04	—	58050.34 ± 364.34	144.02 ± 133.25	13.09 ± 51.77	200.99 ± 25.45	531.94 ± 25.46	0.0 ± 8.93
H904	0.99	0.0	1.48	—	274.46 ± 1.8	2.99 ± 0.72	1.34 ± 0.49	49.47 ± 0.55	147.03 ± 0.65	0.76 ± 0.43
H905	0.69	3.0	0.69	—	0.0 ± 23429.28	36445.24 ± 12984.65	7301.92 ± 4019.43	267.84 ± 1295.04	0.0 ± 1077.46	975.85 ± 284.26
H905	10.0	3.0	0.14	—	99088.72 ± 8990.4	0.0 ± 4204.62	35.0 ± 1447.2	117.74 ± 409.31	1228.29 ± 381.65	0.0 ± 182.35
H905	10.0	2.32	0.17	—	7129.07 ± 1231.69	0.0 ± 655.84	0.0 ± 219.97	0.0 ± 84.8	0.0 ± 81.99	263.95 ± 52.49
H908	6.45	0.33	0.38	—	73.38 ± 3.72	0.0 ± 1.91	0.0 ± 1.32	1.17 ± 1.13	2.77 ± 1.11	0.95 ± 0.6
H908	4.34	0.0	−4.07	—	16.87 ± 2.33	0.0 ± 1.34	1.89 ± 1.05	0.0 ± 1.03	0.0 ± 1.03	0.0 ± 1.51

Continued on Next Page. . .

Chart A.1 – Continued

Object name	EW	c(Hβ)	$f_{Red900/5500}$	$f_{Red400/8500}$	[O II] λ3727 Å [F_λ]	[Ne III] λ3869 Å [F_λ]	[O III] λ4363 Å [F_λ]	[O III] λ4959 Å [F_λ]	[O III] λ5007 Å [F_λ]	[N II] λ5755 Å [F_λ]
H91	10.0	0.52	1.49	1.67	2224.21 ± 75.72	244.42 ± 48.22	12.22 ± 32.68	1281.53 ± 22.47	4215.9 ± 26.44	19.19 ± 27.33
H92	0.16	2.37	0.22	−0.11	0.0 ± 0.0	0.0 ± 23502.5	325.19 ± 10256.35	11567.79 ± 2832.66	0.0 ± 2737.2	0.0 ± 0.0
H92	10.0	0.0	2.51	0.25	0.0 ± 0.0	44.27 ± 8.84	6.31 ± 4.99	163.6 ± 4.5	451.22 ± 5.08	0.0 ± 0.0
H925	1.2	0.61	0.49	0.53	291.76 ± 14.36	7.75 ± 9.66	10.79 ± 6.06	0.0 ± 4.55	0.0 ± 4.11	4.91 ± 7.07
H926	1.66	0.49	0.26	0.87	765.76 ± 11.19	75.28 ± 6.45	14.99 ± 4.33	165.65 ± 3.59	501.55 ± 4.07	0.0 ± 3.6
H93	2.1	0.49	1.01	0.87	16588.18 ± 51.41	96.21 ± 21.86	0.79 ± 14.62	793.54 ± 14.41	2601.84 ± 13.61	50.26 ± 39.09
H93	10.0	0.23	1.25	0.21	26663.12 ± 74.46	10.8 ± 34.94	0.0 ± 30.47	263.11 ± 27.84	887.06 ± 25.49	5.84 ± 21.27
H94	1.09	0.96	12.76	1.42	7401.92 ± 76.72	0.0 ± 38.37	2.5 ± 24.83	108.38 ± 17.24	312.77 ± 17.99	1.61 ± 43.57
H95	0.73	2.55	1.14	1.25	0.0 ± 49715.57	30402.33 ± 39918.59	31271.51 ± 7508.3	0.0 ± 2918.83	0.0 ± 1898.82	0.0 ± 5727.95
H96	0.44	0.0	2.34	3.15	6430.08 ± 30.26	0.0 ± 23.39	54.14 ± 9.99	333.19 ± 9.61	970.13 ± 9.63	30.13 ± 78.31
H963	1.11	0.0	0.22	—	23.96 ± 1.11	0.0 ± 0.65	0.83 ± 0.49	0.8 ± 0.52	0.0 ± 0.54	0.0 ± 0.33
H979	1.32	0.8	1.1	0.6	941.2 ± 21.93	31.2 ± 13.2	17.25 ± 8.5	30.94 ± 6.26	74.37 ± 5.98	0.0 ± 6.63
H98	−2.0	0.0	2.66	—	3373.85 ± 24.64	22.29 ± 17.2	20.58 ± 13.82	100.93 ± 12.4	309.03 ± 11.81	26.46 ± 30.56
H980	3.57	0.57	1.3	1.14	8359.2 ± 59.26	19.1 ± 26.92	0.0 ± 20.28	1257.05 ± 17.02	3624.98 ± 16.03	0.0 ± 22.95
H99	1.06	0.54	0.78	0.96	221.38 ± 8.01	0.0 ± 4.73	0.0 ± 3.19	0.58 ± 2.86	3.71 ± 2.86	2.67 ± 2.94
H99	1.9	0.12	1.04	−0.06	648.85 ± 3.11	4.42 ± 2.12	6.18 ± 1.38	6.26 ± 1.26	22.36 ± 1.28	0.0 ± 1.54
H993	10.0	0.13	0.56	0.98	7228.99 ± 11.01	479.5 ± 4.66	112.23 ± 3.45	762.95 ± 10.27	2169.5 ± 8.5	31.74 ± 0.87
H994	1.31	0.09	0.97	0.14	1564.58 ± 3.11	14.25 ± 1.25	2.44 ± 0.65	117.79 ± 0.85	374.83 ± 0.98	3.82 ± 0.66
H995	3.33	0.38	0.54	0.48	909.48 ± 3.66	0.74 ± 1.49	0.82 ± 0.99	32.74 ± 0.93	88.06 ± 0.92	0.0 ± 0.77
H997	−2.0	0.0	1.18	2.57	1747.93 ± 3.0	93.44 ± 0.97	9.28 ± 0.56	507.03 ± 1.67	1427.9 ± 1.86	2.09 ± 0.76
H998	1.83	0.0	0.93	0.91	53.27 ± 0.98	5.75 ± 0.52	0.56 ± 0.39	18.26 ± 0.39	53.25 ± 0.43	0.16 ± 0.66

Chart A.2: Accepted values of PyNeb- and NEAT-derived total abundances of oxygen, nitrogen, sulfur, and neon relative to hydrogen for H II regions

Object name	PyNeb				NEAT			
	$12+\log(O/H)$	$12+\log(N/H)$	$12+\log(S/H)$	$12+\log(Ne/H)$	$12+\log(O/H)$	$12+\log(N/H)$	$12+\log(S/H)$	$12+\log(Ne/H)$
H1003	—	—	—	—	8.22 ± 0.04	6.60 ± 0.03	6.84 ± 0.05	7.73 ± 0.03
H1004	8.66 ± 0.13	7.05 ± 0.05	6.80 ± 0.03	7.98 ± 0.11	8.68 ± 0.20	7.10 ± 0.07	7.81 ± 0.04	8.10 ± 0.20
H1020	—	—	—	—	8.83 ± 0.25	7.61 ± 0.12	7.21 ± 0.28	8.75 ± 0.35
H1024	—	—	—	—	8.46 ± 0.62	6.95 ± 0.12	7.91 ± 0.10	7.74 ± 0.60
H1032	8.43 ± 0.10	6.99 ± 0.05	6.87 ± 0.10	7.61 ± 0.10	8.28 ± 0.12	7.02 ± 0.04	8.56 ± 0.12	7.46 ± 0.09
H1034	8.58 ± 0.00	7.22 ± 0.00	7.13 ± 0.00	—	8.13 ± 0.21	7.14 ± 0.16	7.95 ± 0.26	—
H1047	—	—	—	—	8.80 ± 0.25	7.42 ± 0.19	8.74 ± 0.66	8.33 ± 0.25
H1069	—	—	—	—	8.86 ± 0.17	7.25 ± 0.07	8.55 ± 0.37	7.88 ± 0.14
H1073	8.37 ± 0.39	7.18 ± 0.22	6.23 ± 0.21	6.77 ± 0.66	—	—	—	—
H1096	—	—	—	—	8.21 ± 0.06	6.34 ± 0.92	7.70 ± 0.58	7.54 ± 0.31
H11	—	—	—	—	8.48 ± 0.18	7.42 ± 0.09	6.99 ± 0.18	7.05 ± 0.22
H116	8.51 ± 0.33	7.31 ± 0.18	6.62 ± 0.29	8.06 ± 0.54	8.53 ± 0.06	7.28 ± 0.03	7.07 ± 0.19	7.65 ± 0.07
H117	8.51 ± 0.05	7.12 ± 0.03	6.29 ± 0.10	7.37 ± 0.08	—	—	—	—
H1181	8.47 ± 0.33	7.19 ± 0.30	8.29 ± 0.72	7.33 ± 0.51	—	—	—	—
H1182	8.10 ± 0.15	6.87 ± 0.08	6.10 ± 0.10	7.75 ± 0.18	7.74 ± 0.44	6.97 ± 0.37	6.69 ± 0.54	7.59 ± 0.67
H1198	8.75 ± 0.41	7.52 ± 0.25	7.39 ± 1.05	—	—	—	—	—
H120	8.18 ± 0.11	7.01 ± 0.06	6.41 ± 0.16	7.37 ± 0.12	8.29 ± 0.12	7.11 ± 0.07	7.58 ± 0.23	7.51 ± 0.17
H1202	8.70 ± 1.21	7.52 ± 0.52	8.28 ± 3.98	—	—	—	—	—
H121	8.82 ± 0.22	7.35 ± 0.09	6.85 ± 0.12	7.88 ± 0.19	8.39 ± 0.10	7.27 ± 0.08	10.31 ± 0.49	7.60 ± 0.11
H126	8.13 ± 0.07	7.17 ± 0.04	6.36 ± 0.10	7.27 ± 0.08	8.36 ± 0.16	7.32 ± 0.06	8.12 ± 0.17	7.59 ± 0.10
H132	8.20 ± 0.08	6.79 ± 0.04	6.25 ± 0.09	7.18 ± 0.07	8.24 ± 0.08	6.90 ± 0.10	7.63 ± 0.12	7.41 ± 0.13
H140	8.59 ± 0.12	6.55 ± 0.06	6.20 ± 0.04	7.69 ± 0.10	—	—	—	—
H145	8.59 ± 0.22	7.18 ± 0.08	6.14 ± 0.21	7.95 ± 0.17	—	—	—	—
H155	—	—	—	—	8.16 ± 0.11	7.01 ± 0.07	8.53 ± 0.37	7.26 ± 0.18
H157	8.82 ± 0.16	7.26 ± 0.10	6.99 ± 0.18	8.37 ± 0.21	—	—	—	—
H16	—	—	—	—	8.62 ± 0.49	7.36 ± 0.35	7.87 ± 0.37	—
H163	8.19 ± 0.14	6.75 ± 0.06	6.30 ± 0.08	7.34 ± 0.12	7.92 ± 0.12	6.71 ± 0.04	7.20 ± 0.13	7.10 ± 0.09
H165	—	—	—	—	8.74 ± 0.13	7.22 ± 0.04	8.46 ± 0.21	7.94 ± 0.15
H169	8.88 ± 0.25	7.00 ± 0.15	6.51 ± 0.14	8.54 ± 0.39	—	—	—	—
H170	—	—	—	—	8.50 ± 0.13	7.24 ± 0.07	6.44 ± 0.13	7.72 ± 0.17
H174	—	—	—	—	8.73 ± 0.64	7.40 ± 0.11	7.98 ± 0.70	7.52 ± 0.22
H179	—	—	—	—	8.46 ± 0.27	7.29 ± 0.07	8.12 ± 0.34	7.22 ± 0.25
H184	8.62 ± 0.96	7.16 ± 0.27	6.54 ± 0.28	7.67 ± 0.77	8.41 ± 0.43	7.36 ± 0.20	7.10 ± 0.31	7.70 ± 0.41
H185	9.16 ± 0.77	7.36 ± 0.38	7.39 ± 0.28	8.61 ± 0.72	8.40 ± 0.22	7.21 ± 0.13	7.22 ± 0.71	8.07 ± 0.28
H187	8.62 ± 0.37	6.94 ± 0.09	6.67 ± 0.04	7.78 ± 0.26	8.60 ± 0.15	6.99 ± 0.04	7.84 ± 0.03	7.84 ± 0.14
H189	—	—	—	—	8.48 ± 0.18	7.15 ± 0.11	7.41 ± 0.32	7.81 ± 0.18
H190	8.40 ± 0.05	7.28 ± 0.03	6.61 ± 0.05	7.76 ± 0.06	—	—	—	—
H192	8.66 ± 0.14	7.34 ± 0.10	6.19 ± 0.07	7.79 ± 0.26	—	—	—	—
H197	8.66 ± 0.17	7.74 ± 0.10	7.27 ± 0.46	7.47 ± 0.30	7.92 ± 0.08	7.36 ± 0.03	7.41 ± 0.48	6.81 ± 0.12
H198	—	—	—	—	8.53 ± 0.06	7.66 ± 0.11	9.60 ± 0.18	7.63 ± 0.10
H201	8.48 ± 0.33	7.23 ± 0.16	6.36 ± 0.12	7.78 ± 0.29	—	—	—	—
H208	—	—	—	—	8.48 ± 0.06	7.51 ± 0.02	8.80 ± 0.25	7.62 ± 0.04
H210	—	—	—	—	8.66 ± 0.58	7.45 ± 0.28	8.25 ± 1.56	5.89 ± 2.37

Continued on Next Page. . .

Chart A.2 – Continued

Object name	PyNeb				NEAT			
	12 + log(O/H)	12 + log(N/H)	12 + log(S/H)	12 + log(Ne/H)	12 + log(O/H)	12 + log(N/H)	12 + log(S/H)	12 + log(Ne/H)
H217	—	—	—	—	8.46 ± 0.05	7.27 ± 0.04	6.62 ± 20.03	7.66 ± 0.20
H217	8.87 ± 0.09	7.38 ± 0.05	6.64 ± 0.06	7.78 ± 0.11	8.83 ± 0.19	7.52 ± 0.10	7.50 ± 0.30	7.92 ± 0.21
H222	—	—	—	—	8.38 ± 0.05	6.95 ± 0.15	7.98 ± 0.12	7.80 ± 0.05
H228	8.72 ± 0.39	7.08 ± 0.18	6.44 ± 0.16	7.59 ± 0.35	8.21 ± 0.19	7.00 ± 0.12	7.18 ± 0.50	7.29 ± 0.20
H237	8.48 ± 0.14	6.89 ± 0.06	6.61 ± 0.13	7.64 ± 0.13	8.63 ± 0.23	7.07 ± 0.07	7.52 ± 0.27	8.03 ± 0.17
H241	—	—	—	—	8.32 ± 0.35	7.26 ± 0.14	6.88 ± 0.70	7.18 ± 0.52
H248	8.67 ± 0.24	6.91 ± 0.11	6.44 ± 0.16	7.96 ± 0.20	—	—	—	—
H250	—	—	—	—	8.54 ± 0.12	7.18 ± 0.05	7.02 ± 17.29	7.55 ± 0.33
H257	8.23 ± 0.08	6.83 ± 0.05	6.19 ± 0.07	7.59 ± 0.15	—	—	—	—
H259	—	—	—	—	8.39 ± 0.05	7.17 ± 0.03	8.49 ± 0.16	7.67 ± 0.07
H264	8.99 ± 0.45	7.44 ± 0.29	7.18 ± 1.09	8.79 ± 0.89	—	—	—	—
H266	—	—	—	—	8.37 ± 0.27	6.95 ± 0.09	7.51 ± 3.61	7.63 ± 0.27
H269	8.59 ± 0.25	7.23 ± 0.16	6.35 ± 0.15	7.43 ± 0.47	—	—	—	—
H271	8.66 ± 0.15	7.19 ± 0.07	6.50 ± 0.08	7.90 ± 0.13	9.09 ± 0.39	7.53 ± 0.18	7.43 ± 0.10	8.51 ± 0.38
H272	8.33 ± 0.05	7.26 ± 0.02	7.07 ± 0.04	7.38 ± 0.05	8.18 ± 0.05	7.23 ± 0.02	7.66 ± 0.06	7.33 ± 0.05
H280	—	—	—	—	8.38 ± 0.28	6.89 ± 0.13	7.02 ± 0.08	7.82 ± 0.12
H282	8.78 ± 0.99	7.00 ± 0.43	6.07 ± 0.54	7.61 ± 0.08	—	—	—	—
H286	8.23 ± 0.08	6.81 ± 0.04	6.35 ± 0.11	—	—	—	—	—
H290	8.78 ± 0.08	7.25 ± 0.07	7.05 ± 0.07	8.02 ± 0.08	8.53 ± 0.10	7.17 ± 0.03	7.87 ± 0.08	7.92 ± 0.12
H292	8.39 ± 0.26	6.51 ± 0.12	6.22 ± 0.07	7.52 ± 0.23	8.03 ± 0.10	6.44 ± 0.07	7.43 ± 0.14	7.40 ± 0.09
H294	8.99 ± 0.51	7.08 ± 0.23	6.91 ± 0.17	7.97 ± 0.46	8.51 ± 0.50	7.04 ± 0.26	8.03 ± 0.27	7.76 ± 0.70
H295	—	—	—	—	8.75 ± 0.16	7.43 ± 0.09	7.36 ± 0.07	8.19 ± 0.18
H296	8.95 ± 0.59	7.11 ± 0.28	6.30 ± 0.28	7.83 ± 0.55	—	—	—	—
H299	8.28 ± 0.26	6.88 ± 0.15	6.37 ± 0.37	6.93 ± 0.41	8.33 ± 0.33	7.08 ± 0.18	6.31 ± 14.03	6.96 ± 0.72
H299	8.62 ± 0.30	7.04 ± 0.16	6.23 ± 0.14	7.21 ± 0.29	—	—	—	—
H303	—	—	—	—	7.94 ± 0.17	6.85 ± 0.11	6.94 ± 0.24	7.43 ± 0.27
H306	—	—	—	—	8.56 ± 0.20	7.08 ± 0.09	6.77 ± 0.10	7.51 ± 0.23
H309	—	—	—	—	8.43 ± 0.13	6.96 ± 0.07	7.17 ± 0.08	7.66 ± 0.13
H31	9.01 ± 0.87	7.23 ± 0.39	6.31 ± 0.35	7.35 ± 0.80	8.86 ± 0.42	7.45 ± 0.22	6.76 ± 0.37	7.43 ± 0.58
H312	8.86 ± 0.29	7.14 ± 0.14	6.29 ± 0.20	8.13 ± 0.26	8.36 ± 0.99	6.97 ± 0.29	7.13 ± 0.25	7.82 ± 0.77
H319	8.68 ± 0.19	7.12 ± 0.09	6.71 ± 0.08	8.05 ± 0.17	—	—	—	—
H32	8.54 ± 0.69	7.41 ± 0.22	7.25 ± 0.19	7.05 ± 0.53	7.90 ± 0.12	7.28 ± 0.09	8.44 ± 0.48	6.62 ± 0.13
H324	8.64 ± 0.32	6.82 ± 0.16	6.49 ± 0.10	7.45 ± 0.29	8.18 ± 0.52	6.78 ± 0.24	6.34 ± 0.49	6.71 ± 0.49
H324	9.30 ± 0.48	7.11 ± 0.33	6.48 ± 0.28	7.56 ± 0.48	8.30 ± 0.26	7.39 ± 0.12	7.08 ± 0.06	7.23 ± 0.26
H327	8.52 ± 0.16	7.47 ± 0.10	6.62 ± 0.09	7.28 ± 0.23	—	—	—	—
H328	—	—	—	—	8.36 ± 0.20	6.64 ± 0.14	6.61 ± 0.15	7.07 ± 0.17
H33	8.14 ± 0.12	6.82 ± 0.05	6.27 ± 0.08	7.20 ± 0.09	8.20 ± 0.13	6.95 ± 0.08	7.52 ± 0.13	7.43 ± 0.10
H335	8.84 ± 0.12	7.15 ± 0.08	6.75 ± 0.19	8.06 ± 0.17	—	—	—	—
H335	—	—	—	—	8.39 ± 0.19	6.80 ± 0.08	7.97 ± 0.18	7.71 ± 0.22
H34	8.43 ± 0.11	7.10 ± 0.07	6.21 ± 0.07	7.46 ± 0.11	8.69 ± 0.55	7.31 ± 0.11	7.00 ± 0.10	7.95 ± 0.21
H340	8.45 ± 0.11	6.73 ± 0.06	6.95 ± 0.16	7.49 ± 0.11	8.40 ± 0.14	6.72 ± 0.06	7.90 ± 0.27	7.52 ± 0.16
H340	8.72 ± 0.14	7.11 ± 0.09	7.05 ± 0.19	—	—	—	—	—
H343	8.30 ± 0.07	6.61 ± 0.04	6.59 ± 0.08	7.15 ± 0.06	8.11 ± 0.10	6.59 ± 0.06	7.83 ± 0.28	7.11 ± 0.12
H347	—	—	—	—	8.74 ± 0.13	6.99 ± 0.06	7.65 ± 0.07	8.25 ± 0.10
H364	—	—	—	—	8.59 ± 0.15	7.18 ± 0.18	8.91 ± 0.86	8.20 ± 0.21
H37	—	—	—	—	8.05 ± 0.30	7.31 ± 0.20	7.63 ± 0.41	8.49 ± 0.34

Chart A.2 – Continued

Object name	PyNeb				NEAT			
	$12 + \log(O/H)$	$12 + \log(N/H)$	$12 + \log(S/H)$	$12 + \log(Ne/H)$	$12 + \log(O/H)$	$12 + \log(N/H)$	$12 + \log(S/H)$	$12 + \log(Ne/H)$
H373	—	—	—	—	8.33 ± 0.06	7.96 ± 0.04	7.50 ± 0.02	8.27 ± 0.31
H374	—	—	—	—	8.64 ± 0.31	7.50 ± 0.18	6.46 ± 0.17	7.47 ± 0.38
H376	—	—	—	—	8.23 ± 0.13	7.68 ± 0.07	7.02 ± 0.11	6.83 ± 0.21
H378	8.43 ± 0.15	7.19 ± 0.07	6.57 ± 0.07	7.58 ± 0.13	8.60 ± 0.11	7.38 ± 0.05	7.90 ± 0.20	7.87 ± 0.12
H381	—	—	—	—	8.33 ± 0.06	7.07 ± 0.06	6.65 ± 65.08	7.50 ± 0.08
H387	—	—	—	—	8.51 ± 0.06	7.47 ± 0.06	9.29 ± 0.26	7.77 ± 0.09
H388	—	—	—	—	9.19 ± 0.21	7.81 ± 0.15	9.66 ± 0.35	8.77 ± 0.61
H390	—	—	—	—	8.69 ± 0.27	7.31 ± 0.06	6.61 ± 0.06	7.68 ± 0.10
H393	8.93 ± 0.34	7.25 ± 0.17	6.47 ± 0.18	8.22 ± 0.35	—	—	—	—
H4	8.81 ± 0.18	7.30 ± 0.09	7.23 ± 0.13	7.77 ± 0.16	9.01 ± 0.19	7.61 ± 0.23	6.69 ± 31.16	8.30 ± 0.17
H40	8.47 ± 0.22	7.11 ± 0.10	6.42 ± 0.13	7.47 ± 0.20	—	—	—	—
H431	8.72 ± 0.81	7.04 ± 0.38	6.94 ± 0.82	7.76 ± 1.00	—	—	—	—
H432	8.77 ± 0.16	7.47 ± 0.10	7.44 ± 0.29	6.63 ± 0.27	—	—	—	—
H434	8.42 ± 0.48	6.96 ± 0.14	6.18 ± 0.26	7.59 ± 0.41	8.21 ± 0.43	6.84 ± 0.15	7.40 ± 0.18	7.42 ± 0.32
H435	8.48 ± 0.08	7.44 ± 0.05	6.73 ± 0.18	7.48 ± 0.14	7.74 ± 0.09	7.15 ± 0.03	6.89 ± 0.18	6.95 ± 0.17
H437	8.57 ± 0.08	7.23 ± 0.05	6.88 ± 0.15	7.63 ± 0.09	8.40 ± 0.12	7.25 ± 0.06	8.26 ± 0.38	7.78 ± 0.15
H44	8.27 ± 0.12	6.88 ± 0.07	6.20 ± 0.11	7.05 ± 0.14	8.70 ± 0.14	7.35 ± 0.11	6.85 ± 0.17	7.85 ± 0.21
H466	—	—	—	—	9.12 ± 0.36	7.72 ± 0.22	7.34 ± 0.18	7.92 ± 0.38
H47	8.36 ± 0.16	7.06 ± 0.07	6.59 ± 0.20	7.22 ± 0.16	—	—	—	—
H477	—	—	—	—	8.09 ± 0.02	6.99 ± 0.02	6.02 ± 0.04	6.80 ± 0.40
H478	—	—	—	—	8.51 ± 0.05	7.35 ± 0.04	8.67 ± 0.17	7.94 ± 0.07
H50	8.73 ± 0.30	7.35 ± 0.18	7.07 ± 0.62	7.23 ± 0.55	—	—	—	—
H515	8.31 ± 0.12	7.16 ± 0.07	6.61 ± 0.13	7.17 ± 0.18	—	—	—	—
H521	8.41 ± 0.10	7.17 ± 0.06	6.57 ± 0.13	7.30 ± 0.24	—	—	—	—
H56	8.49 ± 0.00	7.17 ± 0.00	6.30 ± 0.00	7.92 ± 0.00	7.39 ± 0.23	6.70 ± 0.14	5.94 ± 0.09	6.84 ± 0.27
H57	—	—	—	—	8.27 ± 0.09	7.09 ± 0.11	9.92 ± 0.17	7.22 ± 0.10
H597	8.51 ± 0.28	8.70 ± 0.26	9.26 ± 0.52	8.04 ± 0.36	—	—	—	—
H614	8.26 ± 0.14	6.61 ± 0.07	6.25 ± 0.10	7.02 ± 0.15	7.99 ± 0.10	6.61 ± 0.08	6.84 ± 0.19	7.11 ± 0.41
H62	8.38 ± 0.09	6.91 ± 0.05	6.10 ± 0.06	7.44 ± 0.10	8.03 ± 0.12	6.82 ± 0.05	6.54 ± 0.12	7.34 ± 0.12
H621	—	—	—	—	7.90 ± 0.12	6.66 ± 0.17	7.23 ± 0.25	7.49 ± 0.12
H63	8.66 ± 0.11	7.31 ± 0.06	6.50 ± 0.09	7.48 ± 0.17	9.06 ± 0.44	7.68 ± 0.22	7.53 ± 0.68	7.98 ± 0.18
H64	8.74 ± 0.10	7.33 ± 0.06	6.49 ± 0.09	7.23 ± 0.14	8.54 ± 0.11	7.40 ± 0.18	7.37 ± 0.38	7.21 ± 0.19
H644	8.89 ± 0.40	7.04 ± 0.20	6.26 ± 0.21	6.19 ± 0.56	—	—	—	—
H645	8.62 ± 0.31	6.95 ± 0.15	6.24 ± 0.19	7.32 ± 0.28	—	—	—	—
H646	8.53 ± 0.56	6.94 ± 0.24	6.25 ± 0.50	7.74 ± 1.17	—	—	—	—
H647	—	—	—	—	8.63 ± 0.21	7.14 ± 0.11	8.24 ± 0.29	7.81 ± 0.22
H657	—	—	—	—	8.89 ± 0.14	7.23 ± 0.08	7.80 ± 0.35	8.17 ± 0.18
H659	—	—	—	—	8.54 ± 0.28	7.15 ± 0.16	7.61 ± 0.14	7.79 ± 0.21
H67	8.48 ± 0.15	7.23 ± 0.08	6.85 ± 0.21	7.60 ± 0.16	8.44 ± 0.23	7.25 ± 0.09	9.13 ± 0.26	7.73 ± 0.22
H670	—	—	—	—	8.66 ± 0.13	7.38 ± 0.07	7.92 ± 0.81	7.78 ± 0.21
H672	8.73 ± 0.40	7.21 ± 0.12	6.60 ± 0.08	7.10 ± 0.30	8.72 ± 0.11	7.31 ± 0.07	7.64 ± 0.07	7.32 ± 0.12
H678	—	—	—	—	8.79 ± 0.11	7.29 ± 0.08	9.12 ± 0.22	8.14 ± 0.10
H679	8.36 ± 0.15	7.09 ± 0.09	6.77 ± 0.20	7.17 ± 0.40	7.76 ± 0.12	6.94 ± 0.14	7.04 ± 0.18	6.52 ± 0.93
H681	—	—	—	—	9.23 ± 0.14	7.81 ± 0.07	6.77 ± 0.16	9.00 ± 0.28
H682	8.77 ± 0.11	7.43 ± 0.07	6.49 ± 0.11	7.61 ± 0.18	—	—	—	—
H69	—	—	—	—	8.25 ± 0.12	7.11 ± 0.03	7.48 ± 0.06	7.74 ± 0.13

Chart A.2 – Continued

	PyNeb				NEAT			
Object name	$12 + \log(O/H)$	$12 + \log(N/H)$	$12 + \log(S/H)$	$12 + \log(Ne/H)$	$12 + \log(O/H)$	$12 + \log(N/H)$	$12 + \log(S/H)$	$12 + \log(Ne/H)$
H690	8.63 ± 0.19	7.43 ± 0.07	6.67 ± 0.11	8.05 ± 0.16	—	—	6.45 ± 0.44	—
H692	8.22 ± 0.26	6.87 ± 0.15	6.83 ± 0.31	—	7.99 ± 0.19	6.89 ± 0.11	7.24 ± 0.57	7.47 ± 0.41
H697	—	—	—	—	7.84 ± 0.25	7.03 ± 0.14	9.03 ± 0.57	8.08 ± 0.32
H700	—	—	—	—	8.48 ± 0.08	7.36 ± 0.13	5.82 ± 0.04	7.50 ± 0.03
H701	8.82 ± 0.07	7.34 ± 0.04	6.83 ± 0.05	7.99 ± 0.07	8.18 ± 0.08	7.09 ± 0.02	10.86 ± 0.19	8.07 ± 0.32
H712	—	—	—	—	8.85 ± 0.08	7.81 ± 0.05	9.60 ± 0.12	7.48 ± 0.07
H72	8.29 ± 0.10	7.13 ± 0.05	6.68 ± 0.08	7.58 ± 0.09	8.05 ± 0.06	7.07 ± 0.03	8.41 ± 0.84	7.99 ± 0.29
H727	—	—	—	—	8.98 ± 0.28	7.42 ± 0.11	7.62 ± 0.33	7.13 ± 0.27
H728	8.73 ± 0.10	7.26 ± 0.06	6.43 ± 0.05	7.37 ± 0.13	8.28 ± 0.15	7.20 ± 0.07	7.85 ± 0.10	7.53 ± 0.07
H728	—	—	—	—	8.27 ± 0.07	6.95 ± 0.03	8.25 ± 0.17	7.49 ± 0.05
H735	8.45 ± 0.40	6.07 ± 0.32	6.19 ± 0.45	7.39 ± 0.51	8.30 ± 0.05	7.20 ± 0.05	—	—
H753	8.77 ± 0.33	7.33 ± 0.19	7.07 ± 0.68	6.29 ± 0.52	—	—	7.15 ± 0.40	7.59 ± 0.25
H779	9.07 ± 0.86	7.28 ± 0.52	6.17 ± 0.62	7.63 ± 0.85	8.90 ± 0.11	7.48 ± 0.09	7.55 ± 0.16	7.54 ± 0.12
H78	8.27 ± 0.09	6.95 ± 0.04	6.27 ± 0.08	7.48 ± 0.09	8.21 ± 0.09	7.00 ± 0.19	7.49 ± 0.10	7.60 ± 0.08
H781	8.33 ± 0.08	6.83 ± 0.04	6.75 ± 0.08	7.61 ± 0.08	8.25 ± 0.07	6.87 ± 0.03	7.83 ± 0.06	7.55 ± 0.06
H788a	8.47 ± 0.06	6.96 ± 0.03	6.67 ± 0.07	7.59 ± 0.06	8.34 ± 0.06	6.93 ± 0.02	8.04 ± 0.35	7.89 ± 0.11
H792	8.53 ± 0.08	7.12 ± 0.04	6.65 ± 0.10	7.88 ± 0.08	8.50 ± 0.13	7.16 ± 0.05	8.26 ± 0.41	7.46 ± 0.61
H80	—	—	—	—	8.57 ± 0.58	7.40 ± 0.43	7.07 ± 0.07	7.40 ± 0.06
H807	8.33 ± 0.09	6.85 ± 0.04	6.72 ± 0.04	7.51 ± 0.08	8.15 ± 0.07	6.83 ± 0.02	7.70 ± 0.25	7.75 ± 0.14
H81	—	—	—	—	8.71 ± 0.10	7.49 ± 0.06	8.50 ± 0.07	7.70 ± 0.03
H843	—	—	—	—	8.44 ± 0.02	7.16 ± 0.04	—	—
H848	8.73 ± 1.51	7.14 ± 0.48	6.56 ± 0.30	8.04 ± 1.37	—	—	7.56 ± 0.18	7.46 ± 0.11
H855	8.41 ± 0.08	7.10 ± 0.04	6.91 ± 0.09	7.50 ± 0.09	8.32 ± 0.23	7.04 ± 0.04	—	—
H859	8.41 ± 0.35	7.01 ± 0.30	5.88 ± 0.13	7.38 ± 0.56	—	—	7.87 ± 0.07	7.52 ± 0.06
H862	8.35 ± 0.08	6.92 ± 0.03	6.68 ± 0.04	7.47 ± 0.07	8.30 ± 0.07	6.95 ± 0.03	6.55 ± 0.22	6.14 ± 0.55
H864	8.81 ± 0.59	7.04 ± 0.34	6.51 ± 0.18	7.05 ± 0.85	8.28 ± 0.33	7.07 ± 0.53	7.37 ± 0.18	7.39 ± 0.17
H867	9.30 ± 0.61	7.28 ± 0.37	7.49 ± 2.00	8.15 ± 0.92	8.43 ± 0.17	6.99 ± 0.10	8.09 ± 0.28	7.83 ± 0.17
H873	8.47 ± 0.12	7.26 ± 0.07	6.94 ± 0.20	7.54 ± 0.13	8.61 ± 0.14	7.34 ± 0.06	7.84 ± 0.11	7.32 ± 0.12
H877	8.91 ± 0.19	7.04 ± 0.09	6.62 ± 0.06	7.64 ± 0.18	8.42 ± 0.16	6.85 ± 0.06	—	—
H879	8.40 ± 0.42	6.75 ± 0.24	6.98 ± 0.65	6.41 ± 0.74	—	—	6.91 ± 0.15	7.64 ± 0.17
H884	—	—	—	—	8.58 ± 0.13	6.82 ± 0.05	6.69 ± 0.11	6.80 ± 0.14
H886	8.53 ± 0.19	6.95 ± 0.09	6.53 ± 0.07	7.12 ± 0.18	8.07 ± 0.12	6.78 ± 0.05	8.42 ± 1.10	7.43 ± 0.25
H887	8.44 ± 0.28	7.00 ± 0.12	6.71 ± 0.13	7.51 ± 0.24	8.17 ± 0.24	7.00 ± 0.35	—	—
H90	8.33 ± 0.18	7.97 ± 0.12	7.54 ± 0.22	7.06 ± 0.26	—	—	7.86 ± 0.38	6.85 ± 0.20
H904	8.73 ± 0.26	7.09 ± 0.12	6.71 ± 0.10	7.28 ± 0.27	8.23 ± 0.25	6.97 ± 0.10	6.66 ± 0.15	7.90 ± 0.16
H979	—	—	—	—	8.14 ± 0.02	7.01 ± 0.04	—	—
H994	8.25 ± 0.07	6.90 ± 0.04	6.70 ± 0.12	7.18 ± 0.08	—	—	8.37 ± 0.61	5.38 ± 1.73
H995	—	—	—	—	8.39 ± 0.15	7.14 ± 0.07	6.83 ± 0.14	8.05 ± 0.30
H997	8.62 ± 0.05	7.04 ± 0.02	6.69 ± 0.04	7.77 ± 0.04	8.68 ± 0.15	7.11 ± 0.06	—	—